# Adsorption of K and KO on Hägg iron carbide surfaces and its effect on the adsorption of CO: A DFT study

Thesis submitted in the partial fulfilment for the Masters degree in Chemical Engineering



By

Muhammad Junaid Cariem

B.Sc. (Chemical Engineering)

Supervisor: Professor Eric van Steen

Co-supervisor: Dr. Melissa Petersen

Department of Chemical Engineering
University of Cape Town
Rondebosch
7701
South Africa
2012

**Declarations:**

(i) I hereby grant the University of Cape Town free licence to reproduce for the purpose of research either the whole or any portion of the contents in any manner whatsoever of the above dissertation. I am presenting this dissertation in **FULL/PARTIAL** fulfilment of the requirements for my degree.

(ii) I know the meaning of plagiarism and declare that all of the work in the document, save for that which is properly acknowledged, is my own.

Signature

Date

# ACKNOWLEDGEMENTS

I would like to extend my gratitude to numerous sources for technical and moral assistance:

- Prof. Eric van Steen and Dr. Melissa Petersen for their encouragement, advice and support throughout this work
- My fellow molecular modelling unit students who helped to contribute to this work.
- My wife (Sakeenah), family and friends for their love and support.
- The financial support of UCT.
- The CHPC for access to their computational resources.
- The financial assistance of the National Research Foundation (NRF) towards this research is hereby acknowledged. Opinions expressed and conclusions arrived at, are those of the author and are not necessarily to be attributed to the NRF.

## Synopsis

The Fischer-Tropsch synthesis catalysed by iron is a well established process, used for the conversion of syngas (a mixture of CO and $H_2$) to long chain hydrocarbons. Potassium is typically added as a promoter in iron-based Fischer-Tropsch to improve activity, selectivity and product distribution. The mechanism behind potassium promotion has in the past been explained as a combination of electron donation and electrostatic interaction. However, despite the importance of potassium as a promoter, the nature of the potassium species on the surface; whether it is present as metallic potassium (K) or is present as another species has received relatively little investigation. No research has been published as of yet as to the effects of potassium adsorption on a Hägg iron carbide surface or the effects on CO adsorption when co-adsorbing CO with potassium on a Hägg iron carbide surface.

In this study density functional theory (DFT) has been used to investigate:

- The adsorption of CO on the $Fe_5C_2(100)_{0.00}$ and $Fe_5C_2(100)_{0.098}$ surfaces.
- The adsorption of K, O and KO on the $Fe_5C_2(100)_{0.00}$ and $Fe_5C_2(100)_{0.098}$ surfaces.
- The co-adsorption of K, O or KO with CO on the $Fe_5C_2(100)_{0.00}$ and $Fe_5C_2(100)_{0.098}$ surfaces.

A thermodynamic analysis was done to investigate the stability of K versus the stability of KO at Fischer-Tropsch conditions. The adsorption of CO on the $Fe_5C_2(100)_{0.00}$ and $Fe_5C_2(100)_{0.098}$ surfaces was done as a pre-cursor to investigating the effect of co-adsorbing K, O or KO with CO on the CO adsorption energy, CO stretching frequency and CO bond length. Subsurface carbon on the $Fe_5C_2(100)_{0.00}$ surface caused a decrease in the CO adsorption energy of 0.38eV when compared to CO adsorption on a similar site with subsurface iron. On the $Fe_5C_2(100)_{0.098}$ surface, the lack of subsurface carbon allowed for CO adsorption in the 1F adsorption configuration on top of a valley iron site.

The strength of potassium adsorption on both surfaces was calculated to be similar to that of CO in its most stable state (~1.60eV). Potassium is highly mobile across the surface, with a maximum barrier for K diffusion of 0.02eV calculated on both surfaces. A Bader analysis revealed that potassium donates electrons to the surface (~0.72) and that the electron donation from the potassium to the surface is localised and affects only the iron atoms not the carbon atoms.

Synopsis

The co-adsorption of O with K leads to a significant increase in the stability of O adsorption on both surfaces, with increases in the O adsorption energy of O of ~0.60eV on the $Fe_5C_2(100)_{0.00}$ surface and ~0.40eV on the $Fe_5C_2(100)_{0.098}$ surface. The O also stabilises the K with the maximum barrier for diffusion of K increasing to 0.07eV on the $Fe_5C_2(100)_{0.00}$ surface and 0.15eV on the $Fe_5C_2(100)_{0.098}$ surface. However, these maximum barriers for diffusion are still extremely low, indicating that potassium is still highly mobile on the surface. The charge density difference plot showed some polarisation of the O towards the K and vice versa, indicating interaction between the two species. No orbital overlap between the adsorbed O and adsorbed K was observed in the charge density difference plot. This together with the results from a local density of states (LDOS) plot indicates that the interaction between O and K on the surface is ionic in nature.

The co-adsorption of CO with either K or KO on both the $Fe_5C_2(100)_{0.00}$ and $Fe_5C_2(100)_{0.098}$ surfaces resulted in a significant increase in the calculated CO adsorption energy coupled with an increase in the CO bond length and a decrease in the CO stretching frequency. The magnitude of the increases in calculated CO adsorption energy and CO bond length as well as the magnitude of the decrease in the CO stretching frequency was virtually the same irrespective of whether CO was co-adsorbed with K or KO. The combination of these results shows that K and KO both enhance CO adsorption to a similar degree on Hägg iron carbide surfaces while possibly making CO dissociation more facile.

Co-adsorbing CO with O on the $Fe_5C_2(100)_{0;00}$ surface lead to a significant decrease in the CO adsorption energies, an increase in CO bond length and an increase in the CO stretching frequency in certain cases. This negative effect on CO adsorption is very localised and restricted to CO adsorption sites which are near to the adsorbed O and have subsurface carbon which prevents CO migration away from the O to a more stable site. On the $Fe_5C_2(100)_{0.098}$ surface where no subsurface carbon is present, the CO migrates away from the O to a site unaffected by the presence of O.

A thermodynamic analysis based on a reaction that could occur at Fischer-Tropsch conditions due to the large excess of $H_2O$ and $H_2$ ($K_{ads} + H_2O_{(g)} \leftrightarrows KO_{ads} + H_{2\,(g)}$) showed that the forward reaction for the formation of KO is vastly more thermodynamically favoured. Therefore, KO not K should be present at Fischer-Tropsch conditions.

**Table of Contents**

Table of Contents

Table of Contents

List of figures

List of tables

# Chapter 2 : Introduction

## 1.1. The Fischer-Tropsch Process

### 1.1.1 History

The Fischer-Tropsch synthesis is the catalytic hydrogenation of carbon monoxide over catalysts containing transition metal yielding long chain hydrocarbons. This process was developed in the 1920s by German scientists Franz Fischer and Hans Tropsch (Dry, 2004). The original idea behind the Fischer-Tropsch process was to produce synthetic fuels from coal, as a replacement for diesel or petrol refined from oil as Germany is relatively coal-rich but has low oil reserves (Bowen and Irwin, 2006). Fischer-Tropsch synthesis is currently seen as a possible route to these liquid fuels (in particular diesel) from alternative carbon containing feedstock, such as natural gas or biomass.

Figure 1.1 shows a block diagram of the Fischer-Tropsch process. The first step is the formation of synthesis gas, a mixture of hydrogen and carbon monoxide, from a carbon containing source (e.g. natural gas, oil residue, coal or biomass) (van Steen and Claeys, 2008) via reforming or gasification. These processes are endothermic and the heat required for this process results in the formation of the large quantities of $CO_2$ associated with this process. The synthesis gas contains further contaminants such as $H_2S$, $NH_3$, HCN, halide compounds, and tars (Faaij et al., 2002; Faaij et al., 2004) depending on the source of the feedstock for synthesis gas production. Therefore, the synthesis gas must be purified to prevent poisoning of the catalyst. Furthermore, the $H_2$/CO ratio in the synthesis gas must be adjusted by the water gas shift reaction to the usage ratio of $H_2$/CO in the Fischer-Tropsch synthesis, to avoid a build-up of excess components in the recycle loop.

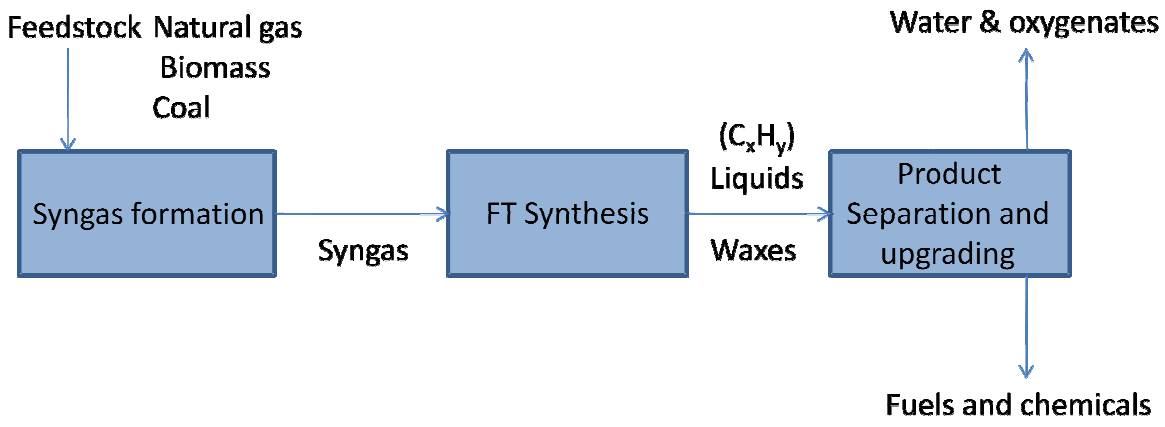


**Figure 2.1:** Simplified block diagram for a typical Fischer-Tropsch process

The purified synthesis gas is then passed over either an iron-based or a cobalt-based catalyst to produce a wide range of hydrocarbons. The light hydrocarbons can be used as fuel gas or recycled back to the reformer (Dry, 2004). Therefore, the formation of these hydrocarbons must be minimized in this process to increase the efficiency of the overall process. The diesel yield of the process can be further maximized by hydro-cracking the heavy hydrocarbons produced in the Fischer-Tropsch synthesis (Faaij el al., 2002).

### 1.1.2 Catalysts for the Fischer-Tropsch synthesis

Iron, cobalt, nickel and ruthenium are the metals that are sufficiently active for the Fischer-Tropsch synthesis to be used commercially (Dry, 2004). Looking at the relative costs of these metals (see Table 1.1), it is clear that iron is the cheapest catalyst.



**Table 2.1:** Relative costs of Metals (2012)

| Metal | Relative Cost |
|---|---|
| **Fe** [1] | 1 |
| **Ni** [2] | 130 |
| **Co** [3] | 260 |
| **Ru** [4] | 28000 |

[1] http://www.indexmundi.com/commodities/?commodity=iron-ore (Accessed 15 March 2012)

[2] http://www.indexmundi.com/commodities/?commodity=nickel (Accessed 15 March 2012)

[3] http://www.consensuseconomics.com/Cobalt_Price_Forecasts.htm (Accessed 15 March 2012)

[4] http://apps.catalysts.basf.com/apps/eibprices/mp (Accessed 15 March 2012)

Nickel is not used commercially in Fischer-Tropsch synthesis due to inherent problems. At low pressures methane is produced selectively. At high pressures, volatile nickel carbonyls are formed resulting in a loss of catalytically active material from the reactor. Ruthenium is too expensive and rare to be used for commercial scale production, as large amounts of it would be required. Therefore, iron and cobalt are the only commercially viable options as a basis for a catalyst for the Fischer-Tropsch synthesis.

There are distinct differences between the use of iron-based and cobalt-based catalysts for the Fischer-Tropsch synthesis. Cobalt is only used in low temperature Fischer-Tropsch synthesis (up to 230$^{o}$C) as the selectivity for the formation of methane increases dramatically at higher temperatures (Dry, 2004). Iron-based catalysts can be utilised in both low temperature and high temperature Fischer-Tropsch synthesis (Dry, 2002). The low temperature iron-based Fischer-Tropsch synthesis is operated at between 240 and 270ºC and produces high molecular weight waxes and diesel range hydrocarbons. High temperature Fischer-Tropsch synthesis is operated between 300 and 350ºC and produces primarily gasoline and short chain olefins.

Iron-based Fischer-Tropsch catalysts show activity for the water-gas shift reaction (in contrast to cobalt-based Fischer-Tropsch catalysts) (Pirola et al., 2009). This means that iron-based Fischer-Tropsch catalysts are more versatile than the cobalt-based Fischer-Tropsch catalysts, since they can be applied for the conversion of synthesis gas with a low hydrogen to carbon monoxide ratio, such as synthesis gas derived from coal or biomass, without the inclusion of an additional water-gas shift reactor.

The rate of formation of organic product compounds in the Fischer-Tropsch synthesis over iron-based catalysts is thought to be inhibited by the production of water (Huff and Satterfield, 1984) (although the inhibition by water is mitigated by the water-gas shift activity, which reduces the partial pressure of water). The rate of reaction over a cobalt-based Fischer-Tropsch catalyst is not inhibited by the production of water (Yates and Satterfield, 1991). This means that a higher conversion per pass can be achieved over a cobalt catalyst compared to an iron catalyst (van Berge, 1997).

## 1.2. The active phase for iron-based Fischer-Tropsch synthesis

Over the years the active phase for iron-based Fischer-Tropsch synthesis has been a much-debated topic. Iron in the precipitated iron catalyst (used for low temperature iron-based Fischer-Tropsch synthesis (Dry, 2004)) is initially present as ferrihydrate, which upon calcination transforms into hematite or maghemite (Motjope et al., 2002). The catalyst has to be activated prior to its use as a Fischer-Tropsch catalyst. There are various methods for pre-treating iron catalysts. The catalyst can be activated via $H_2$ reduction, CO reduction or reduction in synthesis gas (Dry, 2002). In hydrogen, the iron oxides are reduced yielding magnetite and/or metallic iron (depending on the activation temperature and time). Magnetite and metallic iron are transformed into a mixture of iron carbides (such as $\chi$-$Fe_5C_2$ and $\theta$-$Fe_3C$) during the Fischer-Tropsch synthesis. The pre-treatment using synthesis gas or CO results in the dominant phase being Hägg carbide, $\chi$-$Fe_5C_2$ (de Smit et al., 2010).

When studying the structure of the active catalyst it is important to note that the active catalyst is easily oxidized in air (Janbroers et al., 2009). Therefore, any exposure to air should be avoided in order to get an accurate view of the structure of the active phase. The iron-based Fischer-Tropsch catalyst was found to contain both magnetite and iron carbide (Datye et al., 2000; Janbroers et al., 2009; Davis, 2009). Magnetite is thought to be inactive or have very limited activity for the Fischer-Tropsch synthesis (Shroff et al., 1995). Datye et al. (2000) identified the carbide phase as dispersed Hägg iron carbide and $Fe_7C_3$. Dictor and Bell (1985) carried out the Fischer-Tropsch synthesis over reduced and unreduced iron oxide catalysts and concluded that the active phase for iron Fischer-Tropsch is a mixture of Hägg iron carbide ($\chi$-$Fe_5C_2$), $Fe_7C_3$ and α-Fe.

A number of studies indicate that Hägg iron carbide is one of the phases' active for Fischer-Tropsch synthesis, if not *the* active phase (Datye et al., 2000; Janbroers et al., 2009; Davis, 2009; Dictor and Bell, 1985). Therefore, this study focuses on Hägg iron carbide as a model for the active phase in iron-based Fischer-Tropsch synthesis.

### 1.2.1 Hägg iron carbide

Iron carbides are best classified as interstitial carbides with the carbon atoms placed in available interstitial sites in a distorted hexagonally closed packed (hcp) structure of Fe atoms (de Smit et al., 2010). The structure of iron carbides can be classified, according to the site occupation of the carbon atoms in the crystal structure, into trigonal prismatic (TP) carbides and octahedral carbides (O). Hägg carbide is a trigonal prismatic (TP) carbide, in which the carbon atom is surrounded by a prism formed by six iron atoms (see Figure 2.2).

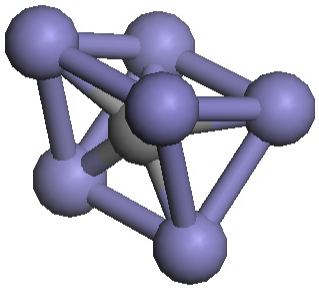

**Figure 2.2:** Carbon in a TP-carbide (e.g. Hägg carbide)

#### 1.2.1.1 Hägg carbide bulk structure

The bulk structure of Hägg iron carbide is characterised by a conventional unit cell consisting of 20 iron atoms and 8 carbon atoms (Steynberg et al., 2008; Sorescu, 2009). The crystal structure of the Hägg carbide was previously determined to be monoclinic (Retief, 1999). However, a more recent study to re-determine the crystal structure of the Hägg carbide found it to be triclinic (du Plessis et al., 2007).The difference between a monoclinic and a triclinic structure is shown in Figure 2.3. A comparison of the angles shows that the β angle of the monoclinic structure is 97.75º (Retief 1999), while in the triclinic structure it is measured to be 97.77º (du Plessis et al., 2007). The α and γ angles of the triclinic structure are measured to be 89.88º and 89.94º respectively (du Plessis et al., 2007). This implies that the triclinic structure shows only a minor deviation from the monoclinic structure (where $\alpha = \gamma = 90^{o}$) and can be classified as pseudo-monoclinic (Steynberg et al., 2008). The conventional cell parameters for Hägg carbide as determined experimentally and the parameters for the monoclinic and triclinic cells are very similar (see Table 2.2).

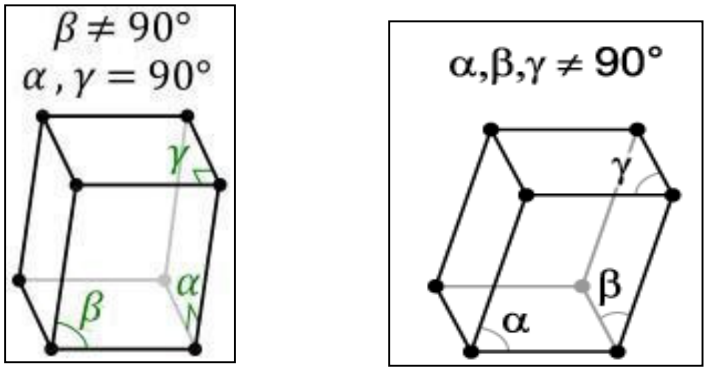


**Figure 2.3:** Monoclinic (left) and triclinic structures

**Table 2.2:** Comparison of monoclinic, triclinic and modelled cell parameters from literature (Retief, 1999; Du Plessis et al., 2007; Cao et al., 2005; Steynberg et al., 2008; Sorescu, 2009; Petersen et al., 2010)

| Method | a (Å) | b (Å) | c (Å) | β (°) |
|---|---|---|---|---|
| ***Experimental studies*** | | | | |
| Retief (1999) | 11.588 | 4.579 | 5.059 | 97.746 |
| du Plessis et al. (2007) | 11.570 | 4.571 | 5.059 | 97.765 |
| ***Computational studies*** | | | | |
| Cao et al. (2005)[1] | 11.562 | 4.573 | 5.060 | 97.630 |
| Steynberg et al. (2008)[2] | 11.568 | 4.523 | 5.002 | 97.750 |
| Sorescu (2009)[3] | 11.580 | 4.508 | 4.994 | 96.638 |
| Petersen et al. (2010)[4] | 11.622 | 4.549 | 5.032 | 97.810 |

[1] Calculated using CASTEP and the PBE-functional, $E_{cut\text{-}off}$ = 340 eV, Gaussian smearing σ = 0.1 eV

[2] Calculated using CASTEP, RPBE-functional, $E_{cut\text{-}off}$ = 340 eV, k-point spacing < 0.05 $Å^{-1}$, Gaussian smearing σ = 0.1 eV

[3] Calculated using VASP and the PBE-functional, $E_{cut\text{-}off}$ = 400 eV, k-point spacing < 0.04 $Å^{-1}$, Gaussian smearing σ = 0.1 eV

[4] Calculated using VASP and the RPBE-functional, $E_{cut\text{-}off}$ = 400 eV, k-point spacing < 0.04 $Å^{-1}$, Gaussian smearing σ = 0.1 eV

Using DFT, Steynberg et al. (2008) calculated that the triclinic structure was more stable than the monoclinic structure, albeit by only 0.04eV per unit cell. Therefore, two structures are energetically and structurally indistinguishable using density functional theory (DFT), given the accuracy of DFT calculations (~0.1eV). Furthermore, Steynberg et al. (2008) obtained a structure resembling an optimised monoclinic structure when performing a geometric optimisation of a triclinic Hägg carbide supercell. Thus, the monoclinic structure

represents the stable structure of Hägg carbide at 0K while at temperatures of Fischer-Tropsch synthesis the triclinic structure might be more stable. The difference between the optimised structure observed in the modelling of Hägg carbide (monoclinic) and the experimentally observed (triclinic) structure might thus be ascribed to the difference in the conditions at which the modelling and experiments are done.

#### 1.2.1.2 Hägg carbide surfaces

Catalysis takes place on the surface of the solid catalyst. A large number of different surfaces can be cleaved from the same bulk crystal structure. The various surfaces expose different arrangements and numbers of the atoms present in the bulk structure. For example, the (010) surface of Hägg carbide will have a different surface arrangement and number of carbon and iron atoms exposed when compared to the (100) surface (see Figure 2.4). Different surfaces also have different stabilities. Surface stability is measured using surface energy ($J/m^2$), a measure of the energy taken to form the surface from the bulk structure taking into account, among other factors, the energy required to break the bonds. A low surface energy is indicative of a high surface stability while a high surface energy means a low surface stability. A surface with a lower stability is less likely to be present under Fischer-Tropsch synthesis conditions, while the opposite is true for a surface with a high stability. Therefore, a comparison of the surface energy of the various surfaces can be used to determine which surfaces are most likely to be present on a crystal of Hägg carbide during the Fischer-Tropsch synthesis.

Steynberg et al. (2008) performed an in-depth investigation into the surface energies of a select number of Hägg carbide surfaces using periodic DFT calculations. The study focussed on a very specific set of Miller index surfaces which were cleaved stoichiometric to the bulk and are symmetric (i.e. the top and the bottom surface are equivalent). The surfaces can either be cleaved through the origin or at a fractional distance from the origin, resulting in different atoms or atom arrangement on the surface. It was found that the (010)0.25 surface (i.e. (010) surface cleaved at a fractional distance of 0.25 from the origin) had the lowest calculated surface energy, meaning it was the most stable surface of the surfaces investigated. However, quite a number of surfaces were found to have similar surface energies (see Figure 2.4). This means that a number of different surfaces can be exposed on a Hägg carbide crystal under Fischer-Tropsch conditions and a selected surface for modelling purposes can only give some insight in the behaviour of iron-based catalysts.

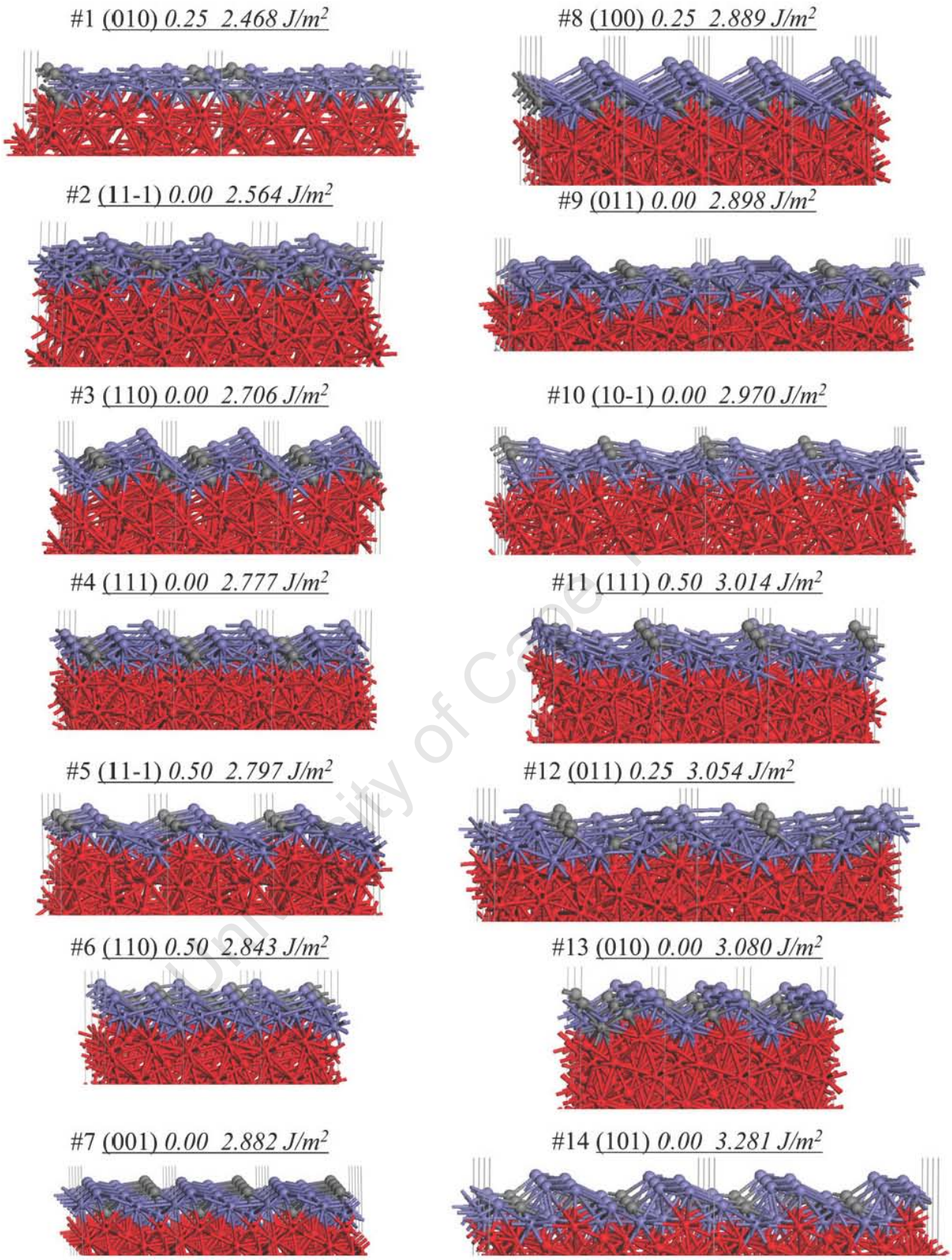


**Figure 2.4:** Comparison of surfaces of Hägg carbide and the calculated surface energies (CASTEP, GGA-PBE, $E_{cut\text{-}off}$ = 340 eV, k-point spacing < 0.05 $Å^{-1}$, Gaussian smearing σ = 0.1 eV, vacuum gap: 10Å; atoms in red were fixed at fractional position of bulk) (Taken from Steynberg et al., 2008)

## 1.3 CO adsorption on iron surfaces

CO is a well-known probe molecule to investigate bonding to catalytically active surfaces. Hence, a large number of computational studies on the adsorption of CO on pure metal surfaces have been published over the last few decades (e.g. Hoffman and Sung, 1985; Maclaren et al., 1987), more recently using DFT (e.g. Carter and Jiang, 2004).

### 1.3.1 CO adsorption on metallic iron

The adsorption of CO on metallic iron has been well investigated over the years, with a number of theoretical studies into CO adsorption on low index Miller index surfaces (Nayak et al., 2001; Stibor et al., 2002; Sorescu et al., 2002; Chen et al., 2004; Carter and Jiang, 2004; Bromfield, et al., 2005).

Carter and Jiang (2004) and Stibor et al. (2002) studied CO adsorption on the most dense iron surface, Fe(110), which has the lowest surface energy. The calculated adsorption energy of CO ranged from 1.28eV to 1.58eV at a CO coverage of 0.25ML using the RPBE functional. The on top site and long bridge sites were calculated to be the most stable adsorption sites at coverages up to 0.5ML. This compares well with the experimentally observed adsorption geometry (Erley, 1981).

On the less dense Fe(100) surface, a number of different adsorption sites were identified by Sorescu et al. (2002). At low coverage ($\theta_{CO}$=0.25ML) the tilted adsorption configuration in the fourfold hollow site was found to be the most stable adsorption configuration, with an adsorption energy of 2.03eV calculated using the RPBE functional. Bromfield et al. (2005) found that this fourfold hollow site was the only true minimum site for CO adsorption on the Fe(100) surface, with the other adsorption states (the on top, bridge site and the tilted bridge geometries) calculated to have imaginary frequencies. As the coverage was increased from 0.25ML to 1ML the adsorption energy of CO was observed to decrease from 1.99eV to 1.47eV. The use of the PW91 functional by Bromfield et al. (2005) resulted in an overestimation of the adsorption energy of CO when compared to experimentally determined values (Moon et al., 1985).

### 1.3.2 CO adsorption on iron carbide surfaces

Relatively few computational studies on the adsorption of CO on Hägg iron carbide surfaces have been performed (Cao et al., 2004; Sorescu, 2009; Petersen et al., 2010), although CO adsorption on another iron carbide, cementite, has been studied (Liao et al., 2007). Furthermore, no experimental studies are known on the adsorption of CO on iron carbide surfaces.

CO can adsorb on Hägg iron carbide surfaces in a number of different configurations, each with its own adsorption energy. The adsorption of CO also depends on the specific surface properties of the surface it is adsorbing to. Some of the properties include the presence of carbon (C) atoms on the surface or below the adsorption site, the degree of stepping in the surface and the degree of coordination of the surface atoms. CO can adsorb only to Fe sites or it can adsorb to both Fe and C atoms on the surface (Sorescu, 2009). Table 2.3 shows the different adsorption energies for CO on the Hägg carbide surfaces ($Fe_5C_2$(001), $Fe_5C_2$(100) and $Fe_5C_2$(110)) calculated using DFT and CASTEP software package. It should be noted that the studies by Cao et al. (2004) and Sorescu (2009) used different programs and different parameters to model the adsorption of CO on the Hägg carbide surface, hence the differences in energies. However, the trends found in the studies are used separately here to attempt to form a picture as to what influences CO adsorption and the barrier to its dissociation. The adsorption energies on these surfaces were found to depend on the degree of coordination of the bonded CO and the type of atoms in the surface it is bonded to. For instance, the adsorption energy for CO is higher when it interacts in the adsorbed state only with Fe atoms. This means that the adsorption mode, in which adsorbed CO interacts only with Fe atoms in the surface, is stronger than the adsorption mode, in which adsorbed CO interacts with both Fe and C atoms in the surface. It should however be noted, that the adsorption mode, in which adsorbed CO interacts with both Fe and C atoms in the surface results in a lengthening of the CO bond length, indicating a lower activation energy for CO dissociation when compared to adsorption to only Fe sites. The average CO bond length for the adsorption of CO onto only Fe sites is 1.2Å, while the average CO bond length for a CO adsorbed onto Fe and C sites is 1.27Å (Sorescu, 2009). It should be noted however, that the nature of the site also plays a role in the stability CO adsorption. This is illustrated in Table 1.3 by the results of Sorescu (2009) where variation in the adsorption energy of a particular CO adsorption configuration is observed.

**Table 2.3:** CO adsorption energies on different Hägg iron carbide surfaces (Cao et al., 2004; Sorescu, 2009). The values for taken from Cao et al. (2004) are the adsorption energies calculated for a specific adsorption configuration at the lowest coverage while the values taken from Sorescu (2009) give the range of the adsorption energies calculated for an adsorption configuration on a specific surface

| Study | Configuration / bonding type | Adsorption Energy (eV) |
|---|---|---|
| | **$Fe_5C_2(010)_{0.25}$** | |
| **Sorescu (2009)[1]** | | |
| | 1F | 1.23 - 1.93 |
| | 1F-t | 1.83 - 1.99 |
| | 2F | 1.90 |
| | 4F | 1.85 – 2.01 |
| | **$Fe_5C_2(100)_{0.00}$** | |
| **Sorescu (2009)[1]** | | |
| | 1F | 1.92 |
| | 1F-t | 1.90 |
| | 3F | 1.93 |
| **Cao et al. (2004)[2]** | | |
| | 1F | 2.21 |
| | 3F | 2.20 |
| | **$Fe_5C_2(110)_{0.00}$** | |
| **Sorescu (2009)[1]** | | |
| | 2F | 1.90 |
| | 3F | 2.07 |
| **Cao et al. (2004)[2]** | | |
| | 2F | 1.16 |
| | 3F | 2.34 |
| | **$Fe_5C_2(111)_{0.00}$** | |
| **Sorescu (2009)[1]** | | |
| | 1F | 1.31 – 2.10 |
| | 2F | 1.94 |
| | 3F | 2.05 |
| | **$Fe_5C_2(001)_{0.00}$** | |
| **Cao et al. (2004)[2]** | | |
| | 3F | 2.10 |
| | 1F-C | 2.10 |

[1] Calculated using VASP software package, PBE functional, cut off energy of 400eV, σ=0.1eV, k-point sampling density of 0.04Å$^{-1}$ and a vacuum gap of 14Å.

[2] Calculated using the CASTEP software package, cut off energy of 340eV, σ=0.1eV and a vacuum of 10Å.

Notation: xF → CO molecule has x number of bonds to Fe atoms, and no bonds to C atoms in the surface. xF-C indicates a bond to a surface C atom. xFe-t refers to a tilted configuration).

The strength of adsorption of CO on iron carbide surfaces is strongly affected by the coverage of the surface with the adsorbed molecule (Cao et al., 2004), since the degree of lateral interaction between adsorbed species increases with increasing coverage. The lateral (repulsive) interaction causes a decrease in the observed adsorption energy of the CO molecules. Table 2.4 shows that as the coverage of the surface with adsorbed CO increases, the energy of adsorption decreases. This can be attributed to increased lateral interactions between the adsorbed CO molecules as the coverage increases.

**Table 2.4:** Coverage dependant adsorption energy of CO on an on top ridge iron site on the $Fe_5C_2(100)_{0.00}$ surface in a 1F adsorption configuration. Calculated using the CASTEP software package, cut off energy of 340eV, σ=0.1eV and a vacuum of 10Å. (Cao et al., 2004)

| Coverage | Adsorption energy (eV) |
|---|---|
| **1/4ML** | 2.20 |
| **1/2ML** | 1.89 |

Petersen et al. (2010) investigated the effect of surface step sites for a number of Hägg carbide surfaces on the strength of CO adsorption. The strength of adsorption of CO on the stepped surfaces was found to be comparable to the adsorption on the flat surfaces. The coordination of both the C and the O to the surface was found to result in a lengthening of the CO bond and a decrease in the activation energy for CO dissociation. The stepped surfaces were found to facilitate multiple coordinated adsorption modes (i.e. Both C and O in close proximity to the surface). Hence, adsorption of the CO molecule to only Fe atoms is not necessarily the most favourable adsorption configuration for the Fischer-Tropsch synthesis. On stepped surfaces the interaction of an adsorbed CO molecule with both Fe and C sites can be more favourable than adsorption to only Fe sites, as the activation of CO and the subsequent dissociation is more favourable if CO is adsorbed to Fe and C atoms (Sorescu, 2009). The importance of stepped sites and surfaces should not be overlooked since CO adsorption on these stepped surfaces is of comparable strength to the adsorption on a flat surface (Petersen et al., 2010). These stepped surfaces facilitate coordination of both the C and the O to the surface, increasing the CO bond length and decreasing the barrier for CO dissociation.

## 1.4 Promoters for iron-based Fischer-Tropsch catalysts

A promoter can be defined as a substance which forms part of the catalyst, enhancing the intrinsic properties of the catalyst without being active on its own. By way of example, a promoter could either enhance the activity or modify the selectivity obtained over a catalyst. A promoter can fall into one of three different classes, depending on the type of promotion (Dry, 2002). Firstly, a promoter can increase the available catalyst surface area by preventing sintering of the catalyst. This type of promoter is typically referred to as a structural promoter. In the low temperature, iron-based Fischer-Tropsch catalysts silica is typically used as a structural promoter, whereas the high temperature iron-based Fischer-Tropsch catalysts may contain alumina or magnesia as a structural promoter (Dry, 2002). In the second type of promotion, the promoter changes the electronic structure of the active catalyst surface. This can lead to a change in the strength of adsorption as well as bond destabilisation of adsorbing reactants. This type of promotion is chemical in nature and therefore, the promoter is referred to as a chemical promoter (Dry, 2004a). In iron-based Fischer-Tropsch catalysts, potassium is typically added as a chemical promoter (Dry, 2002). A third type of chemical promoter used in Fischer-Tropsch synthesis is termed a reduction promoter. Reduction promoters are used to facilitate the reduction of the catalyst. The decrease in the required reduction temperature of the catalyst then results in a decrease in the likelihood of catalyst sintering. In iron-based Fischer-Tropsch, copper is used as a reduction promoter to increase the rate of reduction during the catalyst pre-treatment (Jin et al., 2000).



## 1.5 Effects of potassium promotion on Fischer-Tropsch synthesis

Numerous experimental studies have dealt with the effects of potassium promotion on iron based Fischer-Tropsch synthesis. Potassium has a variety of effects on the FT process, affecting the activity (Dry, 2004a; Blignaut, 2007), selectivity (van der Laan, 1999), product distribution (Ma et al., 2007) as well as methane production (Bell and Arakawa, 1982).

### 1.5.1 Effect of potassium on catalyst activity

Potassium affects the activity of iron-based Fischer-Tropsch catalysts (see e.g. Dry, 2004; Blignaut, 2007). Dry (2004b) reported the effect of $K_2O$ on iron-based catalysts (see Figure 1.5). The activity of the unsupported iron-based catalyst increases with increasing amount of alkali up to a relative level of 2. Increasing the alkali content further led to a decrease in the catalyst activity, which can be understood in terms of blockage of the catalytically active

surface. Similarly, Blignaut (2007) observed that the activity of a supported iron catalyst passes through a maximum as a function of the potassium loading. It was concluded that the maximum activity corresponded to ca. 1 K-atom per 8-9 surface Fe-atoms.

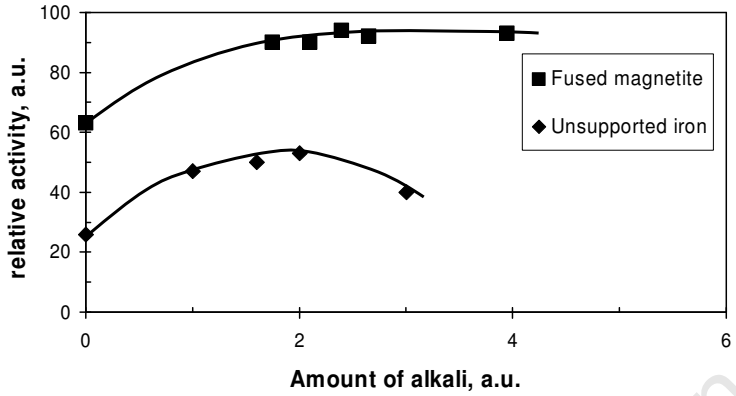


**Figure 2.5:** Effect of potassium on activity of iron-based catalysts (230 °C; $H_2/CO = 2$; 1.8 MPa) (drawn with data from Dry, 2004a).



### 1.5.2 Effect of potassium on selectivity

Potassium has been observed to influence the selectivity of Fischer-Tropsch products by decreasing the selectivity for the formation of shorter hydrocarbon chains ($C_1$-$C_4$) and increasing the selectivity towards longer chain molecules ($C_{5+}$) (Bukur et al., 1990). The presence of potassium affects the carbon number distribution, shifting the product distribution towards higher carbon number products. This shift in the carbon number distribution is illustrated in Figure 2.6 and Figure 2.7 (Ma et al., 2007). The graphs on the left hand side of Figures 1.6 and 1.7 show the carbon number distribution of the product when there is no potassium present in the catalyst. The graphs on the right hand side show the carbon number distribution of the product when potassium is present. There is a clear shift in the carbon number distributions of both the olefins and paraffins towards higher carbon numbers due to the presence of potassium. Furthermore, the addition of potassium also leads to an increase in the ratio of olefins to paraffins (Iglesia et al., 2001; Dry, 2004b)

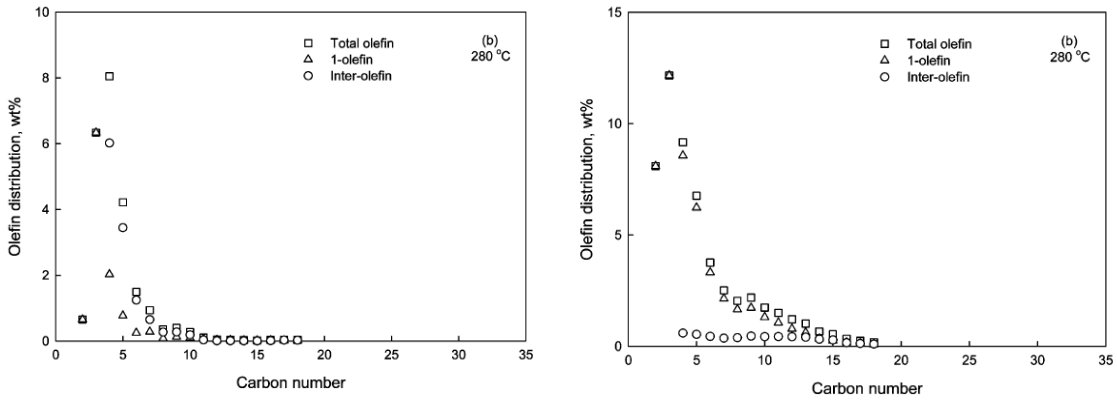


**Figure 2.6:** Distribution of olefins as a function of carbon number over a potassium free iron-based Fischer-Tropsch catalyst (left) compared to potassium containing iron-based Fischer-Tropsch catalyst (right) (taken from Ma et al., 2007) (280ºC; $H_2/CO$ =0.9; 2MPa)

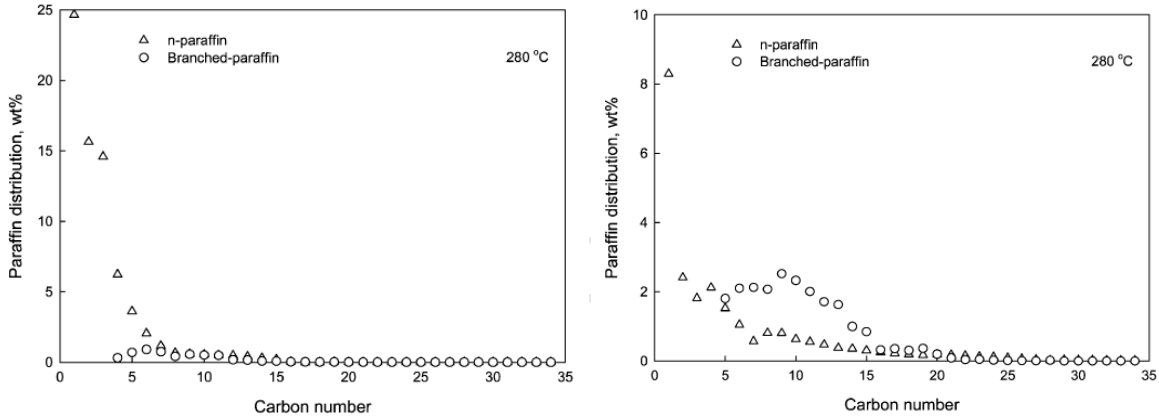


**Figure 2.7:** Distribution of paraffins as a function of carbon number over a potassium free iron-based Fischer-Tropsch catalyst (left) compared to potassium containing iron-based Fischer-Tropsch catalyst (right) (taken from Ma et al., 2007) (280ºC; $H_2/CO$ =0.9; 2MPa)

Figure 2.8 shows the effect potassium has on the methane selectivity and the olefin selectivity in the Fischer-Tropsch synthesis at 330°C. The selectivity towards methane decreases with the increasing of the potassium content in the catalyst while the selectivity towards olefins increases. Potassium is thought to donate electrons to the catalyst surface enhancing CO adsorption and dissociation (Yang et al., 2004). Blignaut (2007) argued that promotion with potassium enhances the surface coverage with C and decreases the coverage with hydrogen. This reduced coverage of hydrogen, is thought to decrease the probability that the product will desorb as a paraffin leading to an increase in the ratio of olefins to paraffins and a shift in the product distribution towards long chain hydrocarbons (Blignaut, 2007).

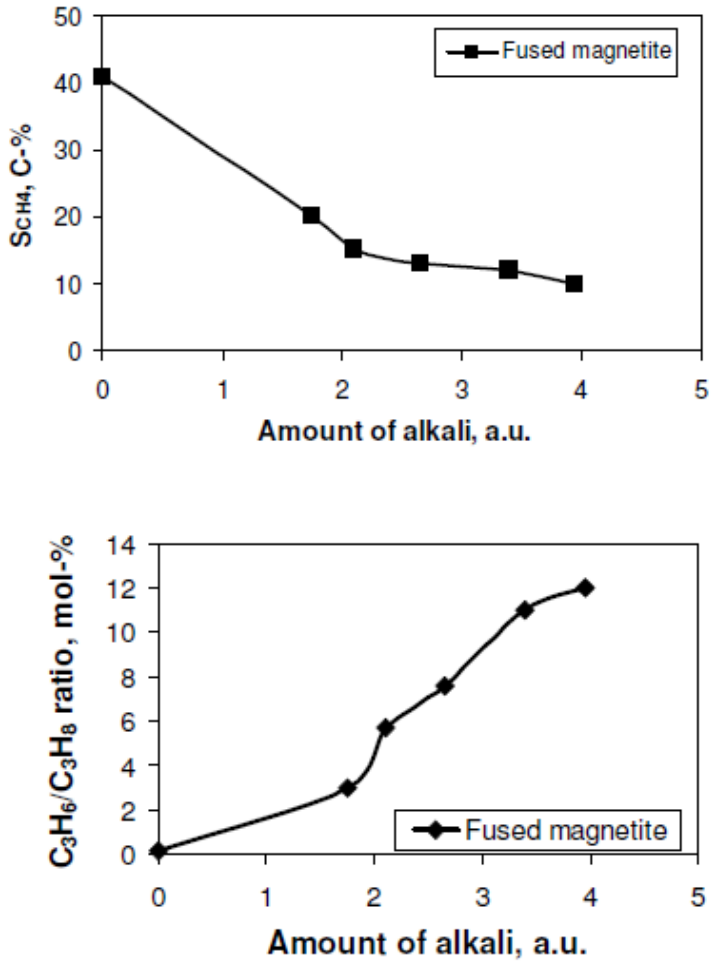


**Figure 2.8:** Effect of potassium on selectivity of iron-based catalysts in the Fischer-Tropsch synthesis at 330°C in a fluidised bed reactor (drawn with data from Dry, 2004b)
Top: Methane Selectivity
Bottom: Olefin to paraffin ratio

## 1.6 Mechanistic understanding of potassium promotion

Potassium is an essential promoter for iron-based Fischer-Tropsch synthesis, enhancing both the catalytic activity and selectivity (Dry, 2004a and b; Yang et al., 2004; Blignaut, 2007). Potassium is thought to donate electrons to iron thereby facilitating CO chemisorption, since CO tends to accept electrons from iron (Yang et al., 2004). Despite its importance, not much is known about the exact mechanism of potassium promotion. Furthermore, the state of potassium on the catalyst surface is not known.

### 1.6.1 Blyholder model

Blyholder (1964) proposed the first molecular orbital model of the bonding of CO to a metal surface. The occupied 5σ orbital of CO overlaps with the empty metal d and s orbitals of the metal atoms. This bond between the CO and metal surface is accompanied by electron donation from the CO to the metal surface. The empty 2π* anti-bonding orbital of the CO can also overlap with an occupied metal d orbital resulting in electron back-donation (Blyholder, 1964). Activation of the CO bond occurs when the band for the 2π* orbital shifts below the Fermi level (Chen et al., 2004). This is depicted in Figure 2.9, a plot of the density of states (DOS) of CO. The adsorption of CO on a metal surface leads to a shift in the DOS of CO, with a downwards shift of both the 5σ and 2π* states. The validity of this model has been confirmed in studies by Aizawa and Tsuneyuki (1998) and Föhlisch et al. (2000).

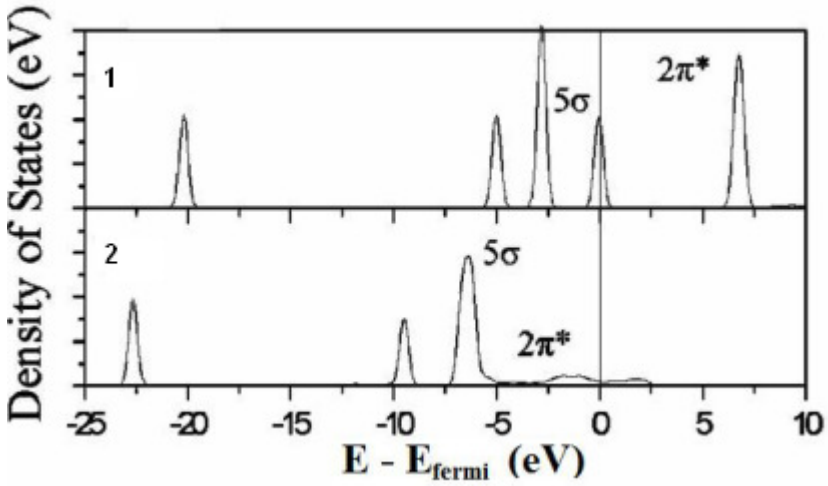


**Figure 2.9:** Change in the DOS of CO during adsorption to a metal surface. 1) The DOS of free CO (taken from Chen et al., 2004). 2) The DOS of CO when adsorbed to a Hägg iron carbide surface (taken from Cao et al., 2004).

### 1.6.2 Adsorption of potassium on metal surfaces

A few computational studies have dealt with the adsorption of atomic potassium on metallic iron, whereas none have dealt with the adsorption of potassium adsorption on Hägg carbide surfaces. The adsorption of potassium on the Fe(100) surface, as well as the co-adsorption of potassium and CO on Fe(100), was studied using VASP and the PBE functional (Sorescu, 2011). The most stable adsorption site for potassium on Fe(100) was found to be the fourfold hollow site. The other adsorption states; the bridge site adsorption and the on-top adsorption configurations were found to correspond to transition states. Zhang et al. (2006) using VASP and the PW91 functional, found that for the adsorption of potassium on Ni(111),

the most favourable adsorption site is the atop site. Jenkins and King (2000), who studied the adsorption of potassium on the Co($10\bar{1}0$) surface using CASTEP, found potassium to have a preference for hollow sites. Huo et al. (2011) investigated the adsorption of $K_2O$ on a range of Fe surfaces and found that favoured adsorption site varied depending on the surface structure. This indicates that the favoured adsorption site for potassium is dependent on the chemistry and structure of the surface being investigated.

Sorescu (2011) reported that the adsorption energy of K (referenced to a gas phase K atom) varies quite substantially with coverage ranging from 1.68eV at a coverage of 0.12ML to 1.26eV at a coverage of 0.5ML on the Fe(100) surface (see Figure 2.10). The adsorption energy increases, along with increasing loss of electrons by the potassium, as the coverage decreases. The overall activation energy for the diffusion of potassium across the Fe(100) surface from one fourfold hollow to another was found to be very low (0.03eV), which corresponds to a low barrier to diffusion indicating that the potassium has high mobility over the Fe(100) surface.

The possibility of substitutional adsorption of the potassium in Fe(100) was also investigated by Sorescu (2011). This was done by removing one of the surface iron atoms, creating a surface defect where potassium could adsorb. It was found that adsorption of potassium in this site could occur, with adsorption energies ranging from 1.95 to 2.12eV. However, it was found that there is a high barrier of ca. 1.8eV to overcome to remove an iron atom from the surface. This is in agreement with an experimental study by Gon et al. (1996) which observed that for substitutional adsorption of potassium only occurs at high temperatures (650K) where the barrier to forming a surface defect can be overcome.

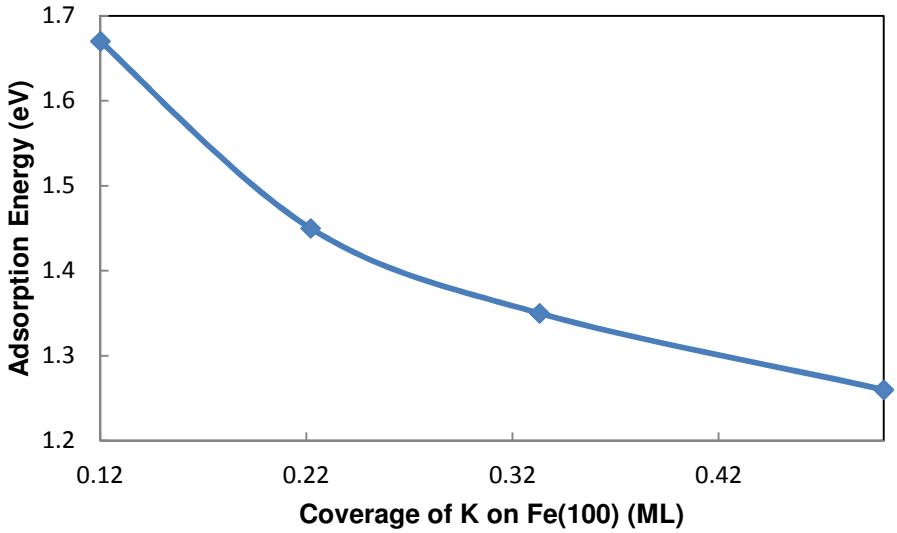


**Figure 2.10:** Adsorption energy of potassium on Fe(100) as a function of coverage (redrawn from Sorescu, 2011). Calculated using the VASP software package, PBE functional, σ=0.1eV, a cut off energy of 400eV, k-point sampling density of 0.035Å$^{-1}$ and a vacuum gap of 15Å.

An in-depth analysis of the adsorption of potassium on Co(10$\bar{1}$0) was performed to elucidate the type of interaction between potassium and a metal surface (Jenkins and King, 2000). Covalent bonding appears to be absent, as there was no evidence of orbital overlap. The potassium was found to donate 0.52 electrons to the cobalt, while the effective potassium radius was found to be 1.86Å, midway between the ionic and covalent radius of potassium (ionic radius: 1.33Å; covalent radius: 2.26Å). This indicates that the behaviour of potassium on a metal surface have elements of ionic bonding.



### 1.5.3 The co-adsorption of potassium and CO adsorption on a metal surface

The effect of potassium on the adsorption of CO has been studied experimentally (Bell and Arakawa, 1983; Somorjai et al., 1982; Derrouiche et al., 2007; Ceelen et al., 1997; Graf and Muhler, 2011) as well as via DFT on metal surfaces such as Ni(111) (Zhang et al., 2006), Rh(111) (Liu and Hu, 2001), Fe(100) (Sorescu, 2011) and the $Mo_2C$(001) surface (Pistonesi et al., 2011). Currently, no computational studies have been performed involving the effect of potassium on CO adsorption on Hägg carbide.

The adsorption strength of CO on a metal surface has been found, experimentally and theoretically, to be enhanced by the presence of potassium (Graf and Muhler, 2011; Sorescu, 2011; Pistonesi et al., 2011). Graf and Muhler (2011) observed that the presence

of potassium promotion of an iron catalyst increased the experimental differential heat of adsorption for CO from 1.07 eV to 1.16 eV. Sorescu (2011) showed that the increase in the heat of adsorption of CO due to the presence of potassium depends on distance between adsorbed CO and adsorbed potassium. Zhang et al. (2006) found in their computational study on the co-adsorption of potassium and CO on Ni(111) surface, that the length of the CO bond increases by 0.01Å to 0.03Å in the presence of potassium. Sorescu (2011) observed that in the co-adsorption of CO and K on Fe(100), the CO bond length increased by 0.01Å to 0.02Å with a red shift in the vibrational frequency of the CO bond of 100 $cm^{-1}$ to 200 $cm^{-1}$ relative to CO adsorption without K present. These shifts in the bond length and vibrational frequency are dependent on the distance of between adsorbed CO and adsorbed potassium. The larger changes in the CO bond lengths and vibrational frequencies were seen when the K-O and K-C distances were both below 3 Å (Sorescu, 2011). Sorescu (2011) also found that potassium decreases the calculated barrier of CO dissociation by up to 0.29eV. The CO bond length was observed to increase and the CO stretching frequency to decrease in the co-adsorbed state.

Similarly, Liu and Hu (2001) observed in a computational study of the co-adsorption of CO and K on Rh(111) a direct interaction between the oxygen on the CO and the potassium if the distance between the CO and K is between 2-3 Å. This resulted in a stabilisation of the transition state for the dissociation of adsorbed CO and a decrease in the barrier for dissociation. However, the change in the dissociation barrier is lower if the distance between the potassium and the CO molecule is larger than 4 Å. This work supports the results obtained by Sorescu (2011), where it was found that the closer interactions between CO and potassium lead to greater increases in the CO bond length and adsorption energy as well as greater decreases in the activation energy for CO dissociation.

Potassium promotion is thought to occur via the increasing of the amount of electrons available on the metal surface for back donation to the CO $2\pi^*$ anti-bonding orbital. This increased back donation results in enhanced activation of the CO bond as evidenced by the increase in the CO bond length and red shift in the CO vibration frequency (Liu and Hu, 2001; Zhang et al., 2006; Sorescu, 2011).

## 1.7 Project aims

Density Functional Theory (DFT) will be used to gain further insight into the mechanism behind the effect that potassium has on CO dissociation. This study will explore the mechanism by which potassium promotes CO adsorption by using DFT. The speciation of different potassium species (K and KO) will be explored as a function of the reaction conditions. Once the potassium species has been adsorbed on the Hägg iron carbide surface, CO will be adsorbed and the effect of the potassium on the adsorption of CO will be explored.

## 1.8 Key questions

- What are the stable adsorption sites for CO on the Hägg iron carbide surfaces?
- What are the stable adsorption sites for K and KO on the Hägg iron surfaces?
- Does having KO co-adsorbed with CO on the surface have a different effect on CO adsorption when compared to K co-adsorbed with CO?
- Under Fischer-Tropsch synthesis conditions which of the potassium species (K or KO) is thermodynamically predicted to be present?

## 1.8 Hypothesis

Potassium is not necessarily present as a metal under FT process condition, and hence the classical interpretation of the role of potassium as a promoter cannot be assumed.

# Chapter 2 : Computational method and model verification

## 2.1 Computational Methods

In theoretical calculations, as with experimental work various parameters need to be optimised before any of the experimental calculations can be done. It is important that these optimisations be accurately completed as these optimised parameters will be used for the rest of the study and they can affect the accuracy of the calculations. However, the computational time is also strongly dependent on these computational input parameters as well as the size of the system (i.e. the number of atoms). Therefore, a good model would yield results that compare favourably with experimental results while being efficient enough such that the calculations are completed on a reasonable timescale. In this section the methods used to obtain these parameters and the validation of our model will be discussed.

### 2.1.1 Density Functional Theory (DFT)

Density Functional Theory (DFT) is a widely used quantum mechanical theory used to model the electronic structure of molecular systems. It provides good prediction for systems containing a large number of electrons such as systems containing transition metals.

The primary aim of DFT is to solve the time-independent Schrödinger equation for the system being studied:

$$\hat{\mathrm{H}}\Psi = E\Psi \qquad (2.1)$$

E is the energy of the system which is obtained when the Hamiltonian operates on a wave function. The Hamiltonian operator, $\hat{\mathrm{H}}$, consists of the sum of kinetic and potential energies.

$$\hat{\mathrm{H}} = -\frac{\hbar}{2\mathrm{m}}\nabla^2 + \mathrm{V} \qquad (2.2)$$

Where ħ is Plank's constant divided by 2π and $\nabla^2$ is the Laplace operator. The Schrödinger equation can only be solved exactly for a hydrogen atom. The solution to this equation for more complex systems can only be approximated.

One of these approximations is the Born-Oppenheimer approximation (Born and Oppenheimer, 1927) which assumes that the positions of the nuclei can be treated as fixed while the electrons move around. This is based on the high velocity of the electrons

compared to the velocity of the nuclei. This means that to calculate the energy of a system with this approximation, only the electronic wavefunction needs to be solved.

DFT is based on the principle that the electronic energy of a system can be determined from the electron density (ρ) distribution (Hohenberg and Kohn, 1964). This means that the energy is a functional of the electron density. The energy functional can be written in terms of electron density, as the sum of two terms:

$$E[\rho(r)] = \int V_{ext}(r)\rho(r)dr + F[\rho(r)] \quad (2.3)$$

where $\int V_{ext}(r)\rho(r)dr$ represents the interaction of the electrons with external potentials, F[ρ(r)] represents the kinetic energy and the energy due to electron-electron interaction. The $V_{ext}$ term can be readily determined. However, the F[ρ(r)] term is unknown. Kohn and Sham (1965) suggested a method to approximate this electron-electron and kinetic energy functionals as a sum of three terms (Kohn and Sham, 1965):

$$F[\rho(r)] = T[\rho(r)] + V_H[\rho(r)] + E_{EX}[\rho(r)] \quad (2.4)$$

where $T[\rho(r)]$ is the kinetic energy component, $V_H[\rho(r)]$ is the electron-electron interaction component and $E_{EX}[\rho(r)]$ is the exchange correlation energy component. Both the kinetic and electron-electron interaction components can be solved using Hartree-Fock theory while the exchange-correlation functional is approximated. To estimate this exchange correlation energy in DFT, different exchange-correlation functionals have been developed. There are two main approaches in representing this exchange-correlation energy, local density approximation (LDA) and generalised gradient approximation (GGA).

The LDA approach is the first and simplest approximation for $E_{XC}$ proposed by Kohn and Sham (1965). In the LDA approach, the exchange-correlation energy is represented as:

$$E_{XC}^{LDA}(\rho) = \int \rho(r)\varepsilon_{XC}^{LDA}(\rho)dr \quad (2.5)$$

where $\varepsilon_{XC}^{LDA}(\rho)$ is the LDA exchange-correlation energy per particle in a uniform electron gas with density ρ(r). In LDA, the local electron density at a position r is treated as constant. This means that the electronic charge is distributed uniformly throughout the system. LDA is known to result in overbinding within molecules and thus underestimating of bond lengths and lattice distances (Huang et al., 2009; Perdew et al., 1992). It has also been observed to predict an incorrect magnetic state for iron (Singh et al., 1991; Wang et al., 1985).

The GGA approach improves on LDA by considering a non-uniform electron gas. The exchange-correlation is dependent on both the electron density and the change in the electron density. There are a number of different GGA functionals available for use as the change in electron density can be expressed in different ways. Some of the more widely applied functionals are the BLYP (Lee et al., 1988), PBE (Perdew et al., 1996), RPBE (Hammer et al., 1999) and PW91 (Perdew et al., 1992).

In the application of DFT in this study a program developed for use with systems with periodic boundary conditions, the Vienna *ab initio* Simulation Package (VASP) (Kresse and Furthmuller, 1996; Kresse and Joubert, 1999) is used. The software uses a plane wave basis set to construct electronic wave-functions. Each electron in a molecular system generates a Blöch wave (Blöch, 1928) forming part of the wavefunction of the molecular system. However, for heavier elements, the number of waves needed to describe the wavefunction increases, increasing the computational cost. To overcome this, pseudopotential representations of atoms are used. Since chemical bonding mainly involves valence electrons, the non-valence electrons can be considered as being in fixed states. Pseudopotentials therefore represent the potential of the nucleus and non-valence electrons.

In this study VASP is used for the calculation of adsorption energies, adsorption geometries, charge distribution, density of states and vibrational frequencies. In VASP the Schrödinger equation is solved using an iterative approach. For a given input geometry the electronic ground state is estimated. The forces for this geometry are then calculated as the derivate of energy with respect to distance ($\frac{dE}{dx}$). A new geometry based on these forces is then predicted. This process continues until the convergence criterion is met (Govender, 2010). This process is illustrated in Figure 2.1.

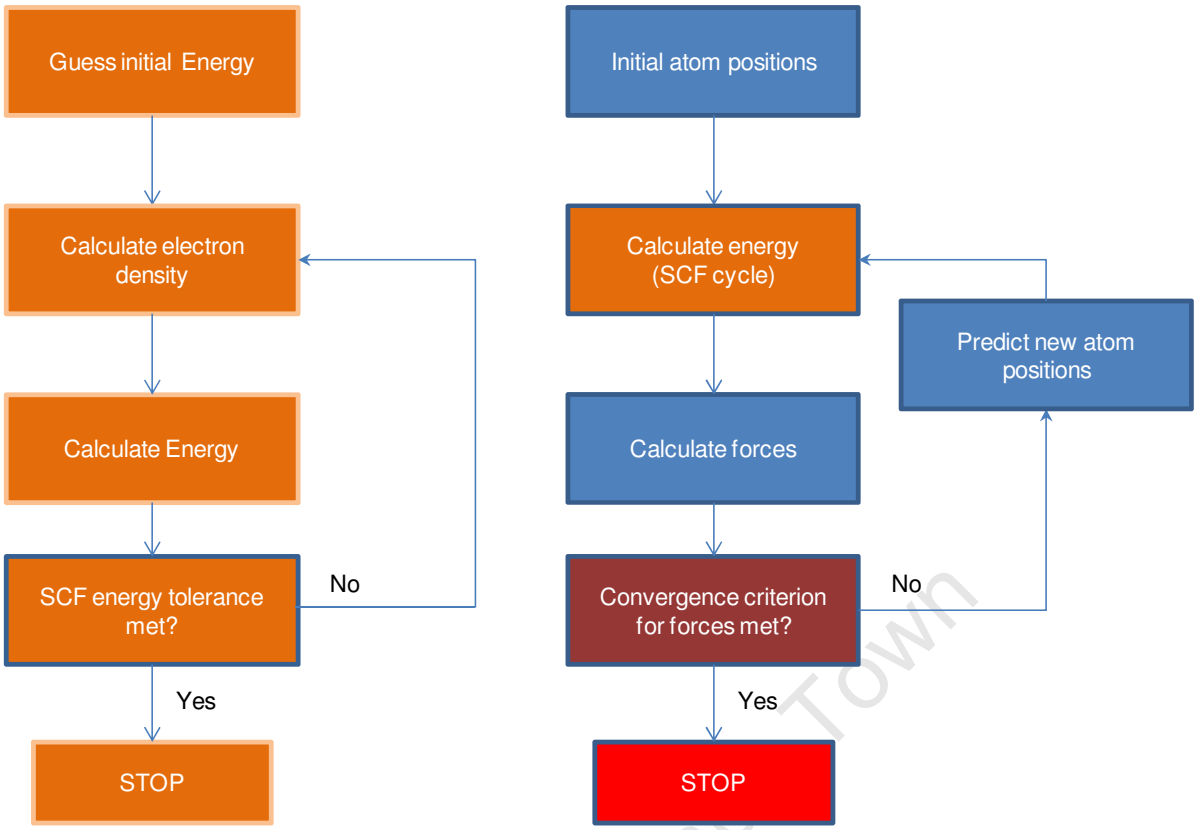


**Figure 2.1:** Flowchart for SCF cycle (left) and DFT geometry optimisation cycle (right) to calculate energies and structures

There are some shortcomings in the current approaches to DFT. Weak interactions such as van der Waal's forces cannot be described accurately, if at all. This is due to the local nature of both LDA and GGA approximations (Prytz, 2010). It has also been found the PBE functional fails to predict the correct adsorption site as well as the magnitude of the CO adsorption energy on certain metal surfaces, such as Cu(111), Rh(111) and Pt(111) (Stroppa and Kresse, 2008). Local and semi-local functionals have been found to be incapable of correctly describing the balance between the donation of charge to the surface and the back donation of charge from the surface to the adsorbate (Stroppa and Kresse, 2008). Zhao et al. (2005) used various semi-local functionals to calculate the barriers for a range of reactions involving atom transfer, nucleophilic substitution, association and unimolecular reactions. It was reported that the semi-local functionals performed poorly, giving a poor comparison to the experimentally determined barriers (Zhao et al., 2005).

## 2.2 General Computational Method

Spin polarised first principle calculations using Density Functional Theory (DFT) were performed using the Vienna *ab initio* Simulation Package (VASP) (Kresse and Furthmuller, 1996; Kresse and Joubert, 1999). The electron-ion interaction was described using the projected augmented wave (PAW) method (Blöchl, 1994; Kresse and Joubert, 1999). As shown by Kresse and Joubert (1999), PAW potentials can provide a better description of magnetic transition metals.

For the optimisation of the bulk structure, the exchange-correlation energy was calculated using the RPBE (Hammer et al., 1999), PBE (Perdew et al., 1996) and PW91 (Perdew et al., 1992) functionals. The sampling of the Brilliouin zone was performed using the Monkhorst-Pack scheme (Monkhorst and Pack, 1976). In all the bulk and surface calculations conducted in this study first order Methfessel-Paxton (Methfessel and Paxton, 1989) smearing was employed, with an σ value of 0.2eV as recommended in the VASP manual for calculations involving metals. In other studies on Hägg carbide, a smearing of 0.1eV is generally used (Cao et al., 2004; Steynberg et al., 2008; Sorescu, 2009; Petersen et al., 2010). This difference in smearing may have an impact on the comparability of the results in this study to the aforementioned studies. The SCF break criterion was set to 0.03eV/Å$^{-1}$ with an FFT grid of 1000 points. A dipole correction perpendicular to the surface was applied in all calculations involving carbide surfaces to account for the highly electronegative species being adsorbed.



For CO adsorption, the adsorption energies of the optimised structures were calculated using a gas phase CO as a reference state.

$$E_{ads,CO} = \left(E_{free\ surface} + E_{gas\ phase\ CO}\right) - E_{Slab\ with\ CO} \qquad (2.6)$$

Where $E_{ads,\ CO}$ is the negative heat of adsorption of C at 0K, $E_{slab\ with\ CO}$ is the calculated energy of the adsorbed CO, $E_{free\ surface}$ is the calculated energy of the clean $Fe_5C_2(100)_{0.00}$ or $Fe_5C_2(100)_{0.098}$ slab and $E_{gas\ phase\ CO}$ is the calculated energy of the gas phase CO molecule.

The adsorption energies of potassium on the optimised surface structures were calculated using a gas phase potassium atom as a reference state.

$$E_{ads,K} = \left(E_{free\ surface} + E_{gas\ phase\ K}\right) - E_{Slab\ with\ K} \quad (2.7)$$

Where $E_{ads,\ K}$ is the negative heat of adsorption of K at 0K, $E_{slab\ with\ K}$ is the calculated energy of the adsorbed K, $E_{free\ surface}$ is the calculated energy of the clean $Fe_5C_2(100)_{0.00}$ or $Fe_5C_2(100)_{0.098}$ slab and $E_K$ is the calculated energy of the gas phase K atom.

For oxygen adsorption the adsorption energy was calculated relative to a gas phase $H_2O$ and a gas phase $H_2$. The rationale for this approach is that at Fischer-Tropsch conditions water and hydrogen will be present.

$$E_{ads,O} = \left(E_{free\ surface} + E_{gas\ phase\ H_2O} - E_{gas\ phase\ H_2}\right) - E_{Slab\ with\ O} \quad (2.8)$$

Where $E_{ads,\ O}$ is the negative heat of adsorption of O at 0K, $E_{slab\ with\ O}$ is the calculated energy of the adsorbed O, $E_{free\ surface}$ is the calculated energy of the clean $Fe_5C_2(100)_{0.00}$ or $Fe_5C_2(100)_{0.098}$ slab and $E_{H2O}$ or $E_{H2}$ are the calculated energies of the gas phase $H_2O$ and $H_2$ species respectively.

For the CO co-adsorbed with K, O or KO the adsorption energy of CO was calculated:

$$E_{ads,CO} = \left(E_{surface\ with\ co-adsorbate} + E_{gas\ phase\ CO}\right) - E_{Slab\ with\ CO\ and\ co-adsorbate} \quad (2.9)$$

Where $E_{ads,\ CO}$ is the negative heat of adsorption of CO at 0K, $E_{slab\ with\ CO}$ is the calculated energy of the adsorbed CO, $E_{surface\ with\ co-adsorbate}$ is the calculated energy of the $Fe_5C_2(100)_{0.00}$ or $Fe_5C_2(100)_{0.098}$ slab with K, O or KO adsorbed on it and $E_{gas\ phase\ CO}$ is the calculated energy of the gas phase CO molecule.

Using this sign convention, a positive adsorption energy corresponds to a stable adsorption configuration.

## 2.3 Bulk Hägg iron carbide model verification

The optimisation of the bulk structure is of critical importance to the rest of the study as the accuracy of the bulk model affects the structural and electronic properties of any surfaces cut from the bulk. Therefore, an accurate model representing the bulk of Hägg carbide is needed that compares well with experimental data. The input parameters which were optimised were the k-point sampling density and the choice of exchange-correlation functional. The cut-off energy was set to a high enough value (520eV) such that it did not affect the accuracy of the rest of the calculations. The cutoff energy was more than 1.3 times the highest ENMAX value for any of the psuedopotentials of the elements used in the study. Hägg carbide $Fe_5C_2$ has been modelled using a monoclinic structure (Steynberg et al., 2008). The experimentally determined bulk structural parameters are shown in Table 2.1 and the bulk Hägg carbide structure is shown in Figure 2.2.

**Table 2.1:** Experimental Hägg carbide lattice parameters (Retief 1999)

| a (Å) | b (Å) | c (Å) | β (°) |
|---|---|---|---|
| 11.588 | 4.579 | 5.059 | 97.75 |

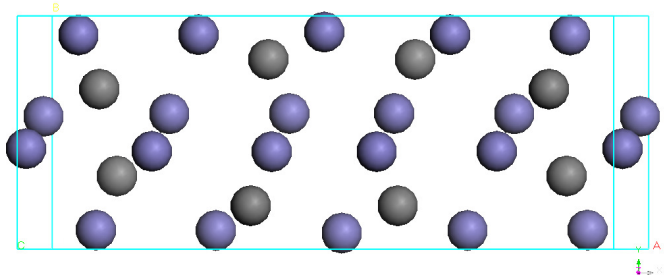

**Figure 2.2:** Bulk Hägg carbide structure



### 2.3.1 k-Point sampling density

The k-point sampling density plays an important role in both the accuracy and computational time of a calculation. A high k-point density will give a more accurate result than a calculation performed with a lower k-point density. However, the time taken to complete the calculation will be higher for the calculation with the high k-point density. Therefore, the k-point sampling density used in the study should meet the set accuracy criteria while minimising the time needed for the calculation to run.

**Table 2.2:** Hägg carbide primitive unit cell lattice parameters (Retief 1999)

| a (Å) | b (Å) | c (Å) |
|---|---|---|
| 6.230 | 6.230 | 5.059 |

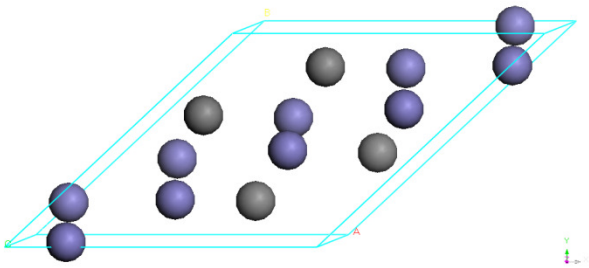

**Figure 2.3:** Experimental primitive Hägg carbide structure



The method used to determine the optimum k-point sampling density was to keep the unit cell fixed and varying the k-point mesh density until the error in the total unit cell energy was converged to within 2meV. The lengths of the primitive Hägg carbide unit cell are not all the same (see Table 2.2), with lattice parameter *c* being unequal to the *a* and *b* parameters. Therefore, the dimensions of the k-point mesh were adjusted according to the ratio of the lengths of the experimental primitive unit cell in reciprocal space. The k-point mesh was varied from 4 × 4 × 3 to 12 × 12 × 10 until the energy converges to within the 1meV. This was done using the PW91, RPBE and PBE functionals. This occurred at a k-point mesh setting of 6 × 6 × 5 for the RPBE functional. For the PBE and PW91 functionals this occurred at a k-point mesh setting of 5 × 5 × 4 and 4 × 4 × 3 respectively. Irreducible k-points refers to the minimum number of k-points required for a given k-point mesh that completely samples the Brillouin zone within reciprocal space taking into consideration any symmetry effects that could reduce the total number of k-points. The results for this optimisation using the RPBE functional can be seen in Figure 2.4. The irreducible k-points for each k-point mesh is plotted against the energy of the primitive unit cell. The results for the PBE and PW91 functionals can be found in the appendix. The optimised k-point mesh setting for the RPBE functional, 6 × 6 × 5, corresponds to 54 irreducible k-points while the optimised k-point mesh settings of the PW91 (5 × 5 × 4) and PBE (4 × 4 × 3) functionals both correspond to 30 irreducible k-points. The optimised k-point mesh settings correspond to k-point sampling densities of ~0.04Å$^{-1}$ for the RPBE functional, ~0.05Å$^{-1}$ for the PBE functional and ~0.06Å$^{-1}$ for the PW91 functional. A k-point sampling density of ~0.04Å$^{-1}$ is commonly used in studies of CO adsorption on Hägg iron carbide (Sorescu, 2009; Petersen et al., 2010).

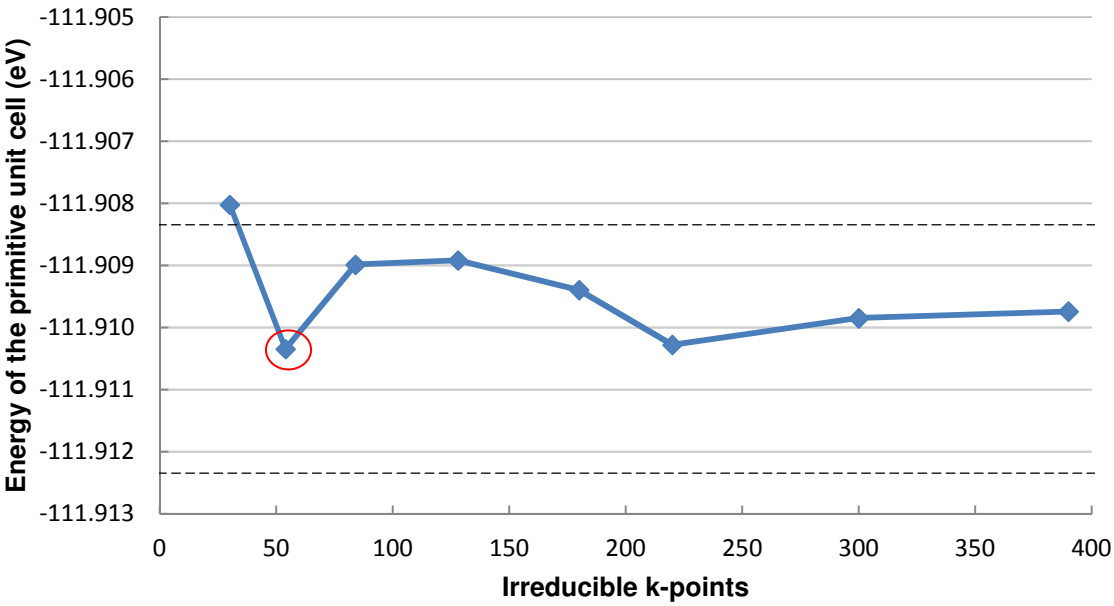


**Figure 2.4:** k-point convergence (RPBE) for bulk Hägg carbide. (Calculated using the RPBE functional, σ = 0.2eV and a cutoff energy of 520eV) Dashed lines indicates convergence criterion of 2meV error in the total energy of the primitive unit cell.

### 2.3.2 Choice of exchange correlation functional

The selection of the exchange-correlation functional is important since using different functionals can yield different results in terms of the modelling of the electronic properties. Functionals also vary in the accurate prediction of adsorbate interaction with a surface. This means that the best functional to use for this study will not be the one that simply predicts the cell parameters and electronic properties the best, but will be the functional that models the Hägg carbide properties accurately when compared to the experimentally determined structure.

In the optimisation of the bulk structure of the Hägg carbide primitive unit cell, a full automatic geometry optimisation was carried out. In this optimisation the cell shape, cell volume and ion positions are allowed to relax until the lowest energy structure is obtained. This optimisation was carried out using the PW91, RPBE and PBE functionals, to determine the optimal functional to proceed with. The results of this optimisation are shown in Table 2.3.

In selecting a functional, the electronic properties are the most important part when it comes to accurate results. In the case of Hägg carbide, this would make the magnetic moment an important property to be predicted accurately. The only available experimental value for the magnetic moment for bulk Hägg carbide is 1.70-1.75$\mu_B$, which was determined via saturation magnetisation experiments (Hofer and Cohn, 1959). This value is the total magnetic moment averaged over all the Fe atoms. Using the PW91 functional the experimentally determined magnetic moment is overestimated (1.9$\mu_B$ versus 1.7-1.75$\mu_B$). An average magnetic moment of 1.73$\mu_B$ was determined using the PBE functional which is within the experimentally determined magnetic moment range. The magnetic moment calculated using the RPBE functional is slightly higher than the measured magnetic moment (1.8$\mu_B$). The overestimation of the magnetic moment when using the PW91 functional is similar to the magnetic moment obtained by Petersen et al. (2010) using a similar methodology. The slight overestimation of the magnetic moment when using the RPBE functional has also been reported by Petersen et al. (2010) and Steynberg et al. (2008). It should be realised that the calculated magnetic moments are sensitive to the choice of radii used to partition the spin density and are therefore dependent on the approach taken (Petersen et al., 2010).

The other parameters which have been used to determine the accuracy of the model are the lattice parameters. In this regard, the agreement with experimental data for all the functionals is very good, with the maximum deviation of 0.07Å from the experimental lattice parameter observed for the *b* parameter using the PBE functional (see Table 2.3). All the tested functionals model the angle β very accurately, within 0.1º of the experimental value as determined by Retief (1999). The results obtained in this study, are comparable to those obtained previously using DFT in terms of the accuracy in predicting the lattice parameters (see Table 2.3).

Based solely on the magnetic moment, it would appear that the PBE functional would be the optimal functional to proceed with since it predicts the average magnetic moment within the range of the experimentally measured magnetic moment. However, the PBE functional also has the largest deviations of any of the functionals from the experimental lattice parameters with a deviation of 0.07Å being observed for the *b* parameter and a deviation of 0.06Å being observed for the *c* parameter. The RPBE functional models the lattice parameters as well as, if not better than, the PBE functional as seen by the smaller maximum deviation from the experimental lattice parameters when using the RPBE functional. Furthermore, the RPBE functional only slightly over-predicts the magnetic moment.

Looking further into the study, where the adsorption of CO on the surface will be investigated, both the PBE and PW91 functionals are both well known to overestimate the adsorption strength of CO on metals (Orita et al., 2004; Bludsky et al. 2005). The RBPE functional has also been found to be more accurate when modelling CO adsorption on metal surfaces when compared to the PBE functional (Stroppa and Kresse, 2008) and the PW91 functional (Abild-Petersen and Andersson, 2007).

To summarise, RPBE functional predicts the lattice parameters as well as, if not better than the PBE functional and only slightly over-predicts the magnetic moment. Also, literature indicates that the RPBE functional models CO adsorption, a key component of this study, more accurately when compared to the PBE functional. Therefore, the RPBE functional is the functional used in the rest of this study.

**Table 2.3:** Comparison of calculated lattice parameters and magnetic moment of χ-$Fe_5C_2$ with experimental and computational data from literature

| Method | a (Å) | b (Å) | c (Å) | β (°) | Magnetic Moment ($\mu_B$) |
|---|---|---|---|---|---|
| **Experimental** | 11.59 [1] | 4.58 [1] | 5.06 [1] | 97.7 [1] | 1.70-1.75 [2] |
| | | | **PW 91** | | |
| ***This study*[3]** | *11.61* | *4.56* | *5.04* | *97.9* | *1.9* |
| **Absolute Error** | 0.02 | 0.02 | 0.02 | 0.12 | |
| **Petersen *et al.* (2010)[4]** | 11.61 | 4.56 | 5.04 | 97.9 | 1.99 |
| **Steynberg *et al.*(2008)[5]** | 11.51 | 4.48 | 4.95 | 97.6 | 1.7 |
| | | | **RPBE** | | |
| ***This study*[3]** | *11.64* | *4.55* | *5.03* | *97.8* | *1.8* |
| **Absolute Error** | 0.05 | 0.03 | 0.03 | 0.05 | |
| **Petersen *et al.* (2010)[4]** | 11.62 | 4.55 | 5.03 | 97.8 | 1.86 |
| **Steynberg *et al.*(2008)[5]** | 11.57 | 4.52 | 5 | 97.7 | 1.83 |
| | | | **PBE** | | |
| ***This study*[3]** | *11.57* | *4.51* | *4.99* | *97.7* | *1.73* |
| **Absolute Error** | 0.01 | 0.07 | 0.06 | 0.08 | |
| **Steynberg *et al.*(2008)[5]** | 11.5 | 4.49 | 4.96 | 97.6 | 1.76 |
| **Sorescu (2009)[6]** | 11.58 | 4.51 | 4.99 | 96.6 | 1.73 |

[1] Experimental lattice parameters from Retief (1999)

[2] Experimental magnetic moment from Hofer and Cohn (1959)

[3] Calculated using VASP with a cutoff energy of 520eV, smearing of 0.2eV and a k-point sampling density of 0.04Å$^{-1}$

[4] Calculated using VASP with a cutoff energy of 400eV, smearing of 0.1eV and a k-point sampling density of 0.04Å$^{-1}$

[5] Calculated using CASTEP with a cutoff energy of 340eV, smearing of 0.1eV and a k-point sampling density of 0.05Å$^{-1}$

[6] Calculated using VASP with a cutoff energy of 400eV, smearing of 0.1eV and a k-point mesh of 2 × 6 × 6

### 2.3.3 Bulk modulus calculation

The bulk modulus of Hägg carbide was estimated by a manual lattice relaxation, keeping the cell shape constant, while the ion positions were allowed to shift. Since the unit cell is not equi-sided, the ratio between the lengths of the sides of the experimental crystal structure was assumed to remain constant whilst the volume was varied. The cell volume was varied around the experimental lattice volume of 132.9Å (from 130.9Å to 133.7Å). Geometry optimisation calculations, in which the ions were allowed to relax, were done at these different, fixed volumes to find the equilibrium lattice volume, in other words the cell volume where the energy of the system is at its lowest point.

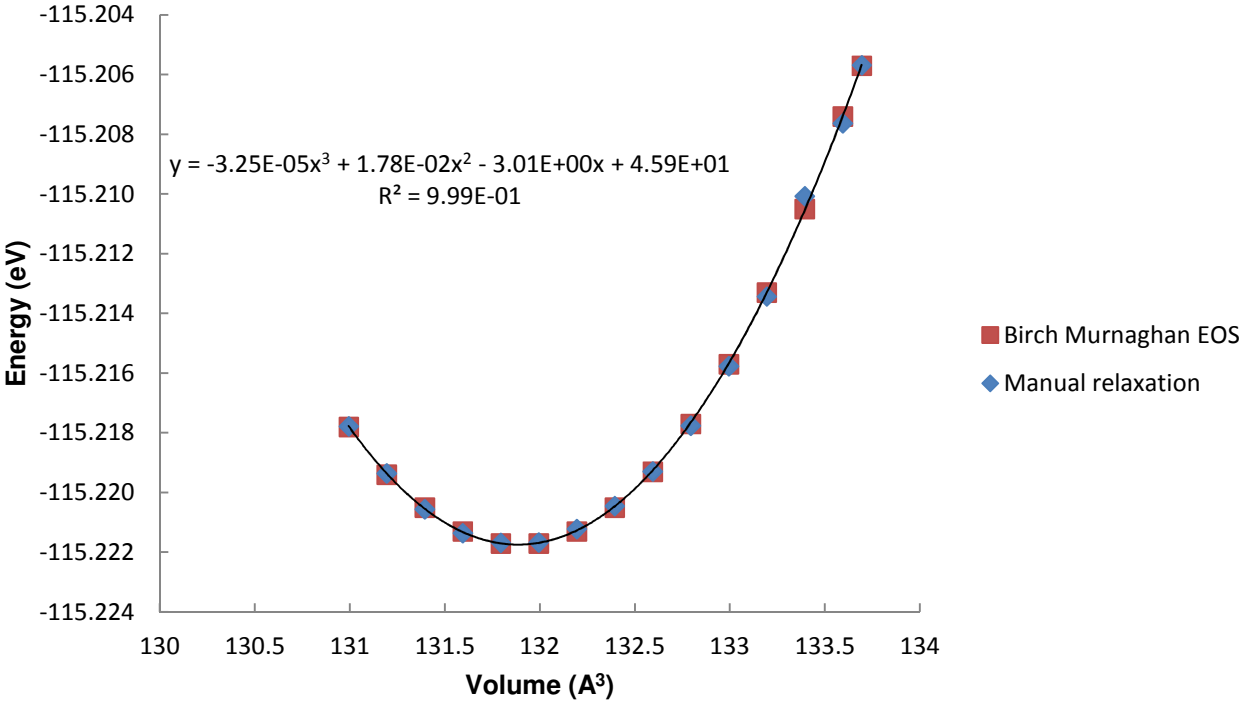


**Figure 2.5:** Energy vs. volume curve comparison of data from the manual relaxation (calculated using the RPBE functional) and the data calculated using the Birch Murnaghan equation

Figure 2.5 shows the data obtained fitted to a third order polynomial, which was the best fit to the trend shown by the data. The equation of the curve:

$$y = -3 \times 10^{-5}x^3 + 1.78 \times 10^{-2}x^2 - 3.01 \times 10^{0}x + 4.59 \times 10^{1} \qquad (2.10)$$

The data obtained from this manual relaxation was applied to the Birch- Murnaghan equation of state:

$$E(V) = E_0 + \frac{9V_0B_0}{16}\left\{\left[\left(\frac{V_0}{V}\right)^{\frac{2}{3}} - 1\right]^3 B_0' + \left[\left(\frac{V_0}{V}\right)^{\frac{2}{3}} - 1\right]^2 \left[6 - 4\left(\frac{V_0}{V}\right)^{\frac{2}{3}}\right]\right\} \qquad (2.11)$$

where $E_0$ is the minimum cell energy, $V_0$ is the corresponding minimum cell volume, $B_0$ the bulk modulus and $B'_0$ is the derivative of the bulk modulus. Using non-linear regression, the values obtained using the manual relaxation was fitted to the Birch Murnaghan equation of state. The $V_0$ values calculated using the manual relaxation was 131.79Å$^3$ with a corresponding $E_0$ value of -115.22eV. The Birch Murnaghan equation of state calculated a $V_0$ of 131.89Å$^3$ and an $E_0$ of -115.22eV showing good agreement with the values calculated using the manual relaxation ($E_0$ of -115.22eV and $V_0$ of 131.79Å$^3$ was calculated with manual relaxation).

The bulk modulus ($B_0$) was calculated using equation 2.12. The bulk modulus describes the amount of pressure required to cause a change in the volume of the crystal lattice. The bulk modulus was calculated using:

$$B(E,V) = V \times \frac{d^2E}{dV^2} \tag{2.12}$$

**Table 2.4:** Calculated Hägg carbide bulk modulus

| Functional | Bulk modulus from empirical fit (GPa) |
|---|---|
| PW91 | 204 |
| RPBE | 216 |
| PBE | 216 |

The bulk modulus for each of the functionals was calculated and compared to available literature values. Sorescu (2009) using the PBE functional and the VASP software package reported a bulk modulus of 228GPa. Esling et al. (2006) reported a valued of 209GPA using the all-electron linearised augmented plane wave (FP-LAPW) method and the WIEN2K software package. The value calculated by Elsing et al. (2006) is comparable with the values calculated in this study while the value calculated by Sorescu (2009) is somewhat higher than what has been calculated in this study. The difference could be due to the method used to calculate the bulk modulus. Unfortunately, there are no experimental values available for the bulk modulus. Therefore, it cannot be used as an additional criterion to determine the most suitable functional to describe Hägg carbide.

## 2.4 Surface model verification

To proceed with the study of the adsorption of potassium species, a surface first has to be chosen. Hägg carbide is not a simple structure. This means that even when focussing only on the low Miller index surfaces, a large number of different surfaces can be cut.

Some of the considerations in choosing the surface to study the speciation of the various potassium species are:

- The surface should be a relatively low energy surface (i.e. stable) so that it could possibly be present during the FT process
- The surface should have a good variety of different sites, so as to provide good scope to the study
- There should be literature data available for CO adsorption and a particular surface for comparison



The recent study by Steynberg et al. (2008) of the structure and surfaces of the Hägg carbide found that there are a number of surfaces with very similar energies, meaning that they may all be available under Fischer-Tropsch conditions. This means that there are a number of different surfaces which could be used to proceed with in this study.

The $Fe_5C_2(010)_{0.25}$ [F] surface is the surface which has been found to have the lowest surface energy of the set considered in that particular study (Steynberg et al., 2008). However, Sorescu (2009) reported recently that the $Fe_5C_2(100)_{0.00}$ surface has an equivalent surface energy. It should be noted that the $Fe_5C_2(100)_{0.00}$ surface is not a symmetrical surface, meaning that the top and bottom faces are not the same. Therefore, this calculated surface energy reflects the average surface energy of the two different faces. In this study we only considered adsorption on the top face as adsorption on the bottom face, at the slab thickness used in this study, had not been investigated in previous studies. This means that there would be no data available with to compare any adsorption results. The $Fe_5C_2(100)_{0.00}$ surface has a good variety of unique surface adsorption sites (see Figure 2.7), with two unique surface iron atoms (R and V), one threefold hollow site with a subsurface iron (red triangle), one threefold hollow site with a subsurface carbon (green triangle) and one unique fourfold hollow site with a centre carbon atom (black square). Sorescu (2009) and Cao et al. (2004) investigated the adsorption of CO on a number of different Hägg carbide surfaces. Both studies included the $Fe_5C_2(100)_{0.00}$ surface, so that the results obtained in this study can be compared to other reported results.

[F] The notation used in this study to label surfaces has been adopted from Steynberg et al. (2008), where for example, (100)0.25 refers to the (100) surface cleaved at 0.25 distance along the A and B axes. This can be illustrated as shown in Figure 2.6.

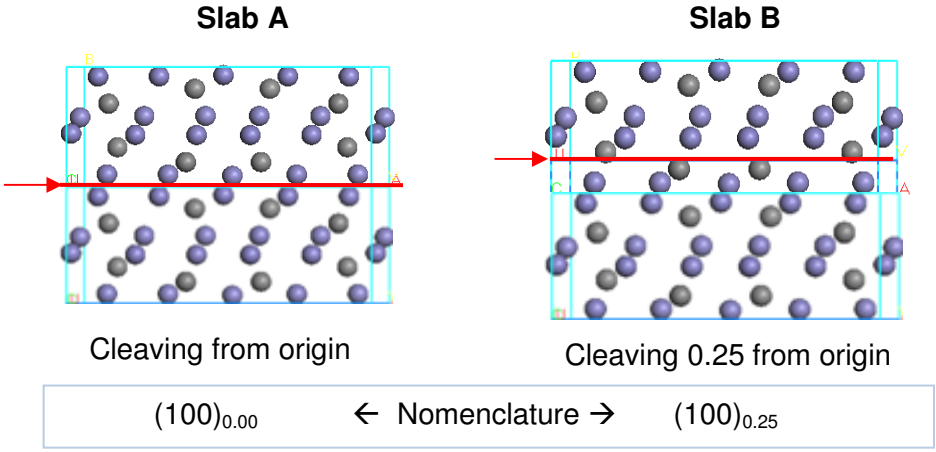


**Figure 2.6:** Naming nomenclature for surface cuts of Hägg iron carbide. The surface will be cleaved where indicated, resulting in two surfaces containing different surface atoms.

Therefore, the surface with which we will be proceeding is the $Fe_5C_2(100)_{0.00}$ surface as it is a relatively stable surface and has a good variety of possible adsorption sites compared to other low energy surfaces. It was also decided to use a different cut of the (100) plane, namely a surface which contains no subsurface carbon so that the effect of subsurface carbon can be observed. Subsurface carbon has been reported to have a negative effect on CO adsorption (Sorescu, 2009; Petersen et al., 2010). The surface that was chosen was the $Fe_5C_2(100)_{0.098}$ surface, which is shown in Figure 2.8. The $Fe_5C_2(100)_{0.098}$ surface, as with the $Fe_5C_2(100)_{0.00}$ surface, has two unique iron atoms (R and V). It contains one threefold hollow site (red triangle) and one unique fourfold hollow site without a centre carbon (black square). Both surfaces have the lattice parameters: *a = 4.5482Å and b = 5.0298Å.*

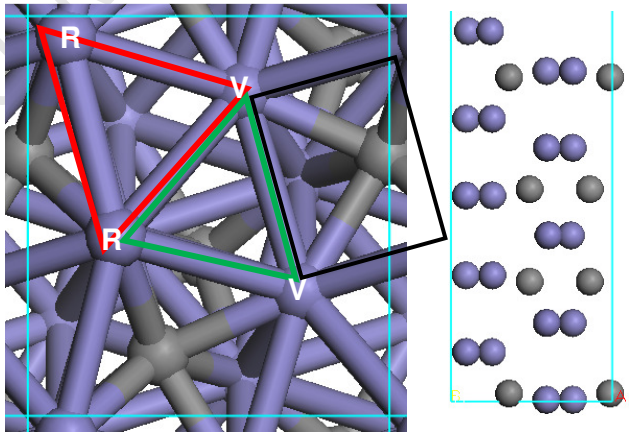


**Figure 2.7:** $Fe_5C_2(100)_{0.00}$ surface top and side view

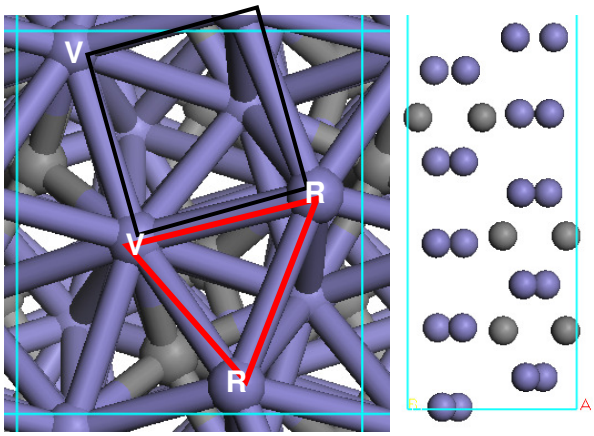


**Figure 2.8:** $Fe_5C_2(100)_{0.098}$ surface top and side view

### 2.4.1 Surface calculations

The surface is represented by a slab periodically repeated in two dimensions. A vacuum space is introduced between periodic slabs in the vertical direction. This vacuum needs to be large enough such that there is no interaction between two consecutive slabs, i.e. the bottom of the top slab should not interact with the surface of the slab below it. However, an increase in the vacuum layer size will increase the calculation time significantly. Therefore, it is important to find the minimum vacuum layer thickness which will yield no interaction between consecutive slabs and the minimum calculation time. Furthermore, the slab thickness is of importance. The computational time increases strongly with increasing slab thickness. However, a minimum slab thickness is required for a proper representation of a surface in contrast with the bulk of the catalyst.

The k-point sampling density obtained during the bulk optimisation was kept constant for the surface calculations. This was done by scaling the k-point grid to the lattice parameters of the surface cell while keeping the k-point sampling density constant. This resulted in a k-point grid of 5 × 5 × 1.

#### 2.4.1.1 Vacuum spacing optimisation

The vacuum spacing optimisation was done by keeping the slab thickness fixed and performing single point energy calculations at different vacuum thicknesses (from 8 to 17Å). The slab thickness used for this optimisation was obtained from literature (Sorescu 2009) on the $Fe_5C_2(100)_{0.00}$ surface and corresponded to a slab thickness of 10.5Å or two bulk units of Hägg carbide, $Fe_{20}C_8$. The $Fe_5C_2(100)_{0.098}$ surface cannot be cleaved stoichiometrically, therefore the same number of layers as present in the $Fe_5C_2(100)_{0.00}$ slab was used for this surface. This resulted in a slab containing 20 Fe atoms and 6 C atoms. The energies obtained for the slabs at different vacuum thicknesses were then compared, with a convergence criterion of 2meV difference between consecutive vacuum thicknesses.

For the $Fe_5C_2(100)_{0.00}$ surface it was found that a vacuum spacing of 9Å was sufficient (see Figure 2.9), with minimal change in the energy of the system as the vacuum spacing increased. In fact, all the calculated energy values (starting with a vacuum layer of 8Å) are within the convergence criterion of 2meV.



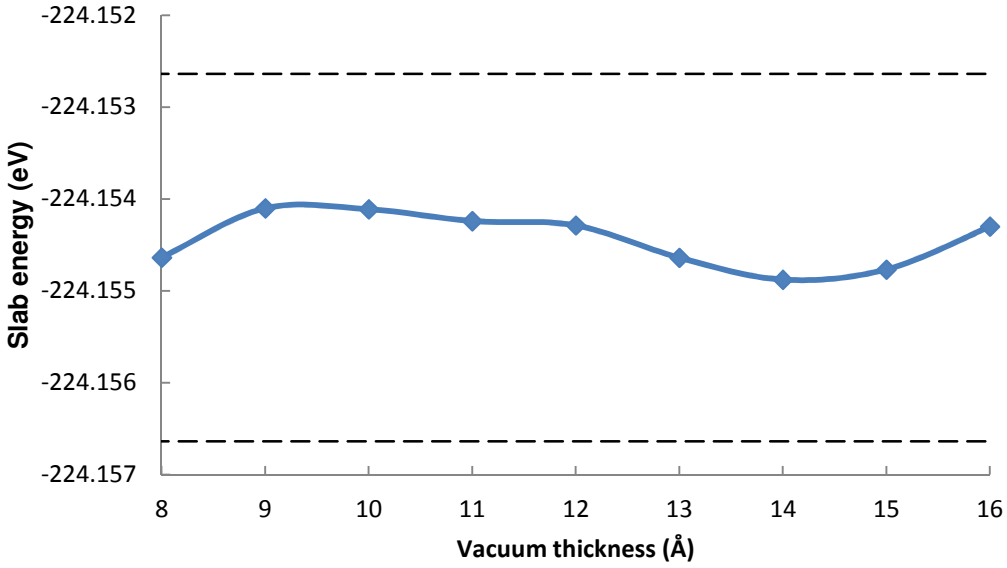


**Figure 2.9:** Optimisation of vacuum spacing for the $F_5C_2(100)_{0.00}$ surface. (Calculated with RPBE functional, σ = 0.2eV, k-point mesh of 5 × 5 × 1 and a cutoff energy of 520eV)

The $Fe_5C_2(100)_{0.098}$ surface, yielded a different picture. It was found that a 15Å vacuum spacing was required for convergence. It should be noted that an anomaly occurred for the calculation using a vacuum spacing of 14Å with a large drop in energy for no apparent reason. A number of calculations were done at this vacuum spacing and around it, changing variables such as the cutoff energy, but this anomaly only occurs at a vacuum spacing of 14Å.

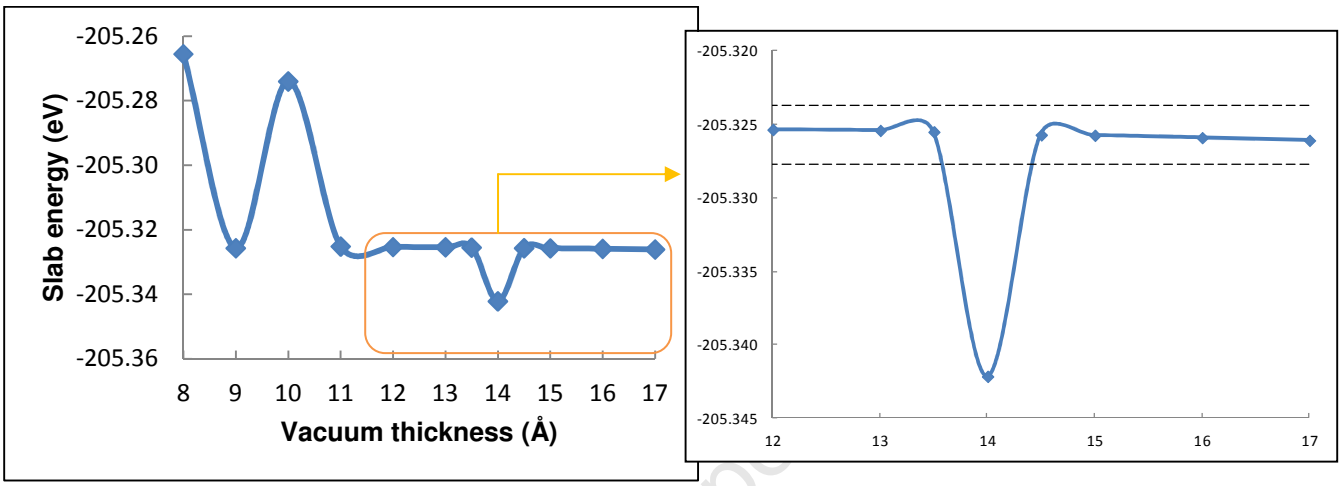


**Figure 2.10:** Optimisation of vacuum spacing for the $Fe_5C_2(100)_{0.098}$ surface. (Calculated with RPBE functional, σ = 0.2eV, k-point mesh of 5 × 5 × 1 and a cutoff energy of 520eV). Dashed lines indicate the convergence criterion of 2meV

For the structures involving CO adsorbed on Hägg iron carbide the vacuum spacing was increased to 12Å on the $Fe_5C_2(100)_{0.00}$ surface to account for the addition of the CO molecule to the system, while for the $Fe_5C_2(100)_{0.098}$ surface 15Å was deemed to be sufficient. The vacuum spacing was re-optimised for the adsorption of potassium on Hägg carbide surfaces (Sec 2.3.1.3).

#### 2.4.1.2 Slab thickness and free layers

The slab thickness is the number of layers of atoms included as part of the surface slab. For a Hägg carbide surface, it is necessary to have a stoichiometric number of atoms (multiples of $Fe_{10}C_4$) in the system for a physically relevant surface energy to be determined. This means that the slab thickness can be described in number of bulk formula units.

The number of free layers refers to the number of layers of atoms allowed to relax during surface optimisations and adsorption optimisations. This is necessary to realistically model what occurs on the surface during adsorption. Upon the adsorption of a species, the surface adjusts, relaxing and repositioning atoms to accommodate the adsorbing species. However, it is not necessary to relax all atoms in the slab as this surface adjustment typically only affects the upper layers of the slab; the effect of the adsorbate diminishes upon moving deeper into slab.

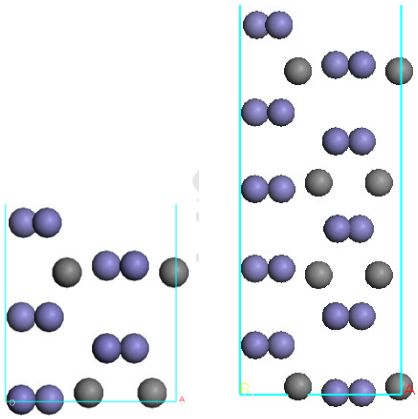

**Figure 2.11:** Slab thickness, one and two bulk units respectively for the $Fe_5C_2(100)_{0.00}$ surface

The slab thickness used in literature is typically one bulk unit (Cao et al., 2005) or two bulk units (Sorescu, 2009). The number of free layers was then varied at each of these thicknesses and the adsorption energy of CO was calculated. The convergence criterion was set to 0.02eV difference between subsequent CO adsorption energies while steadily increasing the number of free layers (e.g. $E_{ads,CO\ (2\ free\ layers)}$ - $E_{ads,CO\ (1\ free\ layers)}$. The change in the system energy (CO adsorbed on the surface) could not be used as a convergence criterion as the energy of the clean surface did not stay constant as the number of free layers were increased. This implies that the surface energy is not converged at low number of free surface layers.

The adsorption energy was defined as:

$$E_{adsorption\ CO} = \left(E_{free\ surface} + E_{gas\ phase\ CO}\right) - E_{Slab\ with\ CO} \quad (2.7)$$

Free layers are defined as shown in Figure 2.12.

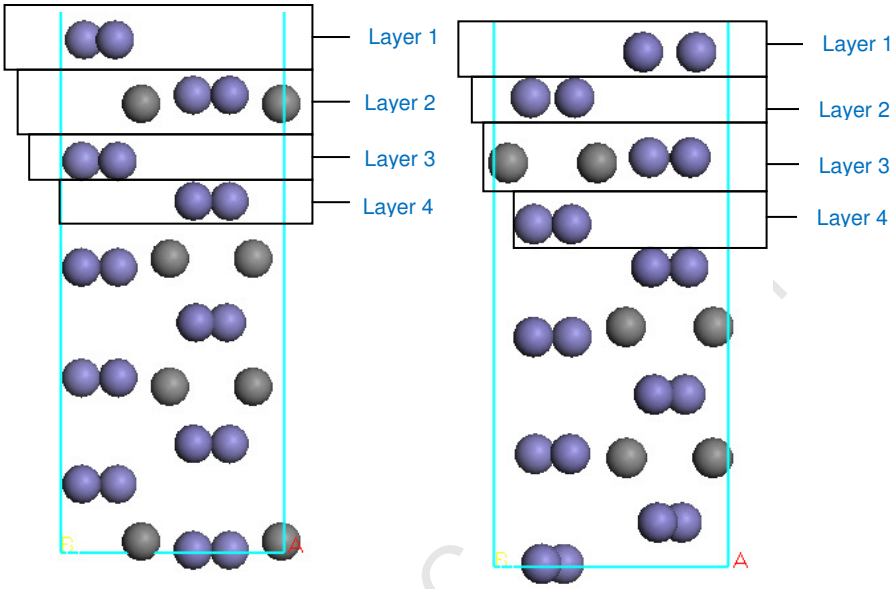


**Figure 2.12:** Numbering of free layer in the $Fe_5C_2(100)_{0.00}$ (left) and $Fe_5C_2(100)_{0.098}$ (right) surfaces respectively

For the $Fe_5C_2(100)_{0.00}$ surface, the calculations on the thinner one bulk unit slab showed that there was no convergence with regards to CO adsorption energy as the number of free layers was increased (see Table 2.5). This means that this slab is not thick enough to be used for an adsorption study. Therefore, the slab containing a single unit was not tested further with the $Fe_5C_2(100)_{0.098}$ surface.

**Table 2.5:** Optimisation of number of free layers for $Fe_5C_2(100)_{0.00}$ surface, one bulk unit ($Fe_{10}C_4$). (Calculated using RPBE functional, σ=0.2eV, k-point mesh of 5× 5 × 1 and a cutoff energy of 520eV)

| Number of free layers | Clean slab energy (eV) | Energy with CO adsorbed (eV) | Adsorption Energy (eV/CO) | $E_2$-$E_1$ (meV/CO) |
|---|---|---|---|---|
| 1 | -108.902 | -126.034 | 1.75 | --- |
| 2 | -108.910 | -126.087 | 1.80 | 50 |
| 3 | -108.914 | -126.154 | 1.87 | 70 |
| 4 | -108.918 | -126.601 | 2.32 | 450 |

However, when using the thicker two bulk unit slab there was a clear, rapid convergence as the number of free layers increased, as is seen in Table 2.6. Convergence is reached when three free layers were used.

**Table 2.6:** Optimisation of free layers in $Fe_5C_2(100)_{0.00}$ surface, with two bulk units as determined with the adsorption of CO. (Calculated using RPBE functional, σ=0.2eV, k-point mesh of 5× 5 × 1, vacuum spacing of 12Å and a cutoff energy of 520eV; convergence criterion: $E_2 - E_1$<20meV)

| Number of free layers | Clean slab energy (eV) | Energy with CO adsorbed (eV) | Adsorption Energy (eV/CO) | $E_2$-$E_1$ (meV/CO) |
|---|---|---|---|---|
| 1 | -224.240 | -241.255 | 1.64 | --- |
| 2 | -224.319 | -241.295 | 1.60 | -40.0 |
| 3 | -224.322 | -241.314 | 1.62 | 17.0 |
| 4 | -224.324 | -241.315 | 1.61 | -1.0 |
| 5 | -224.328 | -241.317 | 1.61 | -2.0 |

To confirm that the vacuum spacing of 12Å was sufficient the heat of adsorption of CO was determined with four free layers and a vacuum spacing of 11Å. The adsorption energy was calculated to be 1.60eV with the 11Å vacuum. This is within the range of the convergence criterion of 0.02eV difference between consecutive CO adsorption energies. Hence it can be concluded that a vacuum spacing of 12Å, a slab containing two single units and four free layers is sufficient for the study of CO adsorption on the $Fe_5C_2(100)_{0.00}$ surface.

The $Fe_5C_2(100)_{0.098}$ slab has the same number of layers as the $Fe_5C_2(100)_{0.00}$ slab. However, The $Fe_5C_2(100)_{0.00}$ slab consists of 28 atoms while the $Fe_5C_2(100)_{0.098}$ slab consists of 26 atoms, i.e. two less C atoms less than the $Fe_5C_2(100)_{0.00}$ slab (see Figure 2.12). This means that an average surface energy cannot be calculated for the $Fe_5C_2(100)_{0.098}$ surface as the slab is not stoichiometric.

The same rapid convergence of the adsorption energy is observed as the number of free layers was increased in the $Fe_5C_2(100)_{0.098}$ surface. Here, convergence was reached when four free layers were used. To maintain commonality, it was decided to proceed using four free layers for both the $Fe_5C_2(100)_{0.00}$ and $Fe_5C_2(100)_{0.098}$ surfaces even though for the $Fe_5C_2(100)_{0.00}$ surface the convergence criterion was satisfied with 3 free layers.

**Table 2.7:** Optimisation of number of free layers in $Fe_5C_2(100)_{0.098}$ surface, containing two bulk units as determined with the adsorption of CO. (Calculated using RPBE functional, σ=0.2eV, k-point mesh of 5× 5 × 1, vacuum spacing of 15Å and a cutoff energy of 520eV; convergence criterion: $E_2 - E_1 > 20$meV)

| Number of free layers | Blank Slab energy (eV) | Energy with CO adsorbed (eV) | Adsorption Energy (eV/CO) | $E_2$-$E_1$ (eV/CO) |
|---|---|---|---|---|
| 1 | -205.523 | -222.314 | 1.41 | --- |
| 2 | -205.550 | -222.334 | 1.41 | -7.00 |
| 3 | -205.565 | -222.452 | 1.51 | 103.00 |
| 4 | -205.569 | -222.454 | 1.51 | -2.00 |
| 5 | -205.570 | -222.457 | 1.51 | 2.00 |

As with the $Fe_5C_2(100)_{0.00}$ surface, the slab thickness and free layers found for the $Fe_5C_2(100)_{0.098}$ surface using the 15Å vacuum gap were tested using a 14Å vacuum to ensure convergence with respect to the vacuum spacing. The adsorption energy with the 14Å vacuum gap was calculated to be 1.50eV, within the convergence criterion of 0.02eV/CO difference between consecutive calculated adsorption energies.



#### 2.4.1.3 Vacuum gap optimisation with K adsorption

Re-optimisation of the vacuum gap when potassium is present on the surface was necessary since the atomic radius of the potassium atom is larger than the characteristic length of a CO molecule. This means that a larger vacuum spacing could be required to prevent interaction between the adsorbed potassium and the adjacent slab. The convergence criterion was set to 0.02eV difference between successive K adsorption energies. The cutoff energy remained unchanged at 520eV.

For the $Fe_5C_2(100)_{0.00}$ surface, the convergence criterion of 0.02eV difference between consecutive adsorption energies was met when the vacuum spacing reached 20Å. This vacuum gap was used for the rest of the adsorption and co-adsorption calculations on this surface. The dipole correction was found to be 0.06eV. To investigate the effect of increasing the vacuum gap would have on the dipole correction and the calculated adsorption energy, the vacuum gap was increased further to 30Å. This resulted in a decrease in the calculated dipole correction to 0.021eV. The calculated adsorption energy also changed, from 1.67eV to 1.69eV, an increase of 0.02eV. This increase in the calculated adsorption energy is just within the set convergence criterion of 0.02eV difference between successive K adsorption energies. Therefore, it was decided to proceed with the 20Å

vacuum gap in light of the fact that using a 30Å vacuum gap would lead to a drastic increase in computational time (using a 30Å vacuum gap resulted in a doubling of the calculation time) while not yielding a change in the calculated results outside the convergence criterion.

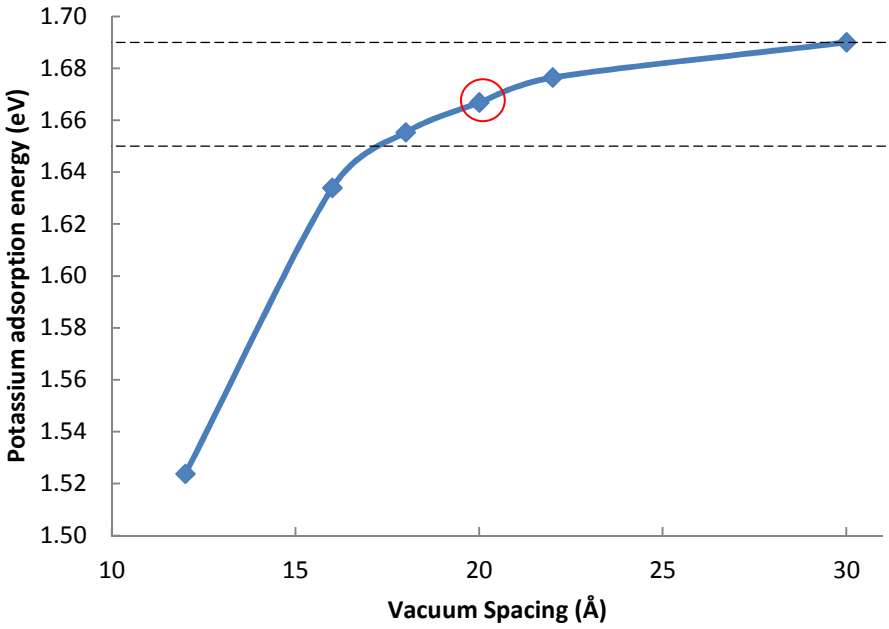


**Figure 2.13:** Optimisation of the vacuum spacing with K adsorption on the $Fe_5C_2(100)_{0.00}$ surface. (Calculated using RPBE functional, σ=0.2eV, k-point mesh of 5× 5 × 1 and a cutoff energy of 520eV; convergence criterion: $E_2 - E_1 < 0.02eV$)

For the $Fe_5C_2(100)_{0.098}$ surface, it was found that using a vacuum spacing of 20Å would be sufficient to meet the convergence criterion of 0.02eV between consecutive adsorption energies. For the $Fe_5C_2(100)_{0.098}$ surface an increase in the adsorption energy of 0.02eV is seen when increasing the vacuum spacing from 20Å to 30Å, as was seen on the $Fe_5C_2(100)_{0.00}$ surface. As with the $Fe_5C_2(100)_{0.00}$ surface, the argument that the large increase in the calculation time associated with using a 30Å vacuum as opposed to a 20Å vacuum would not yield a result outside the convergence criterion applies.

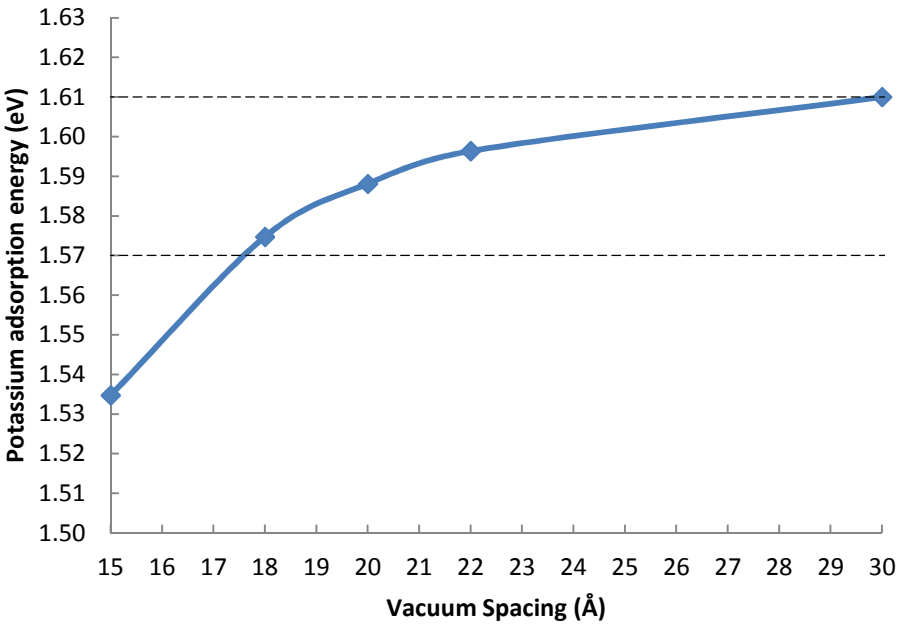


**Figure 2.14:** Optimisation of vacuum spacing with K adsorption on the $Fe_5C_2(100)_{0.098}$ surface. (Calculated using RPBE functional, σ=0.2eV, k-point mesh of 5× 5 × 1 and a cutoff energy of 520eV; convergence criterion: $E_2 - E_1 = 0.02$eV)

The vacuum spacing used in studies of potassium adsorption on other surfaces ranges from 12Å to 15Å (Mutombo et al., 2006; Zhang et al., 2006; Sorescu, 2011). This is quite a bit lower than the vacuum spacing used in this study. Our own study shows that a vacuum gap of at least 20Å is required.

#### 2.4.1.4 Cutoff energy optimisation

The cutoff energy setting used thus far was 520eV. This is high enough such that it would not affect the accuracy of the calculations. However, it would be beneficial to proceed with a lower cutoff energy as to minimise calculation times. Other studies involving CO adsorption on a Hägg carbide surface have used a cut off energy of 400eV (Sorescu, 2009; Petersen et al., 2010). The cutoff energy was optimised by varying it from 400eV to 520eV and comparing the adsorption energy calculated at the lower cutoff energy to the adsorption energy per K calculated at 520eV. If there was less than a 0.02eV difference between the adsorption energies it would be considered converged. It was found that decreasing the cutoff energy to 450eV had no effect on the adsorption energy (see Table 2.8). Therefore, for the rest of the study a cutoff energy of 450eV was applied.

**Table 2.8:** Optimisation of the cutoff energy using the $Fe_5C_2(100)_{0.00}$ surface. (Calculated using RPBE functional, σ=0.2eV, k-point mesh of 5× 5 × 1 and a vacuum gap of 20Å)

| Cut off energy (eV) | K Adsorption Energy (eV) | $E_2$-$E_{converged}$ (eV) |
|---|---|---|
| 400 | 1.70 | 0.02 |
| 450 | 1.67 | 0.00 |
| 520 | 1.67 | 0.00 |

In summary, it was found for the $Fe_5C_2(100)_{0.00}$ surface that the optimal vacuum spacing was 20Å, with respect to K adsorption, with a slab thickness of two bulk units and 4 free layers. For the $Fe_5C_2(100)_{0.098}$ surface, it was found that the optimal vacuum spacing was 20Å, with respect to K adsorption, with a slab thickness of 10 layers and 4 free layers.

**Table 2.9:** Optimised parameters for the respective surfaces

| Parameter | $Fe_5C_2(100)_{0.00}$ | $Fe_5C_2(100)_{0.098}$ |
|---|---|---|
| Slab thickness | 2 bulk units, $Fe_{20}C_8$ (10 layers) | 10 layers ($Fe_{20}C_6$) |
| Free layers | 4 | 4 |
| Vacuum Spacing (Å) | 20 | 20 |
| Cut off energy (eV) | 450 | 450 |



#### 2.4.1.5 DOS analysis

The electronic effects of the adsorption and co-adsorption of K, KO and CO on the $Fe_5C_2(100)_{0.00}$ and $Fe_5C_2(100)_{0.098}$ was investigated by analysing the density of states (DOS) of the systems. The DOS of a system is a property of the system that quantifies the number of states available at each energy level. It will be used to observe the effects adsorption can have on the surface as well as the adsorbate. Furthermore, DOS analysis will be used to further analyse the co-adsorption of the various species; K, KO, O and CO on the Hägg iron carbide surfaces.

## 2.5 Gas phase species

Throughout this study the energies and properties of the gas phase molecules of CO, $H_2$ and $H_2O$ are used. These properties were calculated using the RPBE functional. The CO was placed in a 10Å × 11Å × 12Å box while the $H_2$ and $H_2O$ were placed in 10Å × 10Å × 10Å boxes respectively. The CO molecule was placed in an asymmetric box to break the symmetry of the system and prevent dipole interactions between neighbouring CO molecules. For CO an equilibrium bond distance of 1.14Å, a ZPE-corrected bond dissociation energy of 1045kJ/mol and a vibrational frequency of 2121$cm^{-1}$ are calculated. These values are in good agreement with the experimental values of 1.13Å, 1076kJ/mol and 2170$cm^{-1}$ respectively (Lide, 2009). For $H_2$ an equilibrium bond length of 0.747Å and a vibrational frequency of 4394$cm^{-1}$ are calculated. These values are also in good agreement with experimental values of 0.741Å and 4401$cm^{-1}$ respectively (Huber and Herzberg, 1979). For $H_2O$ an equilibrium bond distance of 0.971Å and a bond angle of 104.4Å were calculated, which are again in good agreement with experimental values of 0.957Å and 104.5$^o$ (Lide, 2009).

# Chapter 3 : Results

## 3.1 CO adsorption on the $Fe_5C_2(100)_{0.00}$ and $Fe_5C_2(100)_{0.098}$ surfaces

The adsorption of CO on these surfaces was investigated on both a p(1×1) and a p(2×1) unit cell.

The $Fe_5C_2(100)_{0.00}$ surface (see Figure 3.1) contains four on top iron sites and two distinct 3 fold hollow sites, one having a subsurface carbon and one without a subsurface carbon. The surface is not flat, with two iron atoms being positioned on a 'ridge' above the other two surface iron atoms in 'valley' positions. The surface has two unique surface iron atoms (R and V), one threefold hollow site with a subsurface iron (red triangle), one threefold hollow site with a subsurface carbon (green triangle) and one unique fourfold hollow site with a centre carbon atom (black square). This carbon atom is not considered a sub surface carbon as it is the top most layer of the slab. The ridge iron atoms (R1, R2, R3 and R4) and the valley iron atoms (V1, V2, V3 and V4) are equivalent iron atoms on the bare $Fe_5C_2(100)_{0.00}$ surface.

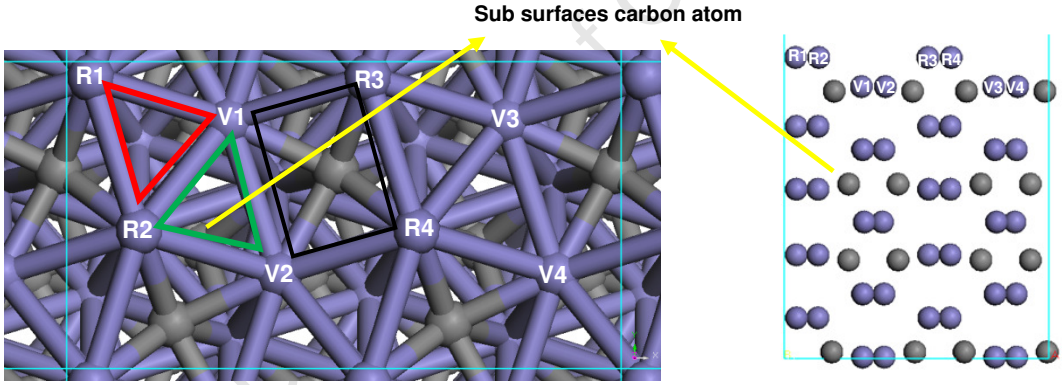


**Figure 3.1:** Labelled p(2×1) $Fe_5C_2(100)_{0.00}$ surface top and side view

On the $Fe_5C_2(100)_{0.098}$ surface (see Figure 3.2), there are four surface iron atoms, with no surface carbon atoms. As with the $Fe_5C_2(100)_{0.00}$ surface, the surface is not flat. Two iron atoms are positioned higher than the other two forming a 'ridge' and 'valley'. The $Fe_5C_2(100)_{0.098}$ surface has two unique iron atoms (R and V). It contains one threefold hollow site (red triangle) and one unique fourfold hollow site without a centre carbon (black square). The ridge iron atoms (R1, R2, R3 and R4) and the valley iron atoms (V1, V2, V3 and V4) are also equivalent iron atoms on the $Fe_5C_2(100)_{0.098}$ surface.

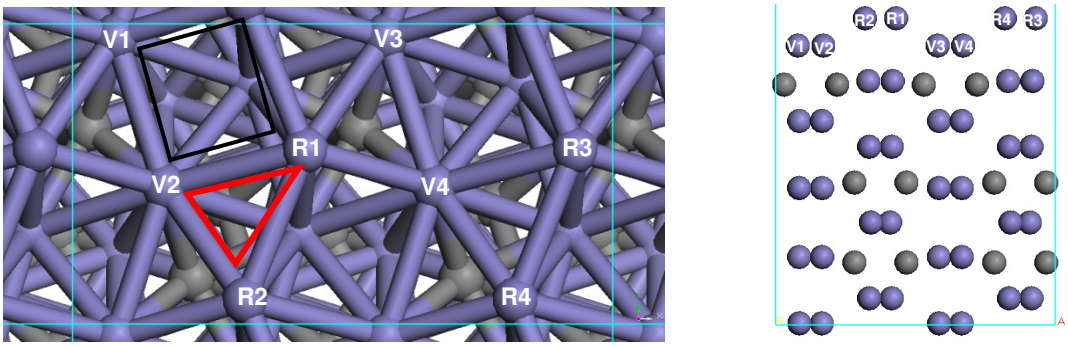


**Figure 3.2:** Labelled p(2×1) $Fe_5C_2(100)_{0.098}$ surface top and side view

### 3.1.1 CO adsorption on the $Fe_5C_2(100)_{0.00}$ surface

Specific notation will be used to describe the adsorption configurations of CO to the surface. The 1F, 2F and 3F adsorption modes refer to the degree of coordination of the CO to the surface. 1F means that the CO is bonded to one surface atom, 2F means that the CO is bonded to two surface atoms and 3F means that the CO is bonded to three surface atoms. CO may be tilted relative to the surface plane; the angle β represents the angle of the CO relative to the surface plane.

The starting configurations used to investigate CO adsorption on this surface are given in Figure 3.3. The on top iron ridge and valley sites as well as both threefold hollow sites were probed to determine which site would yield the most stable configuration for CO adsorption. These starting configurations were also chosen so as to investigate the sites which have been reported to be stable for CO adsorption on the $Fe_5C_2(100)_{0.00}$ surface (Sorescu, 2009).

The adsorption of CO yielded three different stable adsorption configurations with different adsorption energies. The adsorption configurations found in this study are shown in Figure 3.4 for the adsorption configurations on a p(1×1) cell and Figure 3.5 for the adsorption configurations on a p(2×1) cell. The zero point vibrational energy (ZPVE) corrected adsorption energies, bond lengths and vibrational frequencies of the CO adsorption configurations are reported in Table 3.1. When discussing the adsorption energies on this surface, the value given in brackets is the value calculated for the p(2×1) cell.

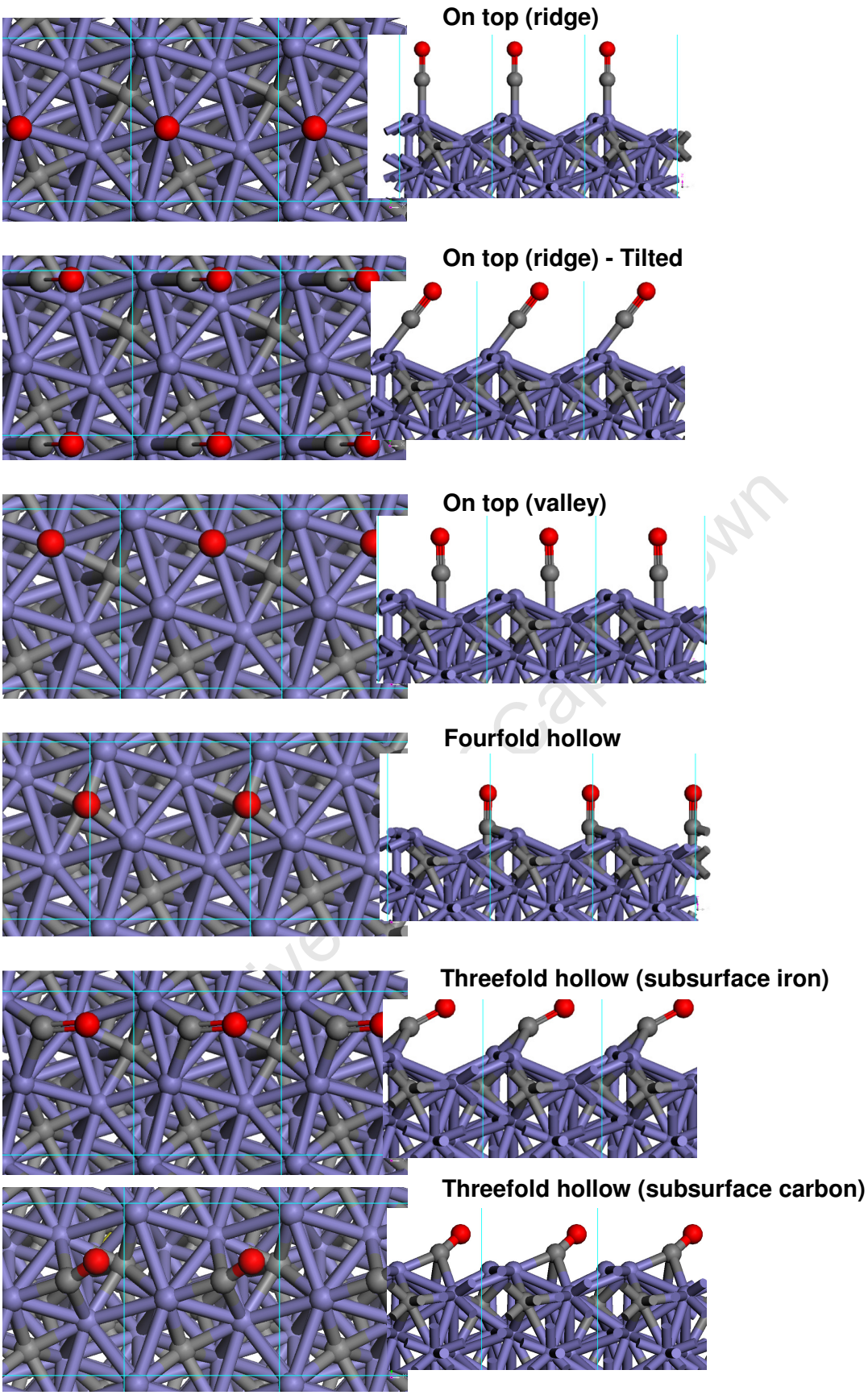


**Figure 3.3:** Starting configurations for CO adsorption on the $Fe_5C_2(100)_{0.00}$ surface

For the 1F adsorption configuration, the CO atom sits vertically directly above a ridge iron atom with a CO bond length of 1.17Å. For the 3F configurations, the CO atom sits above a threefold hollow formed by two ridge iron atoms and a valley iron atom. The CO bond length was calculated to be 1.20Å for the 3F adsorption configuration above the three-fold hollow site with the subsurface iron. For the 3F adsorption geometry above the three-fold hollow site with the subsurface carbon the CO bond length was calculated to be 1.25Å. When moving to the p(2×1) cell, a lengthening of the bond to the valley iron atom was observed for the 3F adsorption configurations. Sorescu (2009) and Cao et al. (2004) calculated similar geometries for the adsorption of CO on the $Fe_5C_2(100)_{0.00}$ surface. However, in the case of the 1F CO adsorption state, we do not calculate a 1F tilted state as one of the stable adsorption configurations of CO as reported by Sorescu (2009). CO adsorption on the fourfold hollow results in migration of the CO from the fourfold site to the threefold hollow site with a subsurface iron.

The most energetically favoured adsorption configuration was found to be the 1F adsorption state, with a calculated adsorption energy of 1.55eV (1.60eV for the p(2×1) cell). The higher coordinated adsorption states, namely the 2F and 3F states are found to have lower adsorption energies, with CO adsorption above the threefold hollow with a subsurface carbon being the least energetically favoured. Increasing the cell from a p(1×1) to a p(2×1), leads to an increase in the calculated CO adsorption energies for all adsorption configurations. This increase the calculated CO adsorption energies is due to the decrease in coverage caused by moving to a larger cell. The adsorption energies of CO on the $Fe_5C_2(100)_{0.00}$ surface calculated in this study are quite a bit lower (~0.3eV) than the adsorption energies calculated on the same surface by Sorescu (2009). This difference in adsorption energies is possibly due to the difference in the functional used to model the adsorption of CO. Sorescu (2009) used the PBE functional while in this study the RPBE functional is used. Sorescu (2009) also finds the 1F and 3F adsorption configurations to be of similar strength whereas in this study the 1F adsorption configuration is more stable. The effect of the subsurface carbon, causing a decrease in the adsorption energy of CO, in the case of the 3F adsorption configuration on the three-fold hollow site with the subsurface carbon is not seen in the studies by Sorescu (2009) or Cao et al. (2004).

The vibrational frequency calculated for the CO stretching frequency for the 1F state was calculated to be 1950$cm^{-1}$. The 3F state on the threefold hollow with the subsurface iron atom was calculated to have a stretching frequency of 1768$cm^{-1}$, while the stretching

frequency of 3F CO adsorption on the threefold hollow with the subsurface carbon was calculated to be 1483cm$^{-1}$. A decrease in the CO bond stretching frequency with increased coordination of the CO molecule to the surface is observed. This implies a weakening of the CO bond which may result in a more facile CO cleavage from these states. The vibrational frequencies of the CO adsorptions in the p(2×1) cell show no major shift from the frequencies calculated in the p(1×1) case. Sorescu (2009) calculates similar vibrational frequencies for the 1F adsorption configuration (1900cm$^{-1}$) and the 3F adsorption configuration on the threefold hollow with the subsurface iron (1701cm$^{-1}$). However, for the 3F adsorption configuration on the threefold hollow with the subsurface iron, Sorescu (2009) calculated a vibrational frequency of 1701cm$^{-1}$, much higher than what is calculated in this study. This indicates that the effect of the subsurface carbon is not seen in the study by Sorescu (2009).

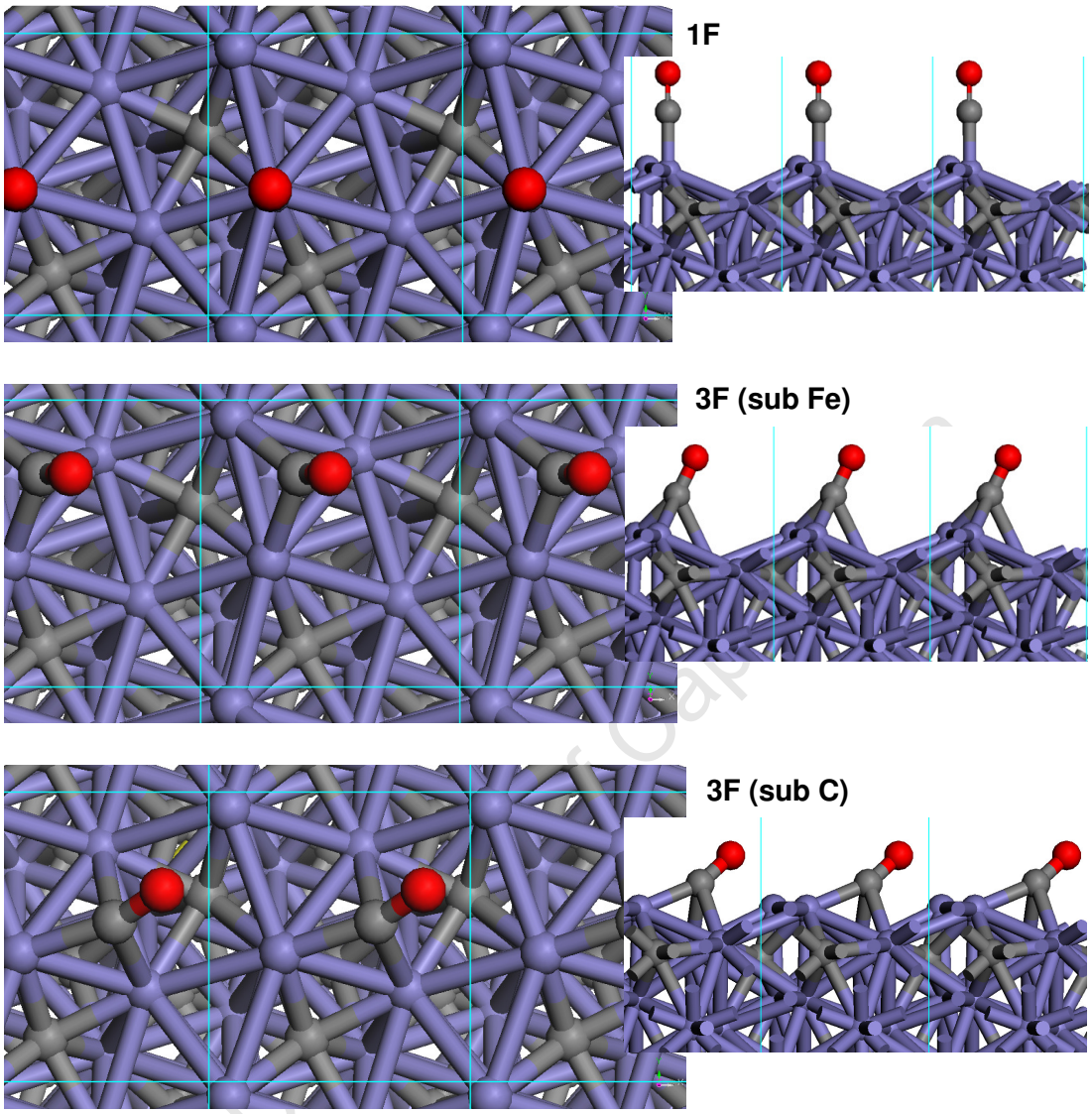


**Figure 3.4:** Calculated p(1×1) CO adsorption configurations on the $Fe_5C_2(100)_{0.00}$ surface (Calculated using RPBE functional, σ=0.2eV, k-point mesh of 5 × 5 × 1 and a cutoff energy of 520eV)

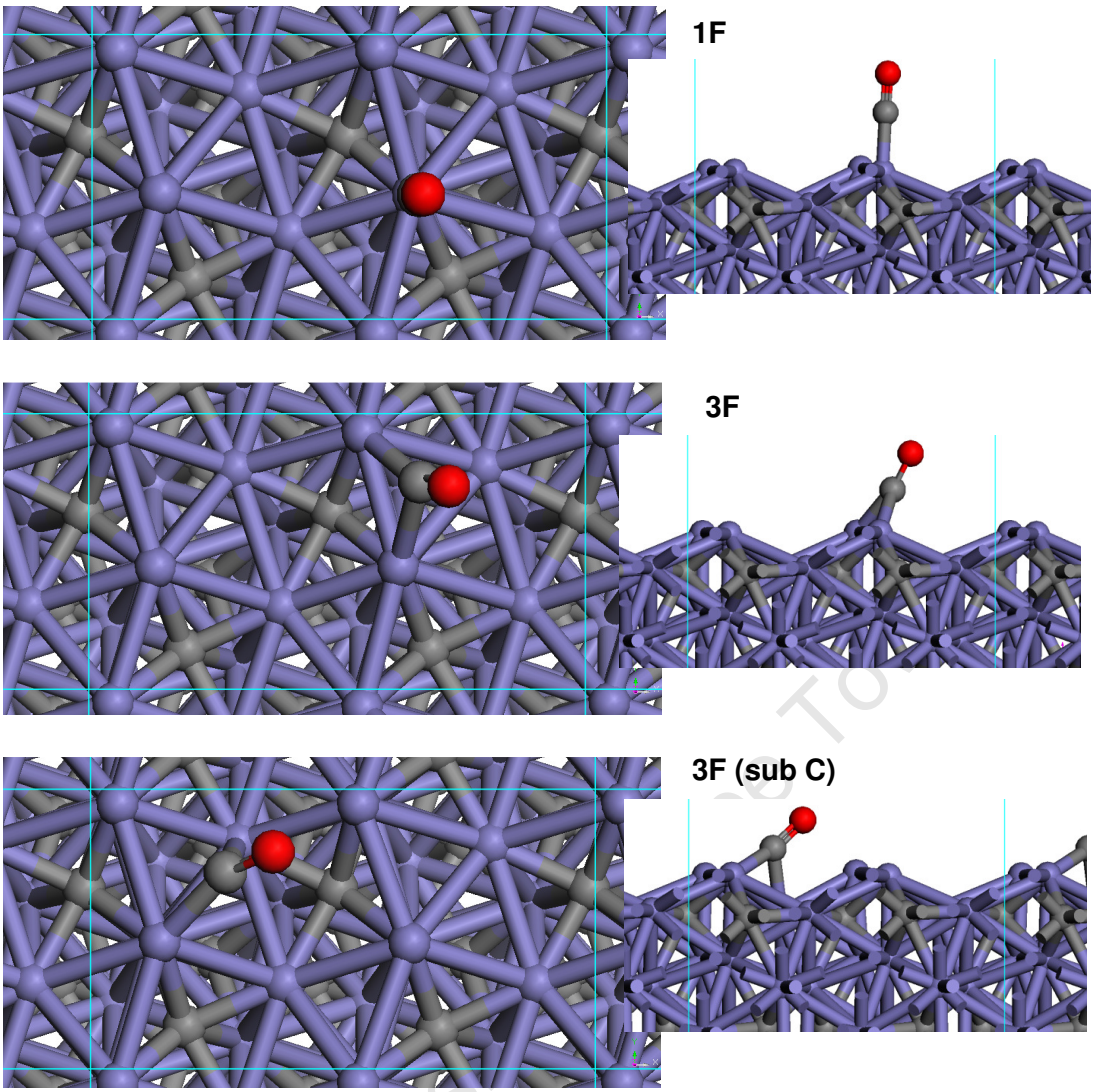


**Figure 3.5:** Calculated p(2×1) CO adsorption configurations on the $Fe_5C_2(100)_{0.00}$ surface (Calculated using RPBE functional, σ=0.2eV, k-point mesh of 3 × 5 × 1 and a cutoff energy of 520eV)

**Table 3.1:** Calculated ZPE-corrected adsorption energies ($E_{ads}$), zero-point vibrational energies (ZPVE), C-O stretching frequencies ($\nu$(C-O)) and structural parameters for CO adsorbed on $Fe_5C_2(100)_{0.00}$. The angle β is defined below (Calculated using RPBE functional, σ=0.2eV and a cutoff energy of 520eV)

| Bond Type | $E_{ads}$ (eV/CO) | ZPE (eV/CO) | $D_{Fe-C}$ Å | $D_{C-O}$ Å | β (°) | v(C-O) ($cm^{-1}$) |
|---|---|---|---|---|---|---|
| **1×1** | | | | | | |
| 1F | 1.55 | 0.20 | 1.79 | 1.17 | 90 | 1950 |
| 3F (sub Fe) | 1.47 | 0.18 | 1.92 (R1); 1.99 (R2); 2.33 (V1) | 1.20 | 63.9 | 1768 |
| 3F (sub C) | 1.09 | 0.17 | 1.87 (R1); 2.19 (V1); 2.09 (V2) | 1.25 | 48.5 | 1483 |
| **2×1** | | | | | | |
| 1F | 1.60 | 0.20 | 1.79 | 1.17 | 90 | 1927 |
| 3F | 1.54 | 0.18 | 1.88 (R1); 2.03 (R2); 2.54 (V1) | 1.20 | 63.4 | 1771 |
| 3F (sub C) | 1.34 | 0.17 | 1.88 (R2); 1.97 (V1); 2.93 (V2) | 1.24 | 46.3 | 1507 |

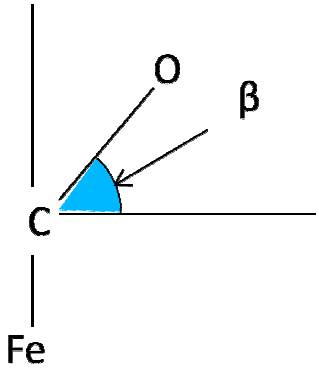


### 3.1.2 CO adsorption on the $Fe_5C_2(100)_{0.098}$ surface

The starting configurations for the adsorption of CO on this surface are given in Figure 3.6. The starting configurations used were chosen to investigate all the sites available for CO adsorption on this surface, namely the on top ridge iron site, the on top valley iron site and the threefold hollow with the subsurface iron. The adsorption configurations found in this study are reported in Figure 3.7 (p(1×1)) and Figure 3.8 (p(2×1)). As shown in Figure 3.7 and Figure 3.8, there are two different stable sites for CO adsorption on the $Fe_5C_2(100)_{0.098}$ surface. Adsorption on the fourfold iron site was attempted, however; it was found that the CO would revert to a 1F valley configuration.

The stable states calculated on the $Fe_5C_2(100)_{0.098}$ surface are 1F states found either in the valley or on the ridge. This is different to the CO adsorption on the $Fe_5C_2(100)_{0.00}$ surface in that no 3F stable states were found. Furthermore, no 1F state was calculated on top of a valley iron atom on the $Fe_5C_2(100)_{0.00}$ surface. The CO bond length was calculated to be 1.17Å for the 1F ridge state and 1.19Å for the 1F valley state. The CO bond length of the CO ridge state on the $Fe_5C_2(100)_{0.098}$ surface is comparable to the bond length of the 1F ridge state on the $Fe_5C_2(100)_{0.00}$ surface.

The zero point vibrational energy (ZPVE) corrected adsorption energies, bond lengths and vibrational frequencies of the CO adsorption configurations are given in Table 3.2. When discussing the adsorption energies and vibrational frequencies on this surface, the value given in brackets is the value calculated for the p(2×1) adsorption state.

The calculated CO adsorption energy showed that the 1F valley state is the most stable state on this surface with a calculated adsorption energy of 1.59eV (1.57eV for the p(2×1)

cell). The 1F ridge adsorption state is less stable with an adsorption energy of 1.45eV (1.34eV for the p(2×1) cell). The adsorption energy was observed to decrease with decreasing coverage on this surface. This is completely opposite to what is seen on the $Fe_5C_2(100)_{0.00}$ surface where the calculated adsorption energy increases with decreasing coverage. This is also opposite to the trend seen in literature, where the calculated adsorption energy of CO is observed to increase with decreasing coverage (Sorescu, 2011). The explanation for this decrease in the adsorption energy of CO on the ridge iron site with decreasing coverage is not known at this stage.

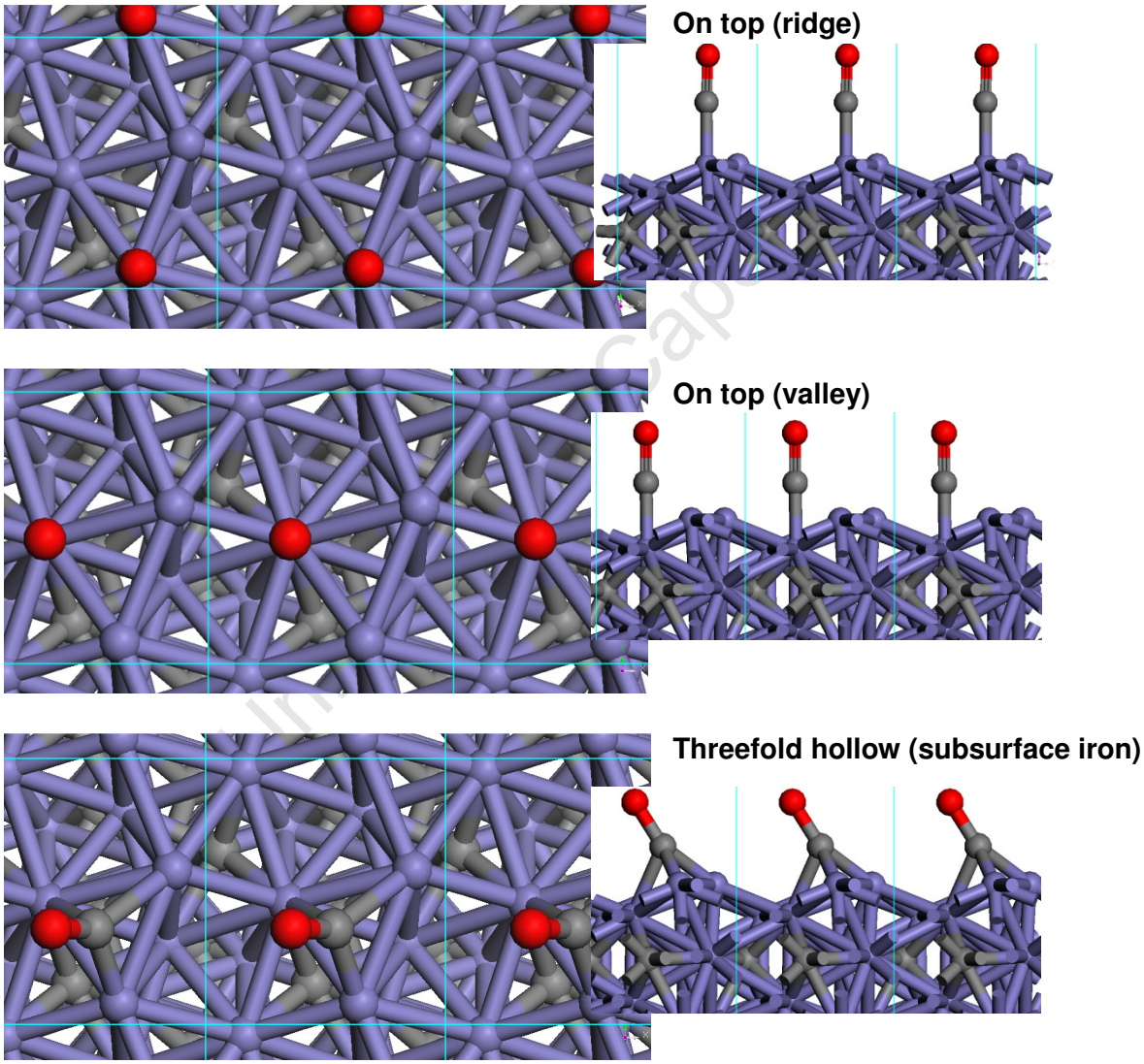


**Figure 3.6:** Starting configurations for CO adsorption on the $Fe_5C_2(100)_{0.098}$ surface

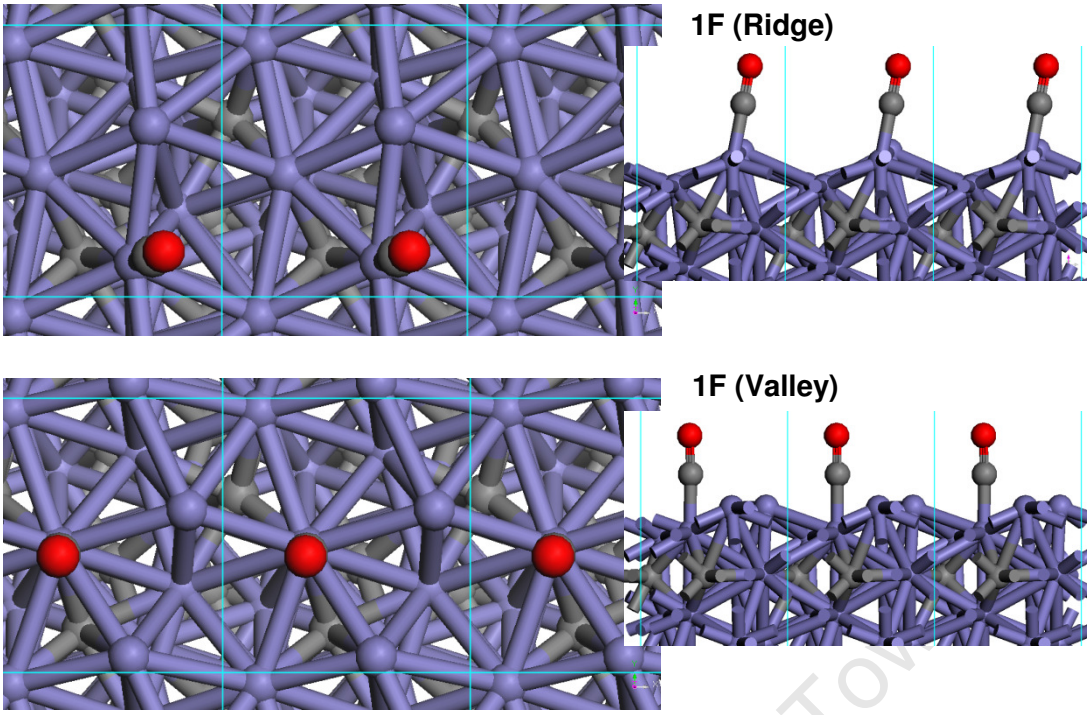


**Figure 3.7:** Calculated (1×1) CO adsorption configurations on the $Fe_5C_2(100)_{0.098}$ surface (Calculated using RPBE functional, σ=0.2eV, k-point mesh of 5 × 5 × 1 and a cutoff energy of 520eV)

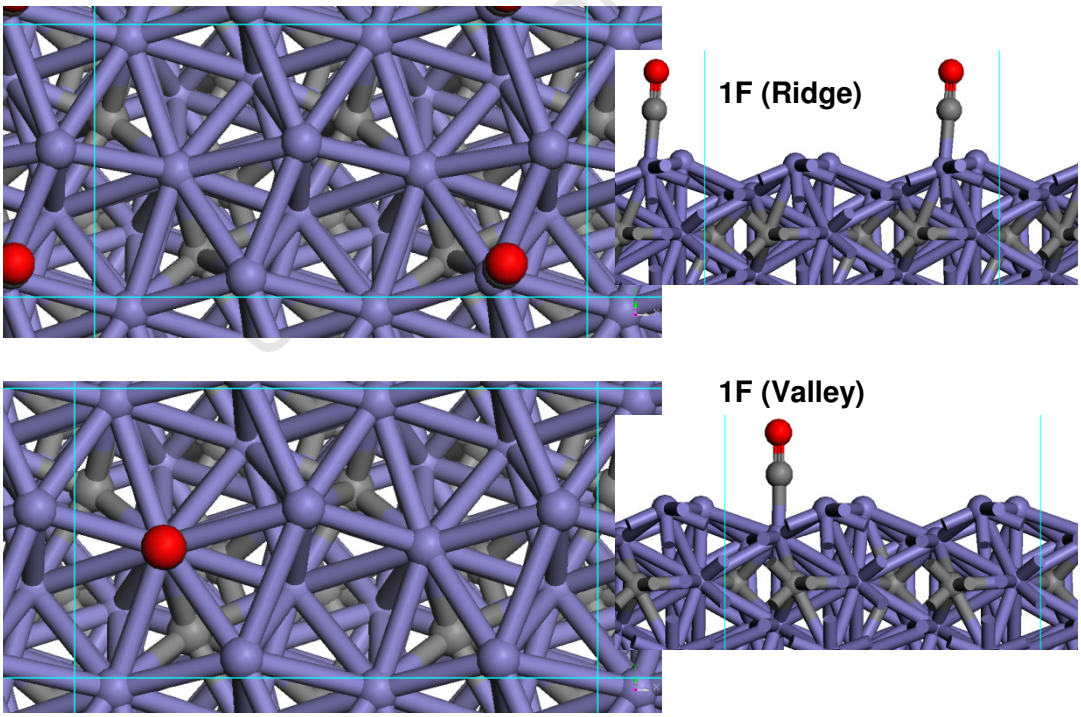


**Figure 3.8:** Calculated CO adsorption configurations on the p(2×1) $Fe_5C_2(100)_{0.098}$ surface (Calculated using RPBE functional, σ=0.2eV, k-point mesh of 3 × 5 × 1 and a cutoff energy of 520eV)

**Table 3.2:** Calculated ZPE-corrected adsorption energies ($E_{ads}$), zero-point vibrational energies (ZPVE), C-O stretching frequencies ($\nu$(C-O)) and structural parameters for CO adsorbed on $Fe_5C_2(100)_{0.098}$ where (R) or (V) refers to the ridge or valley state respectively. (Calculated using RPBE functional, σ=0.2eV, POTIM value of 0.02 and a cutoff energy of 520eV)

| Bond Type | $E_{ads}$ (eV/CO) | ZPE (eV/CO) | v(C-O) ($cm^{-1}$) | $D_{Fe-C}$ (Å) | $D_{C-O}$ Å | β (°) |
|---|---|---|---|---|---|---|
| **1×1** | | | | | | |
| 1F (R) | 1.45 | 0.199 | 1944 | 1.80 | 1.17 | 80.0 |
| 1F (V) | 1.59 | 0.197 | 1839 | 1.78 | 1.19 | 90.0 |
| **2×1** | | | | | | |
| 1F (R) | 1.34 | 0.199 | 1930 | 1.80 | 1.17 | 92.9 |
| 1F (V) | 1.57 | 0.197 | 1826 | 1.78 | 1.19 | 90.0 |

### 3.1.3 Charge analysis of CO adsorption on the $Fe_5C_2(100)_{0.00}$ and $Fe_5C_2(100)_{0.098}$ surfaces

To gain further insight into the adsorption of CO on the chosen Hägg carbide surfaces, the stable adsorption configurations were analysed using a Bader analysis. A Bader analysis assigns electrons to the various atoms in the system by using electronic charge density and minima of electron density to assign volumes to atoms, and consequently charges.

For the surface iron atoms, the charge difference given is the change in the charge on atom when an adsorbate is present from the charge when the adsorbate is absent. The charge difference for the adsorbate, CO, is the difference in the charge from the C and O atoms respectively in their ground-state (i.e. C with four electrons and O with 6 electrons). In the gas phase, CO is already polarised, with the O atom controlling the majority of the electrons and a charge of -0.67 when compared to a ground-state O atom. Once adsorbed, the negative charge on the O atom is calculated to increase while the C atom becomes less positively charge, indicating electron movement from the surface to the CO. The iron atom(s) that play a role in the CO adsorption all have a calculated decrease in electron density upon the adsorption of CO.

The Bader analyses of the various CO adsorption configurations for both surfaces (see Table 3.3 and Table 3.4) shows that in all cases the iron atoms bonded to the CO molecule lose electrons to the CO, with the O atom gaining the majority of the electrons. The Bader analysis of CO adsorption on the $Fe_5C_2(100)_{0.098}$ surface in the 1F valley configuration

showed donation of electrons was spread amongst the surface iron atoms. The results of the Bader analyses on both the $Fe_5C_2(100)_{0.00}$ and $Fe_5C_2(100)_{0.098}$ surfaces, indicates that the effect of increasing the size of the unit cell from p(1×1) to p(2×1) has a negligible effect on the charge transfer from the surface to the CO.

**Table 3.3:** Bader analysis of CO adsorption on $Fe_5C_2(100)_{0.00}$ surface. The charges of the surface iron atoms calculated are calculated relative to the charges on the surface atoms when no adsorbate is present on the surface. The charges on the C and O atoms are calculated relative to ground-state C and O atoms respectively.

| Adsorption configuration | Charge difference | | | | | | | | | |
|---|---|---|---|---|---|---|---|---|---|---|
| | C | O | Fe (R1) | Fe (R2) | Fe (V1) | Fe (V2) | Fe (R3) | Fe (R4) | Fe (V3) | Fe (V4) |
| **p(1×1)** | | | | | | | | | | |
| **1F (Ridge)** | 0.62 | -0.83 | 0.16 | 0.07 | 0.07 | 0.07 | -- | -- | -- | -- |
| **3F (subsurface iron)** | 0.32 | -0.74 | 0.20 | 0.12 | 0.12 | 0.09 | -- | -- | -- | -- |
| **3F (subsurface carbon)** | 0.21 | -0.80 | 0.20 | 0.12 | 0.12 | 0.09 | -- | -- | -- | -- |
| **p(2×1)** | | | | | | | | | | |
| **1F (Ridge)** | 0.52 | -0.80 | 0.02 | 0.15 | 0.04 | 0.03 | 0.02 | 0.02 | 0.03 | 0.04 |
| **2F (Ridge)** | 0.34 | -0.77 | 0.03 | 0.02 | 0.01 | 0.02 | 0.07 | 0.11 | 0.10 | 0.03 |
| **3F (subsurface carbon)** | 0.59 | -0.82 | 0.08 | 0.02 | 0.06 | 0.06 | 0.17 | 0.00 | 0.14 | 0.06 |

**Table 3.4:** Bader analysis of CO adsorption on $Fe_5C_2(100)_{0.098}$ surface. The charges of the surface iron atoms calculated are calculated relative to the charges on the surface atoms when no adsorbate is present on the surface. The charges on the C and O atoms are calculated relative to ground-state C and O atoms respectively.

| Adsorption configuration | Charge difference | | | | | | | | | |
|---|---|---|---|---|---|---|---|---|---|---|
| | C | O | Fe (R1) | Fe (R2) | Fe (V1) | Fe (V2) | Fe (R3) | Fe (R4) | Fe (V3) | Fe (V4) |
| **p(1×1)** | | | | | | | | | | |
| **1F (Ridge)** | 0.47 | -0.67 | 0.03 | 0.18 | 0.02 | 0.01 | -- | -- | -- | -- |
| **1F (Valley)** | 0.40 | -0.81 | 0.08 | 0.02 | 0.12 | 0.02 | -- | -- | -- | -- |
| **p(2×1)** | | | | | | | | | | |
| **1F (Ridge)** | 0.49 | -0.71 | 0.01 | 0.02 | 0.03 | 0.02 | 0.11 | 0.09 | 0.04 | 0.04 |
| **1F (Valley)** | 0.45 | -0.85 | 0.08 | 0.12 | 0.07 | 0.02 | 0.09 | 0.02 | 0.02 | 0.01 |

## 3.2 K adsorption on the $Fe_5C_2(100)_{0.00}$ and $Fe_5C_2(100)_{0.098}$ surfaces

The adsorption of potassium on these surfaces has been investigated using both a p(1×1) and a p(2×1) supercell. The surfaces were labelled as shown previously in Figure 3.1 and Figure 3.2.

### 3.2.1 K adsorption on the $Fe_5C_2(100)_{0.00}$ surface

The starting configurations for the adsorption of potassium on this surface are shown in Figure 3.9. Adsorption of potassium was attempted on all available on top and threefold hollow sites. Potassium was found to adsorb in one of two adsorption configurations (see Figure 3.10), which will be referred to as position 1 and position 2 respectively. Despite appearing to be equivalent, comparing the bond lengths to the surface iron atoms and the distance to the surface plane show differences between the two structures. The adsorption of K on a (2×1) unit cell yielded the same adsorption configurations, with minimal alterations in the bond lengths. Therefore, only the bond lengths for the (2×1) adsorption configurations are reported in Table 3.5 . The distance to the surface plane is 2.43Å for position 1 and 2.46Å for position 2. This surface plane is defined as the plane generated by the ridge iron atoms. The shortest bond length for position 1 and position 2 are 3.31Å and 3.29Å respectively. With respect to geometry, the largest difference between position 1 and position 2 would be the distance to the valley iron atoms. However, this difference in the distance from the valley iron atoms could be due to the mobility of the potassium on the surface in the direction of the valley.

This distance to the surface plane compares well with the adsorption of K that was investigated on Co($10\bar{1}0$) surface (Jenkins and King, 2000), where the distance to the surface planes was between 2.44Å and 2.85Å. Comparing the observed bond lengths to the surface iron atoms with literature values for potassium adsorption on metal surfaces on hollow sites; Sorescu (2011) in a study of potassium adsorption on the Fe(100) surface found that the shortest bond length was approximately 3.50Å for the most stable adsorption configuration (the 4F) of potassium on the Fe(100) surface. This compares well with the bond lengths observed here.

The ZPVE corrected p(1×1) adsorption energy is 1.67eV for both position 1 and position 2. This adsorption energy is slightly higher than the energetically favoured adsorption energy of CO on the p(1×1) cell (1.55eV). This result is comparable to work by Sorescu (2011), where the adsorption energy of K on the Fe(100) surface is found to be of similar strength to that of CO.

When adsorbing K on the p(2×1) unit cell and thus decreasing the coverage, the adsorption energy increased to 1.74eV for position 1 and 1.72eV for position 2. This increase in adsorption energy with decreasing coverage was also observed by Sorescu (2011) in the study of K adsorption on Fe(100), where the adsorption energy was found to increase from 1.28eV (0.5ML coverage) to 1.68eV (0.062ML coverage) for the 4F hollow K adsorption configuration on Fe(100).

The vibrational analysis of both position 1 and position 2 proved to be problematic, with the frequency with K moving along the valley yielding a negative frequency at the chosen POTIM value (0.02) (the POTIM value is the value of the step-size that is applied to the atoms during the vibrational calculation). The size of this value is important as too large a step-size could lead to a step outside the energy well associated with a minimum on the potential energy surface. Too small a step-size could lead to interference from the inherent inaccuracy of DFT calculations. Repeating the same vibrational calculations using the same settings yielded fluctuations in the vibrational frequencies shown in Table 3.6. This indicates that the potential energy surface for K adsorption on the $Fe_5C_2(100)_{0.00}$ surface may be quite flat, making it difficult to obtain an accurate vibrational analysis. To attempt to remedy this and to observe the influence of the POTIM value on the results of the vibrational analysis, a series of vibrational calculations were done at different POTIM values, 0.015 and 0.03 respectively (see Table 3.7). This proved to be inconclusive as the negative frequency persisted at both these values in the case of position 2, while a low positive frequency was seen at a POTIM value of 0.03 in the case of position 1. This indicates that the K could be highly mobile along the valley.

A diffusion study of the diffusion of K along the valley from position 1 to position 2 using a linear function, found that the maximum barrier for the diffusion of K along the surface was 0.02eV. The methodology for used to determine the diffusion barrier can be found in the

Appendix. This is a very low barrier for diffusion and confirms that on the $Fe_5C_2(100)_{0.00}$ surface K has high mobility along the valley. Therefore, the motion of K along the valley will be treated not as a vibrational mode, but as a translational mode. This high mobility of K on the surface is also found by Sorescu (2011) for adsorption of potassium on Fe(100) with a barrier for diffusion of 0.03eV.

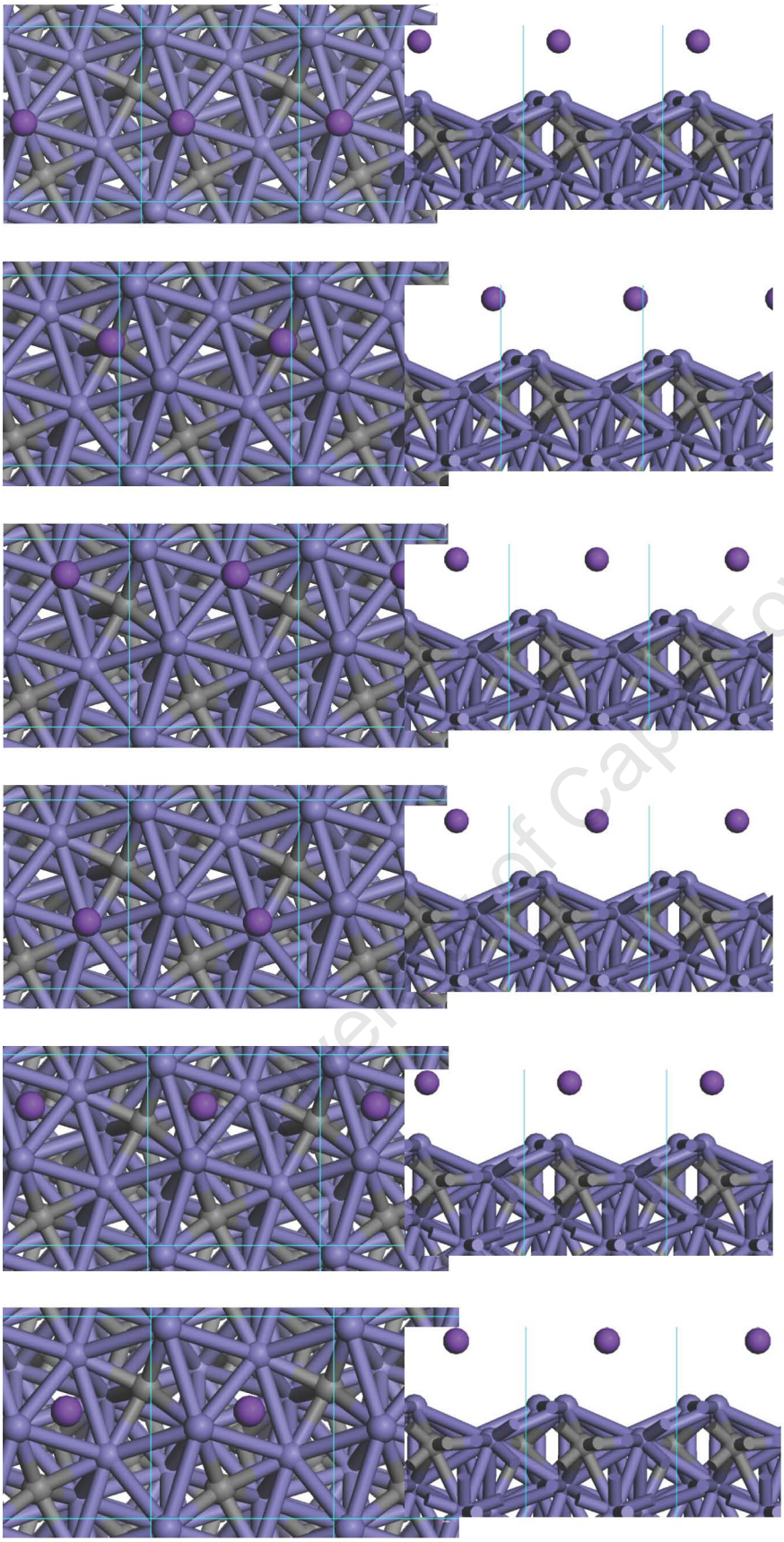

**Figure 3.9:** Starting configurations for K adsorption on the p(1×1) $Fe_5C_2(100)_{0.00}$ surface

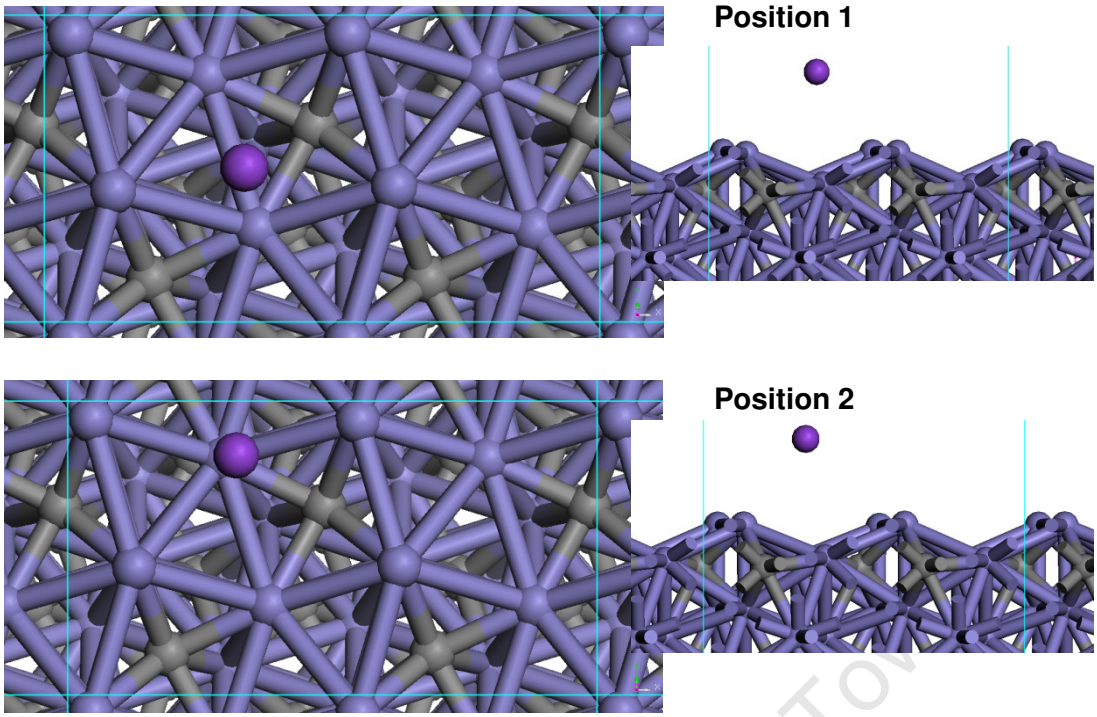


**Figure 3.10:** Calculated K adsorption configurations on the p(2×1) $Fe_5C_2(100)_{0.00}$ surface (Calculated using RPBE functional, σ=0.2eV, k-point mesh of 3 × 5 × 1 and a cutoff energy of 450eV)

**Table 3.5:** Structural parameters for K adsorption on $Fe_5C_2(100)_{0.00}$ surface (Calculated using RPBE functional, σ=0.2eV, k-point mesh of 3 × 5 × 1 and a cutoff energy of 450eV)

| | Position 1 | Position 2 |
|---|---|---|
| **Surface atom** | **Distance from K (Å)** | **Distance from K (Å)** |
| **R1** | 4.32 | 3.55 |
| **R2** | 3.29 | 3.58 |
| **R3** | 3.68 | 3.31 |
| **R4** | 3.47 | 4.16 |
| **V1** | 3.75 | 3.43 |
| **V2** | 3.53 | 4.28 |

**Table 3.6:** Variation in vibrational frequencies for K adsorption (position 2) on $Fe_5C_2(100)_{0.00}$ (Calculated using RPBE functional, σ=0.2eV, a POTIM value of 0.02, k-point mesh of 3× 5 × 1 and a cutoff energy of 450eV)

| Run 1( $cm^{-1}$) | Run 2 ($cm^{-1}$) |
|---|---|
| 93.57 | 101.45 |
| 59.94 | 51.69 |
| -29.19 | -37.83 |

**Table 3.7:** Variation in K frequency along the valley of the $Fe_5C_2(100)_{0.00}$ surface (Calculated using RPBE functional, σ=0.2eV, k-point mesh of 3 × 5 × 1 and a cutoff energy of 450eV)

| | Position 1 | Position 2 |
|---|---|---|
| **POTIM value** | **Frequency ($cm^{-1}$)** | |
| **0.015** | -73.52 | -82.35 |
| **0.02** | -18.69 | -29.19 |
| **0.03** | 15.99 | -15.14 |

### 3.2.2 K adsorption on the $Fe_5C_2(100)_{0.098}$ surface

The starting configurations for the investigation into potassium adsorption on this surface are given in Figure 3.11. Potassium was found to adsorb in only one adsorption configuration (see Figure 3.12) on this surface. The distance to the surface plane generated by the ridge iron atoms on this surface is 2.50Å. The bond lengths to the surface iron atoms for the optimised adsorption configuration are reported in Table 3.8. The shortest Fe-K bond length is found to be 3.53Å.

As with K adsorption on the $Fe_5C_2(100)_{0.00}$ surface, the distance to the surface plane and the observed bond lengths compare well with literature (Jenkins and King, 2000; Sorescu, 2011). The adsorptions on the p(2×1) cell yielded the same adsorption configuration, with minimal variation in the bond lengths.

The adsorption energy of K on the p(1×1) cell was calculated to be 1.59eV. This adsorption energy is lower than the adsorption energy on the $Fe_5C_2(100)_{0.00}$ surface indicating that potassium adsorption on this surface is not as favoured as it is on the $Fe_5C_2(100)_{0.00}$ surface. As with the K adsorption on the $Fe_5C_2(100)_{0.00}$ surface, the adsorption energy for K adsorption is slightly higher than the calculated adsorption energy of CO on this surface (1.55eV).

When adsorbing K on the p(2×1) unit cell, the adsorption energy was found to increase to 1.63eV. This increase in adsorption energy with decreasing coverage was also observed on the $Fe_5C_2(100)_{0.00}$ surface and is consistent with results seen in literature with decreasing coverage (Sorescu, 2011).

The vibrational analysis of K adsorption on the $Fe_5C_2(100)_{0.098}$ surface yielded similar results to the vibrational analysis of K adsorption on the $Fe_5C_2(100)_{0.00}$ surface, with a low negative frequency being observed in the direction of the valley (see Table 3.9). As with K adsorption on the $Fe_5C_2(100)_{0.00}$ surface, it was suspected that K was highly mobile along the valley. The results of a diffusion study confirm this, with the activation barrier for diffusion calculated to be 0.02eV indicating that K is highly mobile along the valley. Therefore, as with K adsorption on the $Fe_5C_2(100)_{0.00}$ surface, the motion of K along the valley will be treated as a translational mode, not a vibrational mode.

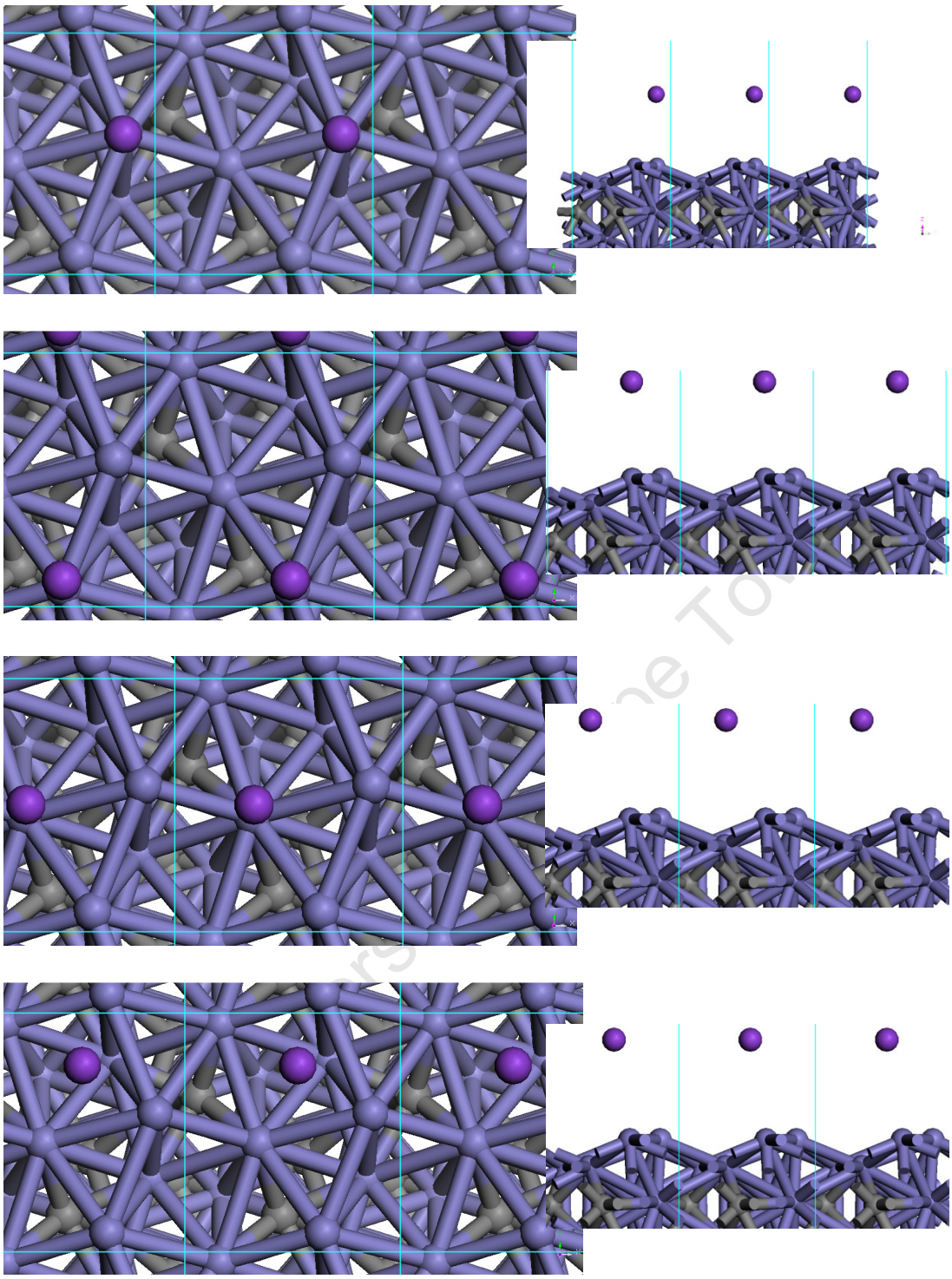

**Figure 3.11:** Starting configurations for K adsorption on the p(2×1) $Fe_5C_2(100)_{0.098}$ surface

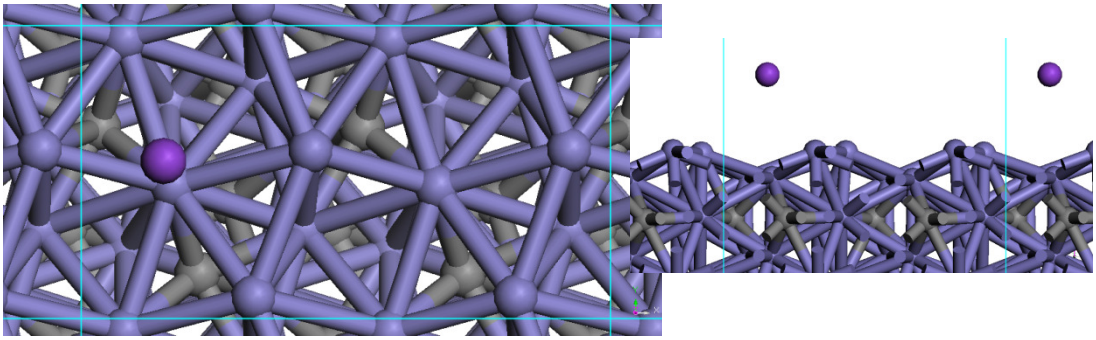

**Figure 3.12:** Optimised K adsorption configuration on p(2×1) $Fe_5C_2(100)_{0.098}$ (Calculated using RPBE functional, σ=0.2eV, k-point mesh of 3 × 5 × 1 and a cutoff energy of 450eV)

**Table 3.8:** Structural parameters for K adsorption on $Fe_5C_2(100)_{0.098}$ (Calculated using RPBE functional, σ=0.2eV, k-point mesh of 3 × 5 × 1 and a cutoff energy of 450eV)

| Surface atom | Distance from K (Å) |
|---|---|
| R 1 | 3.53 |
| R 2 | 3.73 |
| V1 | 3.39 |
| V2 | 3.99 |

**Table 3.9:** Vibrational frequencies for K adsorption on $Fe_5C_2(100)_{0.098}$ (Calculated using RPBE functional, σ=0.2eV, POTIM value of 0.02, k-point mesh of 3 × 5 × 1 and a cutoff energy of 450eV)

| Frequencies ( $cm^{-1}$) |
|---|
| 108 |
| 33 |
| -43 |

### 3.2.3 Bader analysis of K adsorption on the $Fe_5C_2(100)_{0.00}$ and $Fe_5C_2(100)_{0.98}$ surfaces

To gain further insight into the adsorption of K on the chosen Hägg carbide surfaces, the stable adsorption configurations were analysed using a Bader analysis and a charge density distribution plot.

The Bader analysis results show the extent of charge donation from K on both surfaces (see Table 3.10 and Table 3.11). In case of the $Fe_5C_2(100)_{0.00}$ surface, the K loses 0.52 electrons becoming positively charged, +0.52. This is the case for both positions. On the $Fe_5C_2(100)_{0.098}$ surface the loss of electrons of potassium is slightly less resulting in an

effective charge of +0.49. The carbon atoms in the surface play no role in the electron transfer at all. For K adsorption on both surfaces, the majority of the electrons are transferred to the ridge iron atoms. A very small amount of electrons is transferred to the valley iron atoms. Comparing to the K adsorption on the p(2×1) unit cell, the adsorption on this larger unit cell leads to an increase in the electron loss calculated for the K atom. On both the $Fe_5C_2(100)_{0.00}$ and the $Fe_5C_2(100)_{0.098}$ surfaces the electron loss upon K adsorption is calculated to be 0.61.

The Bader analysis also calculates the minimum distance to the surface using the surface of zero charge flux. For the K adsorptions on both surfaces, the minimum distance was calculated to be 1.5Å. This minimum distance is the effective radius of potassium and can be used to determine the type of bonding occurring between the potassium and the surface. An effective radius of 1.5Å is less than the covalent radius of potassium (2.26Å) and slightly more than the ionic radius of potassium (1.33Å). This indicates that the interaction between potassium and the surface should be more ionic than covalent.

**Table 3.10:** Bader analysis of K adsorption on the $Fe_5C_2(100)_{0.00}$ surface. The charges of the surface iron atoms calculated are calculated relative to the charges on the surface atoms when no adsorbate is present on the surface. The charges on the K atom are calculated relative to ground-state K atom (i.e. K with 9 electrons)

| | **Position 1** | **Position 2** |
|---|---|---|
| **Atom** | **Charge** | |
| **K** | 0.61 | 0.61 |
| **R 1** | -0.09 | -0.12 |
| **R 2** | -0.18 | -0.18 |
| **R 3** | -0.17 | -0.17 |
| **R 4** | -0.12 | -0.10 |
| **V1** | -0.03 | -0.03 |
| **V2** | -0.03 | -0.02 |
| **V3** | 0.00 | 0.00 |
| **V4** | 0.00 | 0.00 |

**Table 3.11:** Bader analysis of K adsorption on the $Fe_5C_2(100)_{0.098}$ surface. The charges of the surface iron atoms calculated are calculated relative to the charges on the surface atoms when no adsorbate is present on the surface. The charges on the K atom are calculated relative to ground-state K atom (i.e. K with 9 electrons)

| Atom | Charge |
|---|---|
| **K** | 0.61 |
| **R 1** | -0.11 |
| **R 2** | -0.17 |
| **R 3** | -0.15 |
| **R 4** | -0.07 |
| **V1** | -0.04 |
| **V2** | -0.04 |
| **V3** | 0.00 |
| **V4** | 0.00 |

### 3.2.4 Charge density difference analysis of K adsorption on the $Fe_5C_2(100)_{0.00}$ and $Fe_5C_2(100)_{0.98}$ surfaces

A charge density difference plot can be used to plot the change in the surface electron distribution upon the adsorption of a species, in this case a K atom. The charge density difference distribution being illustrated is:

$$Charge\ density\ difference = Charge_{K\ adsorbed} - (Charge_{free\ surface} + Charge_{gas\ phase\ K})$$

A negative area on the charge distribution plot will be an increase in electrons, while a positive area means a decrease in electrons. The charge density difference plots for both the adsorptions on the $Fe_5C_2(100)_{0.00}$ and $Fe_5C_2(100)_{0.098}$ surfaces show an increase in electron distribution around the iron atoms on the surface. The K atom becomes polarised upon adsorption. There is no indication of orbital overlap or orbital hybridisation in the charge density difference plot. This would be observed in the charge density difference plot as areas where the electron density is shared by two atoms. This again indicates an ionic bonding of potassium to the Hägg iron carbide surface.

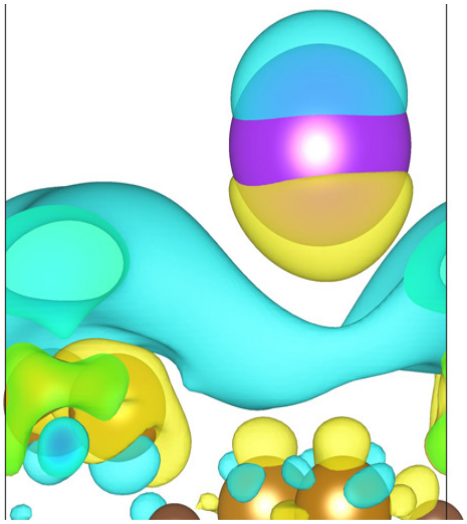

**Figure 3.13:** Charge density difference plot of K adsorption on the $Fe_5C_2(100)_{0.00}$ surface. The blue colour indicates an increase in electrons while the yellow indicates a decrease in electrons.

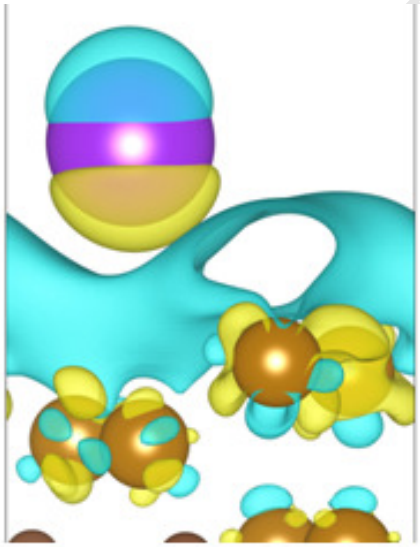

**Figure 3.14:** Charge density difference plot of K adsorption on the $Fe_5C_2(100)_{0.098}$ surface. The blue colour indicates an increase in electrons while the yellow indicates a decrease in electrons.

## 3.3 O adsorption on $Fe_5C_2(100)_{0.00}$ and $Fe_5C_2(100)_{0.098}$

The adsorption of O on these surfaces was only investigated using a p(2×1) supercell. The adsorption of O on the surface is necessary so as to have a base to compare the effect K has on O adsorption when investigating KO adsorption. Since KO adsorption on a p(1×1) cell was not investigated, the adsorption of O on a p(1×1) cell was not needed. The adsorption of O on the surface is the primary step to investigating the co-adsorption of CO with O on the surface. The investigation of O adsorption on both surfaces was done by adsorbing O above all the available on top and hollow sites on the respective surfaces.

### 3.3.1 O adsorption on the $Fe_5C_2(100)_{0.00}$ surface

For O adsorption on this surface, it has been found that there is only one stable configuration (see Figure 3.15). This adsorption geometry consists of O sitting on the bridge site between the two ridge iron atoms. The bond lengths to these iron atoms are 1.81Å and 1.83Å respectively. Comparing to literature, the bond lengths calculated here compare well to results for O adsorption on Fe(100) where bond lengths of 1.82Å have been calculated for bridge site O adsorption (Sorescu, 2011).

The adsorption energy calculated relative to gas phase $H_2O$ and $H_2$ was 0.3eV. A vibrational analysis of O adsorption calculated the vibrational modes of O on this surface to be 578cm$^{-1}$, 354cm$^{-1}$ and 82cm$^{-1}$ (calculated using a POTIM value of 0.02).

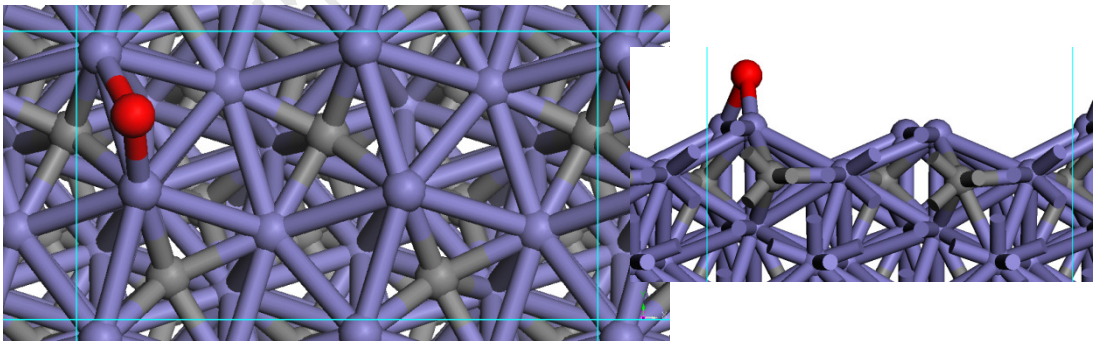

**Figure 3.15:** Optimised O adsorption configuration on p(2×1) $Fe_5C_2(100)_{0.00}$ (Calculated using RPBE functional, σ=0.2eV, k-point mesh of 3 × 5 × 1 and a cutoff energy of 450eV)

### 3.3.2 O adsorption on the $Fe_5C_2(100)_{0.098}$ surface

For O adsorption on this surface, it has been found that there is only one stable configuration shown in Figure 3.16 . This adsorption geometry consists of O sitting on the threefold site formed by the ridge iron atoms and the valley iron atom (V3). The bond lengths to these iron atoms are 1.87Å and 1.88Å to R1 and R2 respectively and 2.00Å to V3 respectively.

The adsorption energy calculated was 0.64eV. As with O adsorption on the $Fe_5C_2(100)_{0.00}$ surface, this adsorption energy was calculated relative to a gas phase $H_2O$ and $H_2$ species. This is more than double the adsorption energy of O on the $Fe_5C_2(100)_{0.00}$ surface indicating that O adsorption on this surface is energetically more favoured. A vibrational analysis of O adsorption calculated the vibrational modes of O on this surface to be 483cm$^{-1}$, 393cm$^{-1}$ and 279cm$^{-1}$ (calculated using a POTIM value of 0.02).

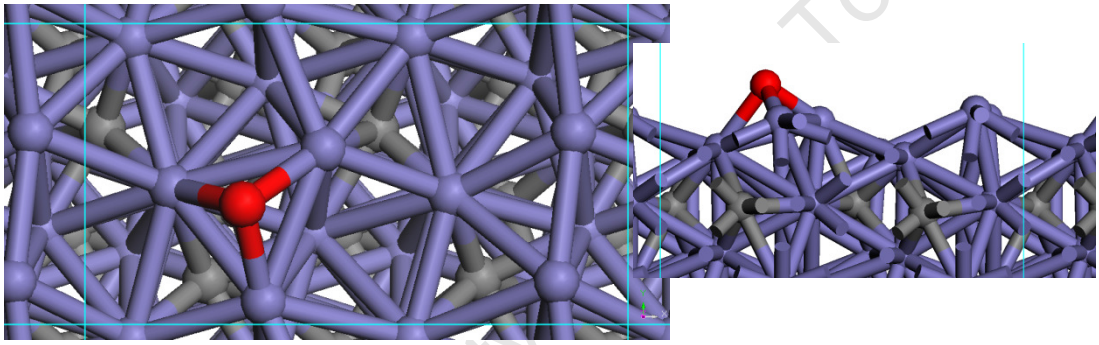

**Figure 3.16:** Optimised O adsorption configuration on $Fe_5C_2(100)_{0.098}$ (Calculated using RPBE functional, σ=0.2eV, k-point mesh of 3 × 5 × 1 and a cutoff energy of 450eV)

### 3.3.2 Bader analysis of O adsorption on the $Fe_5C_2(100)_{0.00}$ and $Fe_5C_2(100)_{0.098}$ surfaces

The Bader analysis of O adsorption on the two surfaces showed the electron withdrawing effect of the presence of O on the surface iron atoms it is bonded to. For the O adsorption on the $Fe_5C_2(100)_{0.00}$ surface, since the O is only directly bonded to two of the surface iron atoms, the majority of the electrons gained by the O atom are donated by these two ridge iron atoms. The O atom is calculated to have a charge of -0.62 when taking a ground-state O atom as a reference. The total electrons lost from the iron atoms were calculated to be 0.62. The two ridge iron atoms both have a charge of +0.24, implying that the majority of the electrons were donated by these two iron atoms. The rest of the charge gained by the O appears to come from all the iron atoms in the bulk of the structure. However, no iron atom, other that the two ridge iron atoms, directly interacting with the O atom donated more than 0.03 electrons when O was adsorbed.

For the $Fe_5C_2(100)_{0.098}$ surface, three iron atoms are affected since the O is bonded to three iron atoms (two ridge and one valley iron atom). It was calculated that each of these iron atoms had a charge of +0.24 when comparing the electrons these atoms had before and after O was adsorbed. The O was calculated to have a charge of -0.83. As with the O adsorbed on the $Fe_5C_2(100)_{0.00}$ surface, the iron atoms not directly bonded to the O atom also contributed to the electron donation to the adsorbed O. However, no other iron atom donated more than 0.03 electrons.

## 3.4 KO adsorption on the $Fe_5C_2(100)_{0.00}$ and $Fe_5C_2(100)_{0.098}$ surfaces

Following the adsorption of the O and K atoms on the respective surfaces, the effect of the presence of K on O adsorption will be investigated. Furthermore, the relative stability of the K and KO at Fischer-Tropsch synthesis conditions will also be investigated. To accomplish this the adsorption of KO on p(2×1) $Fe_5C_2(100)_{0.00}$ and $Fe_5C_2(100)_{0.098}$ surfaces was investigated. The p(1×1) unit cell was not considered due to the size of the K species preventing any co-adsorption study being done due to interactions between neighbouring cells. The starting configurations used in these calculations involved the combination of the calculated stable O and K adsorptions on both surfaces.

### 3.4.1 KO adsorption on the $Fe_5C_2(100)_{0.00}$ surface

KO was found to adsorb in two stable adsorption configurations on this surface (see Figure 3.17). In both adsorption configurations K was found to be in the valley with O in its favoured bridge position. In position 1, the K was found to be 2.54Å from the O atom, while in position 2 the distance between the O and the closest K atom increased to 2.59Å. The distances of the K atom to the surface iron atoms are given in Table 3.12. The distance to the surface plane for K is calculated to be 2.43Å for position 1 and 2.33Å for position 2. This distance to the surface plane (formed by the ridge iron atoms) is smaller than that calculated by Jenkins and King (2000) where the adsorption of K was investigated on Co(10$\bar{1}$0) and the distance to the surface planes was calculated to be between 2.44Å and 2.85Å. The observed bond lengths to the surface iron atoms compare well to the bond lengths for potassium adsorption on the Fe(100) surface (3.50Å) reported by Sorescu (2011).



The adsorption energy of O, when co-adsorbed with K, is calculated to be 0.93eV and 098eV respectively. The adsorption energy of K in the presence of O is calculated to be 2.31eV and 2.36eV for position 1 and 2, respectively. This shows a substantial increase in the adsorption energy of either K or O when they are co-adsorbed on the surface.

Comparing the structural parameters for adsorption of KO on the surface to when only K is adsorbed on the surface the positions of the K atom on the surface do change quite substantially with the O being present with a maximum absolute change of 0.36Å calculated for position 1 and 0.54Å for position 2 (see Table 3.5). These values represent the change in the position of the K in the lateral direction.

The vibrational analysis of KO adsorption on the $Fe_5C_2(100)_{0.00}$ surface, showed that as with K adsorption on the surface, a negative frequency was calculated for K moving along the valley in both position 1 and position 2 indicating that the K is still mobile along the valley even with O present (see Table 3.13).

A diffusion study was undertaken to determine the maximum barrier for K to diffuse along the valley from position 1 to position 2. The maximum barrier for diffusion was calculated to be 0.072eV. This is a larger diffusion barrier for K than the diffusion barrier for K when no O is present on the surface. However, this is still a very low barrier for diffusion meaning that at Fischer-Tropsch conditions, the potassium will be very mobile irrespective of whether O is present on the surface or not. Therefore, this motion along the valley was treated as a translational mode.

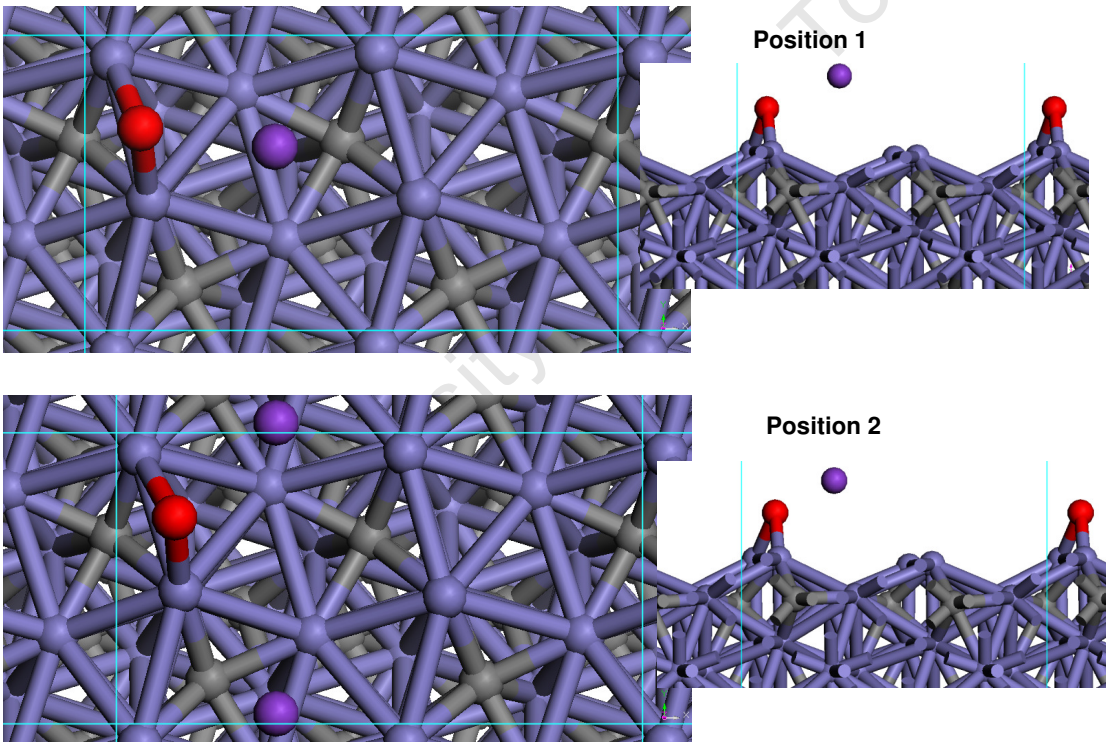


**Figure 3.17:** Optimised KO adsorption configuration on p(2×1) $Fe_5C_2(100)_{0.00}$ surface position 1 and position 2 (Calculated using RPBE functional, σ=0.2eV, k-point mesh of 3 × 5 × 1 and a cutoff energy of 450eV)

**Table 3.12:** Structural parameters for KO adsorption on the p(2×1) $Fe_5C_2(100)_{0.00}$ surface (Calculated using RPBE functional, σ=0.2eV, k-point mesh of 3 × 5 × 1 and a cutoff energy of 450eV)

| | Position 1 | Position 2 |
|---|---|---|
| **Surface atom** | **Distance from K (Å)** | **Distance from K (Å)** |
| **R1** | 3.96 | 3.38 |
| **R2** | 3.38 | 3.56 |
| **R3** | 3.51 | 3.43 |
| **R4** | 3.66 | 4.33 |
| **V1** | 3.84 | 3.70 |
| **V2** | 3.75 | 3.74 |
| **O** | 2.54 | 2.59 |

**Table 3.13:** Vibrational frequencies calculated for KO adsorbed on the p(2×1) $Fe_5C_2(100)_{0.00}$ surface (Calculated using RPBE functional, POTIM value of 0.02eV, σ=0.2, k-point mesh of 3 × 5 × 1 and a cutoff energy of 450eV)

| Frequency ($cm^{-1}$) | |
|---|---|
| **Position 1** | **Position 2** |
| 533.05 | 522.78 |
| 331.16 | 317.77 |
| 212.99 | 198.63 |
| 102.34 | 107.71 |
| 76.07 | 72.88 |
| -3.63 | -13.71 |

### 3.4.2 KO adsorption on the $Fe_5C_2(100)_{0.098}$ surface

KO was found to adsorb in one stable adsorption configurations on the $Fe_5C_2(100)_{0.098}$ surface (see Figure 3.18). The adsorption energy of O relative to gas phase $H_2O$ and $H_2$ was calculated to be 1.05eV, a substantial increase from the adsorption energy of O with K co-adsorbed. As with KO adsorption on the $Fe_5C_2(100)_{0.00}$ surface, K is found to be in the valley. O remains on its favoured threefold hollow site. The distance between the O and the K atom was calculated to be 2.58Å. The distance to the surface plane for K is calculated to be 2.47Å. This distance to the surface plane falls within the range calculated by Jenkins and King (2000) where the adsorption of K was investigated on Co(10$\bar{1}$0) and the distance to the surface planes was calculated to be between 2.44Å and 2.85Å. As with KO adsorption on the $Fe_5C_2(100)_{0.00}$ surface, the observed bond lengths to the surface iron atoms compare well to literature values for potassium adsorption on metal surfaces on hollow sites. Sorescu (2011) in a study of potassium adsorption on the Fe(100) surface found that the shortest bond length was approximately 3.5Å for the most stable adsorption configuration (the 4F) of

potassium on this surface (Sorescu, 2011). The distances of the K atom to the surface iron atoms are given in Table 3.14.

The vibrational analysis of KO adsorption on the $Fe_5C_2(100)_{0.098}$ surface showed that as with KO adsorption on the $Fe_5C_2(100)_{0.00}$ surface, a low frequency was calculated for K moving along the valley (see Table 3.15). The results of a diffusion study of K diffusion along the valley calculated that the maximum barrier for diffusion was 0.15eV. As with the $Fe_5C_2(100)_{0.00}$ surface, this barrier for diffusion is larger than the diffusion barrier for K without O co-adsorbed on the surface. However, this is still a very low barrier for diffusion meaning that at Fischer-Tropsch conditions, the K will still be very mobile. Therefore, this motion along the valley was treated as a translational mode.

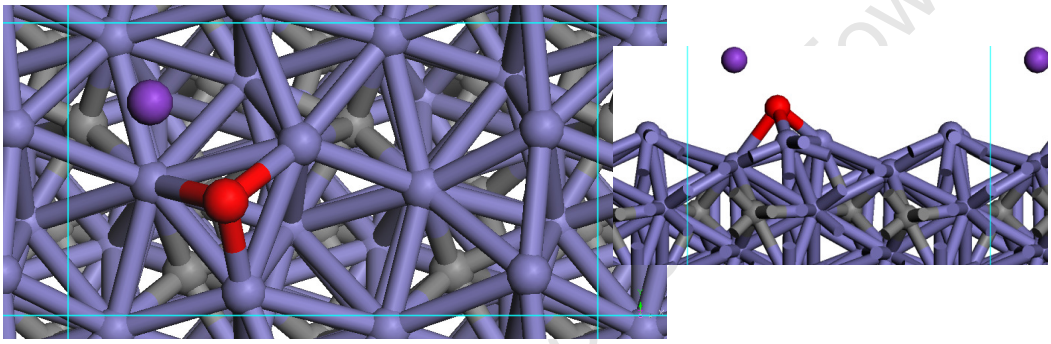

**Figure 3.18:** Optimised KO adsorption configuration on the p(2×1) $Fe_5C_2(100)_{0.098}$ surface (Calculated using RPBE functional, σ=0.2eV, k-point mesh of 3 × 5 × 1 and a cutoff energy of 450eV)

**Table 3.14:** Structural parameters for KO adsorption on the p(2×1) $Fe_5C_2(100)_{0.098}$ surface (Calculated using RPBE functional, σ=0.2eV, k-point mesh of 3 × 5 × 1 and a cutoff energy of 450eV)

| Surface atom | Distance from K (Å) |
|---|---|
| **R 1** | 3.63 |
| **R 2** | 4.40 |
| **R 3** | 3.42 |
| **R 4** | 5.40 |
| **V1** | 3.59 |
| **V2** | 3.45 |
| **O** | 2.58 |

**Table 3.15:** Vibrational frequencies calculated for KO adsorbed on the p(2×1) $Fe_5C_2(100)_{0.098}$ surface (Calculated using RPBE functional, POTIM value of 0.02eV, σ=0.2, k-point mesh of 3 × 5 × 1 and a cutoff energy of 450eV)

| Frequency ($cm^{-1}$) |
|---|
| 470.79 |
| 369.31 |
| 196.11 |
| 129.61 |
| 76.57 |
| 10.14 |

### 3.4.3 Bader analysis of KO adsorption on the $Fe_5C_2(100)_{0.00}$ and $Fe_5C_2(100)_{0.098}$ surface

The Bader analysis of KO adsorption on the surfaces showed that co-adsorption of K with the O lead to an increase in the negative charge on the O atom when compared to the charge on the O atom without K present.

On the $Fe_5C_2(100)_{0.00}$ surface, the increase in the negative charge on the O atom is -0.26. Potassium also becomes more positively charged, losing more electrons when the O is present. The ridge iron atoms under the O which are negatively charged when K is adsorbed lose any electrons they would have gained from K to the O. The ridge iron atoms not bonded to the O atom are unaffected by the presence of the O. As with K adsorption, the valley iron atoms play a minimal role in the electron transfer in KO adsorption.

For KO adsorption on the $Fe_5C_2(100)_{0.098}$ surface, the increase in the negative charge on the O was calculated to be -0.11. As the O atom on this surface is bonded in a threefold hollow, three iron atoms are affected by the presence of the O. The valley iron atom bonded to the O as well as the ridge iron atoms become positively charged.

**Table 3.16:** Bader analysis of KO adsorption on the p(2×1) $Fe_5C_2(100)_{0.00}$ surface. The charges of the surface iron atoms calculated are calculated relative to the charges on the surface atoms when no adsorbate is present on the surface. The charges on the O and K atoms are calculated relative to ground-state O and K atoms respectively. Both the KO and K adsorption being referred to below are position 1.

| | Charge | |
|---|---|---|
| **Atom** | **KO adsorbed** | **K adsorbed** |
| **K** | 0.72 | 0.61 |
| **O** | -0.88 | -- |
| **R 1** | 0.23 | -0.09 |
| **R 2** | 0.15 | -0.18 |
| **R 3** | -0.17 | -0.17 |
| **R 4** | -0.10 | -0.12 |
| **V1** | 0.03 | -0.03 |
| **V2** | -0.01 | -0.03 |
| **V3** | -0.02 | 0.00 |
| **V4** | -0.01 | 0.00 |

**Table 3.17:** Bader analysis of KO adsorption on the p(2×1) $Fe_5C_2(100)_{0.098}$ surface. The charges of the surface iron atoms calculated are calculated relative to the charges on the surface atoms when no adsorbate is present on the surface. The charges on the O and K atoms are calculated relative to ground-state O and K atoms respectively.

| | Charge | |
|---|---|---|
| **Atom** | **KO adsorbed** | **K adsorbed** |
| **K** | 0.71 | 0.61 |
| **O** | -0.94 | -- |
| **R 1** | 0.17 | -0.11 |
| **R 2** | 0.17 | -0.17 |
| **R 3** | -0.16 | -0.15 |
| **R 4** | -0.13 | -0.07 |
| **V1** | -0.03 | -0.04 |
| **V2** | 0.20 | -0.04 |
| **V3** | 0.03 | 0.00 |
| **V4** | -0.05 | 0.00 |

### 3.4.4 Charge density difference plot of KO adsorption on the $Fe_5C_2(100)_{0.00}$ and $Fe_5C_2(100)_{0.098}$ surface

The charge density difference plots for both the adsorptions on the $Fe_5C_2(100)_{0.00}$ and $Fe_5C_2(100)_{0.098}$ surfaces show an increase in electron distribution around the iron atoms on the surface. The region around the O atom also shows an increase in electron distribution while the ridge iron atoms near the O show a decrease in electrons. The K atom is also slightly polarised to the O atom.

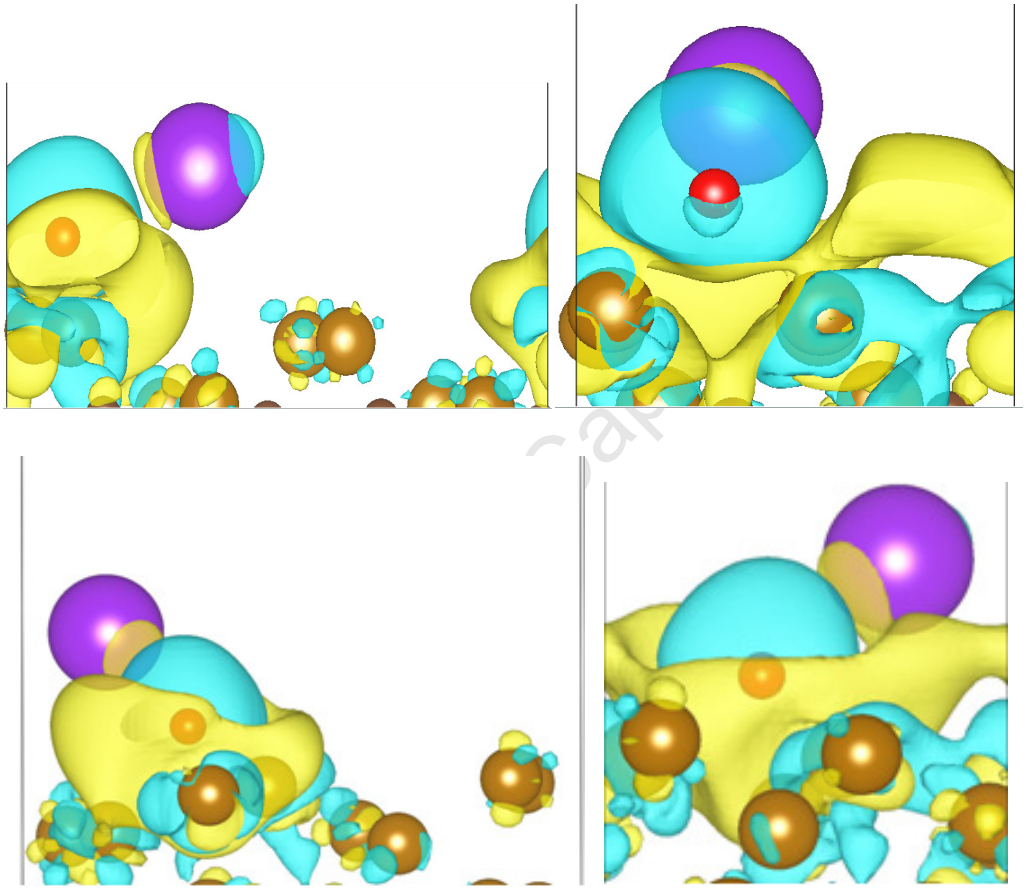

**Figure 3.19:** Charge density difference plot of KO adsorption on the p(2×1) $Fe_5C_2(100)_{0.00}$ surface and the p(2×1) $Fe_5C_2(100)_{0.098}$ surface (below). The blue colour indicates an increase in electrons while the yellow indicates a decrease in electrons. The top left figure is KO in position 1 on the $Fe_5C_2(100)_{0.00}$ surface and the top right figure is KO in position 2 on the $Fe_5C_2(100)_{0.00}$ surface.

## 3.5 Co-adsorption of CO and K, O and KO on the $Fe_5C_2(100)_{0.00}$ and $Fe_5C_2(100)_{0.098}$ surfaces

### 3.5.1 Co-adsorption of CO with K

#### 3.5.1.1 Co-adsorption of CO with K on the $Fe_5C_2(100)_{0.00}$ surface

The starting configurations for the co-adsorption of CO with K on this surface are given in Figure 3.20. The co-adsorption CO with K yielded two different CO adsorption configurations; one on top adsorptions and one bridged adsorption configuration (see Figure 3.21). The ZPE corrected adsorption energies calculated for CO in the co-adsorbed state are given in Table 3.18 along with the ZPVE, CO stretching frequency, Fe-C bond lengths CO bond lengths and CO angles. The italicised figures represent the calculated values for CO adsorption without any co-adsorbed species on this surface. The bond lengths for the CO bond (Table 3.18) show an increase when compared to CO adsorption without K, indicating a weakening of the CO bond. The Fe-C bond length(s) are shorter compared to the Fe-C bonds when K is not present indicating a stronger bonding of the carbon to the surface iron atoms.

These observations for changes in the bond length of CO and Fe-C bond lengths are in good agreement with results reported in literature. A study by Sorescu (2011) into the co-adsorption of K and CO on the Fe(100) surface, found that the presence of K caused an increase in the CO bond lengths of up to 0.03Å in the case of the 1F and 2F adsorption configurations of CO. The Fe-C bond lengths were calculated to decrease by up to 0.02Å for the 1F configuration. In this study the CO bond lengths were calculated to increase by up to 0.04Å for the 1F adsorption configuration and 0.03Å for the 2F adsorption configurations. The Fe-C bond lengths were calculated to decrease by up to 0.04Å for the 1F adsorption configurations and by up to 0.06Å for the 2F adsorption configurations. Comparing the 1F results to the results from Sorescu (2011), there is no difference in the increase in the CO bond length observed. However, the decrease in the Fe-C bond length observed for the 1F adsorption configuration is larger than the decrease observed by Sorescu. This difference could be due to a difference in the surface properties as the study by Sorescu was conducted on the Fe(100) surface.

The calculated adsorption energies of CO increase in all adsorption configurations when K is present. The 1F adsorption configurations show calculated increases in the adsorption energy of between 0.54eV and 0.32eV while for 2F adsorption configurations increases in adsorption energy of 0.37eV and 0.39eV were calculated. The angle of the CO molecule with the surface plane also changes when co-adsorbing with K. The angle decreases so that the O is leaning towards the K atom. This effect is more evident on the 2F CO states.

The results of the vibrational analysis showed that CO bond stretching frequency decreases with K present for all adsorption configurations calculated. The largest decrease in the CO stretching frequency is found in the 1F adsorption configurations (~300$cm^{-1}$).

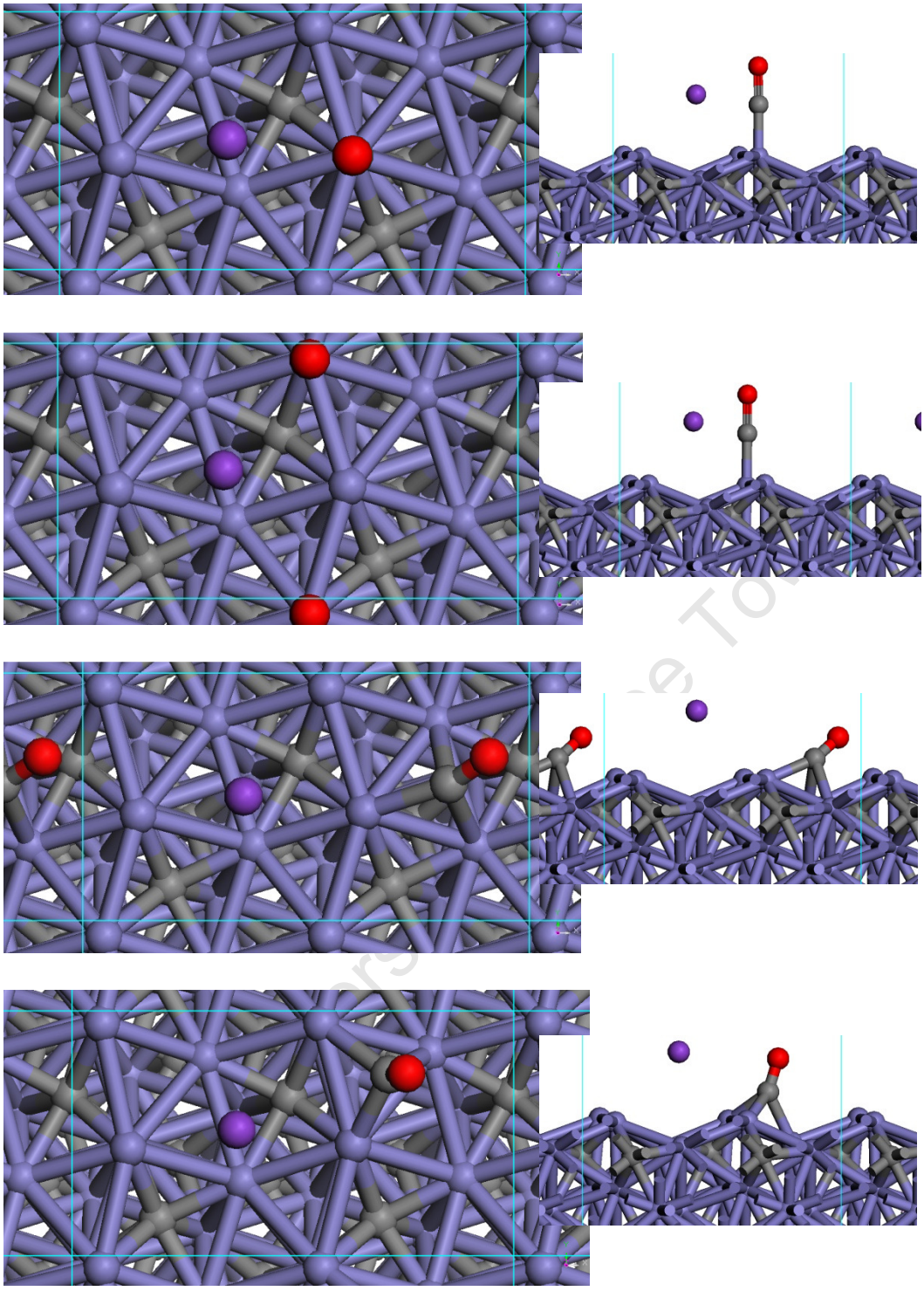

**Figure 3.20:** Starting configurations for the co-adsorption of K and CO on the p(2×1) $Fe_5C_2(100)_{0.00}$ surface

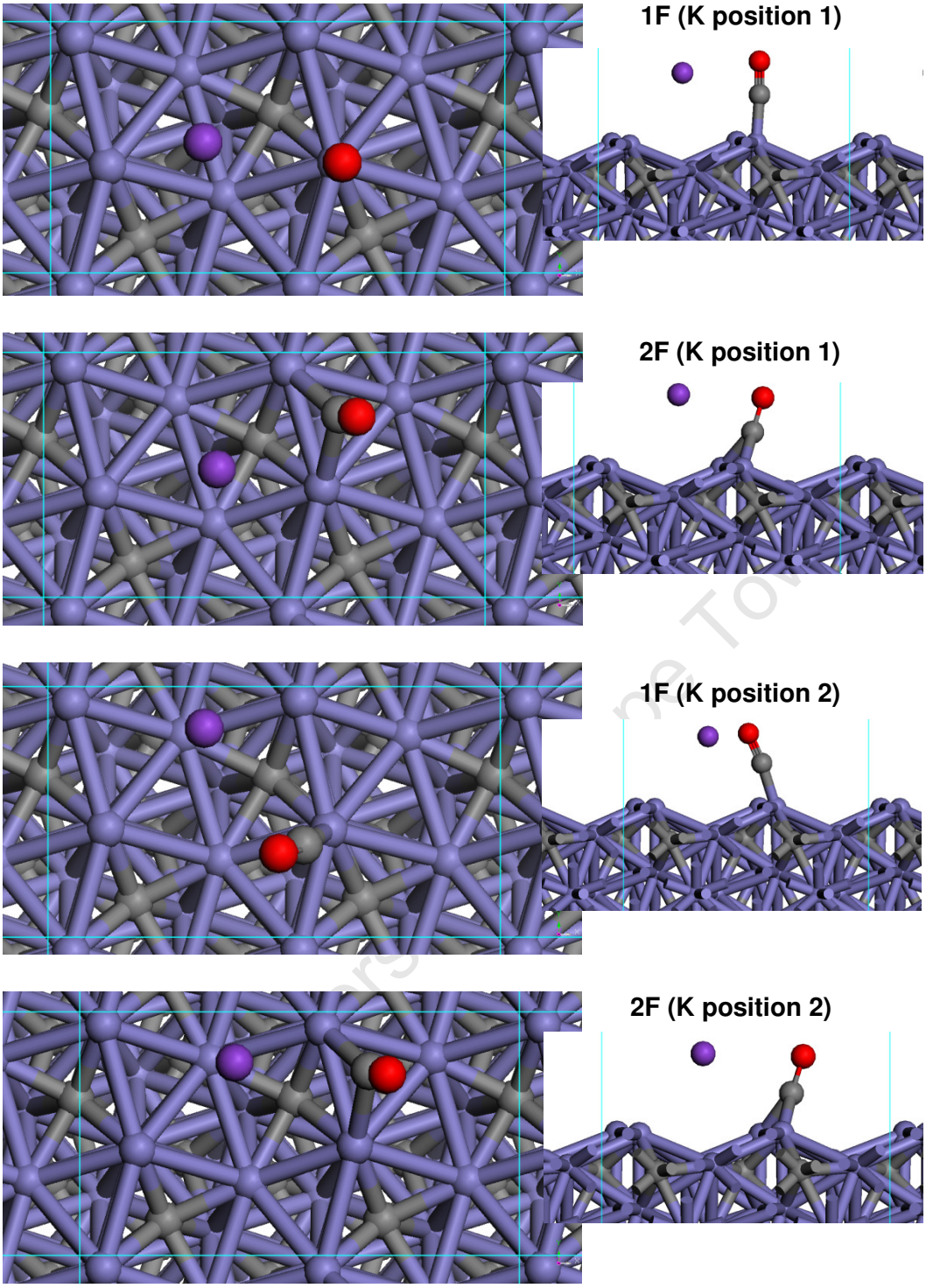


**Figure 3.21:** Optimised adsorption configurations for CO co-adsorption with K (position 1) on the p(2×1) $Fe_5C_2(100)_{0.00}$ surface. (Calculated using RPBE functional, σ=0.2, k-point mesh of 3 × 5 × 1 and a cutoff energy of 450eV)

**Table 3.18:** Calculated ZPE-corrected adsorption energies, ZPVE, CO stretching frequencies, Fe-C distances and CO bond lengths for CO co-adsorption with K on the (2×1) $Fe_5C_2(100)_{0.00}$ surface. The italicised values are the calculated values for CO adsorption without K. (Calculated using RPBE functional, POTIM value of 0.02, σ=0.2eV, k-point mesh of 3 × 5 × 1 and a cutoff energy of 450eV)

| Bond Type | $E_{ads,\ CO}$ (eV) | ZPE (eV) | r(Fe-C) (Å) | r(C-O) (Å) | β (°) | $\nu$(C-O) ($cm^{-1}$) |
|---|---|---|---|---|---|---|
| ***1F*** | *1.60* | *0.202* | *1.79* | *1.17* | *90* | *1927* |
| 1F (K1) | 2.14 | 0.213 | 1.74 | 1.22 | 89.9 | 1699 |
| 1F (K2) | 2.07 | 0.214 | 1.74 | 1.22 | 82.7 | 1702 |
| ***2F*** | *1.54* | *0.177* | *1.88; 2.03* | *1.20* | *63.4* | *1771* |
| 2F (K1) | 1.91 | 0.188 | 1.88; 1.98 | 1.23 | 73.4 | 1611 |
| 2F (K2) | 1.89 | 0.186 | 1.82; 2.02 | 1.22 | 72.4 | 1615 |

#### 3.5.1.2 Co-adsorption of CO with K on $Fe_5C_2(100)_{0.098}$

The starting configurations for the co-adsorption of CO with K on this surface are given in Table 3.22. The co-adsorption CO with K on this surface as with the co-adsorption of CO with K on the $Fe_5C_2(100)_{0.00}$ surface yielded three different CO adsorption configurations, a 1F, 2F and a 3F adsorption configuration (see Figure 3.23). The 1F valley configuration is not found to be one of the stable configurations as the presence of K caused a migration of CO from the valley to the ridge. The same trends in CO bond length and Fe-C bond lengths are seen with co-adsorption of CO with K on this surface as was seen on the $Fe_5C_2(100)_{0.00}$ surface. The adsorption energies calculated for CO in the co-adsorbed state are given in Table 3.19 along with the ZPVE, CO stretching frequency, Fe-C bond lengths and CO bond lengths. The bond length for the CO bond shows an increase in the CO bond when compared to CO adsorption without K (see Table 3.19). The Fe-C bond length(s) are shorter compared to the Fe-C bonds when K is not present.

These observations for changes in the bond length of CO and Fe-C bond lengths are in again in good agreement with what has been reported in literature. Sorescu (2011) reported on the Fe(100) surface that the presence of K caused an increase in the CO bond lengths of up to 0.03Å in the case of the 1F and 2F adsorption configurations of CO. The Fe-C bond lengths were calculated to decrease by up to 0.024Å for the 1F configurations. On this surface changes in the CO bond length of 0.05Å are calculated and decreases in the Fe-C bond length of 0.06Å are calculated.

The calculated adsorption energies for CO increase, irrespective of the adsorption configuration, when K is present. For the 1F adsorption configurations, an increase in the adsorption energy of between 0.42eV was calculated. As with CO co-adsorbed with K, the angle of the CO with the surface plane also changes when co-adsorbing with KO. The angle decreases so that the O of the CO is leaning towards the K atom.

The results of the vibrational analysis of CO co-adsorption with K on this surface showed that CO bond stretching frequency decreases with K present in all adsorption configurations calculated, indicating a weakening of the CO bond. The lowest CO stretching frequency is not found in the 1F adsorption configurations, which are the most stable adsorption configurations, instead the lowest CO stretching frequency is found with the 2F or 3F CO adsorption configurations. As with the results on the $Fe_5C_2(100)_{0.00}$ surface, these trends are consistent with what has been found in literature (Sorescu, 2011).

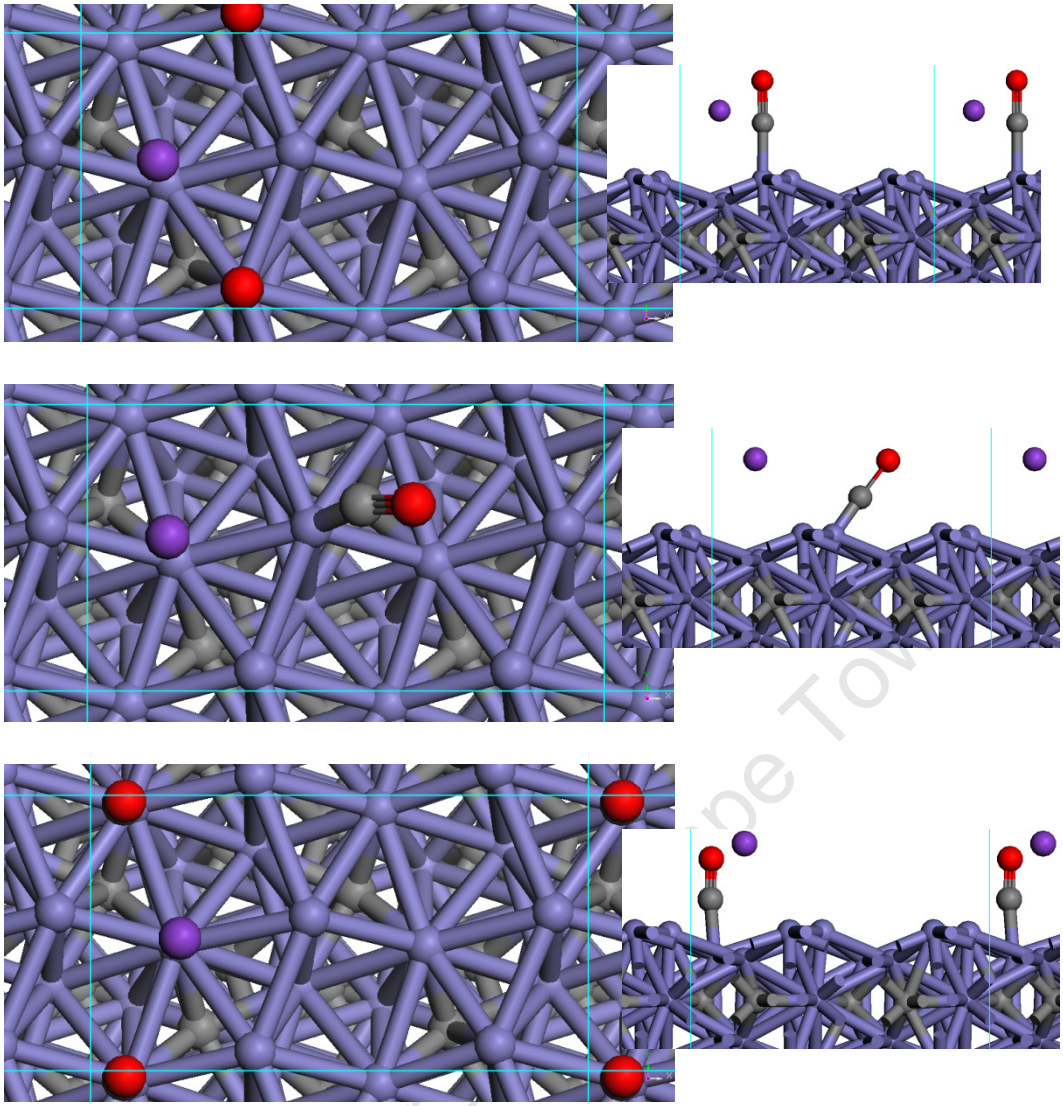

**Figure 3.22:** Starting configurations for the co-adsorption of K and CO on the p(2×1) $Fe_5C_2(100)_{0.098}$ surface

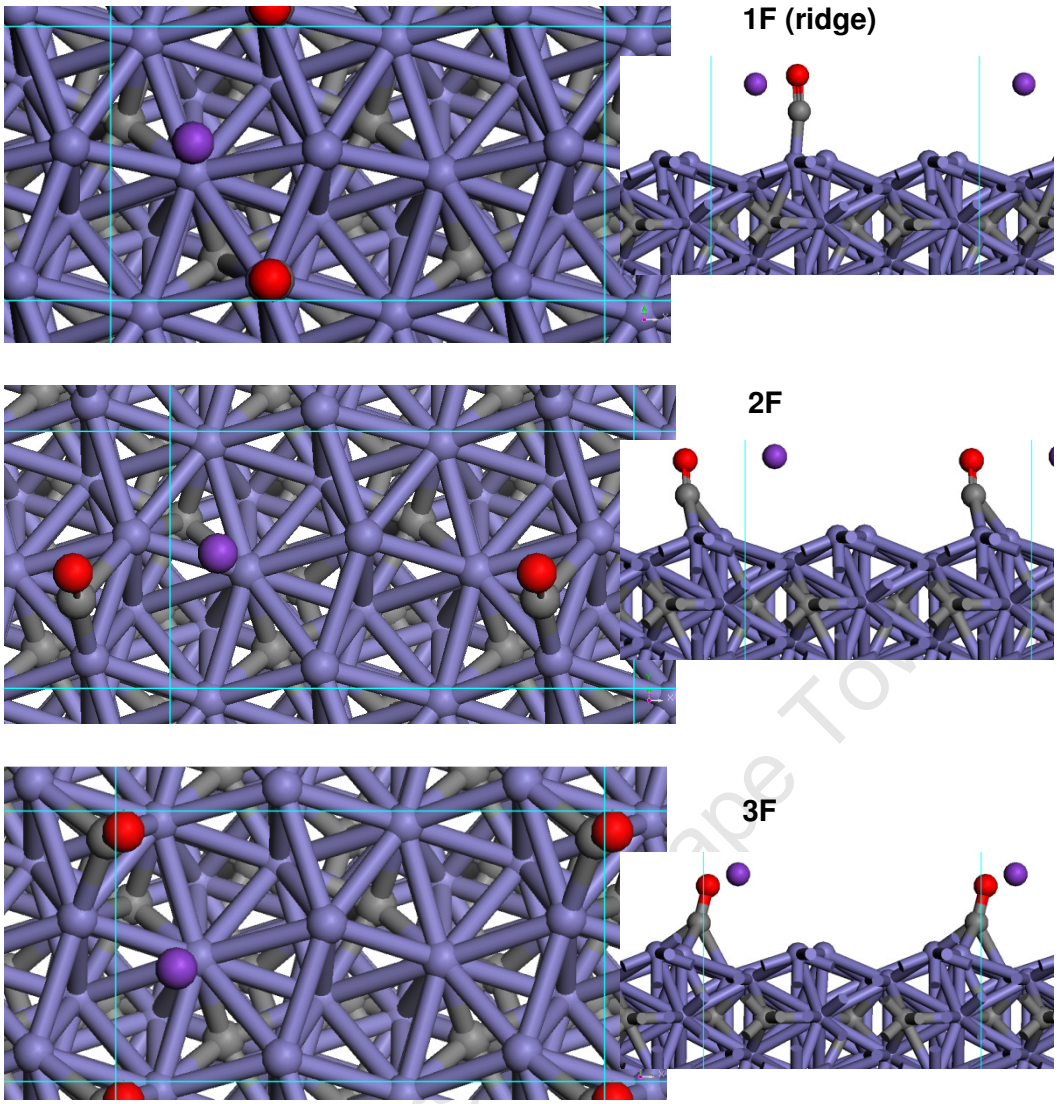


**Figure 3.23:** Optimised adsorption configurations for CO co-adsorption with K on the p(2×1) $Fe_5C_2(100)_{0.098}$ surface. (Calculated using RPBE functional, σ=0.2eV, k-point mesh of 3 × 5 × 1 and a cutoff energy of 450eV)

**Table 3.19:** Calculated ZPE-corrected adsorption energies, ZPVE, CO stretching frequencies, Fe-C distances and CO bond lengths for CO co-adsorption with K on the p(2×1) $Fe_5C_2(100)_{0.098}$ surface. The italicised values are the calculated values for CO adsorption without K. (Calculated using RPBE functional, POTIM value of 0.02, σ=0.2eV, k-point mesh of 3 × 5 × 1 and a cutoff energy of 450eV)

| Bond Type | $E_{ads,\ CO}$ (eV/CO) | ZPE (eV) | v(C-O) ($cm^{-1}$) | r(Fe-C) (Å) | r(C-O) (Å) | β (°) |
|---|---|---|---|---|---|---|
| ***1F(R)*** | *1.45* | *0.199* | *1999* | *1.80* | *1.17* | *89.1* |
| 1F (K) | 1.87 | 0.192 | 1697 | 1.74 | 1.22 | 82.7 |
| ***2F*** | | | | | | |
| 2F (K) | 1.63 | 0.188 | 1662 | 1.79; 2.17 | 1.22 | 86.6 |
| ***3F*** | | | | | | |
| 3F(K) | 1.80 | 0.182 | 1662 | 1.99; 1.93; 2.05 | 1.27 | 76.3 |

### 3.5.1.3 Charge analysis of CO co-adsorption with K on the $Fe_5C_2(100)_{0.00}$ and $Fe_5C_2(100)_{0.098}$ surfaces

A Bader analysis of the calculated stable adsorption configurations was done to gain further understanding of the CO co-adsorption with potassium.

In the case of the $Fe_5C_2(100)_{0.00}$ surface, the K becomes more positively charged when co-adsorbed with CO than when adsorbed alone, with a charge of +0.78 compared to a charge of +0.61 when adsorbed alone on the surface. The O gains more electrons when CO is co-adsorbed with potassium compared to when CO is adsorbed alone on the surface. The iron atoms interacting with the CO lose any electrons gained from the potassium. In the 1F case with K in position 1, this is the ridge iron atom R2, which was calculated to have a slight positive charge in the co-adsorbed configuration. Since the ridge iron atoms are equivalent, the same results would be observed no matter which ridge iron atom(s) were involved in the bonding with CO. The same is observed for the 2F adsorption configuration, with the two ridge iron atoms involved in the bonding losing the electrons gained when K is adsorbed (iron atoms R3 and R4).

On the $Fe_5C_2(100)_{0.098}$ surface the same trend is observed, with the iron atoms interacting with adsorbed CO losing electrons gained via donation of electrons from potassium. Potassium becomes more positively charged, +0.72 to +0.79 compared to +0.61 without the CO present. The iron atoms interacting with CO were also calculated to lose electrons gained from the K atom as was found with the Bader analysis on the $Fe_5C_2(100)_{0.00}$ surface.



**Table 3.20:** Bader analysis of CO co-adsorption with K adsorption on the $Fe_5C_2(100)_{0.00}$ surface. The charges of the surface iron atoms calculated are calculated relative to the charges on the surface atoms when no adsorbate is present on the surface. The charges on the C, O and K atoms are calculated relative to ground-state C, O and K atoms respectively

| Adsorption configuration | Charge difference | | | | | | | | | | |
|---|---|---|---|---|---|---|---|---|---|---|---|
| | C | O | K | Fe (R1) | Fe (R2) | Fe (V1) | Fe (V2) | Fe (R3) | Fe (R4) | Fe (V3) | Fe (V4) |
| ***K 1*** | -- | -- | *0.61* | *-0.09* | *-0.18* | *-0.03* | *-0.03* | *-0.17* | *-0.12* | *0.00* | *0.00* |
| **1F (K1)** | 0.34 | -0.92 | 0.78 | -0.07 | 0.02 | 0.02 | -0.02 | -0.13 | -0.11 | 0.03 | 0.04 |
| **2F (K1)** | 0.20 | -0.86 | 0.73 | -0.05 | -0.15 | 0.01 | 0.02 | -0.03 | -0.04 | 0.12 | 0.02 |

**Table 3.21:** Bader analysis of CO co-adsorption with K adsorption on the $Fe_5C_2(100)_{0.098}$ surface. The charges of the surface iron atoms calculated are calculated relative to the charges on the surface atoms when no adsorbate is present on the surface. The charges on the C, O and K atoms are calculated relative to ground-state C, O and K atoms respectively

| Adsorption configuration | Charge difference | | | | | | | | | | |
|---|---|---|---|---|---|---|---|---|---|---|---|
| | C | O | K | Fe (R1) | Fe (R2) | Fe (V1) | Fe (V2) | Fe (R3) | Fe (R4) | Fe (V3) | Fe (V4) |
| ***K 1*** | | | 0.61 | -0.11 | -0.17 | -0.04 | -0.04 | -0.15 | -0.07 | 0.00 | 0.00 |
| **1F (K)** | 0.34 | -0.95 | 0.79 | 0.04 | -0.07 | 0.01 | 0.00 | -0.13 | -0.04 | 0.04 | 0.01 |
| **2F (K)** | 0.24 | 0.90 | 0.78 | -0.03 | 0.04 | 0.02 | 0.00 | -0.11 | -0.06 | 0.03 | 0.03 |
| **3F (K)** | 0.12 | -0.87 | 0.72 | 0.07 | 0.00 | -0.04 | -0.03 | -0.11 | 0.00 | 0.11 | 0.04 |

### 3.5.2 Co-adsorption of CO with O

#### 3.5.2.1 Co-adsorption of CO with O on $Fe_5C_2(100)_{0.00}$

The starting configurations for the co-adsorption of CO with O on this surface are given in Figure 3.24. The co-adsorption of CO with O on this surface yielded a number of different stable adsorption configurations. The O atom was calculated to remain in its favoured bridge position between two ridge iron atoms. The adsorption configurations for CO when co-adsorbed with O on this surface were found to be the 1F state on the ridge iron atoms opposite the O, a 1F state in the valley and a 2F adsorption configuration in the valley (see Figure 3.25). For the 1F CO state in the valley the CO bond length was calculated to be 1.18Å. The CO bond length was calculated to be 1.17Å and 1.27Å for the 1F state above the ridge iron atom and the 2F state in the valley respectively. The Fe-C bond lengths for the 2F state were calculated to be 1.88Å and 1.90Å respectively. This represents an increase in the CO bond length when compared to CO adsorbed without any other species. For the 1F valley state and 1F ridge states, a Fe-C bond length of 1.80Å was calculated.

The ZPE-corrected adsorption energies, ZPVE, CO stretching frequencies, Fe-C bond lengths and C-O bond lengths are reported in Table 3.22. The calculated adsorption energy of CO in the 1F CO state on the ridge iron atom, is unaffected by the presence of the co-adsorbed O atom, 1.54eV. However, the 1F CO state in the valley is not stable when O is present on the surface. The adsorption energies calculated for this 1F adsorption state as well as the 2F state are significantly lower when compared to CO adsorption alone on this surface, 0.61eV and 0.77eV respectively.

The vibrational analysis showed that the CO stretching frequency for the 1F valley state and the 1F ridge state were 1951cm$^{-1}$ and 1856cm$^{-1}$ respectively. The 2F valley state had a calculated vibrational frequency of 1356cm$^{-1}$. The vibrational frequencies of the 1F adsorption states are higher than the CO stretching frequency for CO adsorbed alone on the surface while the CO stretching frequency of the 2F state is also lower than the frequency calculated for CO adsorbed alone. Therefore, the CO bond in the 2F adsorption configuration is much weaker than the CO bond in the 1F case, meaning that the cleavage of this bond may be more facile.

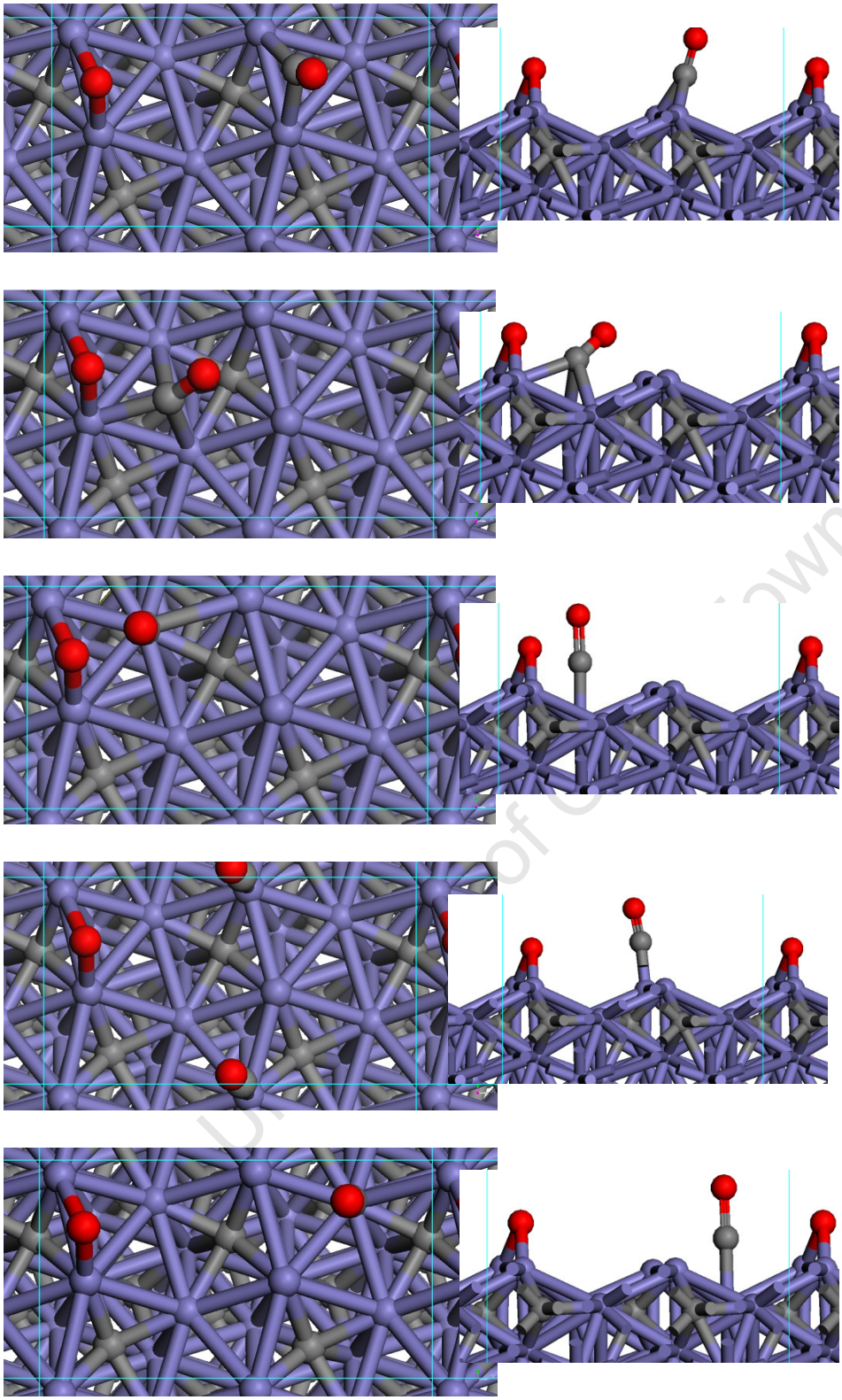

**Figure 3.24:** Starting configurations for the co-adsorption of O and CO on the p(2×1) $Fe_5C_2(100)_{0.00}$ surface

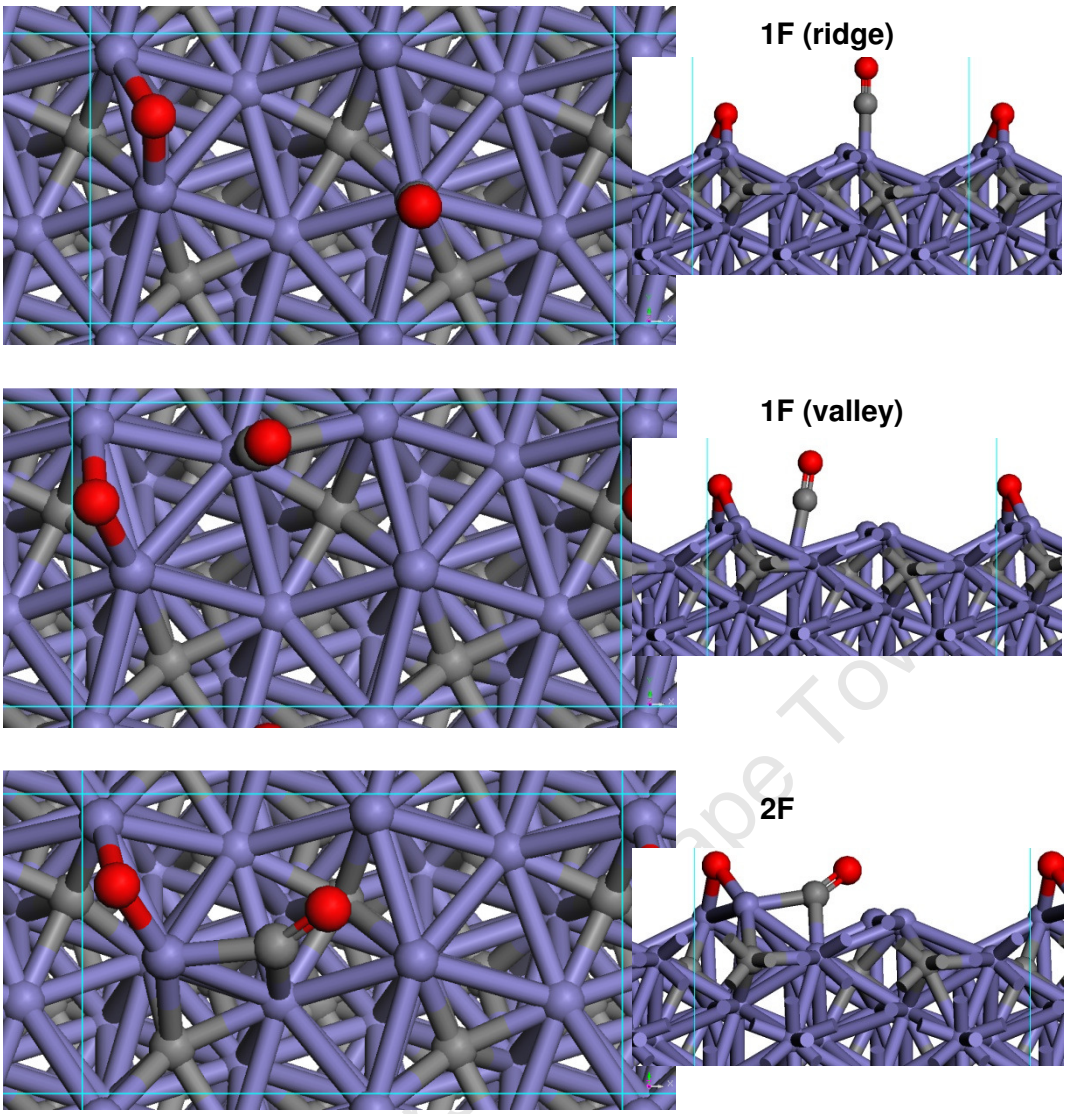


**Figure 3.25:** Optimised adsorption configurations for CO co-adsorption with O on the p(2×1) $Fe_5C_2(100)_{0.00}$ surface. (Calculated using RPBE functional, σ=0.2eV, k-point mesh of 3 × 5 × 1 and a cutoff energy of 450eV)

**Table 3.22:** Calculated adsorption energies, ZPVE, CO stretching frequencies, Fe-C distances and CO bond lengths for CO co-adsorption with O on the (2×1) $Fe_5C_2(100)_{0.00}$ surface. The italicised values are the calculated values for CO adsorption without O. (Calculated using RPBE functional, POTIM value of 0.02, σ=0.2eV, k-point mesh of 3 × 5 × 1 and a cutoff energy of 450eV)

| Bond Type | $E_{ads}$ (eV/CO) | ZPVE (eV) | v(C-O) ($cm^{-1}$) | r(Fe-C) (Å) | r(C-O) (Å) |
|---|---|---|---|---|---|
| ***1F (ridge)*** | *1.60* | *0.202* | *1927* | *1.79* | *1.17* |
| 1F ridge (O) | 1.54 | 0.267 | 1951 | 1.80 | 1.17 |
| 1F valley (O) | 0.61 | 0.264 | 1856 | 1.80 | 1.18 |
| ***2F*** | *1.34* | *0.177* | *1771* | *1.88; 1.97* | *1.24* |
| 2F (O) | 0.77 | 0.249 | 1362 | 1.88; 1.90 | 1.27 |

### 3.5.2.2 Co-adsorption of CO with O on $Fe_5C_2(100)_{0.098}$

The starting configurations for the co-adsorption of CO with O on this surface are given in Figure 3.26. The co-adsorption of CO and O on this surface yielded two 1F CO adsorption states, one in the valley and one found on the ridge iron atom, with O remaining in its favoured threefold hollow site (see Figure 3.27). The valley 1F state was calculated to have a CO bond length of 1.19Å, while the ridge 1F state was calculated to have a CO bond length of 1.17Å. The Fe-C bond lengths were calculated to be 1.80Å and 1.79Å for the 1F ridge state and 1F valley states respectively. This represents no change in the CO bond lengths for both 1F states when compared to the CO bond length of CO adsorbed alone on this surface.

The CO adsorption energies for the 1F valley and ridge state were calculated to be 1.57eV and 1.34eV respectively. This shows minimal change in the adsorption energy of the CO when compared to CO adsorption without any O co-adsorbed. The vibrational analysis of the co-adsorption of O and CO on the $Fe_5C_2(100)_{0.098}$ surface showed that the there was not much change in the CO stretching frequency when compared with CO adsorbed alone on the surface.



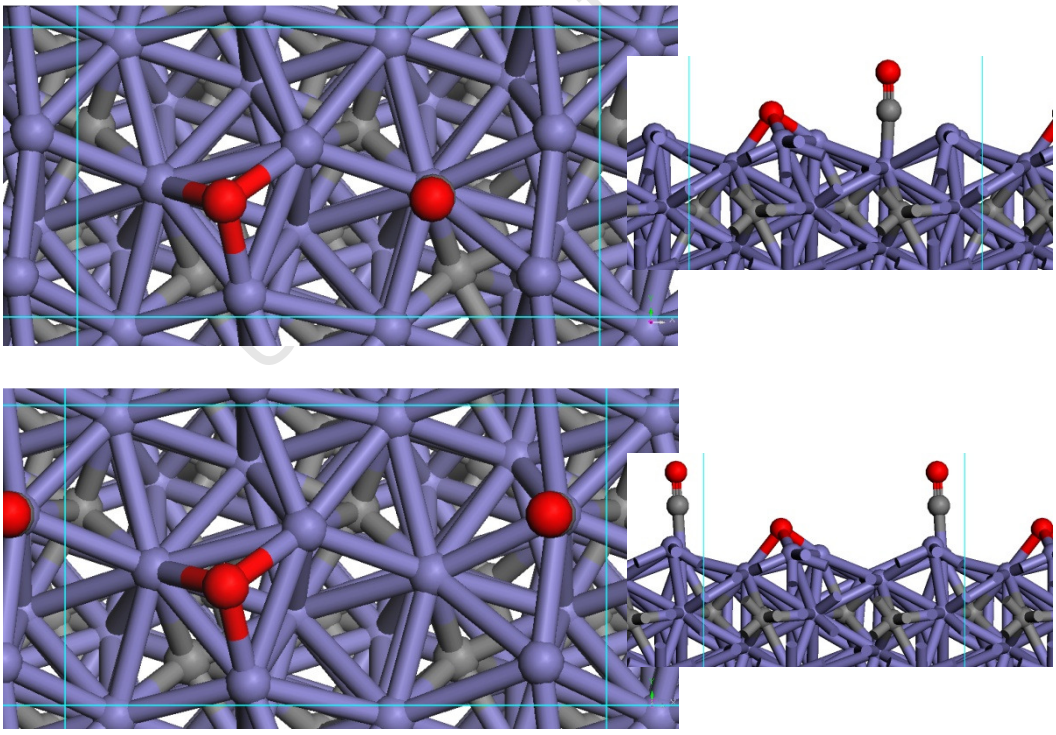

**Figure 3.26:** Starting configurations for the co-adsorption of O and CO on the p(2×1) $Fe_5C_2(100)_{0.098}$ surface

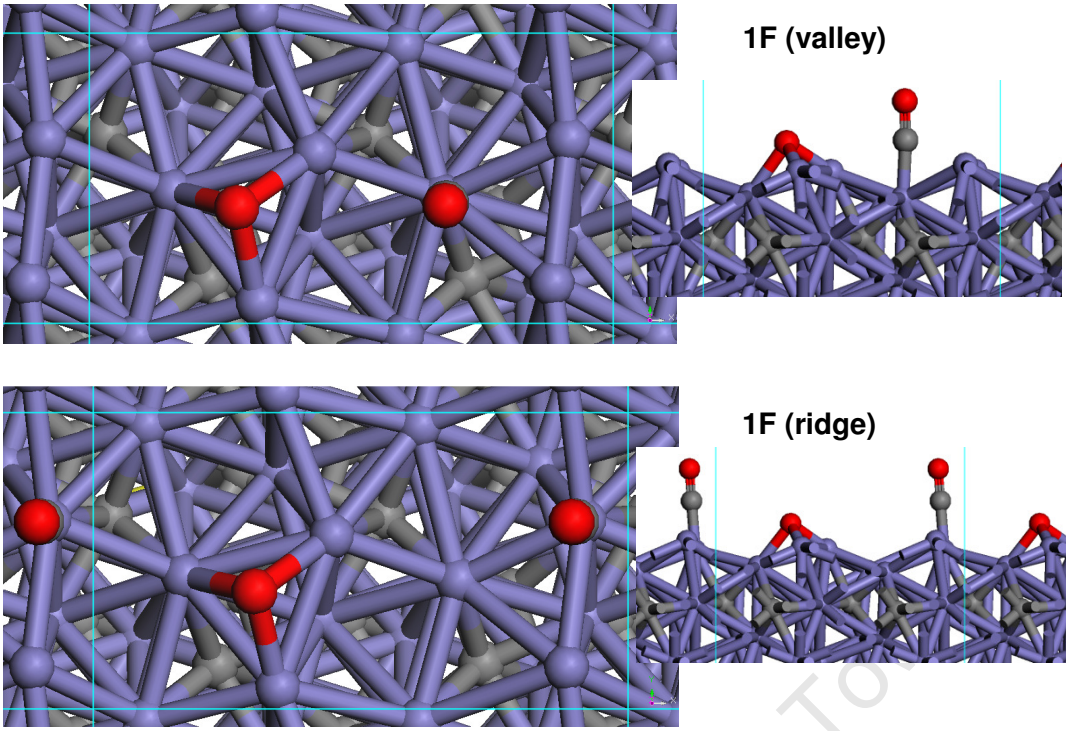


**Figure 3.27:** Optimised adsorption configurations for CO co-adsorption with O on the p(2×1) $Fe_5C_2(100)_{0.098}$ surface. (Calculated using RPBE functional, σ=0.2eV, k-point mesh of 3 × 5 × 1 and a cutoff energy of 450eV)

**Table 3.23:** Calculated adsorption energies, ZPVE, CO stretching frequencies, Fe-C distances and CO bond lengths for CO co-adsorption with O on the p(2×1) $Fe_5C_2(100)_{0.098}$ surface. The italicised values are the calculated values for CO adsorption without O. (Calculated using RPBE functional, POTIM value of 0.02, σ=0.2eV, k-point mesh of 3 × 5 × 1 and a cutoff energy of 450eV)

| Bond Type | $E_{ads,\ CO}$ (eV/CO) | ZPVE (eV) | v(C-O) ($cm^{-1}$) | r(Fe-C) (Å) | r(C-O) (Å) |
|---|---|---|---|---|---|
| ***1F (ridge)*** | *1.34* | 0.199 | *1931* | *1.80* | *1.17* |
| 1F (O) | 1.34 | *0.270* | 1927 | 1.80 | 1.17 |
| ***1F (valley)*** | *1.57* | *0.197* | *1826* | *1.78* | *1.19* |
| 1F (O) | 1.54 | 0.297 | 1811 | 1.79 | 1.19 |

### 3.5.2.3 Charge analysis of the co-adsorption of CO with O on the $Fe_5C_2(100)_{0.00}$ and $Fe_5C_2(100)_{0.098}$ surfaces

A Bader analysis of the calculated stable adsorption configurations was done to gain further understanding of the CO co-adsorption with the O. The results are given in Table 3.24 and Table 3.25. The results of these Bader analyses showed that on the $Fe_5C_2(100)_{0.00}$ surface for the 1F ridge adsorption state, the O had a minimal impact on the adsorption of CO, as the CO adsorbed to iron atoms was unaffected by the electron withdrawing effect of the O atom. However, for the 1F valley state and the 2F state, in both cases a large loss of electrons on the majority of the ridge iron atoms was calculated. In the case of the 2F state, some electron loss is calculated for the valley iron atoms.

Similar results are seen on the $Fe_5C_2(100)_{0.098}$ surface, where the Bader analysis shows the adsorption of O leads to electron loss on the iron atoms bonded to the O while the iron atoms bonded to the CO lose electrons.



**Table 3.24:** Bader analysis of CO co-adsorption with O adsorption on the $Fe_5C_2(100)_{0.0}$ surface. The charges of the surface iron atoms calculated are calculated relative to the charges on the surface atoms when no adsorbate is present on the surface. The charges on the C and O atoms are calculated relative to ground-state C and O atoms respectively. O* refers to the O adsorbed alone on the surface.

| Adsorption configuration | Charge difference | | | | | | | | | | |
|---|---|---|---|---|---|---|---|---|---|---|---|
| | C | O | O* | Fe (R1) | Fe (R2) | Fe (V1) | Fe (V2) | Fe (R3) | Fe (R4) | Fe (V3) | Fe (V4) |
| ***O*** | -- | -- | *-0.62* | *0.23* | *0.22* | *0.03* | *0.05* | *-0.05* | *0.02* | *0.01* | *0.04* |
| **1F ridge (O)** | 0.51 | -0.73 | -0.70 | 0.26 | 0.25 | 0.11 | 0.07 | -0.08 | 0.16 | 0.11 | 0.05 |
| **1F valley (O)** | 0.47 | -0.75 | -0.70 | 0.27 | 0.28 | 0.06 | 0.08 | 0.08 | 0.03 | 0.03 | 0.05 |
| **2F (O)** | 0.19 | -0.81 | -0.70 | 0.25 | 0.33 | 0.11 | 0.06 | 0.18 | 0.17 | 0.02 | 0.10 |

**Table 3.25:** Bader analysis of CO co-adsorption with O adsorption on the $Fe_5C_2(100)_{0.098}$ surface. The charges of the surface iron atoms calculated are calculated relative to the charges on the surface atoms when no adsorbate is present on the surface. The charges on the C and O atoms are calculated relative to ground-state C and O atoms respectively. O* refers to the O adsorbed alone on the surface.

| Adsorption configuration | Charge difference | | | | | | | | | | |
|---|---|---|---|---|---|---|---|---|---|---|---|
| | C | O | O* | Fe (R1) | Fe (R2) | Fe (V1) | Fe (V2) | Fe (R3) | Fe (R4) | Fe (V3) | Fe (V4) |
| ***O*** | -- | -- | *-0.71* | 0.23 | 0.26 | 0.03 | 0.30 | *0.05* | *0.02* | *0.01* | *0.05* |
| **1F ridge (O)** | 0.47 | -0.71 | -0.80 | 0.23 | 0.26 | 0.02 | 0.30 | 0.06 | 0.14 | 0.06 | 0.00 |
| **1F valley (O)** | 0.38 | -0.80 | -0.80 | 0.31 | 0.27 | 0.01 | 0.13 | 0.07 | 0.13 | 0.13 | 0.04 |

### 3.5.3 Co-adsorption of CO with KO

#### 3.5.3.1 Co-adsorption of CO with KO on the $Fe_5C_2(100)_{0.00}$ surface

The starting configurations for the co-adsorption of CO with KO on this surface are given in Figure 3.28. The co-adsorption of KO and CO on the $Fe_5C_2(100)_{0.00}$ surface yielded similar adsorption configurations when compared to the results of the co-adsorption of K and CO. The resulting stable adsorption configurations were found to be the 1F ridge state, a 2F state and a 1F valley state (see Figure 3.29). Table 3.26 shows the comparison of the CO bond lengths and Fe-C length of CO co-adsorbed with KO to CO co-adsorbed with K.

The CO adsorption energies when co-adsorbed with KO were calculated and it was found that the 1F ridge CO configuration was the most stable adsorption configuration with an adsorption energy of 2.16eV. The 2F state has an adsorption energy of 1.86eV. The 1F valley state has the lowest adsorption energy, 1.12eV.

A vibrational analysis of the optimised adsorption configurations calculated that the CO stretching frequency was 1726cm$^{-1}$, 1662cm$^{-1}$ and 1830cm$^{-1}$ for the 1F ridge adsorption state, 2F adsorption state and 1F valley adsorption configuration respectively. This is a decrease in the vibrational frequencies when compared to CO adsorbed alone on this surface.

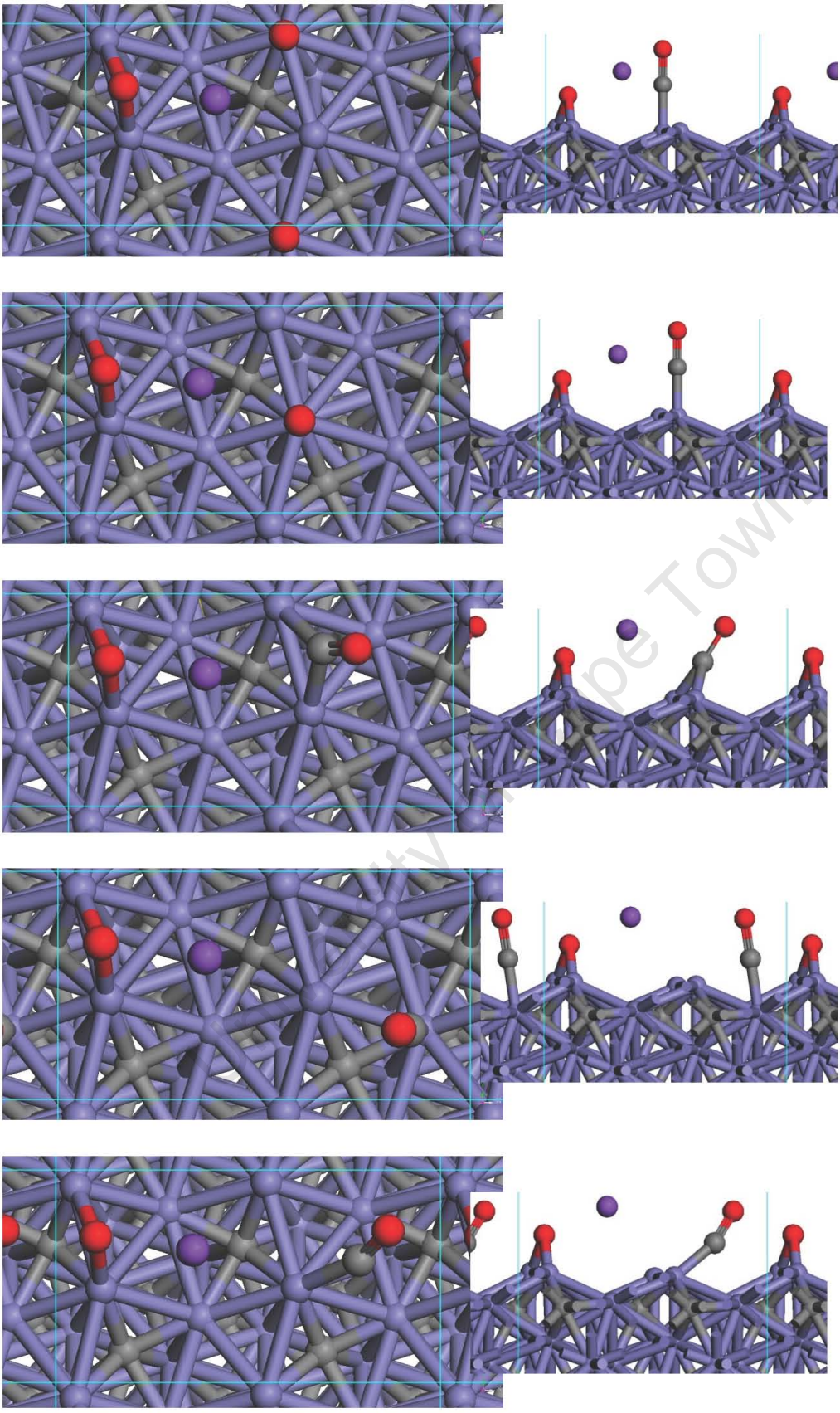

**Figure 3.28:** Starting configurations for the co-adsorption of KO and CO on the p(2×1) $Fe_5C_2(100)_{0.00}$ surface

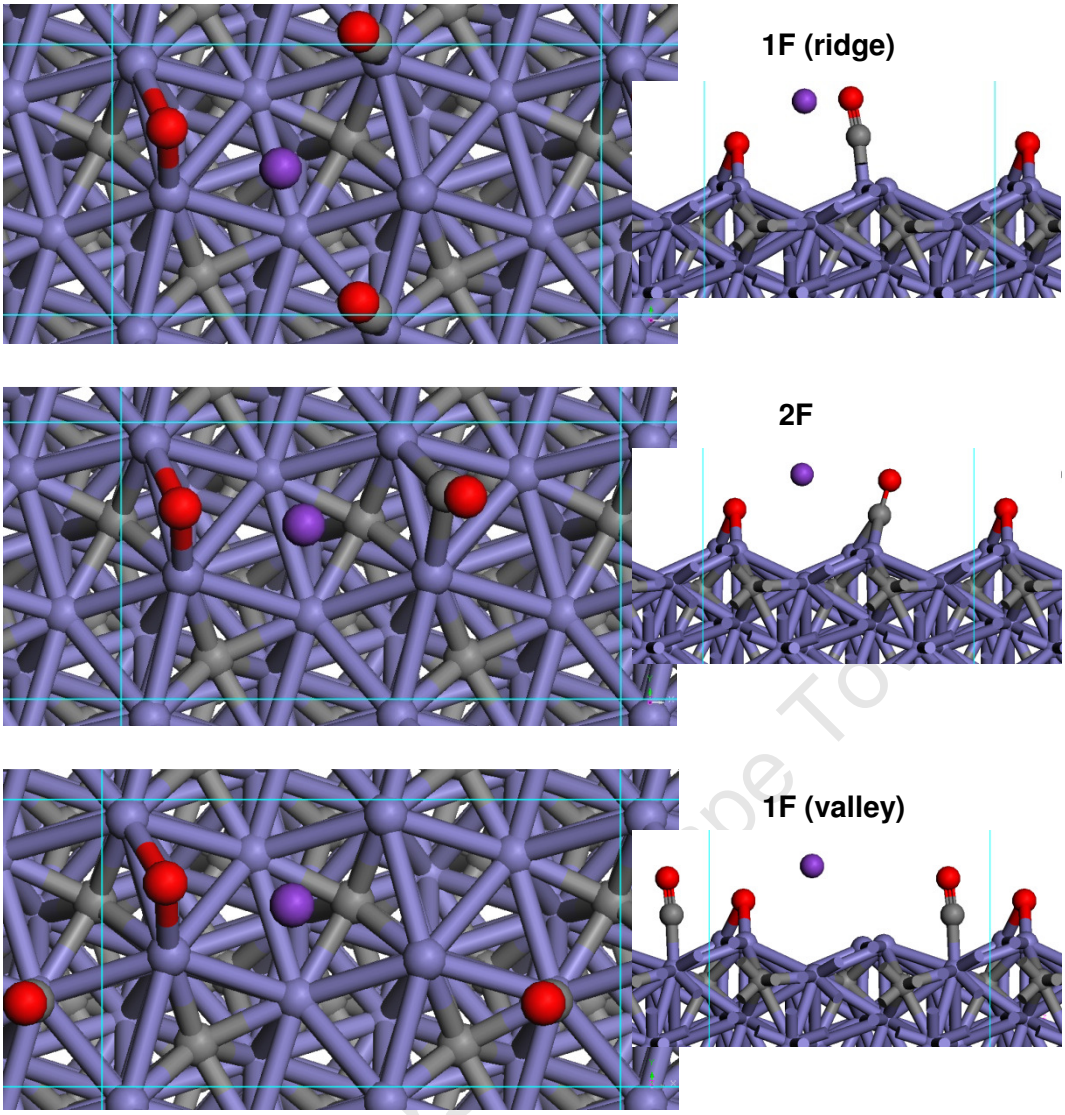


**Figure 3.29:** Optimised adsorption configurations for CO co-adsorption with KO on the p(2×1) $Fe_5C_2(100)_{0.00}$ surface. (Calculated using RPBE functional, σ=0.2eV, k-point mesh of 3 × 5 × 1 and a cutoff energy of 450eV)

**Table 3.26:** Calculated adsorption energies, ZPVE, CO stretching frequencies, Fe-C distances and CO bond lengths for CO co-adsorption with KO on the (2×1) $Fe_5C_2(100)_{0.00}$ surface. The italicised values are the calculated values for CO co-adsorption with K on this surface. (Calculated using RPBE functional, POTIM value of 0.02, σ=0.2eV, k-point mesh of 3 × 5 × 1 and a cutoff energy of 450eV)

| Bond Type | $E_{ads,\ CO}$ (eV/CO) | ZPE (eV) | v(C-O) $cm^{-1}$ | r (Fe-C) Å | r (C-O) Å | β (°) |
|---|---|---|---|---|---|---|
| ***1F (K)*** | *2.14* | *0.213* | *1699* | *1.71* | *1.22* | *89.9* |
| 1F (KO 1) ridge | 2.16 | 0.279 | 1726 | 1.73 | 1.21 | 86.1 |
| 1F (KO 1) valley | 1.12 | 0.278 | 1830 | 1.78 | 1.18 | 86.0 |
| ***2F (K)*** | *1.91* | *0.188* | *1611* | *1.88; 1.98* | *1.23* | *106.6* |
| 2F (KO 1) | 1.86 | 0.257 | 1662 | 1.86; 2.00 | 1.22 | 106.2 |

### 3.5.3.2 Co-adsorption of CO with KO on the $Fe_5C_2(100)_{0.098}$ surface

The starting configurations for the co-adsorption of CO with KO on this surface are given in Figure 3.30. The co-adsorption of KO and CO on the $Fe_5C_2(100)_{0.098}$ surface yielded similar results to the co-adsorption of K and CO on this surface. The resulting stable adsorption configurations were found to be the 1F ridge state and a 1F valley state (see Figure 3.31). Table 3.27 shows the comparison of the CO bond lengths and Fe-C length of CO co-adsorbed with KO to CO co-adsorbed with K.

The CO adsorption energies when co-adsorbed with KO were calculated and it was found that the 1F ridge CO configuration was the most stable adsorption configuration with an adsorption energy of 1.89eV. The 1F valley state has an adsorption energy of 1.75eV. The angle of the CO molecule relative to the surface plane also changes when co-adsorbing with K. The angle decreases so that the O in the CO is leaning towards the K atom.

A vibrational analysis of the optimised adsorption configurations calculated that the CO stretching frequency was 1740cm$^{-1}$ and 1731cm$^{-1}$ for the 1F ridge adsorption state and 1F valley adsorption configuration respectively. This is a decrease in the vibrational frequencies when compared to CO adsorbed alone on this surface. This indicates that with KO co-adsorbed on the surface, the CO bond will be weaker and require less energy to break.

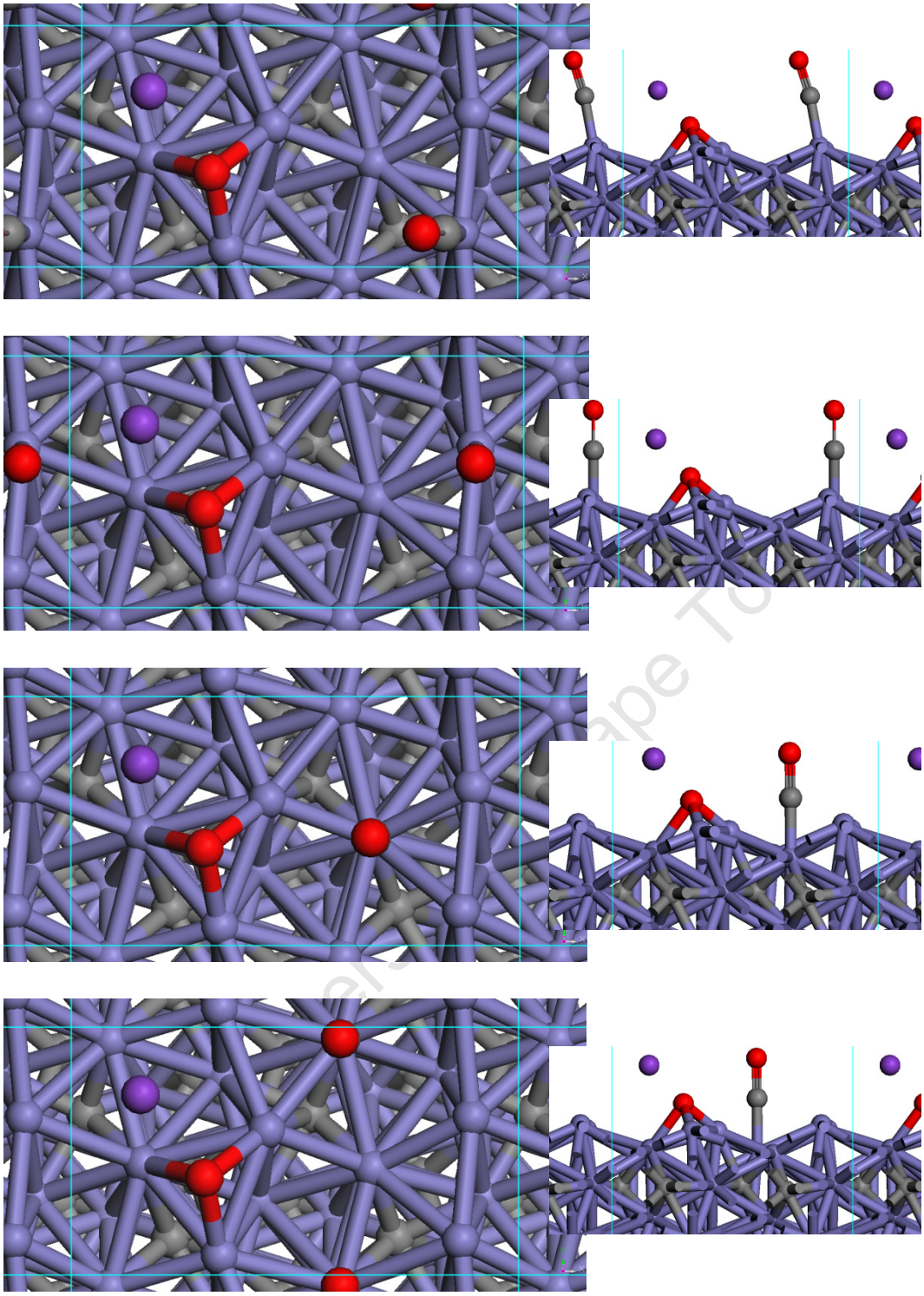

**Figure 3.30:** Starting configurations for the co-adsorption of KO and CO on the p(2×1) $Fe_5C_2(100)_{0.098}$ surface

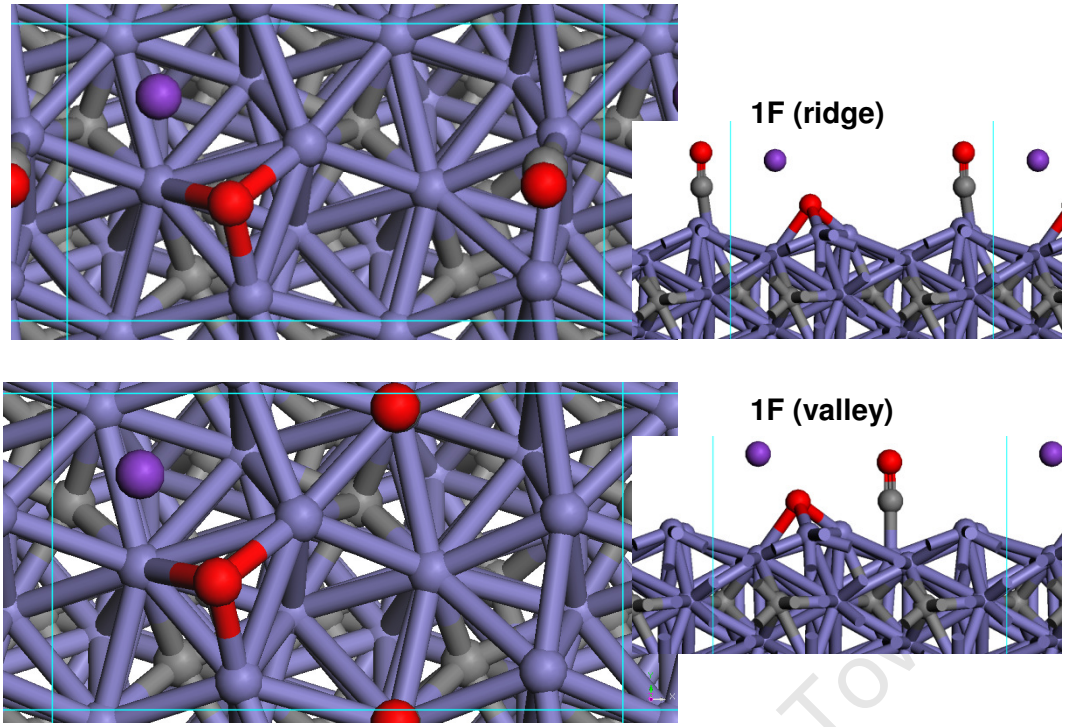


**Figure 3.31:** Optimised adsorption configurations for CO co-adsorption with KO on the p(2×1) $Fe_5C_2(100)_{0.098}$ surface. (Calculated using RPBE functional, σ=0.2eV, k-point mesh of 3 × 5 × 1 and a cutoff energy of 450eV)

**Table 3.27:** Calculated adsorption energies, ZPVE, CO stretching frequencies, Fe-C distances and CO bond lengths for CO co-adsorption with KO on the p(2×1) $Fe_5C_2(100)_{0.098}$ surface. The italicised values are the calculated values for CO co-adsorption with K on this surface. (Calculated using RPBE functional, POTIM value of 0.02, σ=0.2eV, k-point mesh of 3 × 5 × 1 and a cutoff energy of 450eV)

| Bond Type | $E_{ads,\ CO}$ (eV/CO) | ZPE (eV) | v(C-O) $cm^{-1}$ | r (Fe-C) Å | r (C-O) Å | β (°) |
|---|---|---|---|---|---|---|
| ***1F (K) ridge*** | *1.87* | *0.192* | *1697* | *1.74* | *1.22* | *82.7* |
| 1F (KO) ridge | 1.89 | 0.270 | 1740 | 1.77 | 1.21 | 88.9 |
| 1F (KO) valley | 1.75 | 0.268 | 1731 | 1.79 | 1.21 | 89.1 |

### 3.5.3.3 Charge analysis of the co-adsorption of CO with KO on the $Fe_5C_2(100)_{0.00}$ and $Fe_5C_2(100)_{0.098}$ surfaces

A Bader analysis was completed to further investigate the effect co-adsorbing the O atom with the K would have on CO adsorption on the surfaces. The results of the Bader analyses on both surfaces yielded similar results.

The O atom was observed to withdraw electrons from the Fe atoms it is bonded too, as was seen in the Bader analysis of KO adsorption. The CO adsorption leads to electron loss from the iron atoms involved in the CO adsorption, as was seen in the Bader analysis of CO co-adsorption on the surface. The presence of CO lead to electron loss on the iron atoms interacting with the CO as was seen with CO co-adsorption with K on both surfaces.

The electron gain by the O atom co-adsorbed with the K increases in the presence of the CO molecule. The O on the CO also has an increased electron gain when co-adsorbed with KO. The C atom loses more electrons when compared to the electron loss of the C atom when CO is adsorbed alone or co-adsorbed with K or O.

**Table 3.28:** Bader analysis of CO co-adsorption with KO adsorption on the p(2×1) $Fe_5C_2(100)_{0.00}$ surface. The charges of the surface iron atoms calculated are calculated relative to the charges on the surface atoms when no adsorbate is present on the surface. The charges on the C, K and O atoms are calculated relative to ground-state C, K and O atoms respectively. O* refers to the O in KO not the O of CO.

| Adsorption configuration | Charge difference | | | | | | | | | | | |
|---|---|---|---|---|---|---|---|---|---|---|---|---|
| | C | O | O* | K | Fe (R1) | Fe (R2) | Fe (V1) | Fe (V2) | Fe (R3) | Fe (R4) | Fe (V3) | Fe (V4) |
| ***KO*** | -- | -- | -0.88 | 0.72 | 0.23 | 0.15 | 0.03 | -0.01 | -0.17 | -0.10 | -0.02 | -0.01 |
| **1F ridge (KO)** | 0.70 | -1.03 | -1.44 | 0.88 | 0.22 | 0.18 | 0.08 | 0.06 | -0.35 | 0.00 | 0.05 | 0.07 |
| **1F valley (KO)** | 1.01 | -1.06 | -1.84 | 0.86 | 0.28 | 0.18 | 0.05 | 0.00 | -0.30 | -0.28 | 0.25 | 0.00 |
| **2F (KO)** | 0.86 | -1.05 | -1.64 | 0.87 | 0.25 | 0.18 | 0.07 | 0.03 | 0.25 | 0.20 | 0.04 | 0.01 |

**Table 3.29:** Bader analysis of CO co-adsorption with KO adsorption on the p(2×1) $Fe_5C_2(100)_{0.098}$ surface. The charges of the surface iron atoms calculated are calculated relative to the charges on the surface atoms when no adsorbate is present on the surface. The charges on the C, K and O atoms are calculated relative to ground-state C, K and O atoms respectively. O* refers to the O in KO not the O of CO.

| Adsorption configuration | Charge difference | | | | | | | | | | | |
|---|---|---|---|---|---|---|---|---|---|---|---|---|
| | C | O | O* | K | Fe (R1) | Fe (R2) | Fe (V1) | Fe (V2) | Fe (R3) | Fe (R4) | Fe (V3) | Fe (V4) |
| ***KO*** | -- | -- | -0.94 | 0.71 | 0.17 | 0.17 | -0.03 | 0.20 | -0.16 | -0.13 | 0.03 | -0.05 |
| **1F ridge (O)** | 0.32 | -1.80 | -1.12 | 0.87 | 0.24 | 0.24 | 0.05 | 0.25 | -0.08 | -0.02 | 0.01 | -0.10 |
| **1F valley (O)** | 0.18 | -0.86 | -1.47 | 0.81 | 0.30 | 0.17 | -0.14 | 0.14 | -0.08 | -0.03 | 0.06 | -0.04 |

# Chapter 4 : Discussion

## 4.1 CO adsorption

The results of the CO adsorption study on the $Fe_5C_2(100)_{0.00}$ surface showed that the CO adsorbed in either a 1F ridge or in one of two 3F configurations. The most stable of these was calculated to be the 1F adsorption state with an adsorption energy of 1.60eV. However, this adsorption state also had the shortest CO bond length as well as the highest C-O stretching frequency, 1950cm$^{-1}$. This means that this state could have a high CO dissociation energy. The other two adsorption states while being less stable adsorption sites were calculated to have much lower stretching frequencies, 1771cm$^{-1}$ and 1507cm$^{-1}$ indicating that these states could be have a lower dissociation barrier than the more stable 1F state.

The presence of carbon atoms in the surface layer as well as in the subsurface layer has a significant impact on the adsorption energy of CO on this surface. Adsorption of CO on the 3F site containing the subsurface carbon is significantly weaker than CO adsorption on the 3F site with the subsurface iron atom. The difference in the adsorption energies is much more pronounced for CO adsorption on the p(1×1) unit cell, with the adsorption energy of CO on the 3F site with subsurface carbon calculated to be 0.38eV lower than the adsorption energy of CO on the 3F site with the subsurface iron. On the p(2×1) cell, the adsorption energy of CO on the 3F site with subsurface carbon calculated to be 0.20eV lower than the adsorption energy of CO on the 3F site with the subsurface iron. The presence of carbon in the valley also hindered 1F adsorption on the valley iron atoms, causing CO migration from the 1F valley sites to the 3F hollow sites.

Increasing the size of the unit cell from p(1×1) to p(2×1) cell, leads to an increase in the adsorption energy of the 1F CO adsorption configuration by 0.05eV while the 3F adsorption configurations have larger increases in the adsorption energy. The 3F adsorption configuration with the subsurface carbon has an increase in the adsorption energy of 0.25eV while the 3F adsorption on the threefold hollow with the subsurface iron was found to have an increase in the adsorption energy of 0.08eV. A comparison of the p(1×1) and p(2×1) 3F adsorption configurations reveals a lengthening of the bond from the CO molecule to the valley iron atom for CO adsorption on both threefold sites as the size of the unit cell was increased. This shift in the adsorption configuration appears to be the cause of the larger

increase in adsorption energy for the 3F adsorption configurations when compared to the increase in adsorption energy of the 1F adsorption configuration as the unit cell size was increased from p(1×1) to p(2×1). The increase in the adsorption energy due to the shift in the adsorption configuration is smaller for the 3F adsorption configuration on the threefold hollow with the subsurface iron due to the smaller change in the bond length from the CO molecule to the valley iron atom in comparison to the change in bond length observed for the 3F configuration on the threefold hollow with the subsurface carbon. The increase in the bond length to the valley iron atom is 0.90Å for the 3F adsorption configuration on the site with the subsurface carbon while on the 3F site with the subsurface iron the increase in the bond length is only 0.19Å.

The CO stretching frequency for the 1F adsorption configuration (1927cm$^{-1}$) on the $Fe_5C_2(100)_{0.00}$ surface is higher than stretching frequency calculated for both of the 3F adsorption configurations. A stretching frequency of 1771cm$^{-1}$ was calculated for the 3F adsorption configuration on the threefold hollow with the subsurface iron, while a CO stretching frequency of 1507cm$^{-1}$ was calculated for the 3F adsorption configuration on the threefold hollow site with the subsurface carbon on the $Fe_5C_2(100)_{0.00}$ surface. This difference in the stretching frequency can be attributed to the broadening and downward shift of the 2π* anti-bonding states of CO to below the Fermi level when adsorbed in the 3F states seen when comparing the LDOS of the 3F adsorption configurations with the LDOS plot of CO in the gas phase (see Figure 4.1 to Figure 4.4). The site of the 2π* band is lowest for the 3F adsorption on the threefold hollow site with the subsurface carbon on the $Fe_5C_2(100)_{0.00}$ surface. This is consistent with the fact that this CO adsorption configuration has the longest CO bond length.

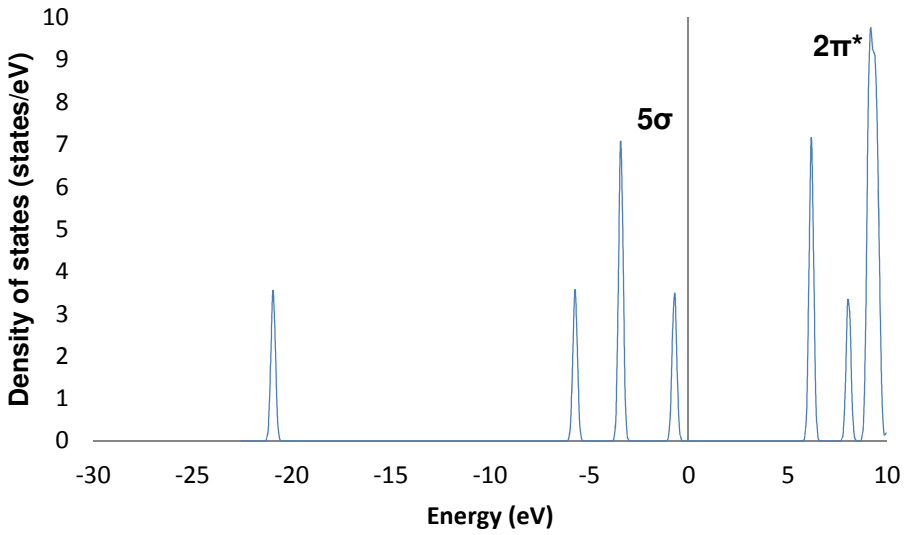


**Figure 4.1** LDOS of gas phase CO (Calculated using RPBE functional, σ=0.2eV, k-point mesh of 3 × 5 × 1 and a cutoff energy of 450eV)

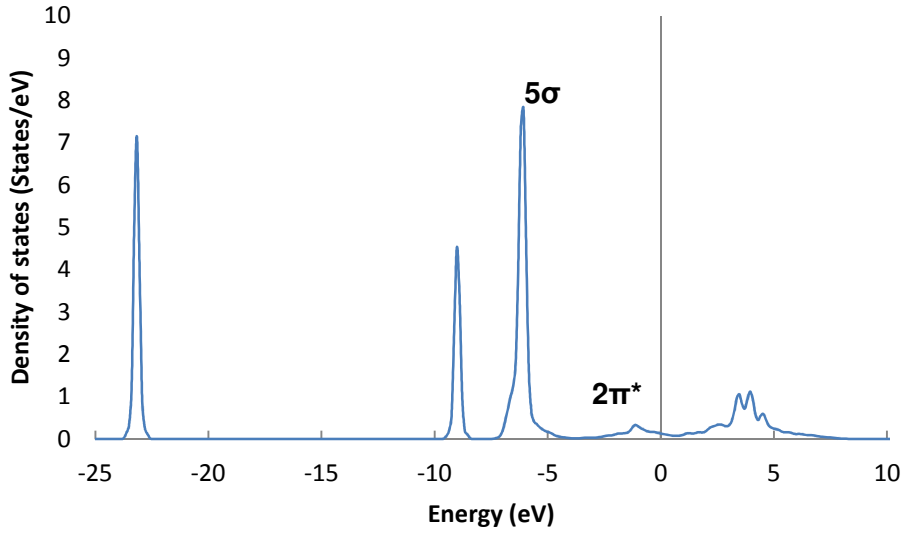


**Figure 4.2** LDOS of CO adsorbed in the 1F CO adsorption configuration on the $Fe_5C_2(100)_{0.00}$ surface (Calculated using RPBE functional, σ=0.2eV, k-point mesh of 3 × 5 × 1, vacuum spacing of 20Å and a cutoff energy of 450eV)

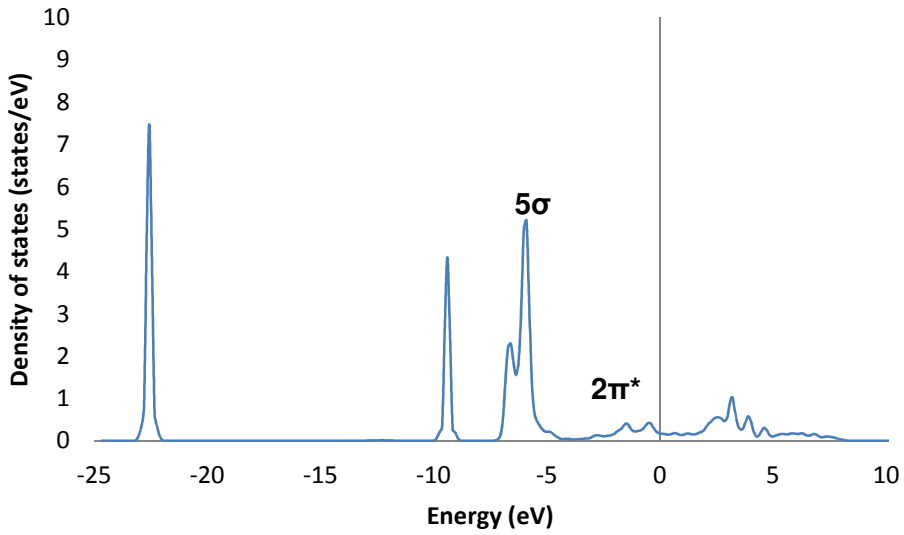


**Figure 4.3:** LDOS of CO adsorbed 3F CO adsorption configuration on the threefold hollow site with the subsurface iron on the $Fe_5C_2(100)_{0.00}$ surface (Calculated using RPBE functional, σ=0.2eV, k-point mesh of 3 × 5 × 1, vacuum spacing of 20Å and a cutoff energy of 450eV)

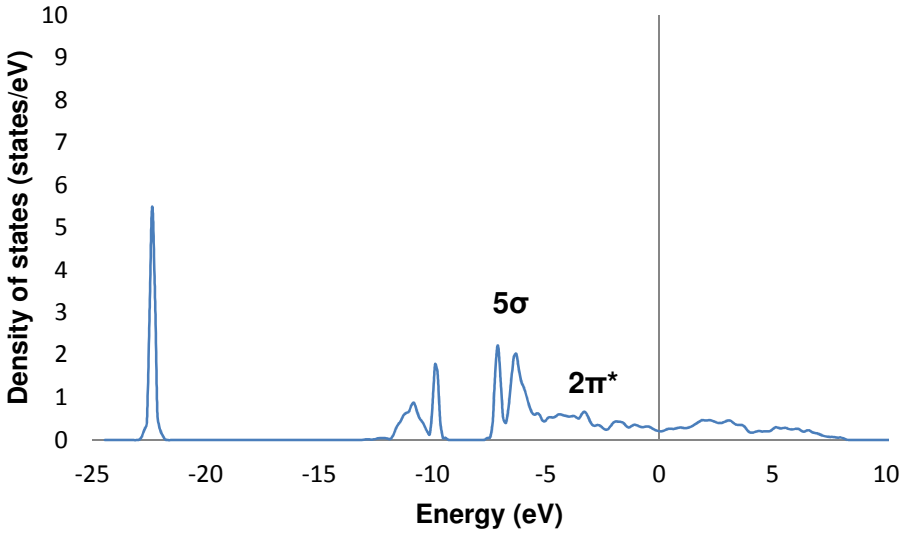


**Figure 4.4:** LDOS of CO adsorbed in the 3F CO adsorption configuration on the threefold hollow site with the subsurface carbon on the $Fe_5C_2(100)_{0.00}$ surface (Calculated using RPBE functional, σ=0.2eV, k-point mesh of 3 × 5 × 1, vacuum spacing of 20Å and a cutoff energy of 450eV)

The adsorption of CO on the $Fe_5C_2(100)_{0.098}$ surface yielded a slightly different picture to what was seen on the $Fe_5C_2(100)_{0.00}$ surface, with the only stable states on this surface being 1F adsorption configurations. The adsorption of CO on the 1F valley iron sites was calculated to be more stable than adsorption of CO on the ridge iron sites. The 1F valley state has a more favourable adsorption energy than the 1F ridge state, making it more stable and easier to dissociate. No 2F or 3F CO adsorption configurations were calculated on this surface. This stability of the valley 1F CO adsorption configuration is due to the lack of subsurface carbon in the upper layers of this surface. Comparing the p(1×1) CO adsorptions to the p(2×1) adsorptions, the adsorption energy decreased slightly in the 1F ridge adsorption configuration. This is completely opposed to what has been seen in literature and what is seen with CO adsorption on the $Fe_5C_2(100)_{0.00}$ surface. No possible explanation has been found for this decrease in adsorption energy. The adsorption of CO on the $Fe_5C_2(100)_{0.098}$ surface was accompanied by a downwards shift of both the 5σ and 2π* bands when compared to LDOS of CO in the gas phase. This is consistent with what is seen for CO adsorption on the $Fe_5C_2(100)_{0.00}$ surface. The LDOS plots for CO adsorption on the $Fe_5C_2(100)_{0.098}$ surface are given in the appendix (see Figure A.18 and Figure A.19).

Comparing CO adsorption on these two surfaces, the lack of subsurface carbon in the $Fe_5C_2(100)_{0.098}$ surface has a significant impact on the calculated stable adsorption configurations. Unlike on the $Fe_5C_2(100)_{0.00}$ surface, CO was found to adsorb on the $Fe_5C_2(100)_{0.098}$ surface in the 1F valley configuration. This can be attributed to the lack of subsurface carbon on this surface resulting in no migration of the CO on the $Fe_5C_2(100)_{0.098}$ surface. The most stable adsorption configurations on both surfaces are of similar strength however, on the $Fe_5C_2(100)_{0.00}$ surface a decrease in the adsorption strength was accompanied by a decrease in the C-O stretching frequency. On the $Fe_5C_2(100)_{0.098}$ surface the opposite is observed with the less stable 1F ridge CO adsorption having a higher CO stretching frequency than the more stable 1F valley site.

## 4.2 K adsorption on the $Fe_5C_2(100)_{0.00}$ and $Fe_5C_2(100)_{0.098}$ surfaces

K adsorption on both surfaces yielded similar results with regards to site preference, vibrational analyses and the maximum barrier for diffusion. The distance to the surface planes as well as the bond lengths. The distance to the surface plane for the optimised K adsorption configurations on the $Fe_5C_2(100)_{0.00}$ surface were calculated to be 2.43Å and 2.46Å respectively while on the $Fe_5C_2(100)_{0.098}$ surface the distance to the surface plane was calculated to be slightly higher, 2.50Å. This is the measured distance from the centre of the K atom to the surface plane and does not represent the distance between the K atom and the electron cloud generated by the surface iron atoms. The Bader analysis calculates this distance as a distance to a zero charge flux plane. For K adsorptions on both surfaces, this minimum distance was calculated as 1.50Å. This distance is in-between the covalent and ionic radius of potassium, 2.26Å and 1.33Å respectively. This, although not conclusive and perhaps not the best method of determining the type of bonding, indicates that the interaction between potassium and the surface should be more ionic than covalent.

The results of the charge density difference plots show no regions of shared charge which would be expected if covalent bonding was dominant. The charge density difference plot does however show polarisation of the potassium to the surface. The charge density difference plot also shows an increase in electron density in the electron cloud formed by the surface iron atoms. This indicates electron donation from the potassium to the surface. This is confirmed by results from the Bader analysis which shows that potassium donates 0.61 electrons to the surface. This is consistent with results seen in literature (Jenkins and King, 2000). The results of the Bader analyses on both the $Fe_5C_2(100)_{0.00}$ and $Fe_5C_2(100)_{0.098}$ surfaces also showed that the electron donation effect of the potassium is very localised, only affecting the ridge iron atoms nearest to the potassium, while leaving the valley iron atoms unaffected. The carbon atoms are unaffected by the potassium electron donation. This was unexpected as carbon is more electronegative than the iron and thus was expected to play a prominent part in the adsorption of potassium. This is consistent with what has been seen in literature, with a study by Sorescu (2011) on potassium adsorption Fe(100) also finding that the electron transfer from the potassium to be localised.

The local density of states (LDOS) analysis for K adsorption showed that the adsorption of K on both surfaces caused a downshift and a broadening of the Fe d-states to energies close to the Fermi level (see Figure 4.5, Figure 4.6 and Figure 4.7). Wilke and Cohen (1996)

investigated K adsorption on a Pd(100) surface using DFT and reported a similar downshift and broadening of the Pd d-states when K was adsorbed on the Pd(100) surface. Regions of overlap of the states of the Fe and the K show no sharing of the states, indicating that ionic bonding is present. This data as well as the data from the charge density difference plot and Bader analysis all indicate that the ionic component dominates the bonding of potassium to the surface.

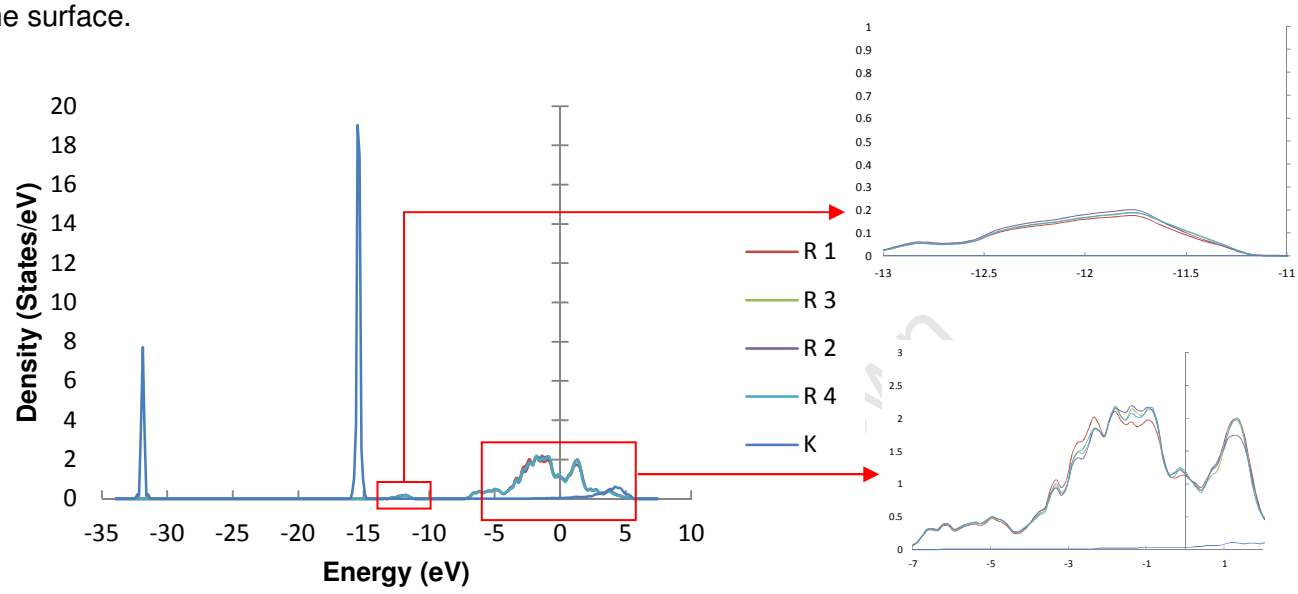


**Figure 4.5:** LDOS plot showing the DOS of the ridge iron atoms and the potassium adsorbate for K adsorption on the $Fe_5C_2(100)_{0.00}$ surface. (Calculated using RPBE functional, σ=0.2eV, k-point mesh of 3 × 5 × 1, vacuum spacing of 20Å and a cutoff energy of 450eV)

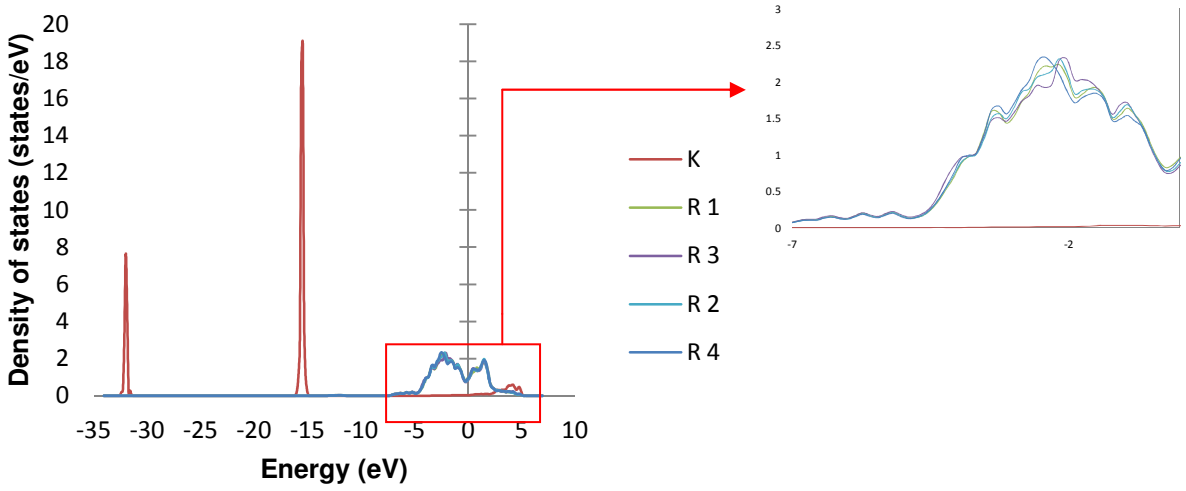


**Figure 4.6:** LDOS plot showing the DOS of the ridge iron atoms and the potassium adsorbate for K adsorption on the $Fe_5C_2(100)_{0.098}$ surface. (Calculated using RPBE functional, σ=0.2eV, k-point mesh of 3 × 5 × 1, vacuum spacing of 20Å and a cutoff energy of 450eV)

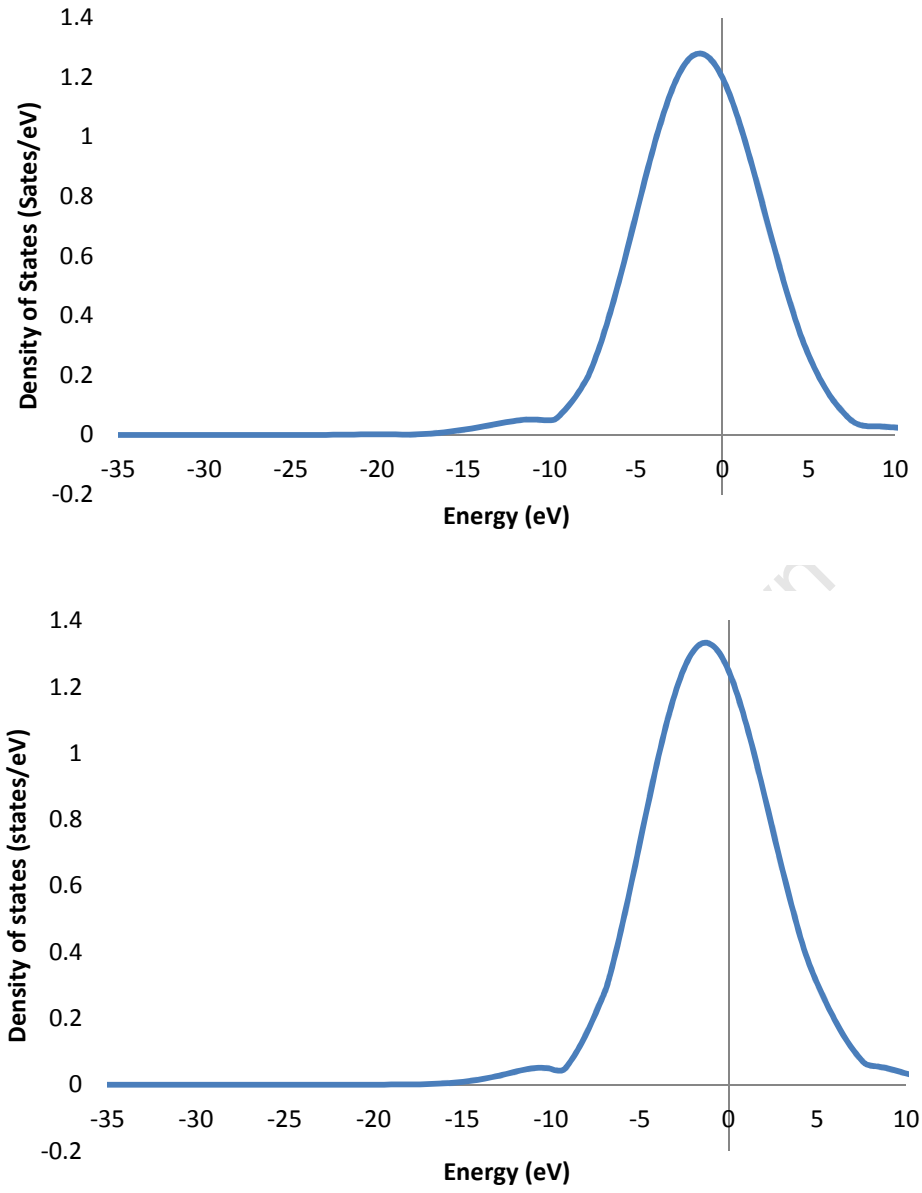


**Figure 4.7:** LDOS plots showing the DOS of the surface iron atoms for the adsorbate free $Fe_5C_2(100)_{0.00}$ surface (top) and the DOS of the surface iron atoms for the adsorbate free $Fe_5C_2(100)_{0.098}$ surface (below). (Calculated using RPBE functional, σ=0.2eV, k-point mesh of 3 × 5 × 1, vacuum spacing of 20Å and a cutoff energy of 450eV)

The diffusion studies of K adsorption on both surfaces showed that K has a very low maximum barrier for diffusion along the valley on both surfaces. This was supported by the data from the vibrational analyses which calculated a negative frequency for K moving along the valley. Diffusion studies into the diffusion of K along the valley on both surfaces found that the maximum barrier for the diffusion of K was very low. This high mobility of K on the surface is also found by Sorescu (2011) for adsorption of potassium on Fe(100) with a barrier for diffusion of 0.03eV.

## 4.3 O adsorption

The adsorption of O on both the $Fe_5C_2(100)_{0.00}$ and $Fe_5C_2(100)_{0.098}$ surfaces yielded different results with regards to the favoured site. On the $Fe_5C_2(100)_{0.00}$ surface, a bridged adsorption configuration was found to be the only stable configuration while on the $Fe_5C_2(100)_{0.098}$ surface, a threefold hollow adsorption configuration was found to be the most stable. The reason for the difference in the stable site is due to the presence of subsurface carbon in the $Fe_5C_2(100)_{0.00}$ surface hindering a threefold adsorption of O on this surface.

For O adsorption on both the $Fe_5C_2(100)_{0.00}$ surface and $Fe_5C_2(100)_{0.098}$ surface, the LDOS plot of the O atoms and the iron atoms bonded to the O atom shows overlap between the states of the O atom and the iron atoms (see appendix, Figure A.14 and Figure A.15). Neither the iron nor O states dominate in the region of overlap. The largest overlap occurs in the d-orbital band of the iron atoms, near the Fermi level. From this and the results of the Bader analyses, which shows a loss of electrons from the iron atoms bonded to the O atom, it can be concluded that the bonding of O on this surface is polar covalent in nature.

## 4.4 KO adsorption

The adsorption of KO on the surface on the $Fe_5C_2(100)_{0.00}$ and $Fe_5C_2(100)_{0.098}$ surfaces showed that the presence of K resulted in an increase in the adsorption energy of O on the surface of up to three times the adsorption energy of O on it own. This was largely due to the increase in surface electrons on the ridge iron atoms via electron donation from the potassium. The charge density difference plots on both surfaces showed the loss of surface electrons from the iron atoms bonded to the O atom. The charge density difference plots also showed a polarisation of the K atom towards the O atom. This is different when compared to the charge density difference plots for K adsorption, where the K atom was observed to be polarised compared to the surface. This polarisation of the K with relation to the O atom is indicative of interaction between the two species, possibly bonding. The LDOS plot of the adsorbed K and O species shows that there are some regions where both K and O share states (see appendix, Figure A.7 and Figure A.8). However, in these regions where the states of the O and K overlap, the states of the O are significantly larger than the number of states of K. This indicates that the interaction between the K and O is ionic in nature. This is supported by the results of the Bader analysis that shows an increase in electron loss on the K atom when co-adsorbed with O when compared to the electron loss on the K atom when it is adsorbed without O. The Bader analyses also show that the ridge iron atoms not

bonded to the O atom are unaffected by the presence of the O atom meaning that they gain the same amount of electrons regardless of whether K or KO is adsorbed on the surface.

Based on these results, we can conclude that the co-adsorption of KO on the $Fe_5C_2(100)_{0;00}$ and $Fe_5C_2(100)_{0.098}$ surfaces results in a significant increase in the stability of O adsorption. Interaction between the K and O species on the surfaces appears to be ionic in nature based on the results of the Bader analyses and LDOS plots. The co-adsorption of O with the K does not affect the electron increase on the ridge iron atoms not bonded to the O atom.

## 4.5 Co-adsorption of CO with K, O and KO

### 4.5.1 Co-adsorption of CO with K

The co-adsorption of CO with K on both the $Fe_5C_2(100)_{0.00}$ and $Fe_5C_2(100)_{0.098}$ surfaces lead to a significant increase in the adsorption energy of CO on the surface. This increase in the adsorption energy was accompanied with an increase in the CO bond length as well as a decrease in the CO stretching frequency indicating a weakening of the CO bond. This is in excellent agreement with what is typically seen in literature for potassium co-adsorption with CO (Sorescu; 2011).

The presence of potassium caused a migration of the CO on both surfaces away from the valley iron atoms and threefold hollow sites towards the electron rich ridge iron atoms. On the $Fe_5C_2(100)_{0.098}$ surface, the valley 1F CO adsorption configuration which was calculated to be the most stable adsorption configuration for CO adsorption, was not calculated when co-adsorbing CO with K as the CO was found to migrate from the 1F valley site to either a 2F adsorption configuration or a 1F adsorption configuration on top of an electron-rich ridge iron atom.

On both the $Fe_5C_2(100)_{0.00}$ and $Fe_5C_2(100)_{0.098}$ surfaces the angle of the CO molecule with respect to the surface plane changes when co-adsorbed with the K so that the O of the CO molecule is leaning towards the K atom. This indicates interaction between the K and the O of the CO. The charge density difference plot shows a polarisation of the K towards the O atom again indicating interaction between the two species. However, the LDOS shows minimal overlap between the K and O (of the CO) states (see appendix, Figure A.13, Figure

A.14 and Figures A.20-A.23). This indicates that the interaction between the two species is ionic in nature.

### 4.5.2 Co-adsorption of CO with O

The co-adsorption of CO with O on the $Fe_5C_2(100)_{0.098}$ surface had no effect on the calculated CO adsorption energies when compared to CO adsorbed alone on the surface. This can be attributed to CO migration away from the valley sites nearest the O atom to the ridge iron atoms. The CO adsorbed on the ridge iron atoms or on the valley iron atoms furthest from the O atom are too far to feel any effects from the adsorbed O atom. The lack of carbon in the surface layer means that CO migration across the surface is unhindered.

The co-adsorption of CO with O on the $Fe_5C_2(100)_{0.00}$ surface is a different scenario. Unlike on the $Fe_5C_2(100)_{0.098}$ surface there is surface carbon on the $Fe_5C_2(100)_{0.00}$ surface which hinders the migration of CO from the threefold hollow sites closest to the O to the ridge iron sites. The CO adsorbed above the 3F hollow sites with the subsurface carbon has a significant decrease in the calculated adsorption energy, 0.57eV when compared to the adsorption energy of CO alone on the surface. The CO adsorbed on the 1F valley site has a low adsorption energy, 0.61eV with O present. These low adsorption energies are accompanied by higher CO stretching frequencies than seen when compared to CO adsorbed without O, indicating an increase in the required dissociation energy. The CO adsorptions on the ridge iron atoms and the 3F adsorptions in the adjacent valley 3F sites are unaffected by the presence of the O atom. As with the co-adsorption of CO and O on the $Fe_5C_2(100)_{0.098}$ surface, these adsorption configurations are too far from the O to be affected by its presence. These results indicate that the negative effect of O on the adsorption energy of CO on both surfaces is short ranged and very localised.

### 4.5.3 Co-adsorption of CO with KO

The co-adsorption of CO with KO on the $Fe_5C_2(100)_{0.00}$ and $Fe_5C_2(100)_{0.098}$ surfaces yielded similar results to the co-adsorption of CO with K. The O atom co-adsorbed with the K atom was expected to have a negative impact on the adsorption of CO due to its electron withdrawing effect. However, on both the $Fe_5C_2(100)_{0.00}$ and $Fe_5C_2(100)_{0.098}$ surfaces the presence of O has minimal impact on the adsorption of CO on the surface.

The results of co-adsorption with KO on the $Fe_5C_2(100)_{0.00}$ surface, show that the presence of KO has a positive effect on the adsorption energy of CO. In the case of the 1F ridge CO adsorption, the adsorption energy of CO when co-adsorbed with KO is comparable to the adsorption energy when co-adsorbed with K. The 2F bridged CO configuration has a slightly lower adsorption energy when compared to the 2F adsorption energy when co-adsorbed with K. The CO stretching frequencies of these two CO adsorption configurations are slightly higher when co-adsorbed with KO than when co-adsorbed with K. However, this is still a large decrease in the stretching frequency when comparing to the stretching frequency of CO when it is adsorbed alone on the surface.

The only exception to the trends seen on this surface is the 1F valley adsorption configuration. When attempting to adsorb CO in a 1F valley site, irrespective off whether CO was adsorbed alone or co-adsorbed CO with K, the CO was observed to migrate away from the valley site to either a 3F or 2F adsorption configuration. However, when co-adsorbing with KO, the O atom prevents the migration of the CO from the valley site to the nearest ridge. Migration to the opposite ridge iron atoms, towards the K atom, is blocked by the surface and subsurface carbon atoms. As a result this adsorption state has a low adsorption energy, 1.12eV and a high CO stretching frequency 1830$cm^{-1}$.

The results of co-adsorption with KO on the $Fe_5C_2(100)_{0.098}$ surface show that the adsorption energy calculated for CO adsorption are very similar to the CO adsorption energies calculated when co-adsorbing CO with K. As with CO co-adsorption with KO on the $Fe_5C_2(100)_{0.00}$ surface, the decrease in the CO stretching frequency is slightly lower when co-adsorbing CO with KO than when CO was co-adsorbed with K. However, there is still a sizeable decrease in the CO stretching frequency when compared to CO adsorption alone on this surface. When co-adsorbing K with CO on this surface, no 1F valley state is calculated, while when co-adsorbing KO and CO, a 1F valley configuration is calculated. This state has an increased adsorption energy (0.18eV increase) and decreased CO stretching frequency (decrease of 95$cm^{-1}$) when compared to CO adsorption on the 1F valley site without KO adsorbed on the surface.

### 4.5.4 Comparing co-adsorption of CO with K, O and KO

Comparing the results of the co-adsorption of CO with the other species on both surfaces, the effect of having KO as opposed to K on the surface has minimal impact on the observed effects seen on CO adsorption. This is true for adsorption on both surfaces except in the isolated case on the $Fe_5C_2(100)_{0.00}$ surface where CO migration from 1F valley configuration (V2) was prevented by a combination of factors. The attempted 1F CO adsorption on the other valley iron atom (V1) was found to lead to CO migration to the 2F configuration.

The co-adsorption of CO with O had no effect on the adsorption energy of CO in all cases on the $Fe_5C_2(100)_{0.098}$ surface, with the presence of O having neither a positive or negative influence. The CO was found to be able to migrate away from the O atom, preventing any interaction between the two species. On the $Fe_5C_2(100)_{0.00}$ surface however, the presence of subsurface carbon prevented the migration of CO from the 1F valley sites and the 3F hollow site with the subsurface carbon. Here the negative impact of O on the adsorption energy of CO is clearly visible. The effect of O on the adsorption stability of CO on both surfaces appears to be short ranged, as adsorption sites further from the O atom remain unaffected by its presence.

In summary, O has a highly localised negative impact on CO adsorption when the CO cannot migrate away from the O due to subsurface carbon. The potential differences in the effects upon having K or KO on the surface appears to inconsequential as both species have the same effects on CO adsorption.

## 4.6 Preliminary Thermodynamic analysis of K → KO system

A preliminary thermodynamic analysis was constructed based on a reaction which could occur at process conditions due to the large amounts of water, KO could be formed. The reaction:

$$K_{ads} + H_2O_{(g)} \leftrightarrows KO_{ads} + H_{2\,(g)}$$

Since this was a preliminary thermodynamic analysis, harmonic motion was assumed. It should be noted however, that at the Fischer-Tropsch conditions the assumption of harmonic motion may not be valid. As was stated in the introduction, Fischer-Tropsch conditions refer to temperatures of 300 to 350ºC and pressures of approximately 30atm.

The aim of the thermodynamic analysis was to determine at process conditions, which potassium species would be present on the surface. The change in Gibbs free energy for the above reaction was calculated.

The Gibbs free energy equation is:

$$G = H - TS$$

Where H is the enthalpy and, T is the temperature and S is the entropy. What has been calculated using DFT is the electronic energy which is the enthalpy not including terms for vibration, rotation and translation. To account for these terms as well as the entropy the data gathered from the vibrational analysis was applied. The expanded equation is now:

$$G = E_{calc} + (H_{vib} + H_{trans} + H_{rot} + RT) - T(S_{vib} + S_{trans} + S_{rot})$$

Where the $E_{calc}$ is the calculated electronic energy and the H and S terms are the enthalpic and entropic contributions of vibration, translation and rotation respectively. For the adsorbed species this equation simplifies, since adsorbed species are relatively fixed to the surface, the enthalpic and entropic contributions of the vibrational and rotational terms can be neglected. However, as was discussed earlier for both K and KO on both surfaces, the maximum barrier for diffusion is very low in the direction of the valley. Therefore, this was treated as a translational mode for both species. The equations used to calculate the corrections were taken from work by Hirano (1993) and are given in the appendix section D.

The results of the analysis, given in Table 4.1, Figure 4.7 and Figure 4.8, shows that the change in the Gibbs free energy is always negative indicating that the formation of KO is

favoured. Figure 4.7 plots the $K_p(H_2/H_2O)$ against temperature and shows $K_p$ is always much greater than 1, meaning that the forward reaction is favoured. Figure 4.8 is a plot of the change in the Gibbs free energy of the system plotted vs. temperature. At all temperatures, the Gibbs free energy is negative, showing that the forward reaction is favoured. Therefore, at equilibrium the concentration of products will be greater the concentration of the reactants. Therefore, at Fischer-Tropsch conditions, the calculated $K_p$ values and the calculated ΔG for this reaction show that there will be KO on the surface, not metallic K.

**Table 4.1:** Change in Gibbs free energy for $K + H_2O \rightarrow KO + H_2$ reaction

| Temperature (K) | ΔG (kJ/mol) | Kp |
|---|---|---|
| 450 | -94.72 | 9.88E+10 |
| 475 | -94.27 | 2.32E+10 |
| 500 | -93.84 | 6.36E+09 |
| 525 | -93.43 | 1.98E+09 |
| 550 | -93.05 | 6.86E+08 |
| 575 | -92.68 | 2.62E+08 |
| 600 | -92.33 | 1.09E+08 |
| 625 | -92.00 | 4.88E+07 |
| 650 | -91.68 | 2.33E+07 |

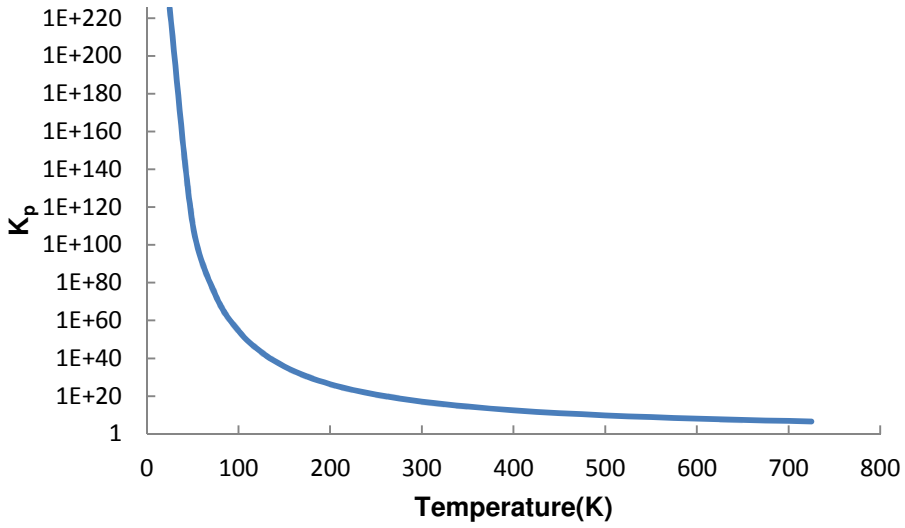


**Figure 4.8:** $K_p$ ($P_{H2}/P_{H2O}$) plotted against temperature (K) on a logarithmic axis

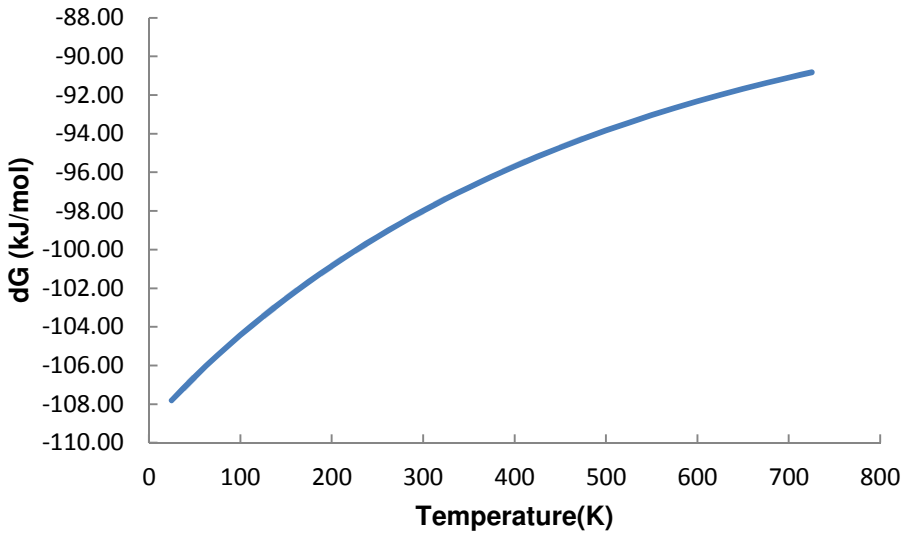


**Figure 4.9:** The change in Gibbs free energy (kJ/mol) for the postulated reaction plotted against temperature (K)

# Chapter 5 : Conclusions

Plane wave DFT calculations has been used to study the adsorption properties of CO, K, O and KO on the $Fe_5C_2(100)_{0.00}$ and $Fe_5C_2(100)_{0.098}$ surfaces. The co-adsorption of CO with K, O or KO on the $Fe_5C_2(100)_{0.00}$ and $Fe_5C_2(100)_{0.098}$ surfaces has also been investigated. A thermodynamic analysis has been used to investigate the nature of the potassium species at Fischer-Tropsch conditions. The following conclusions can be drawn from this work:

- Based on the thermodynamic analysis, KO not K will be present on the surface at Fischer-Tropsch synthesis conditions.
- The presence of subsurface carbon on the $Fe_5C_2(100)_{0.00}$ surface has a significant influence on the stability of CO adsorption causing CO migration and decreasing CO adsorption energies on affected sites.
- Co-adsorbing CO with K or KO on both the $Fe_5C_2(100)_{0.00}$ and the $Fe_5C_2(100)_{0.098}$ surfaces has the same effect on CO adsorption resulting in an increase in the CO adsorption energy, an increase in the C-O bond length and a decrease in the CO stretching frequency. The effects on CO adsorption have virtually the same magnitude irrespective of whether CO is co-adsorbed with K or KO. The increases in the adsorption energy indicate that K and KO both enhance CO adsorption. The increase in CO bond length and the decrease in the CO stretching frequency indicate that CO dissociation should be more facile when the CO is co-adsorbed with K or KO.
- Co-adsorbing CO with O has a very localised negative effect on CO adsorption, causing a decrease in the adsorption energy, a decrease in the CO bond length and an increase in the CO stretching frequency on the $Fe_5C_2(100)_{0.00}$ surfaces in the instances where subsurface carbon prevents CO migration away from O.
- Co-adsorbing K with O causes a significant increase in the adsorption energy of the O on both the $Fe_5C_2(100)_{0.00}$ surface and the $Fe_5C_2(100)_{0.098}$ surface.

Based on the results of this study the hypothesis that K is not necessarily present as a metal atom under Fischer-Tropsch conditions appears to be valid, with KO being found to be more stable than K on the investigated Hägg iron carbide surfaces. With regards to the classical interpretation of potassium as an promoter, based on the results found in this study it appears that regardless of whether potassium is present as K or KO, it still functions as an electron donor. This is consistent with the classical interpretation of potassium's role as a

promoter, where potassium is donates electrons to an adsorbed species strengthening adsorption.

Further investigation into the speciation of potassium on Hägg carbide surfaces is recommended to determine the stability of other potassium species which could possibly be formed at Fischer-Tropsch conditions. The activation energy required for the dissociation of CO when co-adsorbed with K or KO should also be investigated.

## References

Abild-Petersen, F., and M P Andersson (2007), "CO adsorption energies on metals with correction for high coordination adsorption sites – A density functional study" *Surface Science* **601**, 1747-1753.

Aizawa, H., and T. Shinji (1998), "First-principles study of CO bonding to Pt(111): validity of the Blyholder model" *Surface Science,* **399**, L364-L370.

Bell, A. T., and H. Arakawa (1982), "Effects of potassium promotion on the activity and selectivity of iron Fischer-Tropsch catalysts" *Industrial Engineering. Chemical Process Development*, **22**, 97-103.

Bell, A. T., and R. A. Dictor (1986), "A comparison of the activity, selectivity and kinetics of several iron-based Fischer-Tropsch catalysts " *Journal of Catalysis,* **31**, 126-132.

Blignaut, A. (2007), "Influence of basicity in Fischer-Tropsch synthesis over supported iron-based catalysts" Thesis, University of Cape Town

Blöchl, P. E. (1994), "Projector augmented-wave method." *Physical Review B* **50**, 17953.

Bludsky, O., M. Silhan, P. Nachtigall, T. Bucko, L. Benco, and J. Hafner (2005), "Theoretical investigation of CO interaction with copper sites in zeolites: periodic DFT and hybrid quantum mechanical/interatomic potential function study" *Journal of Physical Chemistry B* **109**, 9631-9638.

Born, M., and J. R. Oppenheimer (1927), Translated by Blinder S. M., 2002, "On the quantum theory of molecules" *Annalen der Physik* **84**, 457.

Blyholder, G. (1964), "Molecular orbital view of chemisorbed carbon monoxide" *Journal of Physical Chemistry*, **68**, 2772-2778.

Bonzel, H. P. and H.J. Krebs (1982), "Surface science approach to heterogeneous catalysis: carbon monoxide hydrogenation on transition metals" *Surface Science*, **117**, 1-3.

Bowen, B. H. and M. W. Irwin (2006), "Coal gasification and Fischer-Tropsch CCTR Basic Fact File #1. Technology" (pp. 1-19). Retrieved from http://www.canadiancleanpowercoalition.com/index.php/download_file/-/view/10.

Bromfield, T. C., D. C. Ferre, and J. W. Niemantsverdriet (2005), "A DFT study of the adsorption and dissociation of CO on Fe(100): influence of surface coverage on the nature of accessible adsorption states" *ChemPhysChem*, **6**, 254-260.

References

Bukur, D. B., D. Mukesh and S. A. Pate (1990), "Promoter effects on precipitated Iron catalysts for Fischer-Tropsch synthesis" *Industrial Engineering Chemical Research*, **29**, 194-204.

Cao, D., F. Zhang, Y. Li, and H. Jiao. (2004), "Density Functional Theory study of CO adsorption on $Fe_5C_2$(001), -(100) and -(110) surfaces." *Journal of Physical Chemistry B*, **108**, 9094-9104.

Cao, D., F. Zhang, Y. Li, J. Wang and H. Jiao (2005), "Structures and energies of co-adsorbed CO and $H_2$ on $Fe_5C_2$(001), $Fe_5C_2$(110) and $Fe_5C_2$(100)" *Journal of Physical Chemistry B*, **114**, 10922-10935.

Carter, E. A., and D. E. Jiang (2004), "Adsorption and dissociation of CO on Fe(110) from first principles" *Surface Science*, **570**, 167-177.

Ceelen, N., W. Denier, A. Hille, and G. Materlik (1997), "K adsorption on Fe(100) studied by X-ray standing waves" *Surface Science*, **391**, 59-64.

Chen, Y., D. Cao, Y. Jun, Y. Li, J. Wang, and H. Jiao (2004), "Density Functional Theory study of CO Adsorption on the Fe(111) surface" *Chemical Physics Letters*, **400**, 35-41.

Datye, A K, Y. Jin, L. Mansker, R. Motjope, T. Dlamini and N. J. Coville (2000), "The nature of the active phase in iron Fischer-Tropsch catalysts" *Studies in Surface Science and Catalysis*, **130**, 1139-1144.

David, C. W. (2006), "The tensor of the moment of inertia" *Chemistry Education Materials*, Paper 21 University of Connecticut

Davis, B. H. (2009), "Fischer–Tropsch synthesis: Reaction mechanisms for iron catalysts" *Catalysis Today*, **141**, 25-33.

de Smit, E. D., F. Cinquini, A. M. Beale, O. V. Safonova, W. V. Beek, and P. Sautet (2010), "Stability and reactivity of ε-χ-θ iron carbide catalyst phases in Fischer-Tropsch synthesis: controlling $\mu_c$" *Journal of the American Chemical Soc*iety, **132**, 14928-14941.

Derrouiche, S. P. Gravejat, B. Bassou and D. Bianchi (2007), "Impact of potassium on the heats of adsorption of adsorbed CO species on supported Pt particles by using the AEIR method" *Applied Surface Science*, **253**, 5894-5898.

Dry, M. E. (2002), "The Fischer – Tropsch process: 1950 – 2000" *Catalysis Today*, **71**, 227-241.

References

Dry, M. E. (2004a), “Chapter 7 FT Catalysts”, *Studies in Surface Science and Catalysis,* **152**

Dry, M.E. (2004b), “Fischer-Tropsch technology: Chemical concepts used for engineering purposes” *Studies in Surface Science and Catalysis,* **152**, 211-237.

du Plessis, E. H., J. P. de Villiers and G. J. Kruger (2007), “Re-determination of the crystal structure of x$Fe_5C_2$ Hägg carbide” *Z. Kristallogr.*, **222**, 211-217.

Erley, W. (1981), “Vibrational spectra of CO chemisorbed on Fe(110)” *Journal of Vacuum Science and Technology*, **18**, 472.

Esling, C, H I Faraoun, YD Zhang, and H. Aourag (2006), “Crystalline, electronic and magnetic structures of $Fe_3C$, $Fe_5C_2$ and $Fe_2C$ from first principle calculation” *Journal of Applied Physics* **99**, 1-8.

Faaij, P. C., C. N. Hamelinck and M. R Hardeveld (2002), “Exploration of the possibilities for production of Fischer-Tropsch liquids and power via biomass gasification” *Biomass and Bioenergy*, **23**, 129 - 152.

Faaij, P. C., H. den Uil, C. N. Hamelinck and H. Boerrigter (2004), “Production of FT transportation fuels from biomass; technical options, process analysis and optimisation, and development potential” *Energy*, **29**, 1743-1771.

Föhlisch, A., N. Nyberg, P. Bennich, L. Triguero and J. Hasselström (2000), “The bonding of CO to metal surfaces” *Journal of Chemical Physics*, **112**, 1946.

Gearhart, C. (2008) “David Dennison, the specific heat of hydrogen, and the discovery of nuclear spin: Experimental foundations” *American Physical Society* St. Louis 2008

Gon, A., R. H. Bergmans, A. Brands, W. Ceelen, H. H. Brongersma and C. Creemers (1996), “Substitutional adsorption of K on Fe(100)” *Surface Science*, **350**, 1-10.

Govender, A. (2010),. “Towards a mechanism for the Fischer-Tropsch synthesis on Fe(100) using DFT” PhD thesis, Eindhoven University of Technology

Graf, B., and M. Muhler (2011), “The influence of the potassium promoter on the kinetics and thermodynamics of CO adsorption on a bulk iron catalyst applied in Fischer–Tropsch synthesis: a quantitative adsorption calorimetry, temperature-programmed desorption, and surface hydrogenation study” *Physical Chemistry Chemical Physics,* **13**, 3701-3710.

Hammer, B, L B Hansen, and J K Norskov (1999), "Improved adsorption energetics within density-functional theory using revised Perdew-Burke-Ernzerhof functionals" *Physical Review B* **59**, 7413-7421.

Hirano, T. (1993) *MOPAC Manual* 7th Edition, 71-76.

Hofer, L J E, and E M Cohn (1959), "Saturation magnetizations of iron carbides" *Journal of the American Chemical Society* **81** 1576-1582.

Hohenberg, P., and W. Kohn (1964), "Inhomogeneous electron gas" *Physical Review* **136**, 864.

Huang, G., C. Wang, and J. Wang (2009), "First-principles study of diffusion of Zinc vacancies and interstitials in ZnO" *Solid State Communications* **149**, 199-204.

Huber, K. P. and G. Herzberg (1979), *Molecular spectra and molecular structure IV. constants of diatomic molecules,* Van Nostrand Reinhold Co.

Huff, G. A., and C. N. Satterfield (1984), "Intrinsic kinetics of the Fischer-Tropsch synthesis on a reduced fused-magnetite catalyst" *Industrial and Engineering Chemistry Process Design and Development*, **23**, 696-705.

Huo, C. F., Wu, B. S., Gao, P., Yang, Y., Li, Y. W., and Jiao, H. (2011) "The Mechanism of Potassium Promoter: Enhancing the Stability of Active Surfaces**" *Angewandte Chemie*, **50**, 7403-7406.

Iglesia, E., S. Li, A. Li and S. Krishnamoorthy (2001), "Effects of Zn, Cu, and K promoters on the structure and on the reduction, carburization, and catalytic behaviour of iron-based Fischer–Tropsch synthesis catalysts" *Catalysis Letters*, **77**, 197-205.

Janbroers, S., J. N. Louwen, H. W. Zandbergen and P. J. Kooyman (2009), "Insights into the nature of iron-based Fischer–Tropsch catalysts from quasi in situ TEM-EELS and XRD" *Journal of Catalysis*, **268**, 235-242.

Jenkins, S. J., and D. A. King (2000), "Adsorbate/substrate bonding in Co(1010)/K-c(2x2) elucidated through first-principles theory" *Chemical Physics Letters*, **317**, 372-380.

Jin, Y., and A. K. Datye (2000), "Phase transformations in iron Fischer–Tropsch catalysts during temperature-programmed reduction" *Journal of Catalysis*, **17**, 8-17.

Kohn, W., and L. J. Sham (1965), "Quantum density oscillations in an inhomogeneous electron Gas" *Physical Review* **137**, 1697.

Kresse, G, and J Furthmuller (1996), "Efficient iterative schemes for *ab initio* total-energy calculations using a plane-wave basis set" *Physical Review B* **54**, 11169.

Kresse, G, and D Joubert (1999), "From ultrasoft pseudopotentials to the projector augmented-wave method" *Physical Review B* **59**, 11-19.

Lee, C., W. Yang, and R. Parr (1988), "Development of the Colle-Salvetti correlation-energy formula into a functional of the electron density" *Physical Review B* **37**, 785-789.

Liao, X., D. Cao, S. Wang, Z. Ma, Y. Li and J. Wang and H. Jiao (2007), "Density functional theory study of CO adsorption on the (100), (001) and (010) surfaces of $Fe_3C$" *Journal of Molecular Catalysis*, **269**, 169-178.

Lide, D. R. (2009), *CRC Handbook of Chemistry and Physics* CRC Press/Taylor and Francis, Boca Raton, 89$^{th}$ ed.

Liu, Z., and P. Hu, (2001), "An insight into alkali promotion: a density functional theory study of CO dissociation on K/Rh(111)" *Journal of the American Chemical Society*, **123**, 12596-12604.

Ma, W., E. L. Kugler and D. B. Dadyburjor (2007), "Potassium effects on activated-carbon-supported iron catalysts for Fischer-Tropsch synthesis" *Energy and Fuels*, **18**, 1832-1842.

Maclaren, J. M., D. D. Vvedensky, J. B. Pendry and R. W. Joyner (1987), "Catalytic implications of local electronic interactions between Carbon Monoxide and co-adsorbed promoters on nickel surfaces" *Journal of the Chemical Soc*iety, **83**, 1945-1962.

Methfessel, M., and A. T. Paxton (1989), "High-precision sampling for Brillouin-zone integration in metals" *Physical Review B* **40**, 3616.

Monkhorst, H. J., and J. D. Pack (1976), "Special points for Brillouin-zone integrations" *Physical Review B* **13**, 5188.

Moon, D. W., S. L. Bernasek, D. J. Dwyer and J. L. Gland (1985), "Observation of an unusually low CO stretching frequency on Fe(100)" *Journal of the American Chemistry Society,* **1985**, *107*, 4363.

Motjope, T., H. Dlamini, G. Joorst, G. Stege, and M. Mdleleni (2002), "Changes in physico-chemical properties of iron-based Fischer-Tropsch catalyst induced by $SiO_2$ addition" *Catalysis Letters*, **78**, 201.

Nayak, S. K., M. Nooijen, S. L. Bernasek and P. Blaha (2001), "Electronic Structure Study of CO Adsorption on the Fe (001) Surface" *Journal of Physical Chemistry B*, **105**, 164-172.

Orita, H., N. Itoh, and Y. Inada (2004), "All electron scalar relativistic calculations on adsorption of CO on Pt(111) with full geometry optimization: a correct estimation for CO Site-preference" *Chemical Physics Letters* **384**, 271-276.

Perdew, J, J. Chevary, S. Vosko, K. Jackson, M. Pederson, D. Singh, and C. Fiolhais (1992), "Atoms, molecules, solids, and surfaces: applications of the generalized gradient approximation for exchange and correlation" *Physical Review B* **46**, 6671.

Perdew, JP, K. Burke, and M. Ernzerhof (1996), "Generalized gradient approximation made simple" *Physical Review Letters*, **77**, 3865-3868.

Petersen, M. A., J. A. van den Berg and W. J. van Rensburg (2010), "Role of step sites and surface vacancies in the adsorption and activation of CO on $\chi$-$Fe_5C_2$ Surfaces" *Journal of Physical Chemistry C,***114**, 7863-7879.

Pirola, C., C. L. Bianchi, A. Di Michele, S. Vitali and V. Ragaini (2009, "Fischer Tropsch and Water Gas Shift chemical regimes on supported iron-based catalysts at high metal loading" *Catalysis Communications* **10**, 823-327

Pistonesi, C., M. E. Pronsato, L. Bugyi and A. Juan (2011), "The adsorption of CO on potassium doped molybdenum carbide surface: An ab-initio study" *Catalysis Today*. **181**, 102-107.

Prytz, Ø, and E Flage-Larsen (2010), "The influence of exact exchange corrections in van Der Waals layered narrow bandgap black phosphorus" *Journal of Physics: Condensed Matter* **22**, 015502.

Retief, J. (1999), "Powder diffraction data and Rietveld refinement of Hägg carbide, $\chi$-$Fe_5C_2$" *Powder Diffr*action, **14**, 130-132.

Singh, D., W. E. Pickett, and H. Krakauer (1991), "Gradient-corrected density functionals: full-potential calculations for iron" *Physical Review B* **43**: 628-634.

Shroff, M. D., D. S. Kalakkad, K. E. Coulter, S. D. Kohler, M. S. Harrington, N. B. Jackson, A. G. Sault and A. K. Datye (1995), "Activation of precipitated iron Fischer-Tropsch synthesis catalysts" *Journal of Catalysis*, **156**, 185-207.

Somorjai, A., E. L. Garfunkel and J. E. Crowell (1982), "The strong influence of potassium on the adsorption of CO on platinum surfaces. A thermal desorption spectroscopy and high-

resolution electron energy loss spectroscopy study" *Journal of Physical Chem*istry, **86**, 310-313.

Sorescu, D. C. (2009), "Plane-wave density functional theory investigations of the adsorption and activation of CO on $Fe_5C_2$ surfaces" *Journal of Physical Chemistry C,* **113**, 9256-9274.

Sorescu, D. C. (2011), "Surface science adsorption and activation of CO co-adsorbed with K on Fe (100) surface: A plane-wave DFT study" *Surface Science*, **605**, 401-414.

Sorescu, D. C., D. L. Thompson, M. M. Hurley and C. F. Chabalowski (2002), "First-principles calculations of the adsorption, diffusion, and dissociation of a CO molecule on the Fe(100) surface" *Physical Review B*, **66.**

Steynberg, P J, J. van der Berg, and W.J. van Rensburg (2008), "Bulk and surface analysis of Hägg Fe Carbide ($Fe_5C_2$): a density functional theory study" *Journal of Physics: Condensed Matter* **20**, 064238.

Stroppa, A., and G Kresse (2008), "The shortcomings of semi-local and hybrid Functionals: what we can learn from surface science studies" *New Journal of Physics* **10**, 063020.

Stibor, A., G. Kresse, A. Eichler and J. Hafner (2002), "Density functional study of the adsorption of CO on Fe (110)" *Surface Science*, **510**, 99-102.

Sung, S., R. Hoffmann (1985), "How carbon monoxide bonds to metal surfaces" *Journal of the American Chemistry Society*, **107**, 578-584.

van Berge, P. J. (1997), "Cobalt as an alternative Fischer-Tropsch catalyst to iron for the production of middle distillates" *Studies in Surface Science and Catalysis*, **107**, 207.

van der Laan, G. P. (1999), "Kinetics, selectivity and scale-up of the Fischer-Tropsch synthesis", PhD. Thesis, Univiersity of Groningen

van Steen, E. and M. Claeys. (2008). "Fischer-Tropsch catalysts for the biomass-to- liquid process." *Chemical Engineering and Technology*, **2**, 1-13.

Wilke, S., M. Cohen (1997), "Influence of potassium adatoms on the dissociative adsorption of hydrogen on Pd(100)" *Surface Science Letters*, **380**, 446-454.

Wang, C., B. Klein, and H. Krakauer (1985), "Theory of magnetic and structural ordering in iron." *Physical Review Letters* **54**, 1852-1855.

Yang, Y., H. Xiang, Y. Xu, L. Bai and Y. Li (2004), "Effect of potassium promoter on precipitated iron-manganese catalyst for Fischer-Tropsch synthesis" *Applied Catalysis A: General*, **266**, 181-194.

Yates, I. and C. Satterfield (1991), "Intrinsic kinetics of the Fischer-Tropsch synthesis on a cobalt catalyst" *Energy and Fuels*, **5**, 168-173.

Zhao, Y., Garcia, N. and Truhlar, D. (2005), "Benchmark Database of Barrier Heights for Heavy Atom Transfer, Nucleophilic Substitution, Association, and Unimolecular Reactions and Its Use to Test Theoretical Methods" *Journal of Physical Chemistry A*, **109**, 2012-2018

Zhang, A. H., J. Zhu and W. H. Duan (2006), "Co-adsorption of potassium and carbon monoxide on Ni(111): A density functional theory study" *Physical Review B*, **74**, 045425

# Appendices

## Appendix A - k-Point Convergence tests with PBE and PW91 functionals

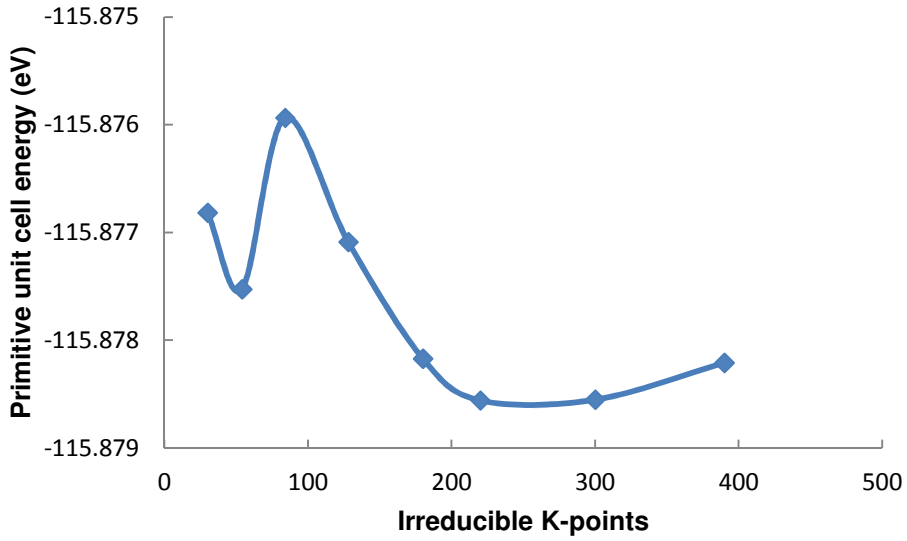


**Figure A.10:** k-point convergence (PBE) for bulk Hägg carbide. (Calculated using the PBE functional, σ = 0.2eV and a cutoff energy of 520eV)

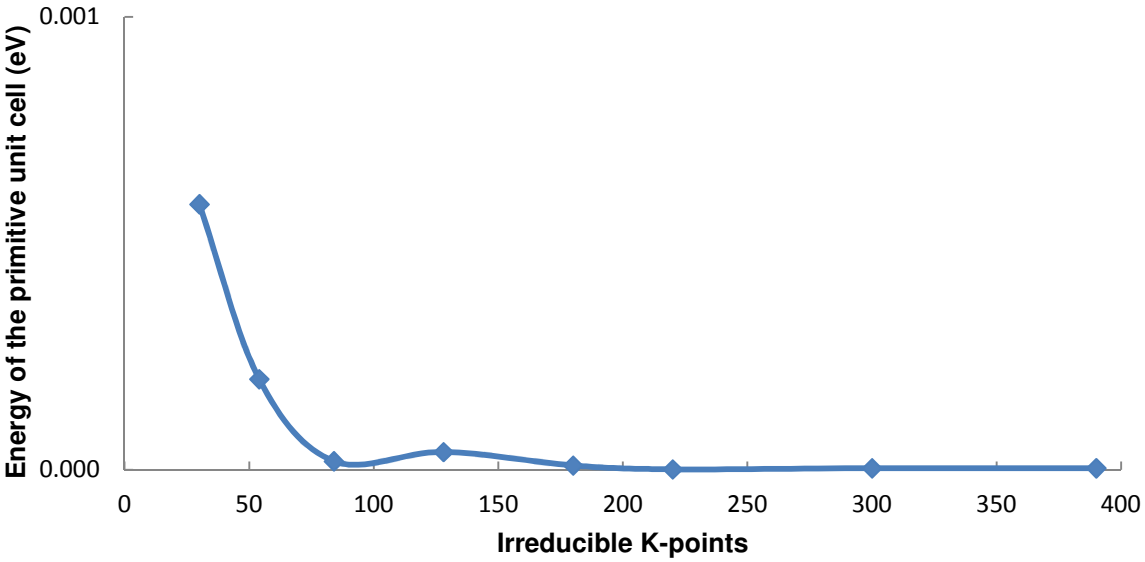


**Figure A.11:** k-point convergence (PW91) for bulk Hägg carbide. (Calculated using the PW91 functional, σ = 0.2eV and a cutoff energy of 520eV)

## Appendix B - LDOS plots for K, KO and O adsorption on the $Fe_5C_2(100)_{0.00}$ and $Fe_5C_2(100)_{0.098}$ surfaces

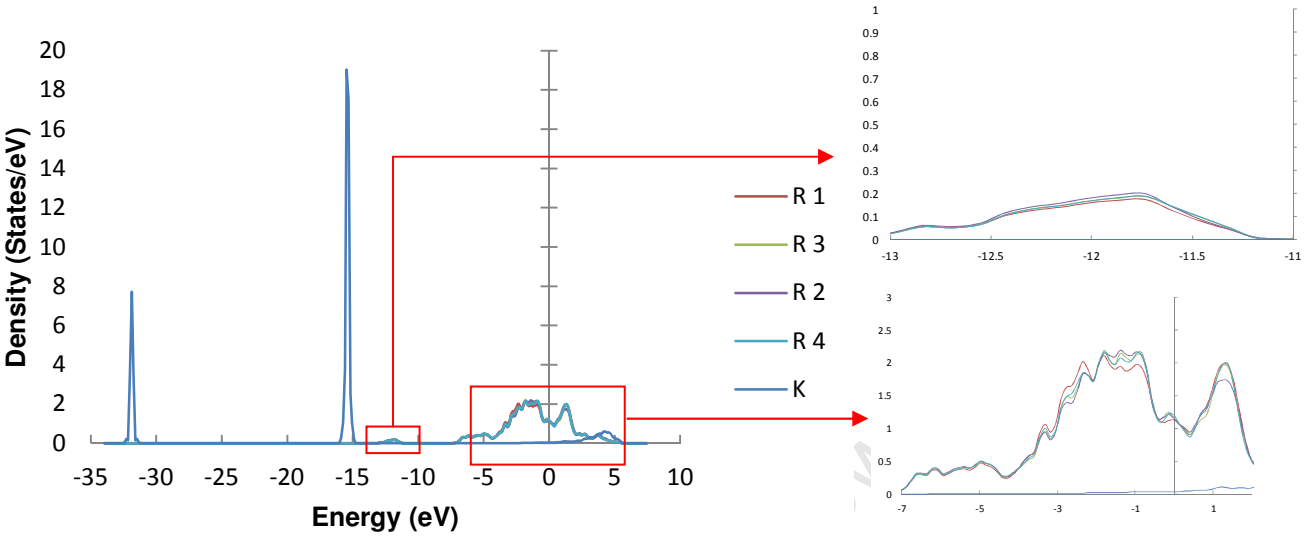


**Figure A.12:** LDOS plot showing the DOS of the ridge iron atoms and the potassium adsorbate for K adsorption on the $Fe_5C_2(100)_{0.00}$ surface. (Calculated using RPBE functional, σ=0.2eV, k-point mesh of 3 × 5 × 1, vacuum spacing of 20Å and a cutoff energy of 450eV)

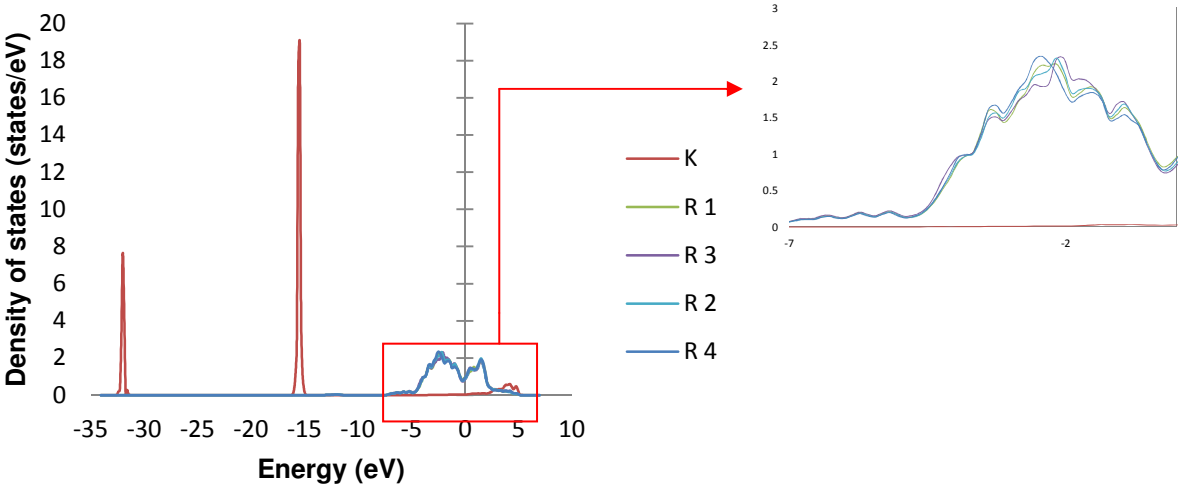


**Figure A.13:** LDOS plot showing the DOS of the ridge iron atoms and the potassium adsorbate for K adsorption on the $Fe_5C_2(100)_{0.098}$ surface. (Calculated using RPBE functional, σ=0.2eV, k-point mesh of 3 × 5 × 1, vacuum spacing of 20Å and a cutoff energy of 450eV)

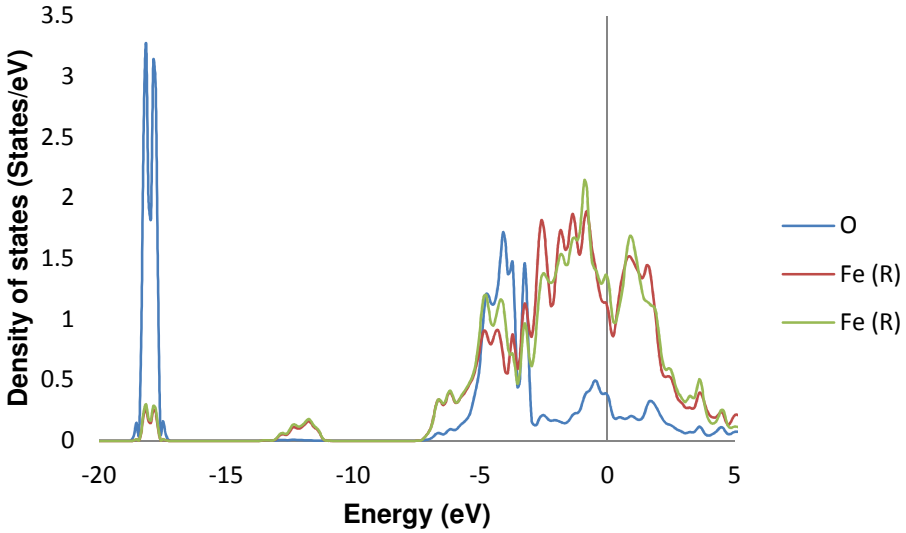


**Figure A.14:** LDOS plot showing the DOS of O and the ridge iron atoms bonded to the O for O adsorption on the $Fe_5C_2(100)_{0.00}$ surface. (Calculated using RPBE functional, σ=0.2eV, k-point mesh of 3 × 5 × 1, vacuum spacing of 20Å and a cutoff energy of 450eV)

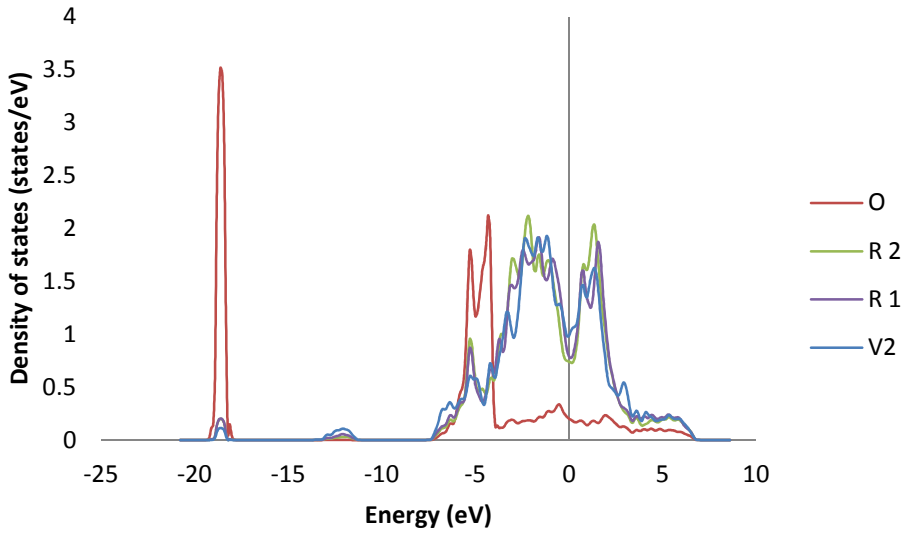


**Figure A.15:** LDOS plot showing the DOS of O and the ridge iron atoms bonded to the O for O adsorption on the $Fe_5C_2(100)_{0.098}$ surface. (Calculated using RPBE functional, σ=0.2eV, k-point mesh of 3 × 5 × 1, vacuum spacing of 20Å and a cutoff energy of 450eV)

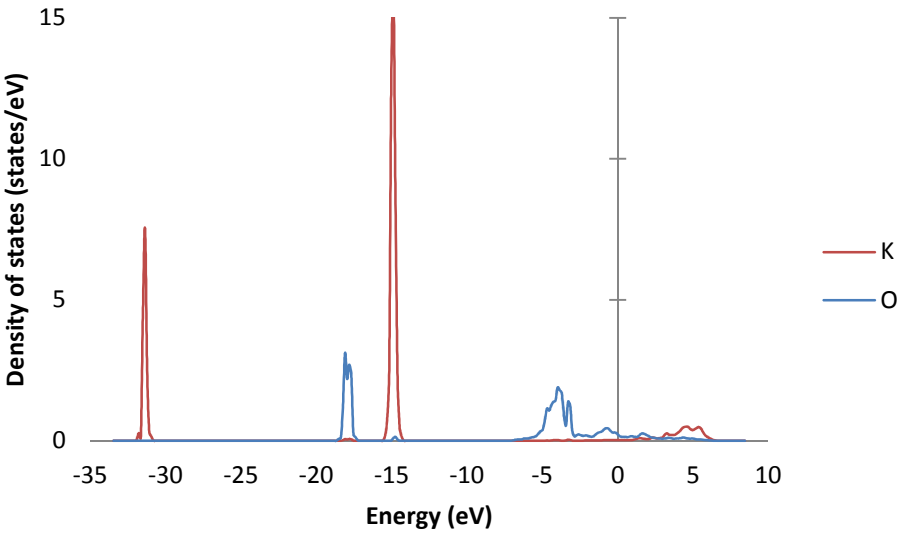


**Figure A.16:** LDOS plot showing the DOS of K and O when co-adsorbed on the $Fe_5C_2(100)_{0.00}$ surface. (Calculated using RPBE functional, σ=0.2eV, k-point mesh of 3 × 5 × 1, vacuum spacing of 20Å and a cutoff energy of 450eV)

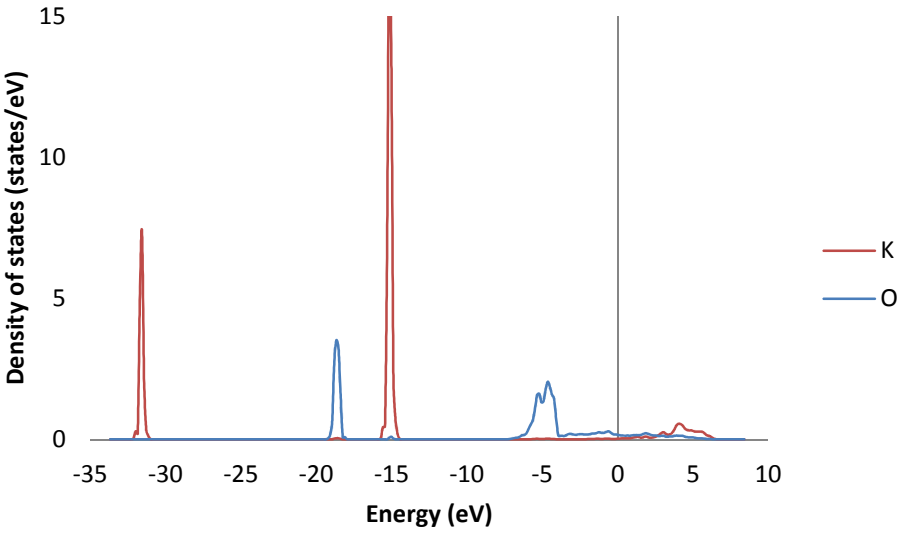


**Figure A.17:** LDOS plot showing the DOS of K and O when co-adsorbed on the $Fe_5C_2(100)_{0.098}$ surface. (Calculated using RPBE functional, σ=0.2eV, k-point mesh of 3 × 5 × 1, vacuum spacing of 20Å and a cutoff energy of 450eV)

## Appendix C - LDOS plots for CO adsorption and co-adsorption

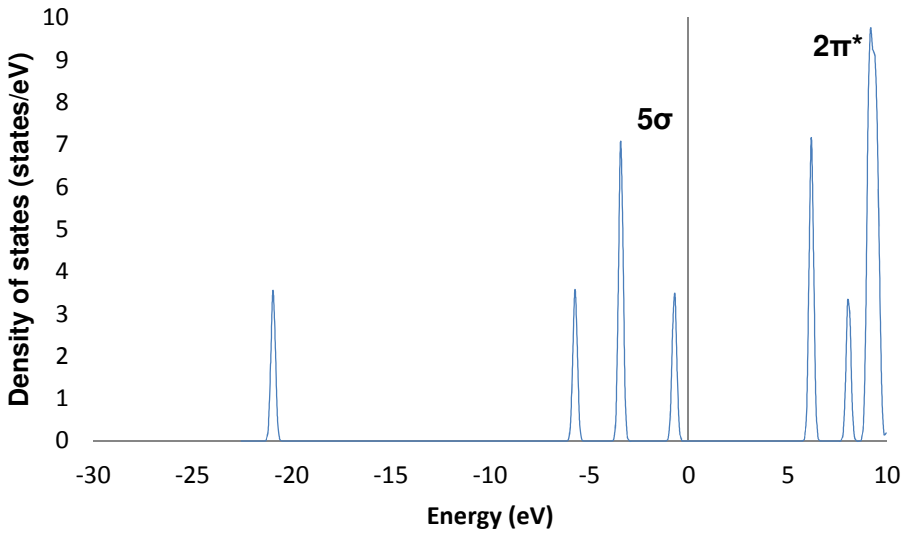


**Figure A.18:** LDOS of gas phase CO (Calculated using RPBE functional, σ=0.2eV, k-point mesh of 3 × 5 × 1 and a cutoff energy of 450eV)

### Appendix C.1 - LDOS plots of CO for CO adsorptions and co-adsorptions on the $Fe_5C_2(100)_{0.00}$ surface

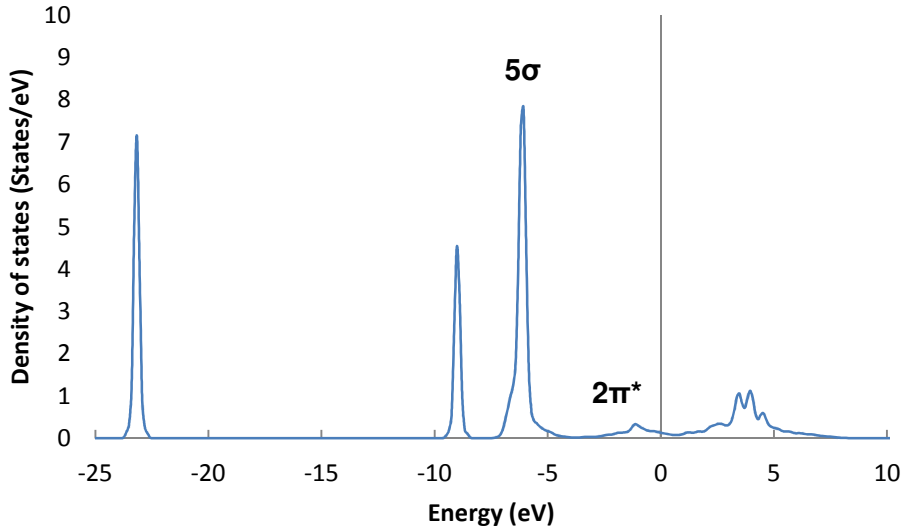


**Figure A.19:** LDOS of CO adsorbed in the 1F CO adsorption configuration on the $Fe_5C_2(100)_{0.00}$ surface (Calculated using RPBE functional, σ=0.2eV, k-point mesh of 3 × 5 × 1, vacuum spacing of 20Å and a cutoff energy of 450eV)

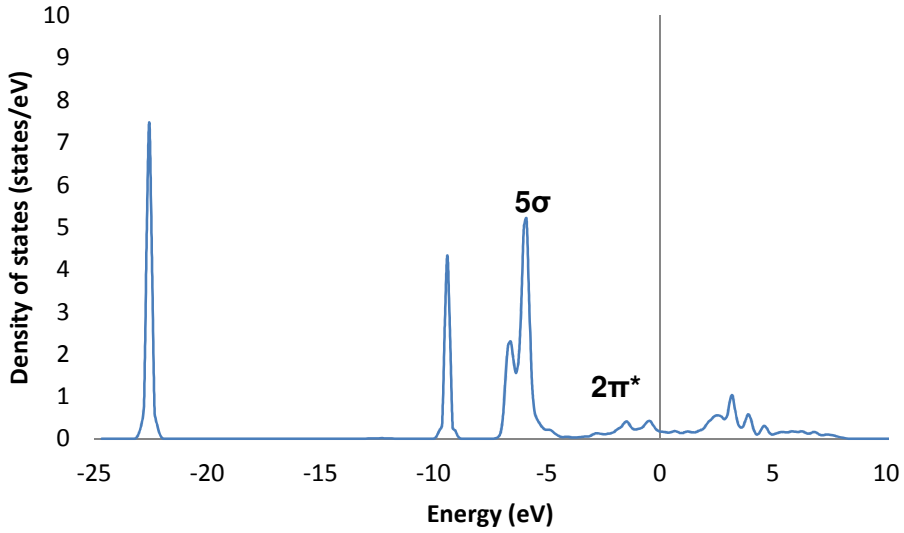


**Figure A.20:** LDOS of CO adsorbed 3F CO adsorption configuration on the threefold hollow site with the subsurface iron on the $Fe_5C_2(100)_{0.00}$ surface (Calculated using RPBE functional, σ=0.2eV, k-point mesh of 3 × 5 × 1, vacuum spacing of 20Å and a cutoff energy of 450eV)

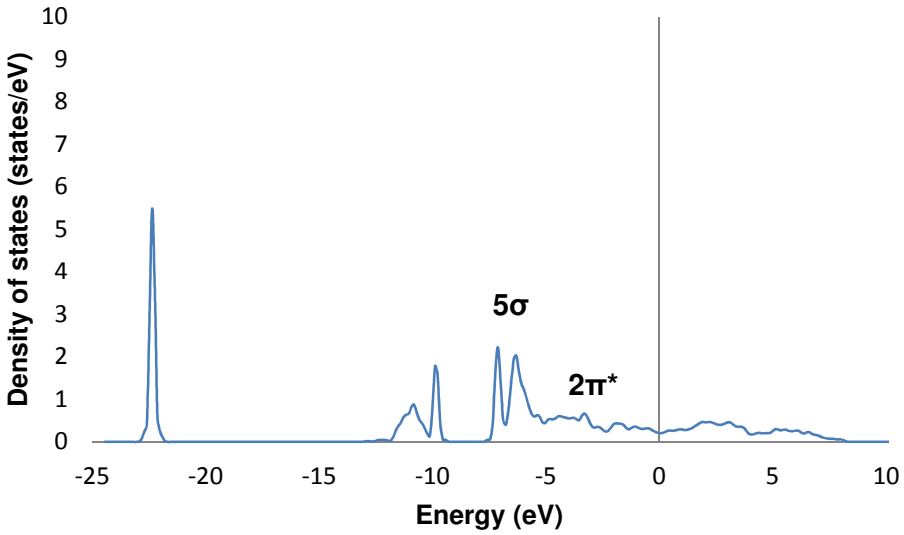


**Figure A.21:** LDOS of CO adsorbed in the 3F CO adsorption configuration on the threefold hollow site with the subsurface carbon on the $Fe_5C_2(100)_{0.00}$ surface (Calculated using RPBE functional, σ=0.2eV, k-point mesh of 3 × 5 × 1, vacuum spacing of 20Å and a cutoff energy of 450eV)

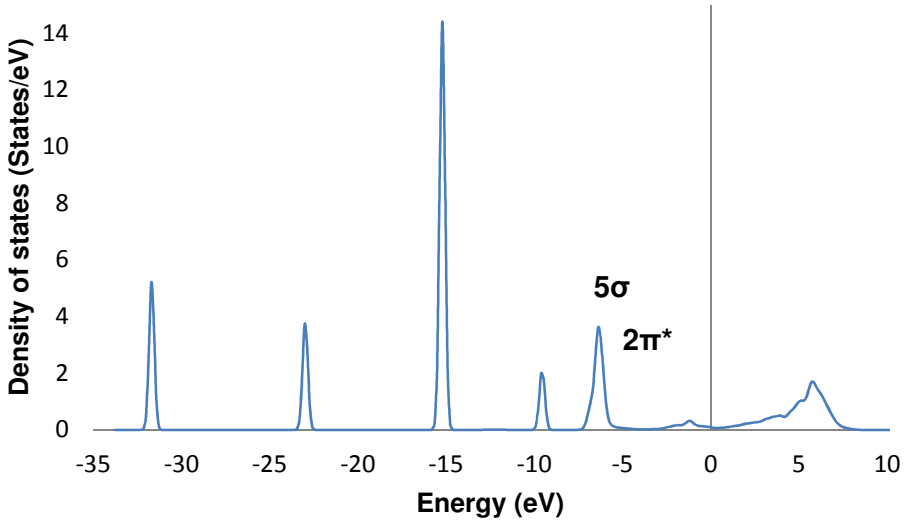


**Figure A.22:** LDOS of CO when co-adsorbed with K on the $Fe_5C_2(100)_{0.00}$ surface. CO in the 1F CO adsorption configuration. (Calculated using RPBE functional, σ=0.2eV, k-point mesh of 3 × 5 × 1, vacuum spacing of 20Å and a cutoff energy of 450eV)

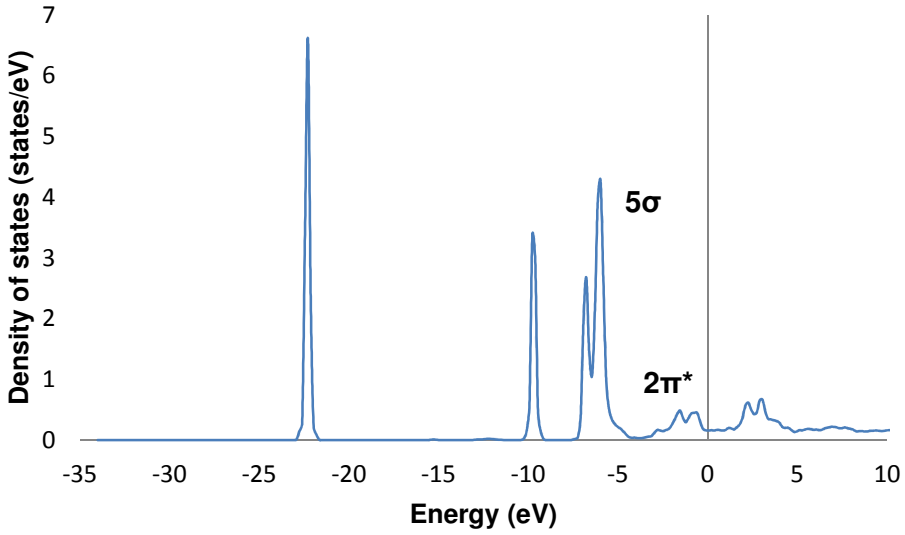


**Figure A.23:** LDOS of CO when co-adsorbed with K on the $Fe_5C_2(100)_{0.00}$ surface. CO in the 2F adsorption configuration. (Calculated using RPBE functional, σ=0.2eV, k-point mesh of 3 × 5 × 1, vacuum spacing of 20Å and a cutoff energy of 450eV)

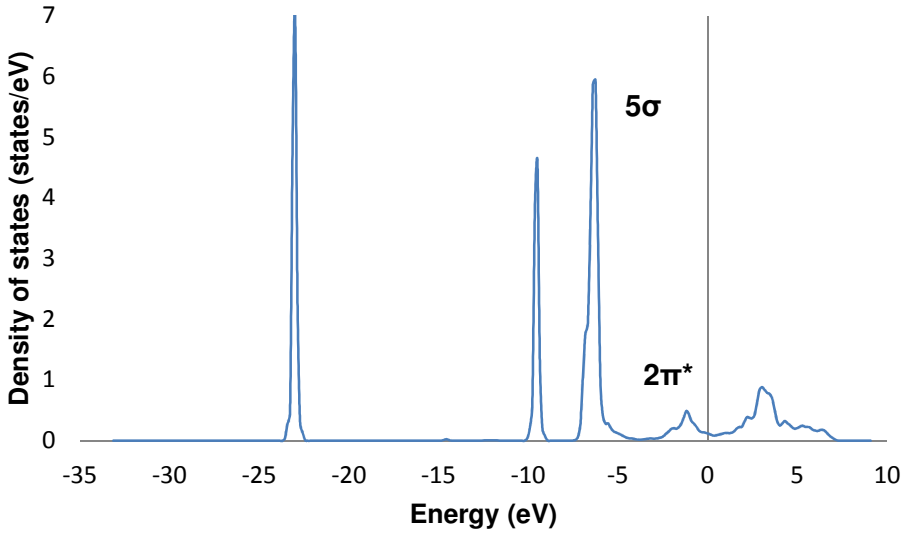


**Figure A.24:** LDOS of CO when co-adsorbed with KO on the $Fe_5C_2(100)_{0.00}$ surface. CO in the 1F ridge adsorption configuration. (Calculated using RPBE functional, σ=0.2eV, k-point mesh of 3 × 5 × 1, vacuum spacing of 20Å and a cutoff energy of 450eV)

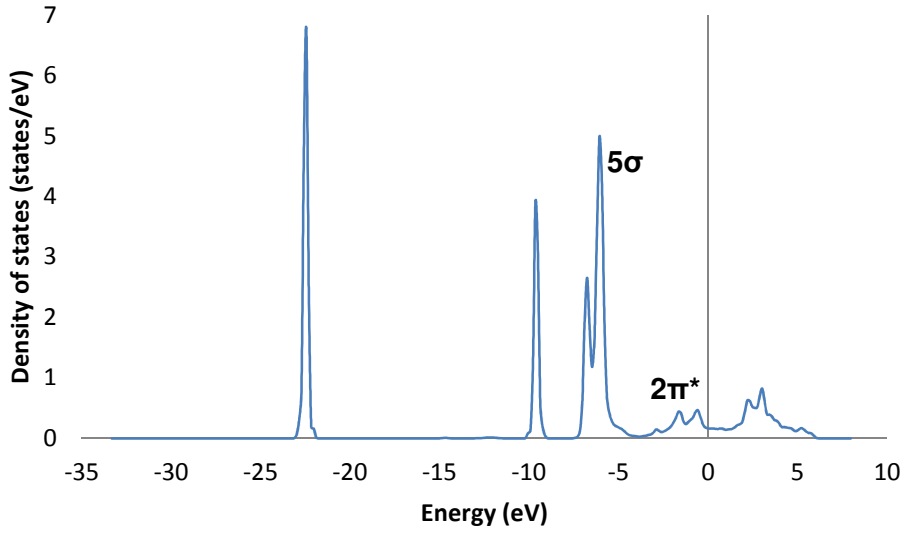


**Figure A.25:** LDOS of CO when co-adsorbed with KO on the $Fe_5C_2(100)_{0.00}$ surface. CO in the 2F CO adsorption configuration. (Calculated using RPBE functional, σ=0.2eV, k-point mesh of 3 × 5 × 1, vacuum spacing of 20Å and a cutoff energy of 450eV)

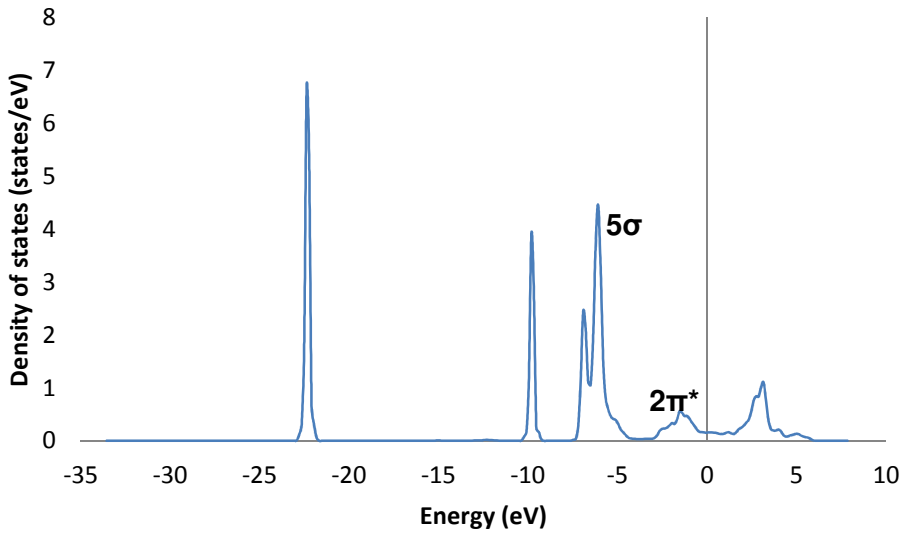


**Figure A.26:** LDOS of CO when co-adsorbed with KO on the $Fe_5C_2(100)_{0.00}$ surface. CO in the 1F valley CO adsorption configuration. (Calculated using RPBE functional, σ=0.2eV, k-point mesh of 3 × 5 × 1, vacuum spacing of 20Å and a cutoff energy of 450eV)



## Appendix C.2 – LDOS plots of CO for adsorptions and co-adsorptions on the $Fe_5C_2(100)_{0.098}$ surface

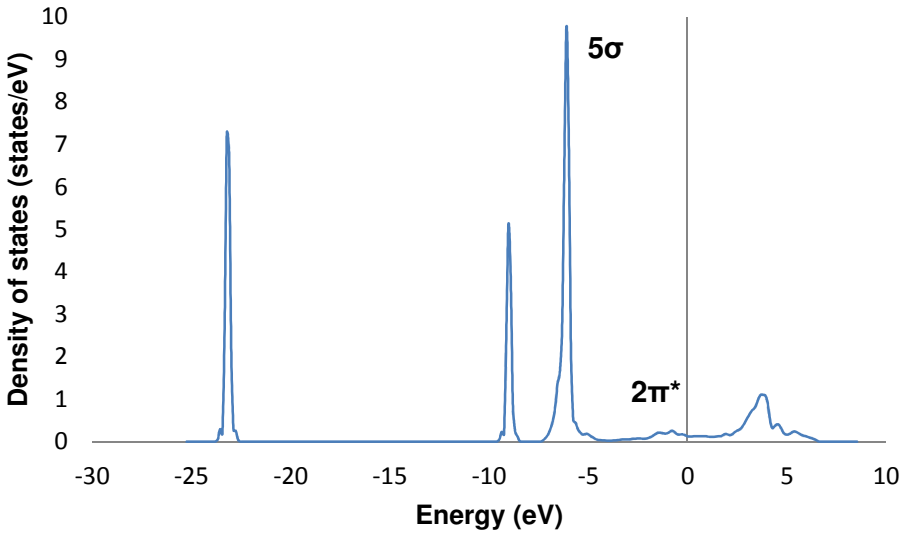


**Figure A.27:** LDOS of CO when adsorbed in the 1F ridge adsorption configuration on the $Fe_5C_2(100)_{0.098}$ surface. (Calculated using RPBE functional, σ=0.2eV, k-point mesh of 3 × 5 × 1, vacuum spacing of 20Å and a cutoff energy of 450eV)

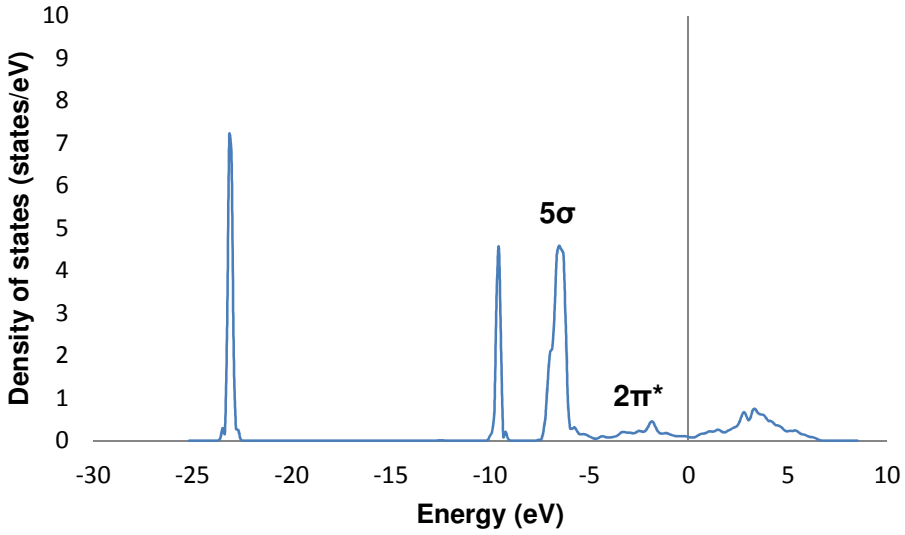


**Figure A.28:** LDOS of CO when adsorbed in the 1F valley adsorption configuration on the $Fe_5C_2(100)_{0.098}$ surface. (Calculated using RPBE functional, σ=0.2eV, k-point mesh of 3 × 5 × 1, vacuum spacing of 20Å and a cutoff energy of 450eV)

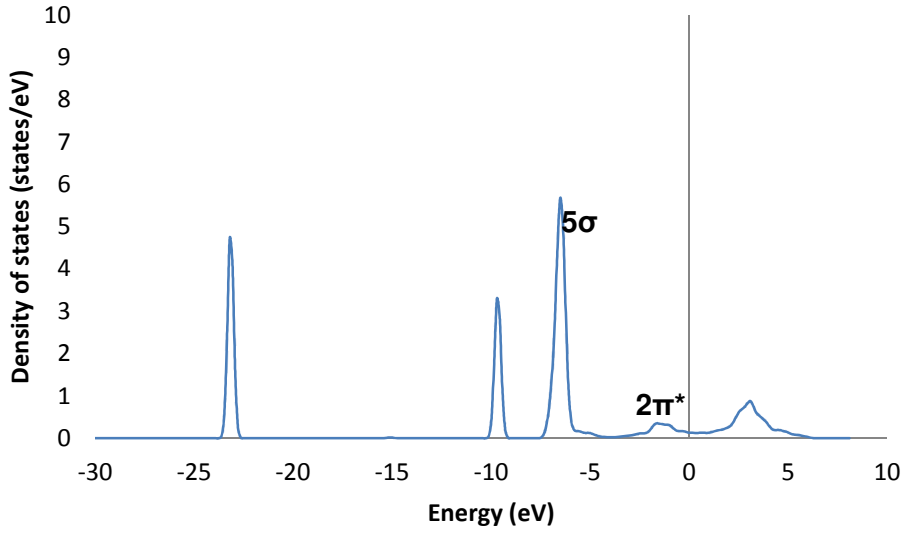


**Figure A.29:** LDOS of CO when co-adsorbed with K on the $Fe_5C_2(100)_{0.098}$ surface. CO in the 1F ridge adsorption configuration. (Calculated using RPBE functional, σ=0.2eV, k-point mesh of 3 × 5 × 1, vacuum spacing of 20Å and a cutoff energy of 450eV)

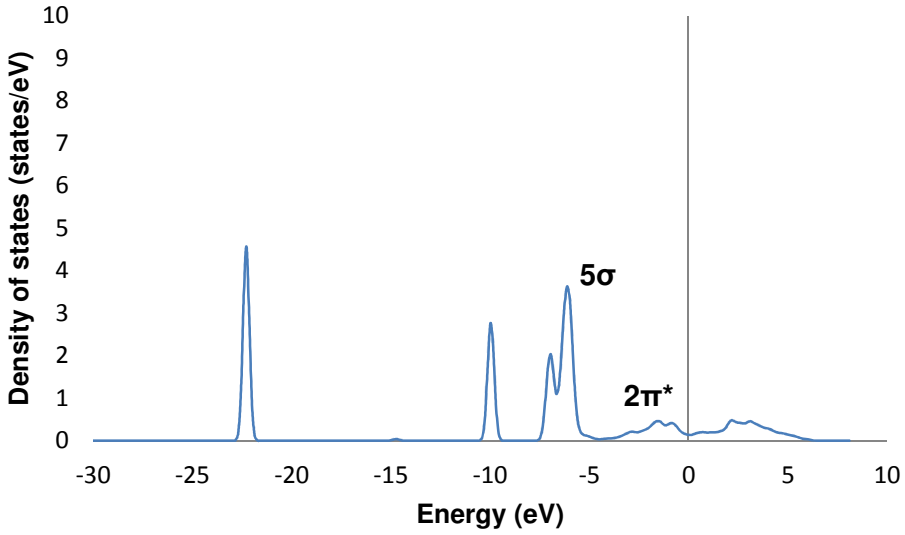


**Figure A.30:** LDOS of CO when co-adsorbed with K on the $Fe_5C_2(100)_{0.098}$ surface. CO in the 2F adsorption configuration. (Calculated using RPBE functional, σ=0.2eV, k-point mesh of 3 × 5 × 1, vacuum spacing of 20Å and a cutoff energy of 450eV)

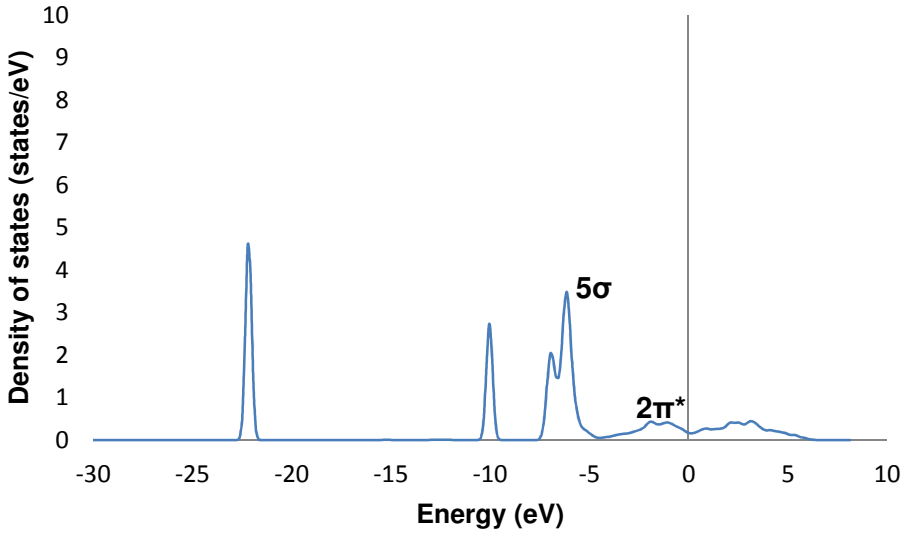


**Figure A.31:** LDOS of CO when co-adsorbed with K on the $Fe_5C_2(100)_{0.098}$ surface. CO in the 3F adsorption configuration. (Calculated using RPBE functional, σ=0.2eV, k-point mesh of 3 × 5 × 1, vacuum spacing of 20Å and a cutoff energy of 450eV)

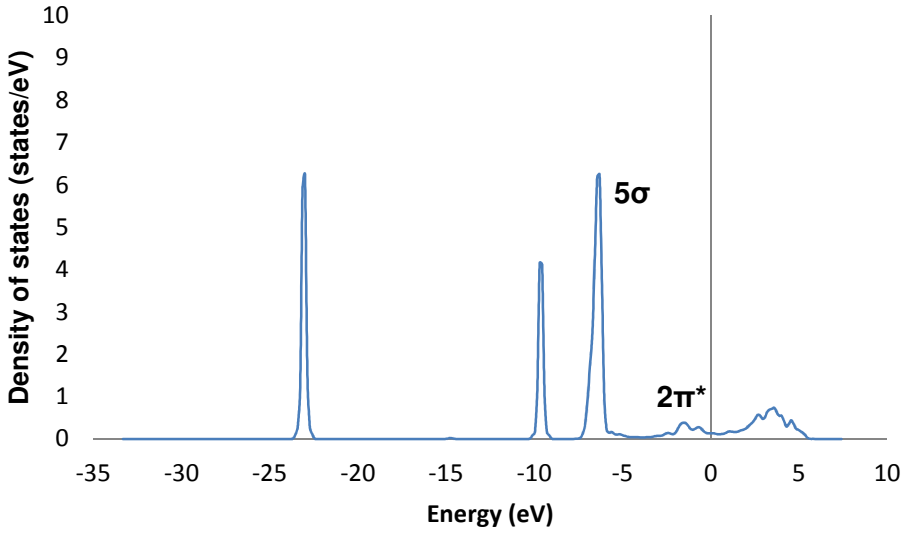


**Figure A.32:** LDOS of CO when co-adsorbed with KO on the $Fe_5C_2(100)_{0.098}$ surface. CO in the 1F ridge adsorption configuration. (Calculated using RPBE functional, σ=0.2eV, k-point mesh of 3 × 5 × 1, vacuum spacing of 20Å and a cutoff energy of 450eV)

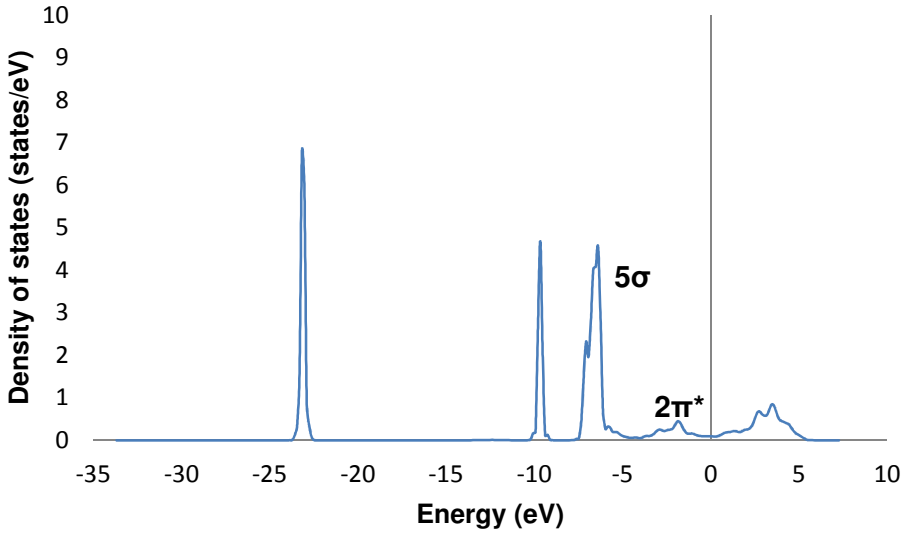


**Figure A.33:** LDOS of CO when co-adsorbed with KO on the $Fe_5C_2(100)_{0.098}$ surface. CO in the 1F valley adsorption configuration. (Calculated using RPBE functional, σ=0.2eV, k-point mesh of 3 × 5 × 1, vacuum spacing of 20Å and a cutoff energy of 450eV)

## Appendix C.4 - LDOS plots of O (on CO) and K states for co-adsorptions on the Fe$_5$C$_2$(100)$_{0.00}$ and the Fe$_5$C$_2$(100)$_{0.098}$ surfaces

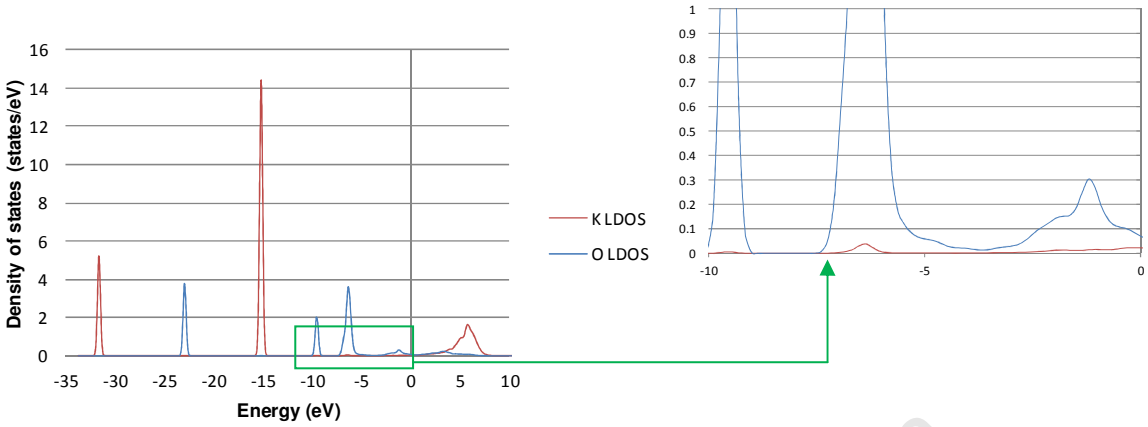


**Figure A.34:** LDOS of K and O (of CO) when CO is adsorbed in the 1F CO adsorption configuration for CO co-adsorption with K on the Fe$_5$C$_2$(100)$_{0.00}$ surface (Calculated using RPBE functional, σ=0.2eV, k-point mesh of 3 × 5 × 1, vacuum spacing of 20Å and a cutoff energy of 450eV)

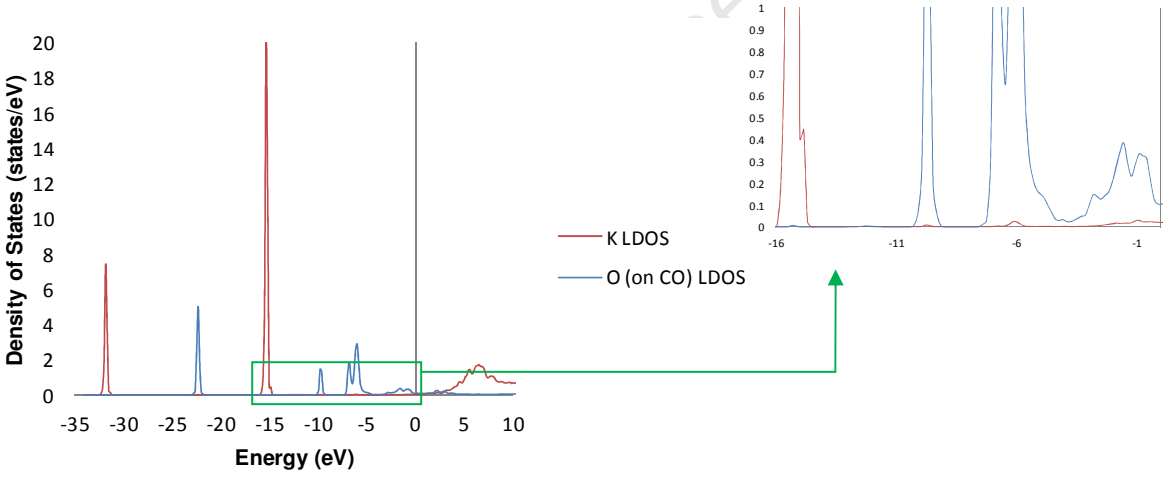


**Figure A.35:** LDOS of K and O (of CO) when CO is adsorbed in the 2F CO adsorption configuration for CO co-adsorption with K on the Fe$_5$C$_2$(100)$_{0.00}$ surface (Calculated using RPBE functional, σ=0.2eV, k-point mesh of 3 × 5 × 1, vacuum spacing of 20Å and a cutoff energy of 450eV)

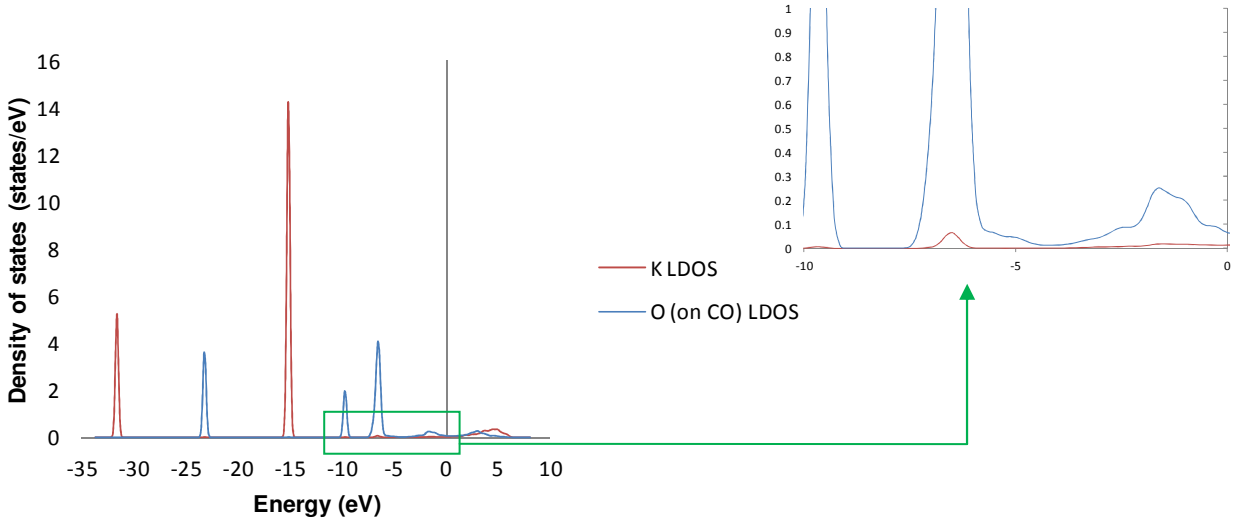


**Figure A.36:** LDOS of K and O (of CO) when CO is adsorbed in the 1F ridge CO adsorption configuration for CO co-adsorption with K on the $Fe_5C_2(100)_{0.098}$ surface (Calculated using RPBE functional, σ=0.2eV, k-point mesh of 3 × 5 × 1, vacuum spacing of 20Å and a cutoff energy of 450eV)

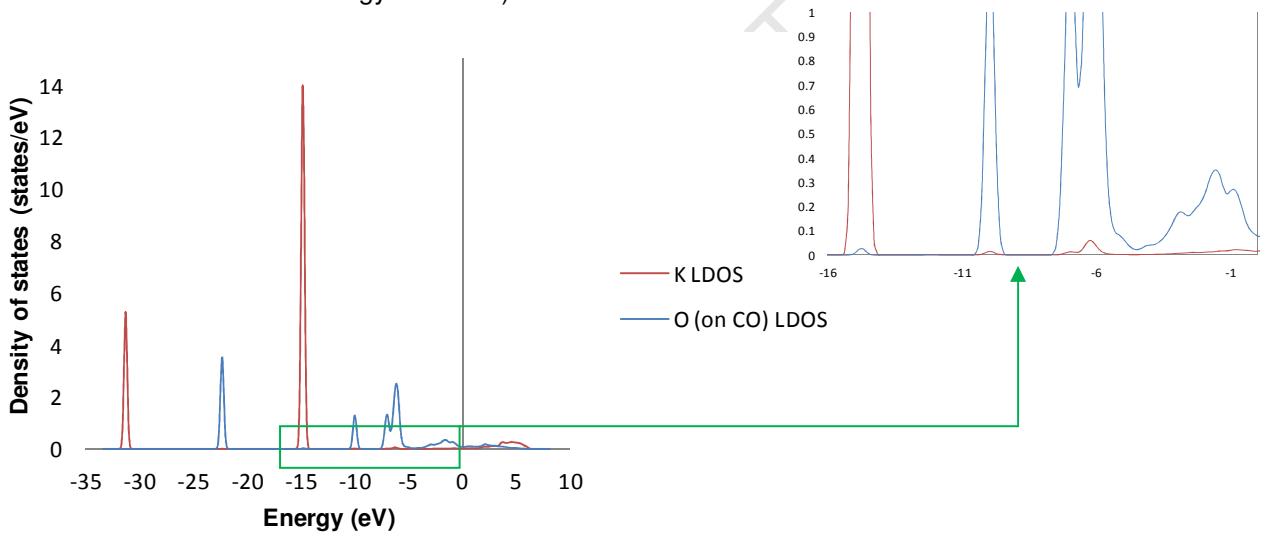


**Figure A.37:** LDOS of K and O (of CO) when CO is adsorbed in the 2F ridge CO adsorption configuration for CO co-adsorption with K on the $Fe_5C_2(100)_{0.098}$ surface (Calculated using RPBE functional, σ=0.2eV, k-point mesh of 3 × 5 × 1, vacuum spacing of 20Å and a cutoff energy of 450eV)

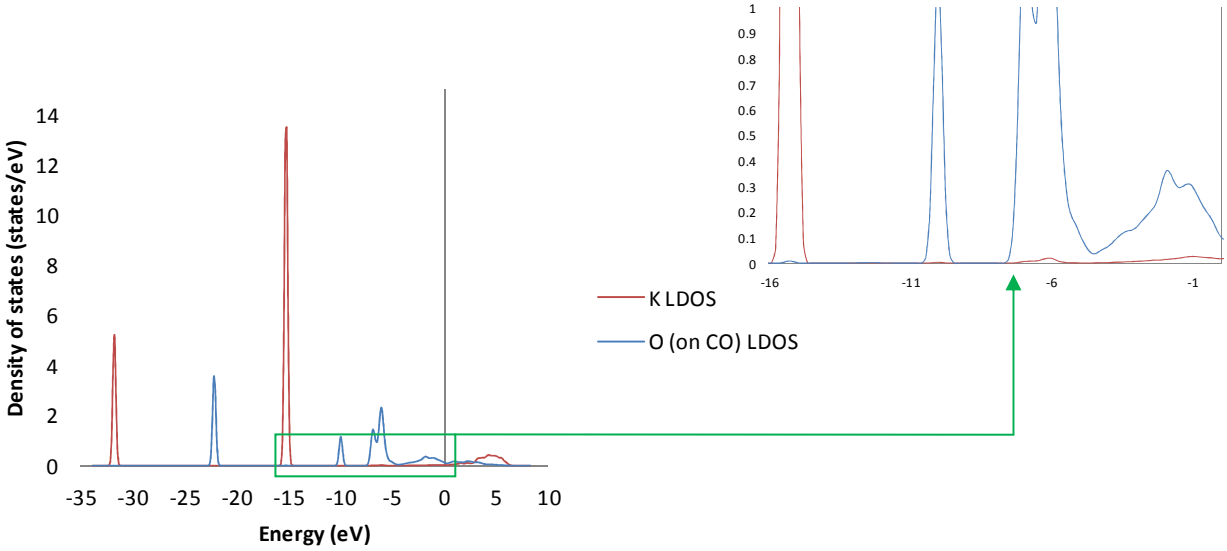


**Figure A.38:** LDOS of K and O (of CO) when CO is adsorbed in the 3F ridge CO adsorption configuration for CO co-adsorption with K on the $Fe_5C_2(100)_{0.098}$ surface (Calculated using RPBE functional, σ=0.2eV, k-point mesh of 3 × 5 × 1, vacuum spacing of 20Å and a cutoff energy of 450eV)

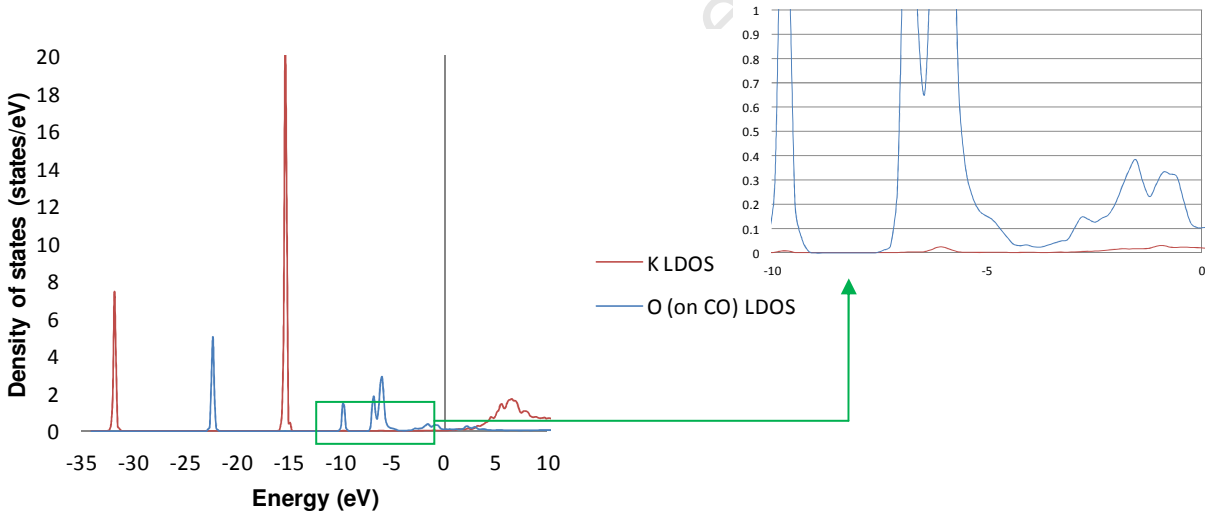


**Figure A.39:** LDOS of K and O (of CO) when CO is adsorbed in the 1F ridge CO adsorption configuration for CO co-adsorption with KO on the $Fe_5C_2(100)_{0.00}$ surface (Calculated using RPBE functional, σ=0.2eV, k-point mesh of 3 × 5 × 1, vacuum spacing of 20Å and a cutoff energy of 450eV)

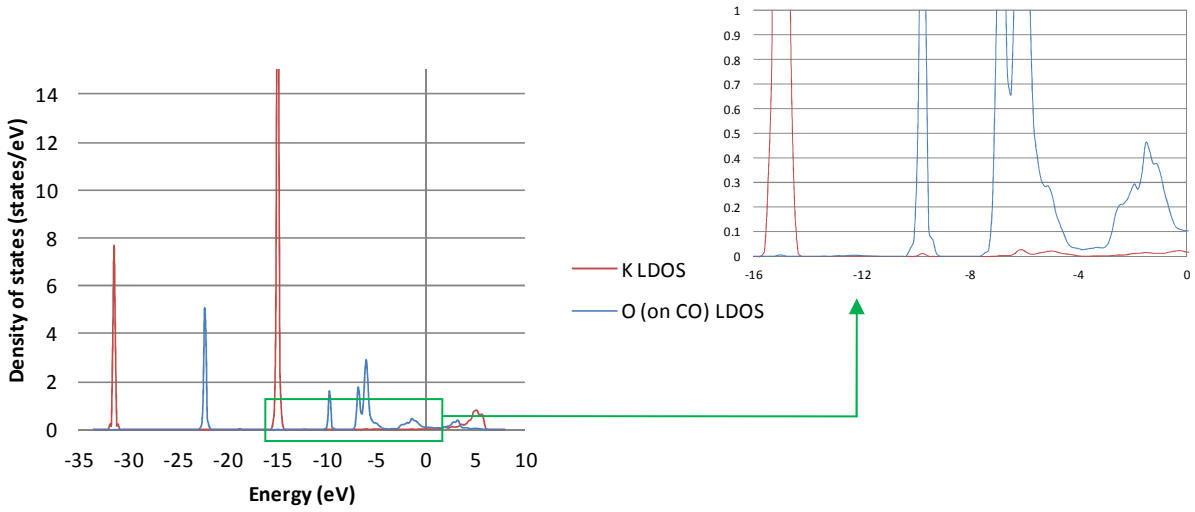


**Figure A.40:** LDOS of K and O (of CO) when CO is adsorbed in the 1F valley CO adsorption configuration for CO co-adsorption with KO on the $Fe_5C_2(100)_{0.00}$ surface (Calculated using RPBE functional, σ=0.2eV, k-point mesh of 3 × 5 × 1, vacuum spacing of 20Å and a cutoff energy of 450eV)

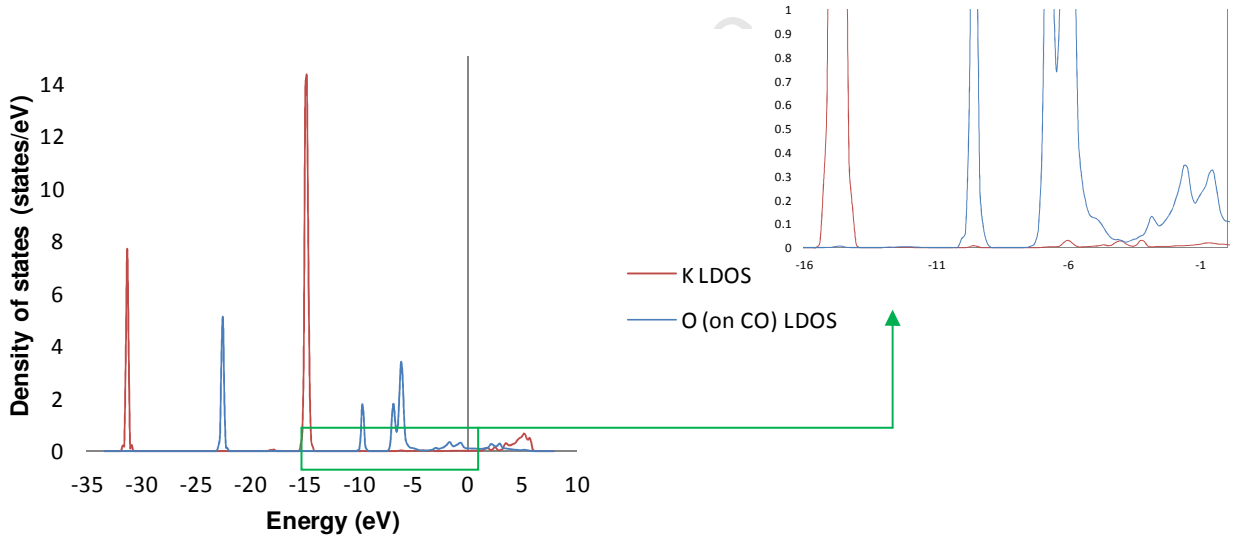


**Figure A.41:** LDOS of K and O (of CO) when CO is adsorbed in the 2F CO adsorption configuration for CO co-adsorption with KO on the $Fe_5C_2(100)_{0.00}$ surface (Calculated using RPBE functional, σ=0.2eV, k-point mesh of 3 × 5 × 1, vacuum spacing of 20Å and a cutoff energy of 450eV)

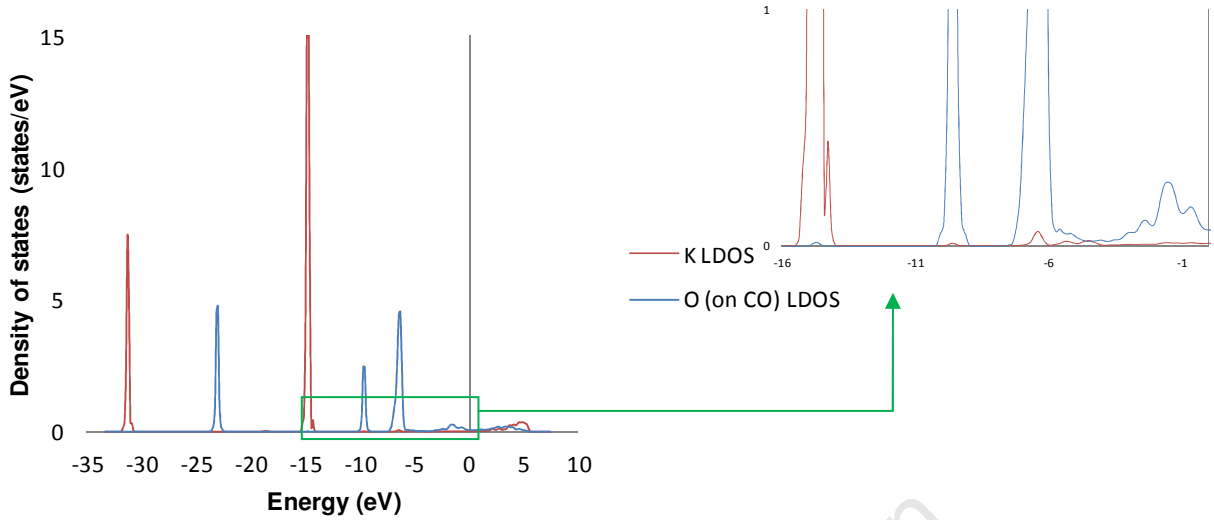


**Figure A.42:** LDOS of K and O (of CO) when CO is adsorbed in the 1F ridge CO adsorption configuration for CO co-adsorption with KO on the $Fe_5C_2(100)_{0.098}$ surface (Calculated using RPBE functional, σ=0.2eV, k-point mesh of 3 × 5 × 1, vacuum spacing of 20Å and a cutoff energy of 450eV)

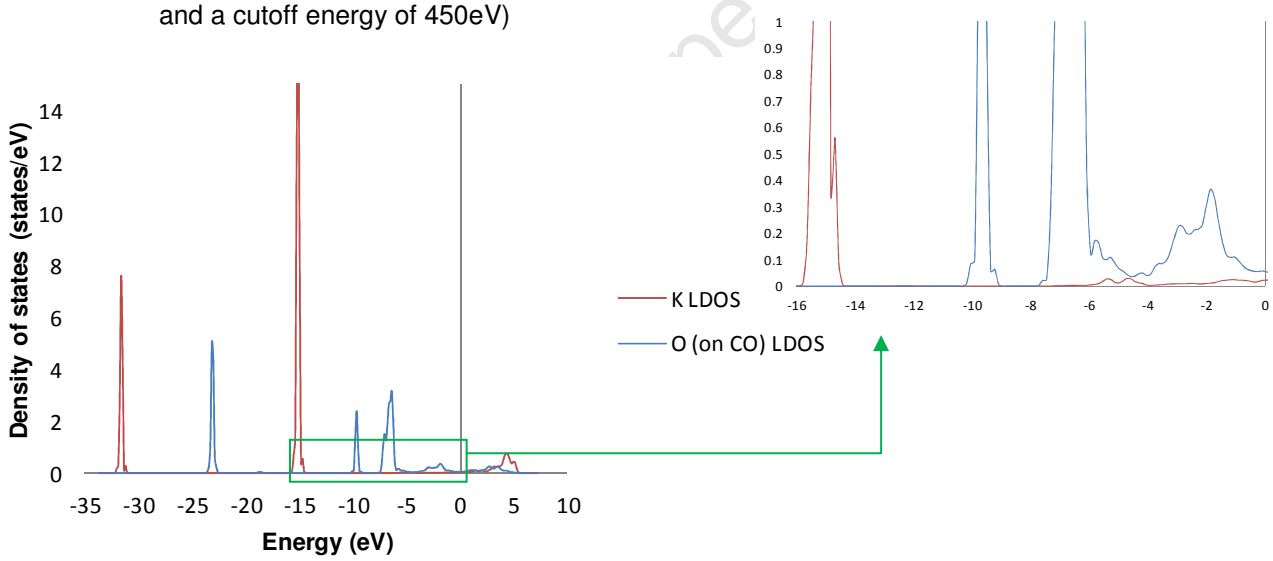


**Figure A.43:** LDOS of K and O (of CO) when CO is adsorbed in the 1F valley CO adsorption configuration for CO co-adsorption with KO on the $Fe_5C_2(100)_{0.098}$ surface (Calculated using RPBE functional, σ=0.2eV, k-point mesh of 3 × 5 × 1, vacuum spacing of 20Å and a cutoff energy of 450eV)

## Appendix D – Thermodynamic Analysis

The thermodynamic analysis was based on the reaction which could occur at Fischer-Tropsch conditions due to the large amount of $H_2O$ present:

$$K_{ads} + H_2O_{(g)} \leftrightarrows KO_{ads} + H_{2\,(g)}$$

The aim of the thermodynamic analysis was to determine at process conditions, which potassium species would be present on the surface. Calculating the Gibbs free energy:

$$G = H - TS$$

Where H is the enthalpy and, T is the temperature and S is the entropy. What has been calculated using DFT is the electronic energy which is the enthalpy not including terms for vibration, rotation and translation. To account for these terms as well as the entropy the data gathered from the vibrational analysis was applied. The expanded equation is now:

$$G = E_{calc} + (H_{vib} + H_{trans} + H_{rot} + RT) - T(S_{vib} + S_{trans} + S_{rot})$$

Where the $E_{calc}$ is the calculated electronic energy and the H and S terms are the enthalpic and entropic contributions of vibration, translation and rotation respectively. For the adsorbed species this equation simplifies, since adsorbed species are relatively fixed to the surface, the enthalpic and entropic contributions of the vibrational and rotational terms can be neglected. However, both K and KO on both surfaces, the maximum barrier for diffusion of K is very low in the direction of the valley. Therefore, this was treated as a translational mode for both species. The equations used to calculate the enthalpy and entropy corrections were taken from work by Hirano (1993) found in the MOPAC manual.

For the corrections to enthalpy:

$$H_{trans} = \frac{3}{2}RT$$

$$H_{rot(linear)} = RT$$

$$H_{rot(non-linear)} = \frac{3}{2}RT$$

$$H_{vib} = \frac{R}{k}\frac{1}{2}\sum_i h\nu_i + \frac{R}{k}\sum_i \frac{h\nu_i \, exp\left(-\frac{h\nu}{kT}\right)}{(1 - exp\,(-\frac{h\nu}{kT})}$$

Where R is the universal gas constant 8.314 $Jmol^{-1}K^{-1}$, T is the temperature in Kelvin, h is Plank's constant ($6.626\times10^{-34}$ Js), k is the Boltzmann's constant ($1.38\times10^{-23}JK^{-1}$) and $v_i$ are the individual vibrational frequencies in Hertz.

For the corrections to entropy:

$$S_{vib} = R\sum_i \frac{\mathrm{hv_i}\exp\left(-\frac{\mathrm{hv}}{\mathrm{kT}}\right)}{(1-\exp\left(-\frac{\mathrm{hv}}{\mathrm{kT}}\right)} - R\sum_i \ln\left(1-exp\left(-\frac{Hv_i}{kT}\right)\right)$$

$$S_{trans} = \frac{5}{2}RlnT + \frac{3}{2}Rlnw - RlnP - 2.31482$$

$$S_{rot(linear)} = Rln\left(\frac{8\pi^2 IkT}{\sigma h^2}\right) + R$$

$$S_{rot(non\ linear)} = \frac{R}{2}\ln\left(\frac{\pi}{\sqrt{\sigma}}\frac{8\pi^2 cI_A}{h}\frac{8\pi^2 cI_B}{h}\frac{8\pi^2 cI_C}{h}\left(\frac{kT^3}{hc}\right)^3\right) + \frac{3}{2}R$$

Where *w* is the molecular weight, $I_x$ is the moment of inertia ($kg.cm^2$), σ is the symmetry number (taken as 2 for both $H_2$ and $H_2O$), P is the pressure (30 atm), *c* is the speed of light ($ms^{-1}$) and the other constants as described above.

The moments of inertia of $H_2O$ was taken from David (2006) with values of $1.09\times10^{-47}$ $kgcm^2$, $1.91\times10^{-47}$ $kgcm^2$ and $3.00\times10^{-47}$ $kgcm^2$. The moment of inertia of $H_2$ was $4.67\times10^{-48}$ $kgcm^2$ (Gearhart, 2008).

The other parameters used to calculate the thermodynamic corrections are detailed in Table A.1. The molecular mass given is the molecular mass used to calculate the translational correction. Therefore, for KO the molecular mass of O was not considered as it did not translate across the surface.

**Table A.1:** Parameters used to calculate corrections to enthalpy and entropy

| Calculated parameters | K | KO | $H_2$ | $H_2O$ |
|---|---|---|---|---|
| Vibrational modes (Hz) | 2.74E+12 | 1.60E+13 | 1.32E+14 | 1.13E+14 |
| | 1.82E+12 | 9.93E+12 | | 1.10E+14 |
| | | 6.39E+12 | | 4.78E+13 |
| | | 3.07E+12 | | |
| | | 2.28E+12 | | |
| Molecular weight ($10^{-3}kgmol^{-1}$) | 39.098 | 39.0983 | 2.01588 | 18.01528 |

## Appendix E – Linear Programming to determine the mobility of K along the surface

Linear programming was used to investigate the mobility of the K atom along the surface between the valley iron atoms. The motion of the K atom along the valley was modelled as a straight line along from the K atoms stable position between the valley iron atoms. This was done for K adsorbed alone and co-adsorbed with O on both the $Fe_5C_2(100)_{0.00}$ and $Fe_5C_2(100)_{0.098}$ surfaces. The motion of the K atom in the z direction, i.e. into the vacuum was allowed to vary. The x and y coordinates of the K atom were held constant at a series of positions along the surface between the valley iron atoms as illustrated in the Figure below. Since there are only two variables and the path is a straight line, selecting a step-size for either the x or the y coordinate means that the other variable is also defined. This is illustrated mathematically in the equation below:

$$y = y_1 + (x - x_1)\frac{y_2 - y_1}{x_2 - x_1}$$

This created a series of K positions along the valley at which geometry optimisations were carried out. These geometry optimisations allowed the optimisation of the K in the z direction, into the vacuum. The electronic energies for the system with K in the different positions was then compared and the difference between the energies gave the change in energy for the diffusion of K across the surface from one position to another.

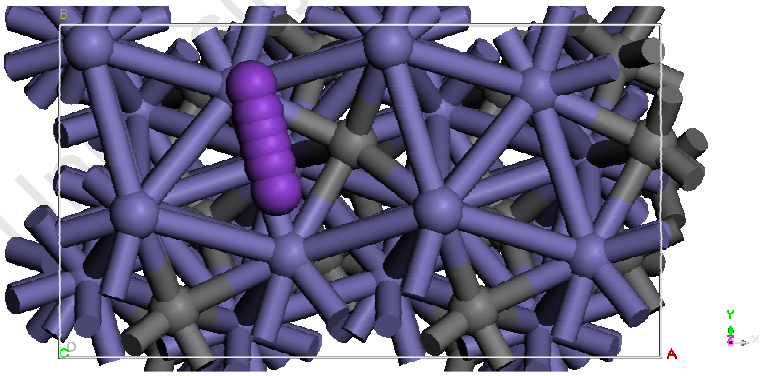

**Figure A.44:** Simulated path of the K atom along via linear programming along the valley of the $Fe_5C_2(100)_{0.00}$ surface.